University of Copenhagen, Denmark
Faculty of Science, PhD School of Science
Niels Bohr Institute

Ph.D. THESIS

A SEARCH FOR SUPERSYMMETRIC LOW MASS HIGGS BOSON AT THE LHC WITH THE ATLAS DETECTOR

Pavel Ježˇ

Academic Advisor: Stefania Xella
Date of submission: 07/11/2011

Abstract

The Next-to-minimal supersymmetric extension of the Standard Model (NMSSM) has one additional gauge singlet field on top of the particle content of the widely known MSSM. This leads to two new neutral bosons in the Higgs sector and one new fermion (5th neutralino). The NMSSM phenomenology can therefore be quite different from MSSM expectations. The "Ideal Higgs" scenario expects existence of a CP-even SM-like Higgs boson h_1 below the LEP mass limits (100-110 GeV) decaying predominantly to the pair of light (less than 11 GeV) CP-odd Higgs bosons a_1 which then decay to the pairs of τ leptons. The mass of a_1 has already been quite constrained from below by B-factories, but limits for the mass of a_1 close to the Υ resonances are still quite weak. This thesis presents a search for the a_1 resonances being produced directly by gluon fusion with both τ leptons decaying leptonically to an electron and a muon and sets new experimental limits in a mass region close to the Υ resonances. The tau trigger is a key element of the study of low mass Higgs bosons, including the indirect production of the a_1 via $h_1 \to a_1 a_1 \to 4\tau$. The LHC data delivers more than one interaction per event - so-called pile-up and the amount of pile-up will increase significantly in 2012. Data and Monte Carlo simulations have been studied to find the effect of pile-up on the tau trigger performance. Eventually, the trigger selection was optimized for the pile-up environment.

Resumé på dansk

Den næst-til-minimale supersymmetriske udvidelse af Standard Modellen (NMSSM) har et ekstra gauge-singlet-felt oven på partikelindholdet af den almindeligt kendte MSSM. Dette fører til to nye neutrale bosoner i Higgs-sektoren og en ny fermion (5. neutralino). NMSSM fænomenologiens kan derfor være meget forskellig fra forventningerne fra MSSM. Det "Ideele Higgs"-scenario forventer eksistensen af en CP-lige og SM-lignende Higgs-boson, h_1, under LEP masse-grænserne (100-110 GeV) henfaldende overvejende til par lette (mindre end 11 GeV) CP-ulige Higgs-bosoner, a_1, som derefter henfalder til et τ-lepton par. Massen af a_1 er allerede blevet betydeligt begrænset nedefra af B-fabrikker, men grænserne for a_1-massen tæt på Υ-resonanser er stadig ret svage.

Denne afhandling præsenterer en eftersøgning efter a_1-resonanser, produceret direkte af gluon-fusion med begge τ-leptoner henfaldende leptonisk til en elektron og en myon og fastsætter yderligere nye eksperimentelle grænser for a_1-massen i en masseregion tæt på Υ-resonanserne.

Tau-triggeren er et centralt element i studiet af Higgs-bosoner med lav masse, herunder indirekte produktion af a_1 via $h_1 \to a_1 a_1 \to 4\tau$. LHC-data leverer mere end én interaktion per event, kendt som ophobning, og mængden af denne ophobning vil stige betydeligt i 2012. Data og Monte Carlo-simuleringer er blevet undersøgt for at finde effekten af disse ophobninger på tau-triggerens ydeevne. Til sidst blev triggerens udvælgelsekriterier optimeret til ophobningen fundet i data.

Contents

List of Figures

List of Tables

Preface

The origin and composition of matter is one of the great questions of humanity. Millenia ago, ancient philosophers in India and Greece postulated that matter consists of tiny, indivisible parts named as *atoms*[1]. However, for a very long time, the atoms were regarded as a mere philosophical concept with little or no relation to the real life. This changed in 1805 when John Dalton identified atoms with elements – basic substances that could not be broken down by methods of chemistry. Some years later, Dmitri Mendeleev found an underlying periodicity in the seemingly chaotic set of elements and published the first functional periodic table. It was the first indications that atoms might have some structure.

In 1897, J. J. Thomson discovered the electron [1], the first of what we now call *elementary particles*, and concluded that they were a component of every atom. Thus the *indivisible* was broken. Just a couple of years later in 1911, H. Geiger and E. Marsden discovered under the direction of E. Rutherford [2], that there is a nucleus inside every atom, that is extremely tiny compared to the atom size itself, and in 1917 Rutherford proved that the nucleus of the hydrogen is present in other nuclei, thus discovering the proton [3]. Even before that, the mechanics of the hydrogen atom has been explained by N. Bohr [4]. Finally in 1932, J. Chadwick discovered the neutron [5] – a neutral companion of the proton in the atomic nuclei. It was a tremendous success of science: all the matter known to a man could have been explained in terms of just three elementary particles. And most of the atomic behaviour could have been described and predicted by the quantum mechanics developed in 1920's by E. Schrödinger, W. Heisenberg, M. Born, W. Pauli, N. Bohr and others, based on the earlier works of M. Planck and A. Einstein [6].

But as always, there were unanswered questions: How can a nucleus hold together if it is made only from positively charged and neutral particles? What is the *strong force* that holds it together? And why the energy seems to be lost in a β radioactive decay? What is the nature of this *weak force* that make nuclei decay? And is it possible to merge the theory of special relativity and electromagnetism with the quantum mechanics?

The first two questions were answered by H. Yukawa's theory of strong interaction that predicted that strong interaction is mediated by mesons [7]. W. Pauli explained the loss of energy in β decays by presence of a weakly interacting particle – neutrino [8], and the weak force has been described by E. Fermi [9]. Finally, quantum electrodynamics – a quantum theory of electromagnetic field – has been formulated in 1940's by H. Bethe, S.-I. Tomonaga, J. Schwinger, R. Feynman and F. Dyson [10, 11].

Meanwhile, new particles were being discovered. First was the muon [12] that was originally thought to be the Yukawa's meson mediating the strong interaction. When it turned out not be the case, we were left with a particle that did not fit anywhere in the neat structure of protons, neutrons and electrons. In 1947, the first true mesons – pions – were discovered in cosmic rays [13]. They were soon followed by kaons [14] and many new particles found at the particle accelerators all over the world. In 1960s, hundreds of particles were known already and

[1] From ancient Greek $\alpha\tau o\mu o\varsigma$ (atomos) meaning "indivisible".

it seemed very unlikely that all of them will be elementary. Particle physics was waiting for its periodic table.

In 1964, M. Gell-Mann and G. Zweig proposed the existence of *quarks* [15], fundamental constituents of matter that combine to form the particles known as hadrons, which form the vast majority of all the particles. The original model used three quarks to describe all hadrons known in 1960's and, similarly as periodic table of Mendeleev, this model was able to predict the existence and properties of some yet-to-be discovered particles.

In the second half of 1960 S. Glashow found a way how to combine quantum electrodynamics and Fermi's theory of weak interaction, thus giving rise to a theory of *electroweak* interaction. In 1967, S. Weinberg and A. Salam incorporated the Higgs mechanism (itself developed by J. Goldstone, Y. Nambu, P. Higgs and others) into Glashow's theory: the *Standard Model* was born [9].

In 1973, the Standard Model was amended by the quark flavour mixing matrix named *CKM matrix* after N. Cabibbo, M. Kobayashi and T. Maskawa, that increased the number of quarks to six [9]. Finally, in early 1970's, the theory of strong force interaction, involving quarks and mediated by *gluons* has been formulated by D. Gross, D. Politzer and F. Wilczek [16, 17]. The Standard Model was completed.

The Standard Model was able to bring order back to particle physics: the matter was described by 12 elementary fermions that interact via 3 forces mediated by 12 elementary bosons. It was able to stand the test of time and many new results that were extraordinarily consistent with its prediction [18]. Only one thing has remained – the experimental confirmation of the Higgs boson, a by-product of the Higgs mechanism providing masses to all Standard Model particles.

Towards the end of the twentieth century, some new experimental results started to suggest that the Standard Model may not be the complete picture of particle physics and many new theoretical extensions (known as Beyond Standard Model theories) have been developed. The theories containing so-called *supersymmetry* were of particular theoretical interest. Those theories postulate the existence of a symmetry between elementary fermions and bosons that is able to provide answers to some of the questions which are left unanswered by the Standard Model.

In 2000's a model called *Ideal Higgs Scenario* was developed as a possible answer to experiments not observing any conclusive signs of the Higgs boson. Borrowing some ideas from the supersymmetric theories, it assumes the existence of several Higgs bosons. One of the bosons is expected to be very light, much lighter than the standard experimental limits on the Higgs boson. The heavy Higgs boson, which was being intensively searched for, will then be able to escape detection by decay to the light bosons which had not been detected [19].

Chapter 1 of this thesis provides a detailed description of the Standard Model as well as discussion of the problems not addressed withing the Standard Model. This is followed by the overview of the main concepts of Supersymmetry and finalized by a detailed account on the Ideal Higgs Scenario.

The experimental search for the evidence of the Ideal Higgs Scenario is a key objective of this work. The data are provided by the world's largest particle accelerator (LHC) and registered by the ATLAS detector. The LHC and the ATLAS are introduced and described in chapter 2.

The most promising search for Ideal Higgs Scenario in the early LHC data is via direct production of the very light boson. It allows to probe the most interesting and challenging case, when the mass of the light Higgs boson is very similar to the masses of well known Υ particles. This situation is extremely well motivated both from theoretical and experimental side: if a_1 exists, its most natural mass will be close to the Υ resonances. Due to relying on the a_1 produced in Υ decay, the mass region above $\Upsilon(1S)$ mass is almost unconstrained by the previous results

from the B-factories.

Chapter 3 presents the analysis developed by the author to search for the directly produced a_1 in a decay to τ leptons. It is the first analysis ever to probe directly the Υ mass region for the presence of very light Higgs boson from the Ideal Higgs Scenario [20]. The results are used to set new limits on the Next-to-the-minimal supersymmetric extension of the Standard Model, within which the Ideal Higgs Scenario can be realized. When combined with the other ATLAS search in the $a_1 \to \mu\mu$ channel, it is possible to limit the existence of a_1 in the whole region between 6 and 12 GeV. Finally with some improvements discussed in this thesis, the analysis could be able to set better limits on the Ideal Higgs Scenario than are the currently best limits from LEP.

During the analysis improvements efforts, a topological electron-muon trigger has been designed, developed and commissioned (section 3.12). It is the first ATLAS trigger that uses topological combination of a two trigger objects of a different types.

With the increasing amount of data collected by the ATLAS experiment, it is possible also to look for the Ideal Higgs Scenario in a decay of heavier Higgs boson to a pair of the very light ones that subsequently decay to tau leptons. Therefore author has studied the performance of the tau trigger in ATLAS [21, 22] in order to improve its selection in the presence of multiple interactions in every event delivered by the LHC. This work resulted in a optimization procedure that is described in chapter 4 and in [23, 24]. The results presented in this thesis provide guidelines for the tau trigger selection in 2012.

The final chapter of this thesis provides a summary and discussion of all results obtained in chapters 3 and 4 together with the future outlook.

Chapter 1

The Theoretical Motivation

1.1 Standard Model

1.1.1 Success of the Standard Model

The Standard Model is currently the best theory for description of the behaviour of elementary particles. It is a renormalizable quantum field theory (QFT) with an internal symmetry group $SU_C(3) \otimes SU_L(2) \otimes U_Y(1)$. Several beautiful books exist on this subject: construction of the quantum field theories and their renormalization are described in [10] or [11]. The electroweak part of the Standard Model is discussed in detail in [9], while the strong interactions are the subject of [15] and [25].

The Standard Model (SM) incorporated all particles known at the time of its inception and predicted several new, most importantly the W and Z bosons. According to the SM, elementary fermions come in three structurally identical families. Each of them contains two quarks and two leptons (for more details see tab. 1.1). They interact via 12 intermediate vector (i.e. spin 1) bosons. The photon is responsible for the electromagnetic interaction, $W^{\pm}$ and Z for the weak interaction, while eight gluons (each with different color charge) mediate the strong interaction. For more details consult tab. 1.2. Note that all above mentioned particles have been discovered and their properties are listed in [18].

According to QFT, particles that we can see in an experiment are described by excitations of quantum fields.

Those fields transform under the SM internal symmetry in a straightforward way: because the gauge group is a tensor product of three groups, it is possible to act by each of them separately (i.e the transformations generated by them commute). Let D be an representation of the group $SU(3)$ or $SU(2)$ or $U(1)$ on an n-dimensional vector space and let Φ be an n-plet of quantum fields. The transformation from the n-plet Φ to the n-plet Φ' is

$$\Phi'_i = D(g)_{ij}\Phi_j \ , \tag{1.1}$$

where we assume summation over repeated indices and g is the element of the group. Because all groups in tensor product $SU(3) \otimes SU(2) \otimes U(1)$ are Lie groups [26], we can rewrite matrix $D(g)$ from the previous equation in a more user friendly way:

$$D(g) = e^{i\Lambda_j T_j} \ , \tag{1.2}$$

where T_j are group generators and Λ_j are unambiguous parameters, i.e. each g has its own set of Λ's. Note that in case of the abelian group $U(1)$, previous relations become much simpler as it has only one irreducible representation that is onedimensional. Therefore, $D(g)$ is just a

	First generation	Second generation	Third generation	Electrical charge	Interaction
quarks	u-up	c-charm	t-top	+2/3	all
	d-down	s-strange	b-bottom	-1/3	all
leptons	e-electron	μ-muon	τ-tauon	-1	elmag., weak
	ν_e - e-neutrino	ν_μ - μ-neutrino	ν_τ - τ-neutrino	0	weak

Table 1.1: Overview of the elementary fermions. First two lines are the list of quarks, bottom two lines list leptons. The column "interactions" states in which Standard Model interaction given particle participate. The meaning of "all" interactions is electromagnetic, strong and weak interaction.

Interaction mediated	Name	Spin	Electrical charge	Mass	Count
weak	$W^\pm$	1	±1	80.4 GeV	2
	Z^0	1	0	91.2 GeV	1
electromagnetic	γ	1	0	0	1
strong	g	1	0	0	8

Table 1.2: Overview of the elementary bosons according to the interaction they mediate. The count indicates the total number of particles in a given category: there are two W bosons and 8 gluons. Masses from [18].

complex number on a unit circle and can be rewritten as $D(g) = e^{i\Lambda Y}$ where Y is an arbitrary parameter, whose meaning will be described later.

The most peculiar thing about the Standard Model is that its particles are not in a single representation, but rather in 5 distinct representations of $SU(3) \otimes SU(2) \otimes U(1)$. The schematic picture is in fig. 1.1. Left-handed up-type and down-type quarks form $SU(3)$ triplet and $SU(2)$ doublet, left-handed charged lepton and neutrino form $SU(3)$ singlet and $SU(2)$ doublet, right-handed up-type quarks form $SU(3)$ triplet and $SU(2)$ singlet, the same is true for down-type quarks. The fifth representation contains righthanded charged lepton and is $SU(3)$ and $SU(2)$ singlet. As fig. 1.1 suggests, all representations have also different hypercharges, i.e. transform properties under $U(1)$. The hypercharge assignment may seem somehow haphazard, but it gives correct electrical charges and, moreover, leaves the SM anomaly free[1].

From the organization of the multiplets we can clearly see how particles interact. For example, left-handed quarks interact via both strong interaction ($SU(3)$ triplet) and weak interaction ($SU(2)$ doublet), while right-handed quarks interact only strongly ($SU(2)$ singlets). We can also see that the weak interaction violates parity (only left-handed particles interact weakly), which was discovered long before the SM was formulated.

The SM is a good way of classifying elementary particles and predicting very basic phenomenology. Note, however, that at least since the 1990's it has been accepted that the Standard Model is not the final and complete description of the subatomic particles. This will be described in section 1.1.2.

[1] Anomaly is a failure of theory to restore the symmetry when the symmetry breaking parameter goes to zero. For example QED posses exact chiral symmetry (conservation of helicity) if we set the mass of electron to zero. In SM the anomaly is caused by triangular Feynman diagram (fig. 1.2). If we want this anomaly to cancel identically, we obtain strict restriction on the hypercharges: only one of them can be chosen arbitrarily and others are then fixed [27, 28].

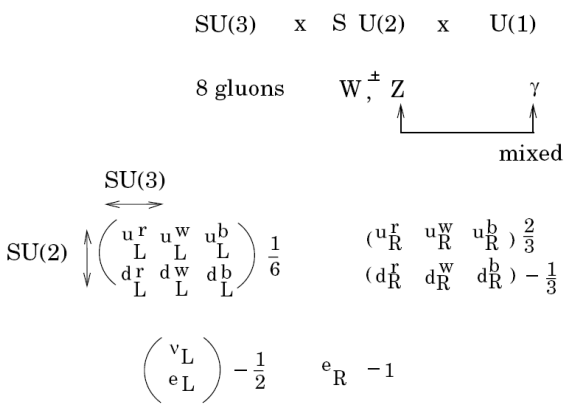

Figure 1.1: Scheme of the Standard Model representation. Fig. shows the 3 gauge groups of the SM together with respective gauge particles. It also shows 5 multiplets made from the SM fermions together with their hypercharge. Arrows indicate in which direction the gauge groups $SU(2)$ and $SU(3)$ act. Originally from [29].

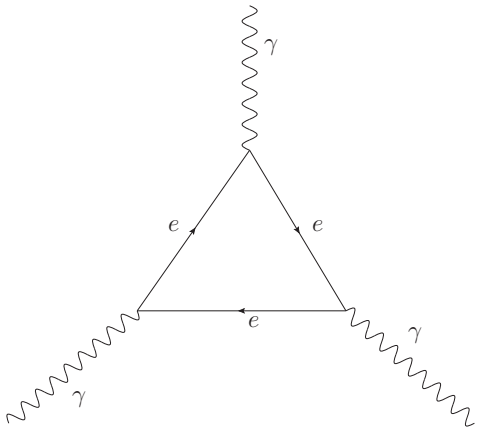

Figure 1.2: Feynman diagram of a 3-point photon interaction via electron loop. By choosing hypercharges of the SM appropriately, the contribution from this diagram would be zero. It is also referred to as "anomaly cancellation condition".

Besides acting as a Mendeleev table of particle physics, the Standard Model has also very rich dynamical content which can be formulated in an extremely economical way.

The general gauge transformation can be written as in (1.1). It can be viewed as a *global* gauge transformation, because it is identical in all space-time points. However, the SM assumes that the gauge invariance is not global, but rather local[2], i.e. the transformation should be (using (1.2) and dropping vector indices)

$$\Phi'(x) = e^{i\Lambda_j(x)T_j}\Phi(x) \tag{1.3}$$

This simple principle has tremendous consequences. If we take the Dirac Lagrangian of a

[2]The motivation for this decision is the fact that the information does propagate with the finite speed, so the gauge transformation cannot happen simultaneously at all spacetime points where the transformed field is defined.

free spin $\frac{1}{2}$ particle, represented by a field ψ

$$\mathscr{L}_0 = i\bar{\psi}\gamma^\mu\partial_\mu\psi - m\bar{\psi}\psi \ , \tag{1.4}$$

we can immediately see, that it is has global $U(1)$ invariance because Dirac conjugate ($\overline{\psi} = \psi^\dagger\gamma_0$) transforms as

$$\overline{\psi}' = \overline{\psi}e^{-i\Lambda} \ . \tag{1.5}$$

However, when we demand that $\Lambda = \Lambda(x)$, the Lagrangian (1.4) loses the symmetry, because the differentiation of the composite function in the first term ("kinetic term") produces another term which was not in the original Lagrangian. In order to restore symmetry, we are forced to introduce a term whose transformation properties will cancel those of the kinetic term. In practice this means that we are introducing a new field (particle) A_μ which will transform like

$$A'_\mu(x) = A_\mu(x) + \frac{1}{g}\partial_\mu\Lambda(x) \ , \tag{1.6}$$

and the new term in Lagrangian will be $\mathscr{L}_{int} = g\bar{\psi}\gamma^\mu\psi A_\mu$ where g is arbitrary real number. It is straightforward to show that $\mathscr{L}_0 + \mathscr{L}_{int}$ is indeed local gauge invariant. From the mathematical point of view we have moved from the ordinary derivative to the covariant derivative defined as

$$D_\mu = \partial_\mu - igA_\mu \ . \tag{1.7}$$

which in turn allows us to write new Lagrangian in a very aesthetically pleasing way

$$\mathscr{L} = i\bar{\psi}\gamma^\mu D_\mu\psi - m\bar{\psi}\psi \ . \tag{1.8}$$

What is the physical meaning of the newly added term? It is nothing else than the interaction between an electron, positron and photon: the basic vertex of the QED[3]. We can conclude that the requirement of the local gauge invariance brings interaction to the static field theory.

The same procedure (properly modified for non-abelian groups) is applied also in the case of $SU(2)$ and $SU(3)$. Because of the non-commutative nature of those two groups, we obtain (apart from QED-like fermion-antifermion-boson vertex) vector boson cubic and quartic self-interaction. Strangely enough, all those vertices have been experimentally confirmed.

However, our choice of representations of the SM gauge group has a serious phenomenological problem: because of the different transformation properties of left- and right-handed fermions, we cannot have any mass terms ($\sim m(\overline{\psi}_R\psi_L + \overline{\psi}_L\psi_R)$) in the Lagrangian as they explicitly break the local gauge invariance. Also, we cannot have any gauge boson mass terms, because they spoil gauge invariance as well.

Among the many solutions to this problem, the spontaneous symmetry breaking (SSB) approach is by far the simplest way how to give masses to the elementary fermions and vector bosons. The basic idea is that the Standard Model has the full gauge symmetry only at some high energy scale, but at the energy scales that we have been probing so far, the Standard Model is in a ground state that does not have the full symmetry. The spontaneous symmetry breaking is quite common in nature: consider ferromagnetic materials that lose their spatial rotation invariance when cooled below the Curie temperature.

In the Standard Model the SSB is achieved by adding to the Lagrangian a term with a scalar field which has all space-time and gauge symmetries of the theory but its ground state does not.

[3]Quantum Electrodynamics. See [10, 11, 9] for more details.

The added term should have the form of the "Mexican hat potential", i.e. something like $\partial_\mu\phi\partial^\mu\phi^* - \mu^2\phi\phi^* + \lambda(\phi\phi^*)^2$, in case of complex scalar field ϕ. For $\lambda = 0$ we would get the Klein-Gordon equation with reversed sign for the mass term. So let's suppose $\lambda > 0$. In this case, the potential is bound from below and its ground state is infinitely degenerate (complex circle) and has a value of $\mu/\sqrt{2\lambda} = v/\sqrt{2}$. So in the ground state we have broken the original $U(1)$ symmetry of the Lagrangian. Next, we can factorize the original complex field

$$\phi(x) = \rho(x)\exp\left(i\frac{\pi(x)}{v}\right)$$

where both ρ and π are real fields. As another step we can choose the minimum value ("vacuum expectation value") as a reference point and expand the original field around this value:

$$\rho = v + \sigma$$

If we put all this back into the scalar field Lagrangian we obtain

$$\mathscr{L} = \frac{1}{2}\partial_\mu\sigma\partial^\mu\sigma + \frac{1}{2}\partial_\mu\pi\partial^\mu\pi - \lambda v^2\sigma^2 + \text{interaction terms} \tag{1.9}$$

where "interaction terms" are cubic or quartic in σ (yielding trilinear and quadrilinear Higgs boson self-interaction). Notice, that we got a mass term for the field σ (yielding mass $\sqrt{2\lambda}v$) and no mass term for field π, indicating it is unphysical. It can be shown [30] that this is a general property of spontaneous symmetry breaking. For each broken continuous symmetry we obtain one massless boson (called Goldstone boson). Also, at least one massive scalar boson always survives this procedure (so-called Higgs boson).

In case of the SM, the original $SU(2)\otimes U(1)$ symmetry is spontaneously broken down to the $U(1)$ symmetry. Three continuous symmetries are broken ($SU(2)$ has 3 generators) meaning we need to add at least 4 real scalar fields, locally invariant under $SU(2)\otimes U(1)$. The easiest way to satisfy that requirement is to introduce a complex $SU(2)$ doublet Φ instead of one complex field in the previous example.

The next steps are the same: we factorize and shift the zero to the ground state value. However, because we still have a residual $U(1)$ symmetry after the SSB, we can choose the gauge in which the complex phase of our field is 1, so we can get rid of the unphysical Goldstone bosons.

What remains is the mass term for the Higgs boson (as in the previous case) but also other terms that were not present before. Because all the derivatives in the SM Lagrangian are covariant, the Higgs boson automatically couples to the vector bosons and moreover, as the result of the field expansion around its ground value, the terms with vacuum expectation value v appear. But terms of type v^2-boson-boson are exactly the mass terms for the particular boson we were looking for. This also means that the Higgs-vector boson coupling is proportional to the mass of the vector boson.

Even more surprising is that if we rewrite the Lagrangian with the scalar potential in term of physical fields representing the photon and weak intermediate bosons, we obtain only 3 mass terms for W's and Z and no mass term for the photon.

The elementary fermions can be given masses via the Yukawa mechanism. That is, we add terms to the Lagrangian where the complex Higgs doublet couples to the doublet of left-handed fermions L and to the one right-handed fermion:

$$\mathscr{L}_{Yukawa} = -h_e\overline{L}\Phi e_R - h_e\overline{\overline{L}\Phi e_R} \tag{1.10}$$

Such a combination is a singlet under all gauge groups.

Afterwards, we can do the same as previously, so a complex doublet turns into a field of form $\binom{0}{v+\sigma}$. When we work out the matrix multiplication, we obtain fermion mass terms and also fermion-Higgs interaction. The important thing is that the coupling constants of these interactions are again proportional to the respective fermion masses.

Note, however, that this procedure will give masses only to the "down-type" fermions (electrons and down, strange and bottom quarks). To give masses to the "up-type" quarks, one should use

$$\widetilde{\Phi} = i\tau_2\Phi^* \tag{1.11}$$

where Φ^* is the complex conjugate of the complex Higgs doublet and τ_2 is the Pauli matrix

$$\tau_2 = \begin{pmatrix} 0 & -i \\ i & 0 \end{pmatrix} . \tag{1.12}$$

The quantity $\widetilde{\Phi}$ transforms under $SU(2)$ in the same way as original doublet Φ so it can give masses to the "up-type" quarks in the way described above.

Because SSB is able to give masses to all elementary particles, it is an integral part of the SM. However, as the Higgs boson has not been discovered yet, we cannot tell if the Standard Model SSB is realized in Nature[4].

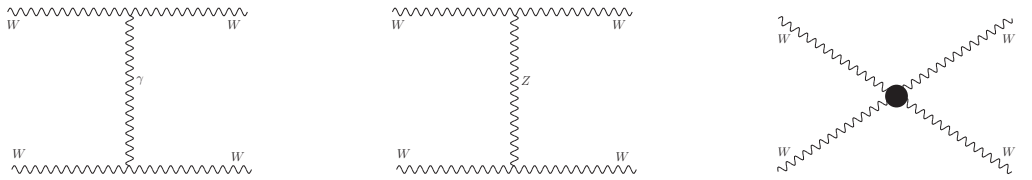

(a) WW scattering via γ (b) WW scattering via Z (c) direct WW scattering

Figure 1.3: The Feynman diagrams representing the processes mediating the WW scattering. Figs. 1.3(a) and 1.3(b) represent a t-channel of the processes included in the matrix elements $\mathcal{M}_{WW}^{(\gamma)}$ and $\mathcal{M}_{WW}^{(Z)}$, respectively. Finally the matrix element $\mathcal{M}_{WW}^{(direct)}$ is represented by the diagram in fig. 1.3(c).

The Higgs mechanism is not the only way to introduce masses to the particles of the Standard Model. There is, however, a good motivation for the existence of the scalar boson that has a coupling to the gauge boson proportional to the mass. Consider WW scattering – the representative diagrams are shown in fig. 1.3. The detailed calculation (see e.g. [9]) reveals that many divergences of the single diagrams cancel in the sum. There is, however, a residual quadratically divergent contribution of the form

$$\mathcal{M}_{WW}^{(\gamma)} + \mathcal{M}_{WW}^{(Z)} + \mathcal{M}_{WW}^{(direct)} = -g^2\frac{s}{4m_W^2} + O(1) \tag{1.13}$$

The coupling g is non-zero, so there is no way how this divergence can be eliminated without introducing a new particle with a new interaction. The divergence is indeed canceled with a new diagram involving the scalar exchange. This is shown in fig. 1.4. The matrix element of this interaction is

$$\mathcal{M}_{WW}^{(\sigma)} = g_{WW\sigma}^2\frac{s}{4m_W^4} + O(1) \tag{1.14}$$

[4]Even if we would find the Higgs boson in the future, it would not be enough to prove SSB. To demonstrate the existence of the electroweak SSB, all the parameters of the Higgs boson will have to agree with the predictions and some of them (like cubic and quartic Higgs self-coupling) are extremely difficult to measure [31].

	Measurement with Total Error	Systematic Error	Standard Model Fit	Pull
m_Z[GeV]	91.1975 ± 0.0021	0.0017	91.1875	0.0
Γ_Z[GeV]	2.4952 ± 0.023	0.0012	2.4957	-0.2
m_W[GeV]	80.392 ± 0.029	N/A	80.372	0.7
Γ_W[GeV]	2.147 ± 0.060	N/A	2.091	0.9
m_t[GeV]	171.4 ± 2.1	1.8	171.7	-0.2

Table 1.3: Several results from electroweak sector of the SM obtained at LEP and Tevatron. Total errors (column 2) include systematic errors (column 3). The pull is the difference between measurement and fit in units of the total measurement error. The numbers are from [32].

It is obvious that the divergences in (1.13) and (1.14) cancel if (and only if)

$$g_{WW\sigma} = g m_W \tag{1.15}$$

This shows us that a scalar boson that couples to the W bosons proportionally to their mass is necessary in order to preserve unitarity of the Standard Model.

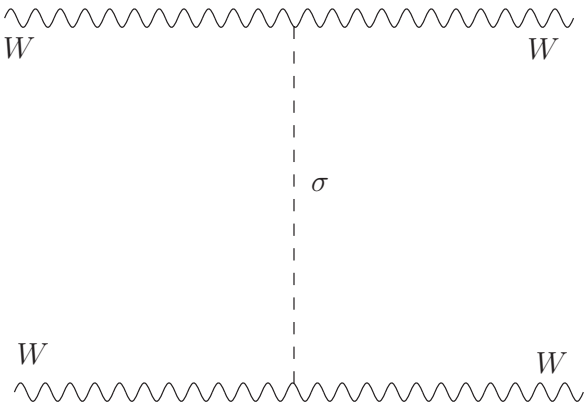

Figure 1.4: The Feynman diagrams of the process when WW scattering is mediated by the scalar boson. It is represented by the matrix element $\mathcal{M}^{(\sigma)}_{WW}$.

The previous paragraphs showed the core ideas of the SM, which is remarkably simple and *principled*. The Standard Model is a renormalizable quantum field theory with local $SU(3) \otimes SU(2) \otimes U(1)$ gauge invariance. The symmetry is spontaneously broken, giving rise to particle masses. This also means that the Standard Model predictions are unambiguous and that (in general) cannot be modified "a bit" to fit the results[5]. Some tests of the electroweak sector of the SM are summarized in tab. 1.3. We can see the remarkable agreement between the theory and the experiment.

The same is true also for the strong sector of the SM: Quantum Chromodynamics (QCD). The basic parameter of the strong interaction is the strong coupling constant. Its measurements are summarized in fig. 1.5. Each point in the plot is the result of hundreds of independent

[5]For example, the SM gives prediction of the Higgs boson production cross-section as a function of its mass. If the Higgs boson will be discovered, but its rate will be too high or too small compared to the prediction, it will indicate that the Standard Model is not correctly describing the electroweak SSB and some more elaborate model is needed to explain the data.

measurements, with different techniques and particles, yet the agreement with the theory is astonishing. Fig. 1.5 shows also another remarkable fact: the coupling constant is "running", i.e. the strength of interaction depends on its energy scale. It is decreasing with the energy: this property of QCD is called asymptotic freedom and allows the Standard Model to be extrapolated far beyond the energies of the current colliders.

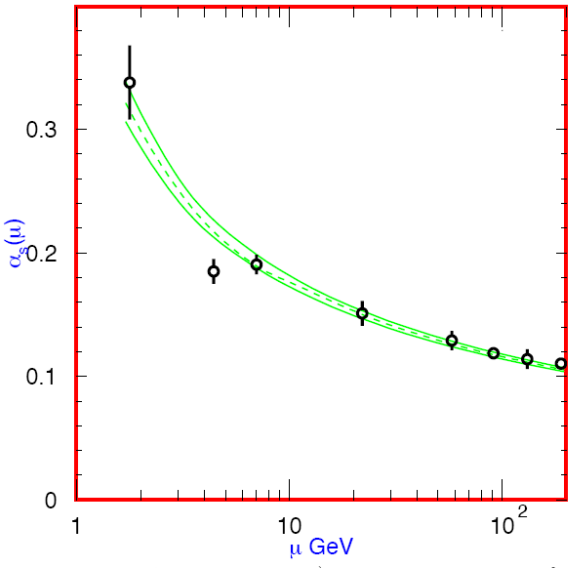

Figure 1.5: Summary of the values of strong coupling $\alpha_S(\mu)$. Dashed line is the theoretical value (note the decrease with μ), solid lines are 1 σ uncertainty. Circles with error bars are experimental results. Figure taken from [18].

1.1.2 Shortcomings of the Standard Model

Several experiments have already observed phenomena that are either described wrongly in the original formulation of the Standard Model, or not described at all. The most important of them are neutrinos, the dark energy and the dark matter, CP asymmetry and obviously gravity. Nevertheless, there are also several issues in the Standard Model that are not wrong *per se*, but rather very odd. They are listed in the section "Aesthetic flaws".

Neutrinos

The story of the neutrino resembles the story of the ugly duckling turning into a beautiful swan. It started as a desperate idea of Wolfgang Pauli to rescue the energy conservation and turned out to be one of the most interesting particles and very promising probe of new physics.

The careful reader might have noticed that there is no right-handed neutrino in the Standard Model, implying that a neutrino is expected to be *exactly* massless. However, at the end of the twentieth century, the Super-Kamiokande collaboration discovered that this is not the case [33, 34]. That is one of the strongest indications that the Standard Model is not the complete theory of particle physics and that some of the Beyond Standard Model (BSM) theories would offer more accurate description of the subatomic world[6].

[6]The neutrino mixing can be accommodated easily in the SM via the PNMS matrix which is the lepton analogue of the CKM matrix from the quark sector. It is, however, difficult to explain origin of neutrino masses within the framework of the Standard Model–why the Higgs coupling to neutrinos is 5 orders of magnitude smaller than

Recently, the OPERA collaboration claimed [36] that neutrinos propagate with a speed that is greater than the speed of light in vacuum. If this result will be confirmed, it will have consequences also on the validity of the Standard Model — for example the neutrinos could no longer be considered invariant under the Lorentz transformation so the whole concept of the weak interaction (derived under the assumptions of Lorentz invariance of all participating particles) will have to be revisited.

In spite of many experiments in the field of neutrino physics and gargantuan theoretical efforts, the neutrinos still remain one of the greatest mysteries of particle physics.

Dark Matter and Dark Energy

In 1933 Fritz Zwicky observed for the first time that the Universe contains considerable amount of non-luminous matter [37]. Throughout the 20th century many other experiments confirmed the existence of this substance that was given the name "Dark Matter". Part of it is formed by neutrinos, but the nature of most of the Dark Matter (so-called Cold Dark Matter: CDM) is an unsolved question.

At about the same time when the discovery of the neutrino oscillations permanently changed the world of particle physics, the cosmologists proved that the expansion of the Universe is accelerating due to a yet-unknown form of energy – Dark Energy – that amounts to almost three quarters of the mass of the Universe [18].

Neither CDM or Dark Energy are contained in the Standard Model. The SM can describe "only" the baryonic matter (that accounts for 4.6 % of the Universe mass) and the photon radiation (5.8 % of the mass of the Universe).

CP asymmetry

In our universe, the matter is clearly dominating over the antimatter. On the other hand, the Standard Model contains almost perfect symmetry between matter and antimatter. Is the asymmetry in the SM large enough to be able to create all the matter we observe today after most matter annihilated with the antimatter in the aftermath of the Big Bang? It turns out not to be the case.

In the Standard Model, the matter-antimatter symmetry can be viewed as the invariance under the simultaneous charge and parity transformation (CP symmetry). Already in the 1950's the CP asymmetry was observed experimentally in mixing of neutral Kaons and the Standard Model later showed that it originated from the complex phase in the quark flavour mixing matrix (so-called CKM matrix). Nevertheless, this asymmetry is too small to account for the matter-antimatter difference in the Universe.

The other source of CP asymmetry in the Standard Model can be the QCD Lagrangian. It is quite easy to add CP-violating terms there, but no CP violation has been observed in the strong sector which is also very puzzling.

Finally, by adding neutrino flavour mixing matrix (so-called PNMS matrix) to the lepton sector, additional CP asymmetry can arise from the complex of the PNMS matrix. Unfortunatelly, the mixing matrix parameters are known only partially at the moment, so additional experimental effort is necessary to check the CP asymmetry in the neutrino sector.

to all other particles. Therefore often SM extensions are used to explain origin of this discrepancy (e.g. see-saw models [35]).

Gravity

The Standard Model was by design made not to include gravity that had not been yet described on the subatomic scale. Nevertheless, the possible future "Quantum theory of everything" should contain the gravity.

Aesthetic flaws

On top of the serious shortcomings listed above that tell us that the Standard Model will never be anything else than a very good effective theory in a certain energy range, there are some peculiarities in the Standard Model that are "too odd to be real". Those are typically known as the *Hierarchy* and the *Fine tuning problem*. The hierarchy problem can be summarized in a question "Why is the electron so light and the top quark so heavy?". There are large differences in the mass scales between fermions without any clear pattern or explanation. Nevertheless, the mass spectrum of the Standard Model can be accepted as yet another set of constants of Nature.

The fine tuning problem is more serious - it corresponds to the question "Why is the Higgs mass so small?". Of course, we do not know yet what the mass of the Higgs boson is, but we know that since the Higgs boson is giving mass to the W and Z bosons in the Standard Model, its mass should be of the "Electroweak scale" (of the same order of magnitude as the W and Z boson masses). However, the loop corrections to the scalar masses are of the order of the largest scale in the theory. If we assume that the Standard Model is valid all the way up to the Planck scale (when gravity becomes too important to be neglected), we obtain loop corrections that are many orders of magnitude larger that the resulting corrected mass. This means that those corrections will have to be incredibly fine tuned in order to cancel each other in a way to yield the expected low Higgs boson mass. This does not seem very natural, so this is also called the "naturalness problem".

To better understand the nature and the origin of the fine tuning problem, let us consider a photon, electron and scalar boson and their 1-loop self-energy corrections. The corresponding diagrams are in fig. 1.6.

Consider at first the photon self-energy (fig. 1.6(a)). The contribution to the 2-point function from this diagram is divergent (as all one-loop diagrams in QED). However, after doing a dimensional regularization, the contribution vanishes identically. The reason is *exact* $U(1)$ gauge symmetry which "protects" the mass of the photon - it is massless in all orders of perturbation theory.

Slightly different situation is in case of electron self-energy (fig. 1.6(b)). This diagram is also quadratically divergent, and unlike the previous case, the divergence is not canceled by renormalization. It is rather replaced by a logarithmic divergence resulting in a correction which is proportional to the electron mass. This can be understood in terms of an approximate chiral symmetry – it is exact only for massless particle – and indeed, setting the electron mass to zero will completely cancel the contribution from diagram 1.6(b).

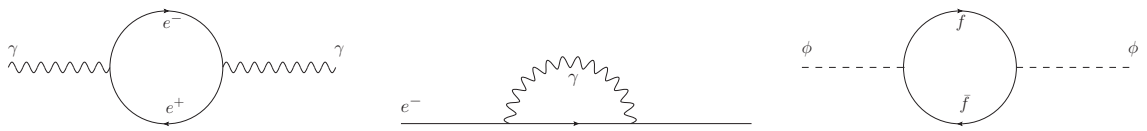

(a) Photon (b) Electron (c) Higgs boson

Figure 1.6: The Feynman diagrams of the one-loop mass corrections to the photon (fig. 1.6(a)), electron (fig. 1.6(b)) and the scalar (Higgs) boson (fig. 1.6(c)).

But for the scalar boson (fig. 1.6(c)) the situation is much worse. In this case there is no symmetry (exact or approximate) to protect it, so the divergence coming from the fermion loop remains quadratic, leading to corrections which are about 30 orders of magnitude larger than the expected mass for the Higgs boson, so a fine tuning of contributions at every order of perturbation theory is necessary to obtain the correct value. Such an approach is very implausible and led to the proposal of an additional symmetry. This symmetry between fermions and bosons that would cancel this divergence in the scalar boson mass is called *Supersymmetry* and it is described in detail in section 1.2.

1.2 Supersymmetry

The Supersymmetry (SUSY) is the symmetry between fermions and bosons. It was proposed as a way to solve the fine tuning problem, however it turns out that SUSY can address many other problems of the Standard Model and it is also required by string theory. Last, but not least, SUSY is formulated as a rather straightforward extension of the Standard Model so it provides many testable predictions. For this reasons, SUSY has become the favourite BSM theory among many physicists. The following section will give a brief overview of the SUSY concepts based on the references [38], [39] and [40].

1.2.1 Inclusion of the Supersymmetry in the Standard Model

How to accommodate a new symmetry in our theory? All space-time symmetries are in the Poincaré group. Ten generators of the space-time symmetries form Poincaré algebra that is defined by commutation relations between them. The natural approach would be to find generators of SUSY and define commutators with other space-time symmetries. However, the Coleman–Mandula theorem [41] states that it is impossible to add to the Poincaré algebra a new symmetry in any but trivial way. This is the case of the Standard Model which has, in addition to space-time symmetries, also a gauge symmetry which commutes with all space-time symmetries so that the resulting symmetry group is a tensor product of the Poincaré group and a gauge group.

The limitations of the Coleman-Mandula theorem can be avoided by going beyond Lie Algebras and embracing graded Lie algebras (i.e. Lie algebras involving also anticommutators). The Haag–Lopuszanski–Sohnius theorem [42] states that Supersymmetry (symmetry between fermions and bosons generated by a fermionic generator with the spin $\frac{1}{2}$) is the only possible extension of the Poincaré group of the space-time symmetries. SUSY defined in this way states that for every fermion there is a bosonic partner of the same mass and vice versa. If this would be true, the fine tuning problem will be solved exactly as the bosonic and fermionic contributions will cancel each other. However, we know that this is not the case as until today we have not observed any superpartner of any known particle, so SUSY must be obviously broken in a similar way as the electroweak symmetry of the Standard Model. If the scale of SUSY breaking (the mass scale of the superpartners) is not too high (i.e. of the $O(1\text{ TeV})$), then it would still be good enough for solving the fine tuning problem as the corrections to the scalar mass will be of the scale of the mass itself, which is still reasonable.

1.2.2 SUSY superpotential

This section will introduce the concept of the superpotential which is central to the theoretical motivation of the experimental search presented in later parts of this thesis. The detailed derivation of the generic SUSY Lagrangian is in appendix A.

In SUSY, the quantum fields are organized to so-called supermultiplets. The chiral supermultiplets (see appendix A for definition) contain a complex scalar field ϕ, a left-handed Weyl fermion field ψ and a complex auxiliary field F. The contents of supermultiplets are linked by the SUSY transformations:

$$\delta_S\phi = \sqrt{2}\xi\psi \tag{1.16}$$
$$\delta_S\psi = \sqrt{2}\xi F + i\sqrt{2}\sigma^\mu\overline{\xi}\partial_\phi \tag{1.17}$$
$$\delta_S F = -i\sqrt{2}\partial_\mu(\psi\sigma^\mu\overline{\xi}) \tag{1.18}$$

where ξ is an anticommuting Grassmann variable defined in appendix A. The scalar (boson) field transforms to fermion field and vice versa, as expected in SUSY. The free part of the Lagrangian is

$$\mathscr{L}_{\text{free}} = -\partial^\mu\phi^{*i}\partial_\mu\phi_i - i\psi^{\dagger i}\overline{\sigma}^\mu\partial_\mu\psi_i + F^{*i}F_i \tag{1.19}$$

which is summed over repeated indices i that correspond to different supermultiplets. The most general renormalizable[7] interaction terms are

$$\mathscr{L}_{\text{int}} = \left(-\frac{1}{2}W^{ij}\psi_i\psi_j + W^iF_i + x^{ij}F_iF_j\right) + \text{c.c.} - U \tag{1.20}$$

where W^{ij}, W^i, x^{ij} and U are polynomials in the scalar fields ϕ_i, ϕ^{*i}, with degrees 1, 2, 0 and 4, respectively. Because $\mathscr{L}_{\text{free}}$ is SUSY invariant, $\mathscr{L}_{\text{int}}$ must be SUSY invariant as well in order to have supersymmetric theory. This requirement simplifies (1.20) to

$$\mathscr{L}_{\text{int}} = \left(-\frac{1}{2}W^{ij}\psi_i\psi_j + W^iF_i\right) + \text{c.c.} \tag{1.21}$$

Moreover, SUSY invariance implies that W^{ij} must be analytical in the complex fields ϕ_k (in other words, it cannot contain ϕ^{*k}. Therefore its form is

$$W^{ij} = M^{ij} + y^{ijk}\phi_k \tag{1.22}$$

where M^{ij} is a symmetric mass matrix for the fermion fields and y^{ijk} is a Yukawa-type coupling of a scalar and two fermions that must be symmetric under exchange i, j, k. We can therefore write

$$W^{ij} = \frac{\partial^2}{\partial\phi_i\partial\phi_j}W$$

where we have introduced object

$$W = \frac{1}{2}M^{ij}\phi_i\phi_j + \frac{1}{6}y^{ijk}\phi_i\phi_j\phi_k \tag{1.23}$$

called the *superpotential*. It is not a scalar potential in the ordinary sense - it is an analytical function of the scalar fields ϕ_i. Nevertheless, superpotential is extremely useful concept because it allows us in a compact way define the interactions between scalar and fermion fields but also the scalar potential necessary for the SSB (see appendix A).

[7] Each term must have field content with total mass dimension ≤ 4.

1.2.3 Supersymmetry breaking and the MSSM

Supersymmetry predicts that the supersymmetric partners of the Standard Model particles have the same mass and also the same coupling constant (interaction strength).

But as far as we know this is not true. This means that SUSY must be somehow broken. The first idea is of course to try to break SUSY spontaneously, as we did in the case of the SM.

This approach, however, brings many problems. If we assume that the vacuum state is not supersymmetric (logical consequence of SUSY SSB), we immediately obtain non-zero vacuum energy, which might bring problems in cosmology (there is a significant difference between value obtained from SUSY SSB and the value anticipated by cosmologists [18]). Also, SSB does not solve the problem of particles-sparticles mass difference entirely: in SSB the traces over the mass matrices still remain the same for fermions and sfermions, making it difficult to give *all* sfermions masses significantly higher than their SM counterparts.

As a result, most models do not try to explain SUSY breaking dynamically, but instead introduce "soft breaking terms" into the Lagrangian to parametrize out ignorance about the breaking mechanism. These terms explicitly break supersymmetry and cause sparticles to be heavier than particles, yet they conserve the cancellation of the quadratic divergences, which was the original motivation for SUSY. However, this also means that sparticles cannot have masses much higher than SM particles - about $O(1\text{ TeV})$ at maximum.

The soft SUSY breaking terms are

- scalar mass terms $-m_i^2|\phi_i|^2$
- trilinear scalar interaction $-A_{ijk}\phi_i\phi_j\phi_k$
- gaugino mass term $-\frac{1}{2}m_l\overline{\lambda}_l\lambda_l$
- bilinear terms $-B_{ij}\phi_i\phi_j$
- linear terms $-C_i\phi_i$

If we introduce such terms, the quadratic divergences will still be canceled, but this is not true for any other SUSY breaking terms (e.g. fermion masses) [39].

The simplest realistic SUSY model which satisfies all phenomenological constraints is called the *Minimal supersymmetric standard model* (MSSM). The minimal means that it introduces as few new particles and interactions as possible. In principle it just introduces a SUSY partner for every SM particle with all consequences.

At first, we have to define the superfields we will need for construction of the MSSM Lagrangian. As it was mentioned earlier, SM fermions live in 5 representations of the SM gauge group, so that we will need 5 chiral superfields which will represent them: Q, which contains quark and squark $SU(2)$ doublets and $SU(3)$ triplets, U and D which contains quark and squark $SU(2)$ singlets and $SU(3)$ triplets, L, which contains lepton and slepton $SU(2)$ doublets and $SU(3)$ singlets and finally E which contain lepton and slepton $SU(2)$ and $SU(3)$ singlet.

Unlike in the SM, all those fields are left-handed, so the $SU(2)$ singlet fields (which are right-handed in the SM) contain anti-fermions rather than fermions.

We have to assign a superpartner for the Higgs boson too. In this case, however, it is not entirely straightforward. In the Standard Model we use the complex conjugate of Higgs field to give masses to up-type quarks (1.11). However, such terms are not allowed by SUSY, because the superpotential is an analytical function of the superfields. Inevitably, there must be two SM Higgs doublets to be able to give masses to all elementary fermions.

		Spin 0	Spin $\frac{1}{2}$	$(SU(3), SU(2), U(1))$
quarks and squarks	Q	$(\tilde{u}_L, \tilde{d}_L)$	(u_L, d_L)	$(3,2,\frac{1}{6})$
	U	$\tilde{u}_R^*$	$u_R^\dagger$	$(\overline{3},1,-\frac{2}{3})$
	D	$\tilde{d}_R^*$	$d_R^\dagger$	$(\overline{3},1,\frac{1}{3})$
leptons and sleptons	L	$(\tilde{\nu}_L, \tilde{e}_L)$	(ν_L, e_L)	$(1,2,-\frac{1}{2})$
	E	$\tilde{e}_R^*$	$e_R^\dagger$	$(1,1,1)$
higgs and higgsinos	H_u	(h_u^+, h_u^0)	$(\tilde{h}_u^+, \tilde{h}_u^0)$	$(1,2,\frac{1}{2})$
	H_d	(h_d^+, h_d^0)	$(\tilde{h}_d^+, \tilde{h}_d^0)$	$(1,2,-\frac{1}{2})$

Table 1.4: Chiral superfields of the MSSM. The first five rows are standard multiplets of the SM, bottom two lines are SM model Higgs doublet + SUSY partner. In the last column we can find in which representation of the gauge group the multiplet is.

	Spin $\frac{1}{2}$	Spin 1	$(SU(3), SU(2), U(1))$
gluinos and gluons	$\tilde{g}$	g	(8,1,0)
winos and W-bosons	$\widetilde{W}^\pm, \widetilde{W}^0$	$W^\pm, W^0$	(1,3,0)
bino and B-boson	$\tilde{B}$	B	(1,1,0)

Table 1.5: Vector superfields of the MSSM. In the third column there are SM gauge bosons, in the second column are their SUSY partner. In the last column we can find in which representation of the gauge group the multiplet is.

This means that prior to the SSB we would have 8 SM Higgs bosons (2 complex doublets). Spontaneous symmetry breaking of $SU(2)$ symmetry turns 3 of them to unphysical Goldstone bosons, so we are left with 5 Higgs bosons: A - neutral pseudoscalar, h and H - "light" and "heavy" neutral scalar and H^+ and H^- - the charged Higgs bosons. So in MSSM we need 2 additional left-chiral superfields to describe 2 Higgs doublets, and they give us in total 5 particles and 5 sparticles. Chiral superfields of the MSSM are summarized in tab. 1.4.

We also have to define superpartners for the vector bosons. So we have one vector superfield which contains 8 gluons g and 8 gluinos $\tilde{g}$. They will appear automatically if we use $SU(3)$ as a gauge group during the construction of the vector superfields.

In analogy we introduce a superfield with three weak vector bosons $W^\pm$ and W^0 and three winos $\tilde{W}$. Of course we need a superfield with $U(1)$ gauge boson and its supersymmetric partner: bino $\tilde{B}$. Because of the Electroweak SSB, binos and winos are not mass eigenstates, but instead they mix with each other to form physical states that are observable in the experiment. Vector superfields of MSSM are summarized in tab. 1.5.

Having defined the superfields, we have to set the superpotential (defined by (1.23)). It is constrained by the gauge group but it is not fixed entirely. We can employ the idea of minimality, i.e. we introduce only these terms which are necessary to build a realistic model. Alternatively, we can demand that the lepton and baryon number is conserved, nevertheless, the result will be the same as in the previous case.

After imposing the above restrictions we get following superpotential:

$$f_{\mathrm{MSSM}} = \sum_{i,j=1}^{3} [(\lambda_E)_{ij} H_d L_i E_j + (\lambda_D)_{ij} H_d Q_i D_j + (\lambda_U)_{ij} H_u Q_i U_j] + \mu H_u H_d \,. \tag{1.24}$$

There, i and j are generation indices, λ's are matrices with respective Yukawa couplings and also we assume contraction over $SU(2)$ and $SU(3)$ indices and a SUSY superfield product

$$H_u H_d = H_u^+ H_d^- - H_u^0 H_d^0 \,; \qquad Q D_R = \sum_{i=1}^{3} Q_n (D_R)_n \,.$$

The reader may notice that the structure of the first 3 terms the same as in the case of the SM: the first term is the Higgs boson giving masses to leptons, next we have Higgs boson giving masses to down and up quarks. Finally, there is a new term, so called "μ-term" that gives rise to the higgsino mass term $\mu(\widetilde{H}_u^+ \widetilde{H}_d^- - \widetilde{H}_u^0 \widetilde{H}_d^0)$ and "negative mass" term in the scalar potential (necessary for the electroweak SSB) $|\mu|^2(|H_u^0|^2 + |H_u^+|^2 + |H_d^0|^2 + |H_d^-|^2)$.

Also note, that this choice of superpotential brings another conservation law, so called "R parity conservation". This means that interaction vertices introduced by (1.24) contain an even number of superpartners. This means that there is no interaction of type incoming sparticle, outgoing particle(s), i.e. the lightest supersymmetric particle (LSP) is absolutely stable because it cannot decay.

Because all SUSY particles should be heavy, the LSP is a good candidate for dark matter observed by astrophysicists, especially if it is color and electrically neutral (no interactions with photons is necessary to keep the matter dark).

Last step in the construction of the theory is the SUSY breaking. As was stated earlier, it is not easy to do it spontaneously, so MSSM introduces soft breaking terms. Unfortunately, that brings in about 100 new parameters.

However, under some assumptions it is possible to reduce the number of those parameters significantly. The first assumption is that the scalar masses, gaugino masses and trilinear scalar couplings unify at the scale where also the running couplings of the strong, weak and electromagnetic interaction unify (so-called GUT scale[8]). The unified values are m_0, $m_{\frac{1}{2}}$ and A, respectively. The $\tan\beta$ is defined as the ratio of vev's of the 2 Higgs doublet

$$\tan\beta = \frac{\langle H_u^0 \rangle}{\langle H_d^0 \rangle} \,. \tag{1.25}$$

The value of $\tan\beta$ and the value of the Z mass is used to fix the norm of μ and the mass of one of the Higgs bosons - traditionally it is the pseudoscalar boson A. This also unambiguously sets the bilinear scalar couplings. Finally, we are left the sign of μ as the last free parameter. These are the 5 free parameters of the so-called constrained MSSM (cMSSM):

$$m_0,\ m_{\frac{1}{2}},\ A,\ \tan\beta,\ \mathrm{sig}(\mu) \tag{1.26}$$

If we request additional relations between those parameters, some even more constrained models can be derived (e.g. mSUGRA [43]).

[8] In the Standard Model, the running interaction constants do not unify. However, presence of additional particles in SUSY changes the evolution of the strength of the interactions and the unification of all three gauge particle interactions is possible at a scale of 10^{15} GeV.

1.3 Next-to-the-minimal SUSY extension of the Standard Model

1.3.1 Motivation to go beyond MSSM

The μ problem

The superpotential of MSSM (1.24) contains the μ term ($\mu H_u H_d$) that has no analogue in the Standard Model. Because it is made of superfields, it influences both the neutralino sector (where the μ term provides a mass for higgsino) but more importantly also the scalar potential of the Lagrangian that has changed significantly, compared to the Standard Model, because of the presence of the 2 Higgs doublets. The full scalar potential reads [39]

$$V = \frac{1}{8}\left(g^2 + g'^2\right)\left(|H_d|^2 - |H_u|^2\right)^2 + \frac{1}{2}g^2|H_d^\dagger H_u|^2 + \mu^2\left(|H_d|^2 + |H_u|^2\right) + V_{\text{soft}}\ , \tag{1.27}$$

where V_{soft} are the soft SUSY breaking terms. The quartic Higgs self-coupling is no longer independent parameter, but it is clearly linked with the gauge coupling. This feature is very uncommon in the non-supersymmetric theories. If we would assume that $V_{\text{soft}} = 0$, the potential will have trivial minimum at $H_u = H_d = 0$, so the spontaneous symmetry breaking and mass generation via the Higgs mechanism will be impossible. So we can see that breaking of SUSY and breaking of the electroweak gauge symmetry are tightly linked and the latter is not possible without the former.

After adding the relevant soft SUSY breaking terms, the potential becomes

$$V = \frac{1}{8}\left(g^2 + g'^2\right)\left(|H_d|^2 - |H_u|^2\right)^2 + \frac{1}{2}g^2|H_d^\dagger H_u|^2 + m_d^2|H_d|^2 + m_u^2|H_u|^2 + [b(H_u \cdot H_d) + h.c.]\ , \tag{1.28}$$

where $m_d^2 = \mu^2 + m_{H_d}^2$ and $m_u^2 = \mu^2 + m_{H_u}^2$. Now we would like to find the minimum of this potential and make sure that it is a) bounded from below and b) has nonzero vacuum expectation value. Those two conditions are equivalent to the following inequalities

$$\begin{aligned} 2b &< 2|\mu^2| + m_{H_u}^2 + m_{H_d}^2 \\ b^2 &> (\mu^2 + m_{H_d}^2)(\mu^2 + m_{H_u}^2) \end{aligned} \tag{1.29}$$

Finally at the minimum satisfying the conditions in (1.29) we can see that

$$\begin{aligned} \sin(2\beta) &= \frac{2b}{m_{H_u}^2 + m_{H_d}^2 + 2|\mu|^2} \\ m_Z^2 &= \frac{|m_{H_d}^2 - m_{H_u}^2|}{\sqrt{1 - \sin^2(2\beta)}} - m_{H_u}^2 - m_{H_d}^2 - 2|\mu|^2 \end{aligned} \tag{1.30}$$

where $\tan\beta$ has been defined in eq. (1.25). The equations (1.30) shows that in order to achieve electroweak SSB, all the parameters $m_{H_u}^2$, $m_{H_d}^2$, b and μ must be within an order of magnitude or two of the mass of the Z boson. However, μ is the parameter of the superpotential, linked to the SUSY nature of the Lagrangian and as such it has no knowledge about the SUSY breaking scale which governs the values of the soft breaking parameters $m_{H_u}^2$, $m_{H_d}^2$, b. In fact, the natural value of μ should be either 0 or something close to the Planck or GUT scale. The fact, that the parameter μ must have value close to the electroweak and SUSY breaking scale is called the "μ problem".

Experimental Constraints

The phenomenology of the MSSM is rather limited and therefore it might be more and difficult to find such parameters that pass the constraints on the mass and annihilation cross-section of the LSP from the relic density measurements. Additional particles may bring both new types of events to study and allow to pass the experimental constraints more naturally. The current constraints from the ATLAS experiment are shown in fig. 1.7. They clearly show that the lower limit on the squarks and gluino masses in MSSM is now $\gtrsim$ 1 TeV meaning that the SUSY breaking scale is also at least that high. This can cause MSSM to fail to solve the fine tuning problem in the Higgs sector (SUSY can solve the fine tuning problem only if the SUSY breaking scale is not too different from the electroweak scale).

Fine tuning in MSSM

Being broken SUSY, MSSM does not solve the original fine tuning problem completely, and still requires some fine tuning that can be rather large given the tight experimental constraints mentioned in the previous paragraph.

1.3.2 The NMSSM

Next-to-the-minimal SUSY extension of the Standard Model (NMSSM) has been designed to solve the "μ problem" of MSSM. This is done by replacing the μ parameter by a gauge singlet Higgs field and the μ parameter is then generated dynamically when that field acquires the vacuum expectation value of the electroweak scale. The new field also brings additional Higgs bosons and higgsinos, thus extending the MSSM phenomenology and makes it easier for the model to pass experimental constraints. On top of this, due to less stringent bounds in the Higgs sector, less fine tuning is required in the NMSSM than was necessary to use in the MSSM.

The main difference between MSSM and NMSSM is in the superpotential that now becomes [46]

$$f_{\mathrm{NMSSM}} = \sum_{i,j=1}^{3} [(\lambda_E)_{ij} H_d L_i E_j + (\lambda_D)_{ij} H_d Q_i D_j + (\lambda_U)_{ij} H_u Q_i U_j] + \lambda S H_u H_d + \frac{\kappa}{3} S^3 \,. \quad (1.31)$$

If compared to the eq. (1.24), we can see that μ was replaced by λS and one extra term, cubic in the singlet field S has been added. If not for the latter, the new global $U(1)$ symmetry of S in term $\lambda S H_u H_d$ term could have lead to an extra massless CP-odd scalar, the so-called Peccei-Quinn axion [47, 48]. We can also see that after the spontaneous symmetry breaking, an effective μ is generated:

$$\mu = \lambda \langle S \rangle \quad (1.32)$$

The vacuum expectation value of the new Higgs field is of the electroweak scale, so the constraints in equations (1.30) can easily be satisfied without any miraculous cancellations. The new parameters connected with the singlet field will also appear in the SUSY breaking part of the lagrangian. The additional terms in the V_{soft} are

$$V_{\mathrm{soft,NMSSM}} = m_S^2 |S|^2 + \lambda A_\lambda H_u H_d S + \frac{1}{3} \kappa A_\kappa S^3 \quad (1.33)$$

where all the terms with the μ are appropriately replaced.

In contrast to the MSSM, where the Higgs sector is described just by 2 parameters ($\tan\beta$ and M_A), the NMSSM Higgs sector requires 6 parameters:

$$\lambda,\ \kappa,\ A_\lambda,\ A_\kappa,\ \tan\beta,\ \mu_{\mathrm{eff}} = \lambda \langle s \rangle \quad (1.34)$$

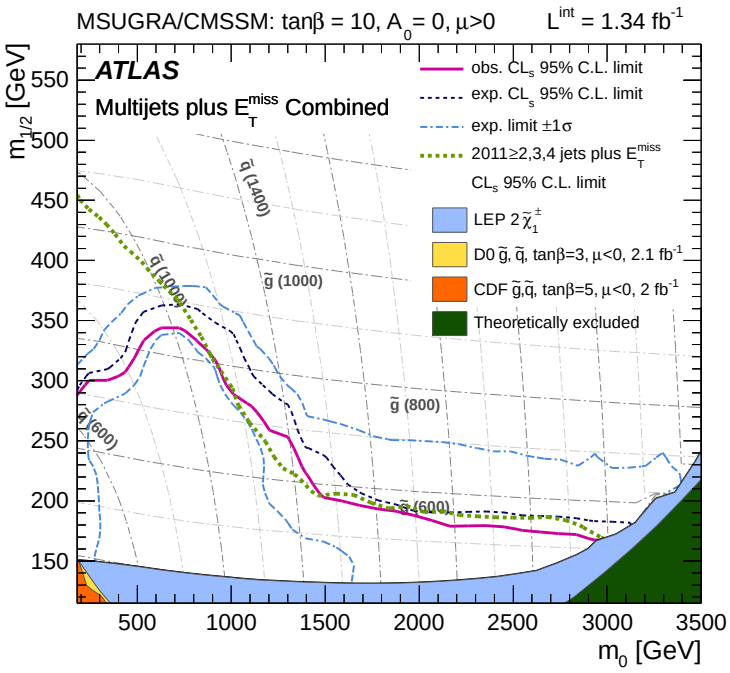

(a) MSUGRA/cMSSM

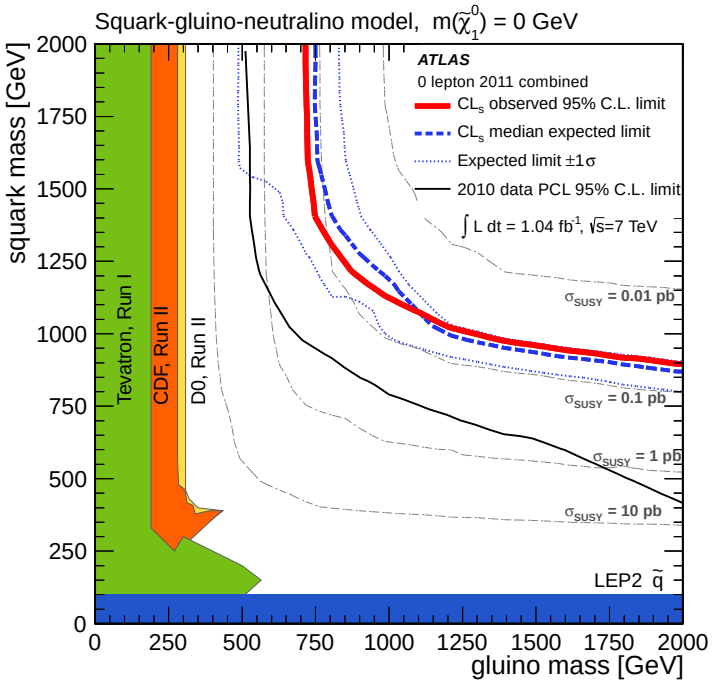

(b) simplified SUSY

Figure 1.7: The limit on scalar and gaugino mass in cMSSM/mSUGRA is shown in fig. 1.7(a). The plot is from [44]. The fig. 1.7(b) shows the limit on the mass of sparticles in the simplified SUSY models with massless LSP [45].

The addition of the new superfield results in three new particles: 2 gauge singlet higgs bosons and 1 gauge singlet higgsino. Those particles mix with the original Higgs bosons and neutralinos

of the MSSM, so in the end NMSSM has 5 neutral Higgs bosons (3 CP-even: h_1, h_2 and h_3 and 2 CP-odd: a_1 and a_2), two charged Higgs bosons (h^+,h^-) and 5 neutralinos. All other particles are the same as in the MSSM (tabs. 1.4 and 1.5). Due to the mixing with the gauge singlet, the production cross-sections and decay branching ratios of the Higgs bosons and neutralinos can be very different in the NMSSM compared to the MSSM. Even in case of the identical mass spectrum, the distinction between MSSM and NMSSM is possible by measuring the production and decay rates in the Higgs and neutralino sector [49].

1.3.3 Ideal Higgs Scenario

The new singlet Higgs field greatly increases the phenomenology in the Higgs sector compared to the MSSM [46]. A very interesting scenario not possible at MSSM is the one where the lightest CP-even Higgs boson h_1 can escape the LEP lower limit of 114.4 GeV if it decays to a pair of lighter CP-odd Higgses a_1 again decaying to τ leptons: $h_1 \to 2a_1 \to 4\tau$. The necessary condition is that $m_a < 2m_B$[9] to prevent decay of a_1 to $b\bar{b}$ that would have been detected. Furthermore, if $m_{h_1} < 105$ GeV, this model gives a better agreement with the electroweak precision measurements than the Standard Model [50]. If also the branching fraction of $h_1 \to 2a_1$ is greater than 75%, the model can even explain the 2.3 σ excess observed at LEP in $M_{b\bar{b}}$ around 100 GeV for $m_{h_1} \sim 100$ GeV. Such a scenario is referred to as the *Ideal Higgs Scenario*.

Moreover, if $m_{a_1} > 8$ GeV an enhanced $a_1 b\bar{b}$ coupling can explain the deviation of the measurement of the anomalous magnetic moment a_μ from the Standard Model prediction [51]. The search for the evidence of the Ideal Higgs Scenario is one of the topics of this thesis and this section will give a brief overview of its phenomenology. More details can be found in [50] and references therein.

As can be seen from the previous paragraph, the Ideal Higgs Scenario is independent of the NMSSM: it just requires that masses and branching ratios have the right sizes. The requirement of supersymmetry is not necessary for the validity of the Ideal Higgs Scenario, the crucial point is the existence of the 2 Higgs doublets. The NMSSM is just one of the frameworks in which the Ideal Higgs Scenario can be realized.

The crucial part in the experimental validation of the Ideal Higgs Scenario is the observation of the decay of the lightest CP-odd boson a_1. It couples to fermions via

$$\mathscr{L}_{a_1 f\bar{f}} = iC_{af\bar{f}} \frac{ig_2 m_f}{2m_W} \bar{f}\gamma_5 f a_1 \tag{1.35}$$

where $C_{af\bar{f}}$ is a Yukawa-type scalar-fermion-fermion coupling and g_2 is the gauge coupling of electroweak $SU(2)$.

For models, where the (charged) lepton and down-type quark masses are generated by the same combination of Higgs fields, $C_{a_1\tau\tau} = C_{a_1\mu\mu} = C_{a_1 b\bar{b}}$. This is typical in the two-Higgs doublet models (2HDM) of either type-I or type-II [31]. In the MSSM (and more generally in all type-II 2HDM[10]) $C_{a_1\tau\tau} = C_{a_1\mu\mu} = C_{a_1 b\bar{b}} = \tan\beta$ where $\tan\beta$ is the ratio of vacuum expectation values of different Higgs doublets as defined in (1.25). The coupling to the up-type quarks is given by: $C_{a_1 t\bar{t}} = \cot\beta$.

In the NMSSM, the form of $C_{a_1 f\bar{f}}$ is a little bit more complicated ([52] and [53]): $C_{a_1\tau\tau} = C_{a_1\mu\mu} = C_{a_1 b\bar{b}} = \tan\beta\cos\theta_A$, where $\cos\theta_A$ is defined by

$$a_1^{(NMSSM)} = \cos\theta_A a^{(MSSM)} + \sin\theta_A a_S \tag{1.36}$$

[9] $2m_B$ is the threshold for creating b hadron pairs. Its value is about 10.5 GeV.

[10] In the type-II 2HDM one Higgs doublet couples to "up-type" fermions and the other to "down-type" fermions.

where $a^{(MSSM)}$ is the CP-odd scalar of the MSSM and the a_S is the additional CP-odd singlet scalar of the NMSSM. It is straightforward to express the relation between the fundamental parameters of NMSSM and the $\cos\theta_A$. Using results in [54] and [55], one can express the mixing between the 2 Higgs doublets and the singlet as

$$\cos 2\theta_A = -\frac{M_{11}^2 - M_{22}^2}{\sqrt{(M_{11}^2 - M_{22}^2)^2 + 4(M_{12}^2)^2}} \tag{1.37}$$

with M_{ij} defined as

$$\begin{aligned} M_{11}^2 &= \frac{2\lambda s}{\sin 2\beta}(A_\lambda + \kappa s) \\ M_{12}^2 &= \lambda v(A_\lambda - 2\kappa s) \\ M_{22}^2 &= 2\lambda\kappa v^2 \sin 2\beta + \lambda A_\lambda \frac{v^2 \sin 2\beta}{2s} - 3\kappa A_\kappa s \end{aligned} \tag{1.38}$$

where $s = \langle S \rangle$ is the vacuum expectation value of the singlet Higgs field, $v^2 = \langle H_u^0 \rangle^2 + \langle H_d^0 \rangle^2$ and $\tan\beta = \frac{\langle H_u^0 \rangle}{\langle H_d^0 \rangle}$.

The branching ratio of a_1 decays to various leptons are shown in fig. 1.8. For $\tan\beta > 1.5$ the decay to τ lepton pair is dominant (BR is 0.5 to 0.9) in the mass range $2m_\tau < m_{a_1} < 2m_B$. The decay to muons, however, is very suppressed if the decay to τ's is kinematically possible. The BR($a_1 \to \mu\mu$) is smaller than 0.5% for $2m_\tau < m_{a_1} < 2m_B$. Note also, that at tree level the branching ratio is independent of $\cos\theta_A$ [50].

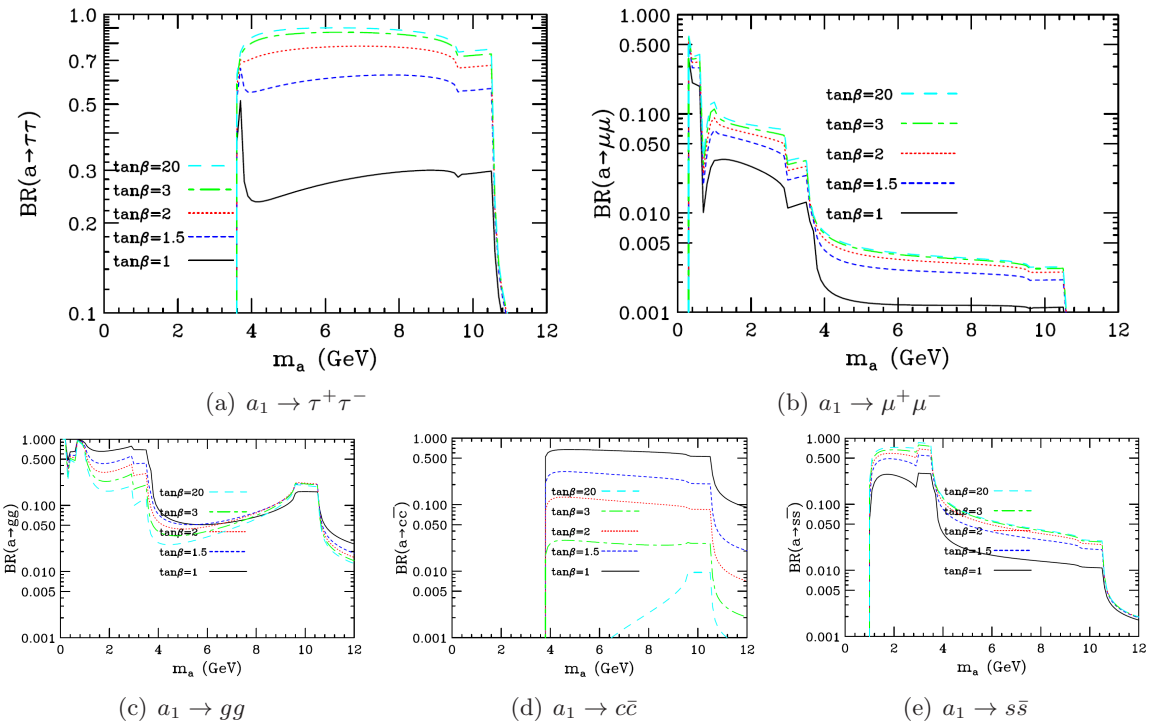

(a) $a_1 \to \tau^+\tau^-$ (b) $a_1 \to \mu^+\mu^-$

(c) $a_1 \to gg$ (d) $a_1 \to c\bar{c}$ (e) $a_1 \to s\bar{s}$

Figure 1.8: The decay fractions of a_1 to different fermions as a function of a_1 mass. Note that for masses above 10.5 GeV the decay to $b\bar{b}$ is completely dominant. The plots are from [19].

Experimental limits

The existence of a_1 can be probed via production of a primary heavy particle that then decays to a_1. This approach has been used in B-factories and LEP to set limits on $C_{a_1 b\bar{b}}$ coupling. This can be directly translated to the NMMSM context to limit $\cos\theta_A$ because $C_{a_1 b\bar{b}} = \tan\beta \cos\theta_A$. This is shown in fig. 1.9 for various values of $\tan\beta$. As the maximum allowed value is positive for all m_{a_1}, it is always possible to choose $\cos\theta_A$ so that the limits on $C_{a_1 b\bar{b}}$ as a function of $\tan\beta$ are satisfied. The constraints are strongest for $m_{a_1} \lesssim 9$ GeV, where limits obtained at B-factories from studying Υ decays are relevant, and deteriorate rapidly above that.

In a generic type-II 2HDM, all points in fig. 1.9 for which $\cos\theta_A^{\max} < 1$ correspond to choices of m_{a_1} and $\tan\beta$ that are not consistent with the limits. We can see that values of $\tan\beta > 1.5$ are disfavoured for $m_{a_1} \lesssim 10$ GeV. We can also see that all values of $\tan\beta$ are excluded below $2m_\tau$ which is roughly 3.5 GeV.

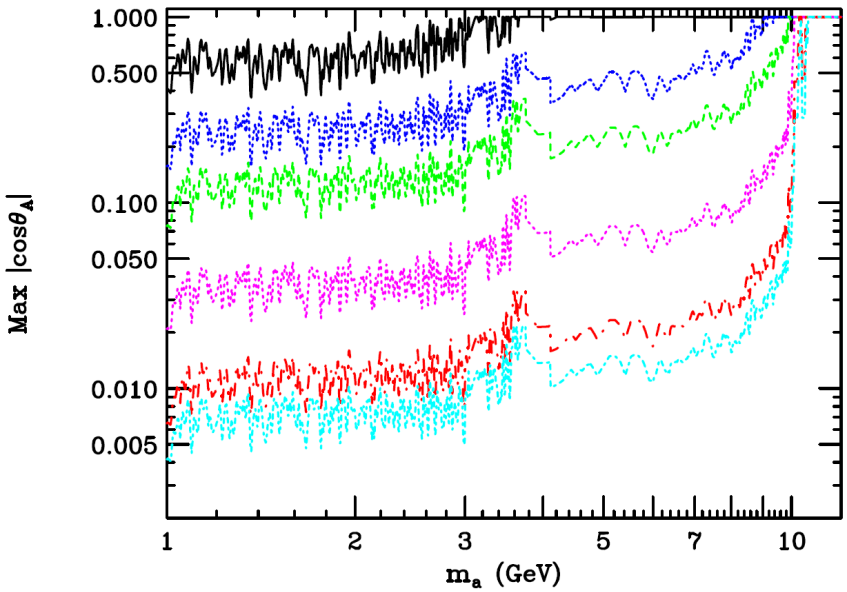

Figure 1.9: Limit on the upper value of $|\cos\theta_A|$ in the NMSSM as a function of m_{a_1}. Different curves correspond to $\tan\beta = 1$ (top curve), 1.7, 3, 10, 32 and 50 (bottom curve). The plot is from [19].

Focusing on the Ideal Higgs Scenario (i.e. demanding that $m_{h_1} \sim 100$ GeV, $m_{a_1} \lesssim 2m_B$ and $BR(h_1 \to a_1 a_1) > 0.75$, we can set allowed ranges of $\cos\theta_A$ as a function of $\tan\beta$. It is possible to make those limits more stringent by further requiring small level of fine-tuning (that was one of the motivations of adding additional scalar field to the MSSM). The limits with and without the small fine tuning requirement are shown in tab. 1.6. The level of fine-tuning is characterized by G defined in [55] and small fine-tuning is defined as $G < 20$.

The upper limit on $|\cos\theta_A|$ is coming from upper limit on $C_{a_1 b\bar{b}}$ and the lower limit is the result of $BR(h_1 \to a_1 a_1) > 0.75$ requirement. For too small values of $|\cos\theta_A|$ the a_1 is almost a singlet and thus very weakly coupled to the rest of the Higgs bosons. From tab. 1.6 and fig. 1.9 we can conclude that the existence of the a_1 is highly constrained for the masses below $2m_\tau$ (max $|cos\theta_A| < 1$), while the values above have not been yet excluded, e.g. for $\tan\beta = 10$. However, for $\tan\beta > 30$ all masses up to 8 GeV are excluded.

Some additional constraints have been set by the ALEPH experiment in 2010 [56]. The

$\tan\beta$	$\cos\theta_A$ ranges	$\cos\theta_A$ ranges, small fine tuning
1.7	< -0.3 or > 0.1	[-0.6, -0.5] or ~ 0.1
2	< -0.3 or > 0.1	[-0.7, -0.5]
3	< -0.06	[-0.35,-0.08]
10	< -0.06 or > 0.035	[-0.12, -0.08] or [0.06, 0.08]
50	< -0.04 or > 0.04	[-0.06, -0.04] or ~ 0.04

Table 1.6: Values of $\cos\theta_A$ allowed for Ideal Higgs Scenario. First column show full range, the second column shows the range where only small fine-tuning is necessary. Values are from [50].

measurement was setting limit on a quantity

$$\xi^2 \equiv \frac{\sigma(e^+e^- \to Zh_1)}{\sigma(e^+e^- \to Zh_{SM})} BR(h_1 \to a_1 a_1) \left[BR(a_1 \to \tau^+\tau^-)\right]^2 \tag{1.39}$$

as a function of m_{h_1} and m_{a_1}. The results are shown in fig. 1.10.

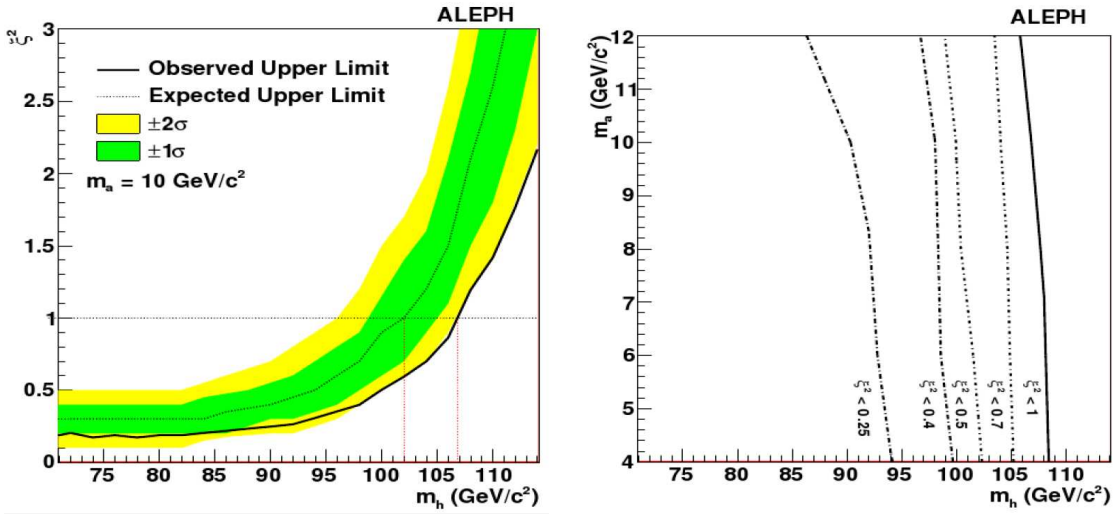

(a) (b)

Figure 1.10: The limit on ξ^2 as function of m_{h_1} for $m_{a_1} = 10$ GeV (fig. 1.10(a)). The contours of upper limits on ξ^2 as a function of m_{h_1} and m_{a_1} (fig. 1.10(b)). The plots are from [56].

To see the effect of the ALEPH limits on the Ideal Higgs Scenario, a scan over the NMSSM space was performed by varying the soft SUSY breaking parameters A_λ and A_κ. For each set of parameters the value of ξ^2 was calculated and finally all those results were plotted as a function of m_{h_1} [19]. The comparison of the ξ^2 values predicted from the theory with the limit is shown in fig. 1.11 for two different values of $\tan\beta$.

In a summary, the combined limits from B-factories managed to exclude 2HDM type-II models with $a_1 < 2m_\tau$ and also for $\tan\beta > 30$ all masses up to 8 GeV. The NMSSM is only weakly constrained for $m_{a_1} \lesssim 8$ GeV and none at all between 8 GeV and 2 m_B.

The limits from LEP Higgs searches and requirement of small fine tuning provide very strong constraints on the Ideal Higgs Scenario (tab. 1.6).

The summary of the ALEPH limit on the Ideal Higgs Scenario is

- For all $\tan\beta \leq 2$, there are non-excluded scenarios with $m_{h_1} \leq 100$ GeV

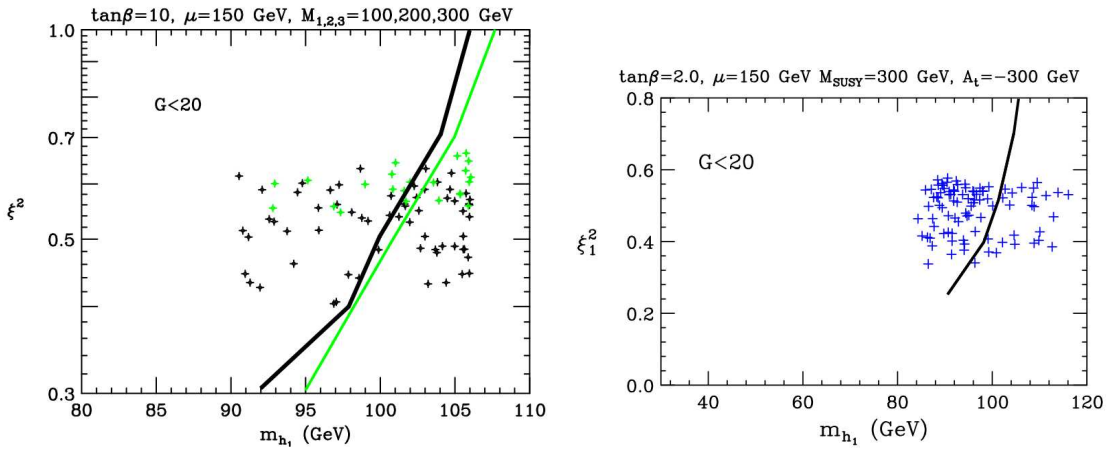

(a) $\tan\beta = 10$ (b) $\tan\beta = 2$

Figure 1.11: The combination of the ξ^2 calculation from [19] and limit from [56]. The figures show the value of ξ^2 for the different models obtained by varying SUSY breaking parameters. The green points correspond to the 7.5 GeV$< m_{a_1} <$ 8.8 GeV, the black points are for the mass 8.8 GeV $< m_{a_1} < 2m_B$. All points must satisfy small fine-tuning requirement ($G < 20$). The black line represents the ALEPH limit for $m_{a_1} = 10$ GeV and the exclusion zone is to the left of the line. The green line is the limit for m_{a_1}=4 GeV to show the dependency of the limit on the a_1 mass. The figures are originally from [19], but the exclusion lines have been added to them by the thesis author. The results for $\tan\beta = 10$ (fig. 1.11(a)) and $\tan\beta = 2$ (fig. 1.11(b)) are presented.

- For $\tan\beta = 3$ there are few viable scenarios with $m_{h_1} \leq 100$ GeV that have ξ^2 values just at the limit
- For $\tan\beta = 10$, the scenarios with $m_{h_1} \sim$ 100–105 GeV and $m_{a_1} \lesssim 2m_B$ easily pass the limit
- For $\tan\beta = 50$ the majority of scenarios are excluded, but a few with very small fine-tuning survive and also realize the Ideal Higgs Scenario

To conclude this section, the current experimental limits force m_{a_1} to be rather close to the $b\bar{b}$ threshold as the lower mass possibilities have been quite constrained by the B-factories results. Coincidentally, the situation when m_{a_1} is as heavy as possible without decaying to $b\bar{b}$ is also most favoured from the theoretical point of view because such scenarios need only small amount of fine tuning.

The exploration of the mass region close to $2m_B$ is very difficult at B-factories that can only search for a_1 in Υ decays - that is why limits in fig. 1.9 are sharply rising above $\Upsilon(1S)$ mass. However, at hadron colliders it is possible to create a_1 directly via gluon fusion so the masses close to and above $\Upsilon(nS)$ can be probed there.

The cleanest channel for hadronic collider searches is $a_1 \to \mu\mu$. It is, however, limited by a very small branching fraction (0.003 – 0.005) and a large background from $\Upsilon(nS)$ decays. This limitation can be overcome by exploiting $a_1 \to \tau\tau$ channel. A large branching ratio of this decay (> 0.7) can help with the background from Υ decays. Therefore a search for the $gg \to a_1 \to \tau\tau$ process has been done with the ATLAS experiment and its results are given in this thesis.

Chapter 2

The Large Hadron Collider and the ATLAS experiment

2.1 LHC

2.1.1 Introduction

The Large Hadron Collider (LHC) [57] is the world's largest and most powerful particle accelerator. It has been constructed in the collaboration of 44 countries from all over the world. The purpose of the LHC is to accelerate beams of protons to very high energy and collide them at a few designated places to provide data for particle physics experiments. The concept of the LHC has been discussed since the beginning of 1980's and the machine was finally turned on in September 2008. Unfortunately, after just a few weeks of running it had to be shut down due to an accident that caused severe machine damage. After the year of reparations and testing, the LHC has been restarted in November 2009.

In the beginning, LHC operated only as a storage ring, i.e. it kept the proton beams at the injection energy of 450 GeV per proton. The first collisions happening with a low intensity at the centre-of-mass energy of 900 GeV have been used to commission the machine and also the detectors. In March 2010, the LHC finally accelerated the protons to 3.5 TeV energy (the highest energy that machine experts consider safe in order to prevent accidents like the one in 2008 from happening) and collisions at $\sqrt{s} = 7$ TeV have started. The intensity of the proton beams gradually increased and finally, by the end of 2010 LHC delivered around 50 pb^{-1}.

The amount of delivered data (also called total *integrated luminosity*) is often expressed in the units of inverse cross-section. Therefore it is very easy to convert the amount of delivered data to the number of expected events:

$$N = \sigma \times \mathscr{L}$$

where σ is the process cross-section, $\mathscr{L}$ is the integrated lumionosity and N is the number of expected events. The collisions at 7 TeV continued in 2011 with even higher intensity and over 5.5 fb^{-1} (1 fb^{-1} = 1000 pb^{-1}) has been delivered to all experiments. The amount of data as a function of time is shown in fig. 2.1. The LHC can also collide heavy ions (namely lead nuclei). The first heavy ion run happened in November 2010 and the second is scheduled for November 2011.

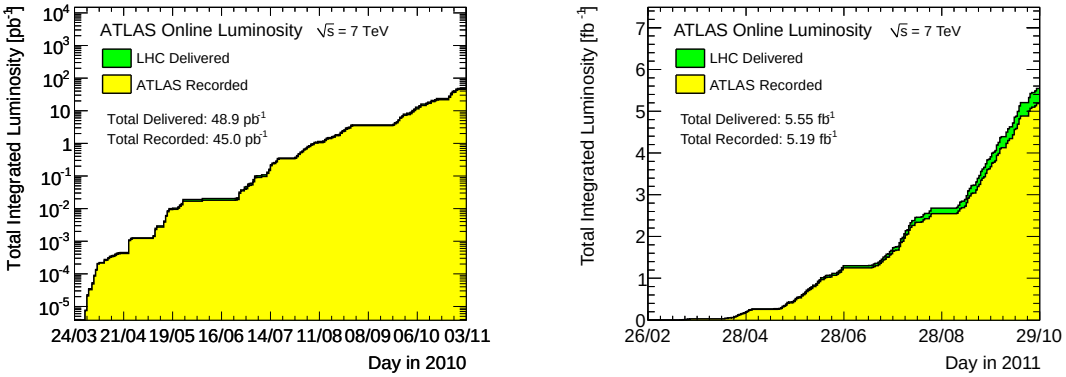

(a) 2010 (b) 2011

Figure 2.1: Summary of the data delivered by the LHC and recorded by the ATLAS detector as a function of time in 2010 and 2011. Note very different scales in figs. 2.1(a) and 2.1(b): the first one is logarithmic and in pb^{-1}, while the latter is linear and in fb^{-1}. Both plots show also high ATLAS data taking efficiency.

2.1.2 LHC design and operation

The LHC is a part of the CERN[1] accelerator complex (fig. 2.2). After the protons are extracted from the hydrogen atoms, they are first accelerated in a linear accelarator (Linac2) to the energy of 50 MeV. Then they go to PS Booster to obtain an energy of 1.4 GeV. The beam is then fed to the PS (proton synchrotron) to be accelerated to the energy of 25 GeV. Then the protons are injected to the SPS (super proton synchrotron), that accelerates them further to 450 GeV, and afterwards the proton beams are injected to the LHC that finishes the acceleration at 3.5 TeV per proton. Beams can circulate and collide for many hours (typically 10 to 20 hours, the longest fill in 2011 was 26 h long) before their intensity deteriorates so much that beam must be dumped and new proton beams are injected.

The LHC is 27 km long and it is placed in an underground tunnel that used to host the LEP collider that was decommissioned in 2001. Most of the LHC volume is filled by superconducting magnets (dipoles ans quadrupoles) that keep protons on their circular track and focus them to the interaction points. The forward proton acceleration happens at a single place of the LHC ring (so proton bunches get an acceleration kick once per revolution).

The LHC can deliver proton beams of very high intensity. The design instantaneous luminosity is 1×10^{34} $\text{cm}^{-2}\cdot\text{s}^{-1} = 10$ nb^{-1}/s, which is 20 times more than the maximal intensity delivered by the Tevatron (the most powerful particle accelerator until LHC was started). Such a high intensity is achieved by having many protons in the beam and by squeezing them, thus increasing their intensity and also their chance to collide with the protons from the opposite beam. The highest instantaneous luminosity achieved by the LHC so far is 3.65×10^{33} $\text{cm}^{-2}\cdot\text{s}^{-1}$.

The proton beams at LHC can be composed of numerous bunches (each of them containing 10^{11}-10^{12} protons). The LHC has been designed to deliver beams with a bunch separation of 25 ns (resulting in 40 MHz input event rate), but so far no physics run used separation smaller than 50 ns. The 25 ns operation is being tested and might be used in 2012. The LHC started with just one bunch per beam, but this number was increasing ever since and in 2011, LHC operated with up to 1331 colliding bunches in each beam. Nevertheless, 25 ns separation would allow us to have up to 2900 bunches in each beam.

[1] European Organization for Nuclear Research: www.cern.ch

particles used	protons and heavy ions (Pb^{82+})
circumference	26.659 m
injected beam energy	450 GeV (protons)
maximal (designed) beam energy at collision	3.5 TeV (7 TeV)
maximal (designed) beam inst. luminosity	3.65×10^{33} (10^{34}) $cm^{-2}s^{-1}$
maximal (designed) integrated luminosity/year	5.5 (100) fb^{-1}
maximal (designed) protons per bunch	10^{12} (10^{11})
operating temperature	1.9 K
revolution frequency	11.2455 kHz

Table 2.1: Overwiew of some of the LHC parameters. At the places where designed and actual value differ, both are shown with the design value in brackets.

The beam squeezing results in having on average more than one *pp* collision per bunch crossing. The highest average number of collisions (observed at the very end of 2011 run) is 32, while the design value is 23. The main parameters of the accelerator are summarized in tab. 2.1. The full documentation of the LHC is available at [57].

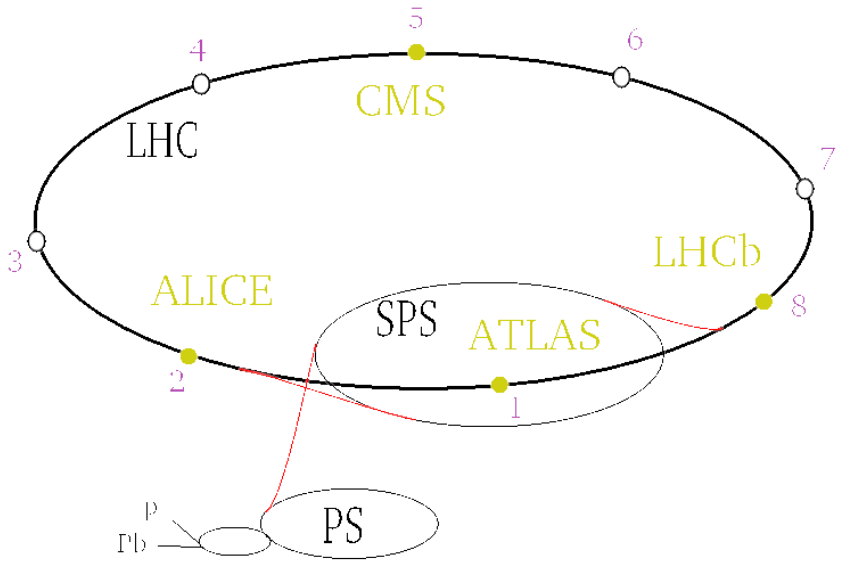

Figure 2.2: The scheme of the CERN accelerator chain together with location of LHC experiments and other important areas at LHC: Points 3 and 7 are used for beam cleaing. The forward proton acceleration happens at point 4 and finally the beams are being dumped at the Point 6. Figure taken from from [58].

Along the course of the accelerator ring, there are four big detectors which measure the outcome of the collisions. These include 2 specialized detectors (ALICE, LHCb) and two general purpose experiments (ATLAS, CMS). The latter have no specific task, but are rather aimed at detecting as much as possible and so study the physics at the energy which has not been accessible before. Here is the brief description of LHC experiments:

ALICE (**A** **L**arge **I**on **C**ollider **E**xperiment) is a detector specially designed to study the collisions of heavy ions [59]. Experiments in the CERN in 1990's and in the Brookhaven National Laboratory in 2000's showed that at very high temperatures the quarks are

probably not confined inside hadrons but they are rather free in a state which was called the quark-gluon plasma (QGP). It is expected that this state of matter exists naturally inside heavy neutron stars and that it was also one of the initial stages of the Universe.

LHCb (**L**arge **H**adron **C**ollider **b**eauty) is an experiment devoted to the measurement of CP violation, especially in the B mesons decay [60]. It is expected that it could be most clearly seen in the difference between the decay of B_d meson ($d\bar{b}$) to J/ψ ($c\bar{c}$) and K^0 ($d\bar{s}$) and the decay of $\overline{B_d}$ meson to respective antiparticles. By studying the difference in the decay times, we would be able to determine the complex phase of CKM matrix [9].

CMS (**C**ompact **M**uon **S**olenoid) is one of the two general purpose detectors at LHC [61]. The name "compact" means that it is somewhat smaller than ATLAS (about 8 times in volume), but has about twice its weight. The name also signalizes that CMS is optimized for tracking muons. Its magnet is the largest solenoid ever built, producing a magnetic field of the strength of 4 T. The scientific goals of the CMS are similar to that of ATLAS, namely

- The search for origin of the spontaneous symmetry breaking (Higgs boson)
- The search for physics beyond the SM - for example supersymmetric particles
- The study of heavy ion collisions and of the formation of the quark-gluon plasma, emulating thus the very first moments after the Big Bang

The construction of two detectors with similar goals fulfils the natural requirement on experimental physics - that any result should be independently confirmed. Also, thanks to the combined statistics from both experiments, it is possible to obtain more precise results.

ATLAS (**A** **T**oroidal **L**HC **A**pparatu**S**) is a general purpose detector designed to exploit the full LHC potential. The ATLAS is larger and more complex than any other detector. The main lines of the ATLAS research are:

- The search for the Higgs boson or any other mechanism of the electroweak symmetry breaking
- The precise measurement of mass of heavy particles like top quark or W boson
- The search for supersymmetric particles or any other new models of physics
- The studies of compositeness of fundamental fermions

To fulfill these goals the ATLAS consists of several components which together provide as much information about the collision as possible. The whole experiment will be described in detail in the following section.

2.2 ATLAS detector hardware

The structure of ATLAS resembles an onion: it is composed of several coaxial layers of different subdetectors that will be described in detail in the next sections. The complete view of the detector can be seen in fig. 2.3. The innermost part is the inner detector, which itself is composed of three other subsystems (Pixel, SCT and TRT). Its purpose is to measure the tracks of charged particles (using semiconductor trackers and drift tubes) and also tell charged leptons from hadrons (i.e. mostly discriminate between electrons and pions). Inner detector

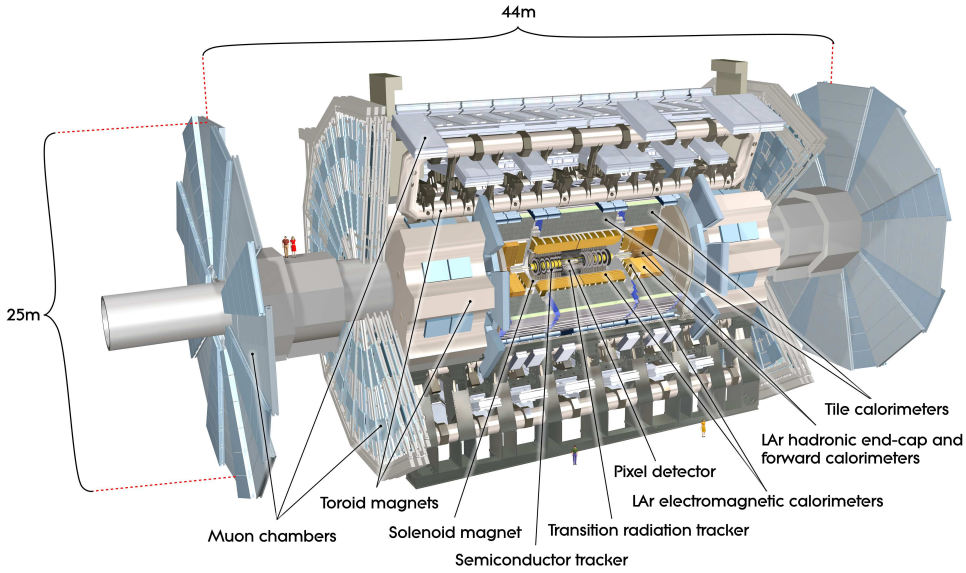

Figure 2.3: Overall view of the ATLAS detector. Several human figures are displayed there to show the scale of the detector. Figure is from [62].

is contained in a cylindrical solenoid whose magnetic field bends tracks of charged particles, allowing the measurement of charge and momentum.

The middle part of ATLAS is the calorimeter system. It is composed of an electromagnetic calorimeter, which captures leptons and photons, and an hadronic calorimeter that should capture most of the hadrons escaping from the center of the detector.

Around the calorimeters there are eight big toroidal magnets with air core that create a magnetic field to bend highly energetic muons which pass through the calorimeters. These particles are detected in the muon chambers which are assembled on the top of the toroid magnets. There are also muon wheels in the front and in the back of ATLAS to capture forwards/backwards flying muons.

The only Standard Model particle which cannot be detected directly in ATLAS is the neutrino. The presence of neutrinos can be spotted only from the missing transverse energy. However, in the BSM models, there are other particles which cannot be seen in ATLAS: e.g. the WIMP (weakly interacting massive particle, that is a candidate for the Dark Matter).

The scheme of particle identification in ATLAS is in fig. 2.4. Next sections will introduce ATLAS subsystems in more detail. The full documentation can be found in [63].

2.2.1 ATLAS coordinate system

The global ATLAS coordinate system uses both Cartesian and cylindrical coordinates. The centre of the coordinate system is in the center of the detector: the expected place of the pp collisions. The x coordinate is horizontal and pointing to the centre of the LHC ring. The y coordinate is pointing upwards and finally, z axis is parallel to the beam direction and it points in the direction of point 8 (cf. fig. 2.2). The cylindrical coordinates use z axis and radius r and angle ϕ in the transverse xy plane. The ϕ angle is measured from the positive direction of the x axis towards positive y axis and r distance is measured from the origin in the transverse plane. The angle with respect to the z axis is denoted θ.

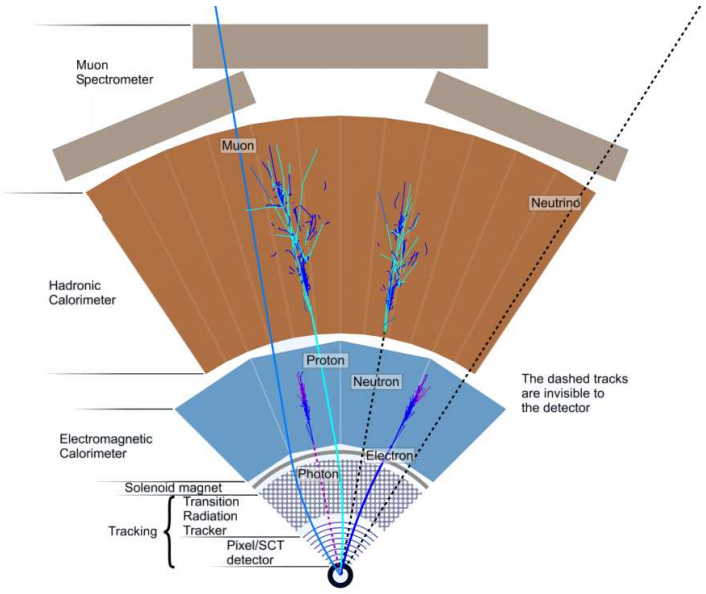

Figure 2.4: Scheme of particle identification in ATLAS. Charged particles are detected in the inner detector, and the curvature of their tracks can be used to measure the charge and momentum. Most photons and leptons are captured by the electromagnetic calorimeter. Hadrons are stopped in the hadron calorimeter. High energy muons leave hits in the muon spectrometer and neutrinos can be detected only from missing energy. Figure is from [64].

In addition, a useful quantity called *pseudorapidity* η is defined as

$$\eta = -\ln \tan\left(\frac{\theta}{2}\right) \tag{2.1}$$

In the xy plane ($\theta = \frac{\pi}{2}$) the η is zero and it increases with decreasing angular distance to the z axis. For the directions parallel to the z axis, the pseudorapidity is $\pm\infty$ depending on the direction. Pseudorapidity is identical to the rapidity for massless objects.

Pseudorapidity η is often used together with azimuthal angle ϕ to measure angular distance of objects ΔR. Assuming we have 2 objects with coordinates (ϕ_1, η_1) and (ϕ_2, η_2), distance is defined as $\Delta R = \sqrt{(\phi_1 - \phi_2)^2 + (\eta_1 - \eta_2)^2}$.

2.2.2 Inner detector

The inner detector performs high-precision tracking and vertexing as close to the interaction point as possible: the innermost layer is only 50.5 mm away from the beam. It is composed of three subdetectors: Pixel detector, SCT (semiconductor tracker) and TRT (transition radiation tracker). The first two use semiconductors to detect the charged particles. The main difference is that Pixel detector uses 2D array of detecting elements ("pixels"), SCT has only one-dimensional "strips". The TRT uses collection of straw tubes to collect many hits from the passing charged particles. It also uses transition radiation signal to distinguish pions from electrons.

The cross section of the central part of the inner detector is shown in fig. 2.5. The inner detector has coverage up to $|\eta| < 2.5$, with the exception of TRT that has coverage only for $|\eta| < 2.0$.

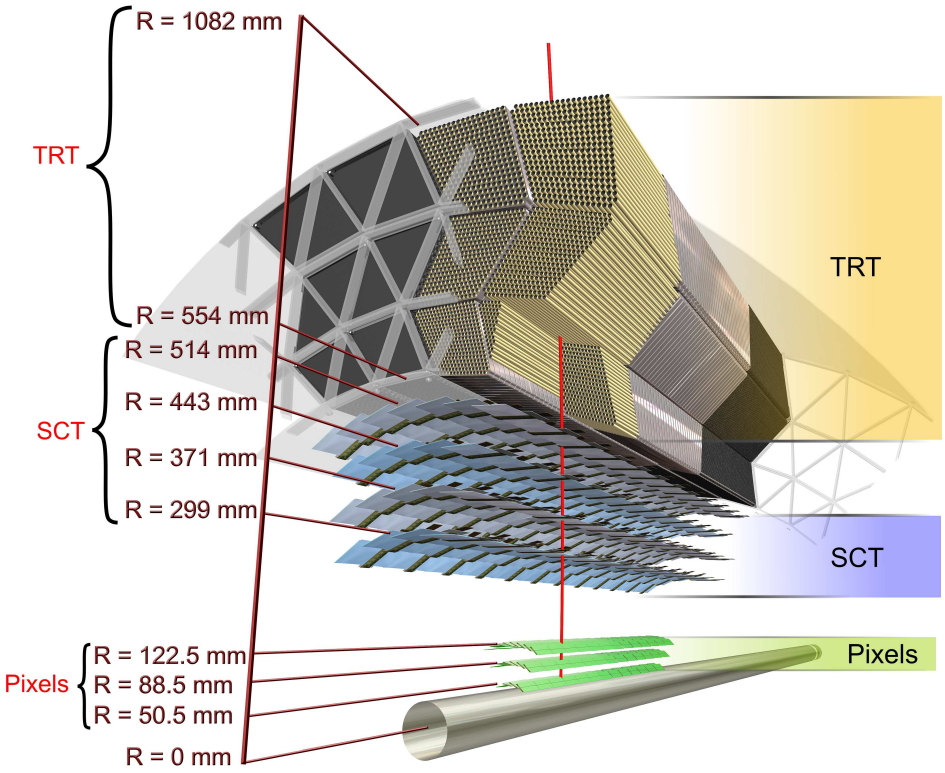

Figure 2.5: Cross section of the inner detector. From bottom, there is the beam pipe, the Pixel detector, SCT and the TRT. Figure is from [65].

Pixel Detector

The innermost part of the inner detector is the Pixel detector. It is a semiconductor tracker: it registers when a charged particle passes through the active volume of the detector (a "hit"). The positions of those hits is subsequently used by the tracking algorithms to reconstruct the tracks.

The Pixel Detector has three cylindrical layers in the center forming so-called "barrel" and 3 disks in the forward and backward region: so-called "endcaps". The layer closest to the beam ($r = 5.05$ cm) is know as the B-layer.

The detection of the charged particles is done by 1744 pixel modules: 288 on the endcap discs and 1456 on the barrel layers. One pixel module is about 7 cm long and 2 cm wide. There is an array of pixels on every module. Because pixels are arranged to form a two-dimensional field, they can offer extremely precise measurement of two coordinates of the track in the module coordinate system. The third coordinate is of course the module location. The performance parameters of the pixel detector are listed in tab. 2.2.

On both barrel and endcaps, the modules overlap to assure that the detector is hermetic with respect to outgoing particles[2].

[2]This is not completely true. There are known to be tiny 'holes' in the overlap regions. Also, not all modules

System	Element size	Resolution	η coverage
Pixels	50 $\times$ 400 μm	$\sigma_{R\phi} = 14$ μm $\sigma_z = 87$ μm $\sigma_R = 87$ μm	$\pm$ 2.5
SCT	75 or 112.5 μm $\times$ 12 cm	$\sigma_{R\phi} = 15$ μm $\sigma_z = 770$ μm	$\pm$ 2.5
TRT	4 mm diameter 150 cm long	$\sigma_{R\phi} = 170$ μm	$\pm$ 2.0

Table 2.2: Inner detector parameters

After the 2011 *pp* run, the fraction of operational channels is 96.4% out of 80 millions.

SCT

The Semiconductor tracker is designed very similarly to the Pixel Detector, but instead of pixels it uses the silicon strips for detection. The active parts of SCT form a one-dimensional array, i.e. SCT is very precise in the ϕ direction, but less precise in the z coordinate (along the beam axis). Tab. 2.2 shows details.

There are 2 active layers on either side of each SCT module and the small difference in r coordinate of both layers allows us to measure particle's z coordinate. The track going through the whole SCT should pass through 8 strip layers, providing 4 space points.

There are about 6.5 million channels with the operational fraction over 99%.

TRT

The Transition radiation tracker is the last (and largest) part of the inner detector. It is built from straw detectors, whose diameters are 4 mm. The central wire in each of them has 30 μm in diameter. In the barrel, the straws are 144 cm long, in the endcap they are a bit smaller.

TRT detects the transition radiation photons which were created by passing highly energetic particles and so it can distinguish between the electrons and hadrons (typically pions) because each creates a different number of these photons.

The TRT can give about 36 hits for on average for a particle. The large number of hits helps to increase robustness and precision of the momentum measurements. There are about 351 000 channels with the operational fraction of 97.5 %.

2.2.3 Calorimetry

The primary purpose of the calorimeter system is to measure the energy of photons and electrons/positrons (Electromagnetic calorimeter) and hadrons (Hadronic calorimeter). The calorimeters are very dense and usually make the particle stop and therefore deposit all its energy in a form of electromagnetic or hadronic shower. The calorimeters have large pseudorapidity coverage ($|\eta| < 4.9$) to capture most of the decay products from collisions.

ATLAS calorimeters consist of two different types. The first one is the electromagnetic (EM) Liquid Argon (LAr) calorimeter which has high granularity to provide precise measurement of electron and photon transverse energy. The second part of the ATLAS calorimetry are the

have overlap.

hadronic calorimeters that have coarser granularity which is sufficient for the jet reconstruction and missing E_T measurements. The schematic view of the ATLAS calorimeters is in fig. 2.6.

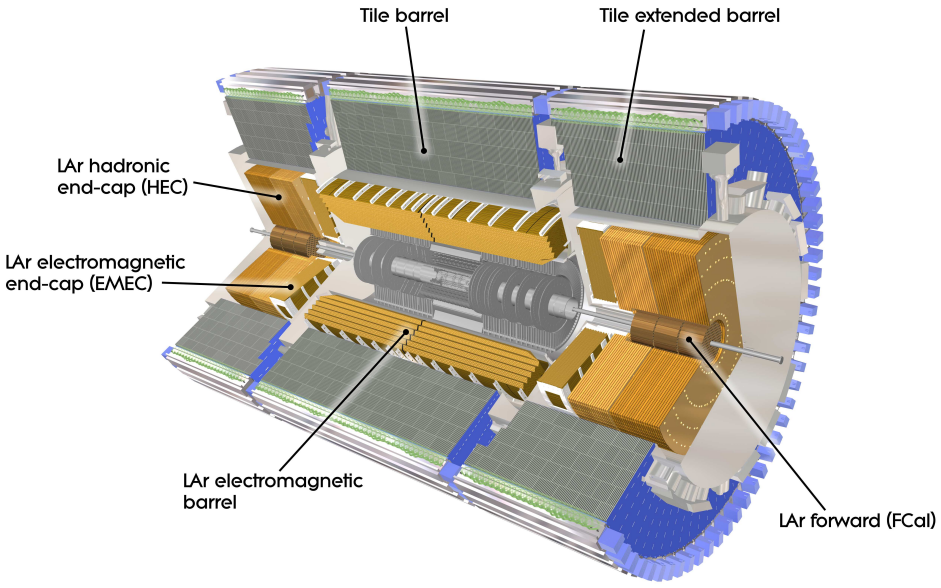

Figure 2.6: Scheme of the ATLAS calorimeter system. Figure shows both EM Liquid Argon (LAr) and hadronic calorimeters. Figure is from [66].

Calorimeters must provide good containment for electromagnetic and hadronic showers, and must also limit punch-through into the muon system. Hence, calorimeter depth is an important design consideration. The total thickness of the EM calorimeter is > 22 radiation lengths (X_0) in the barrel and > 24 X_0 in the end-caps.

LAr electromagnetic calorimeter

The EM calorimeter is a lead-LAr detector with accordion-shaped kapton electrodes and lead absorber plates over its full coverage. The accordion geometry provides complete ϕ symmetry without azimuthal cracks. Over the region devoted to precision physics ($|\eta| < 2.5$), the EM calorimeter is segmented in three sections in depth. For the rest of the acceptance the calorimeter is segmented in two sections in depth and has a coarser lateral granularity. In the region of $|\eta| < 1.8$, a presampler detector is used to correct for the energy lost by electrons and photons upstream of the calorimeter. The presampler consists of an active LAr layer of thickness 1.1 cm (0.5 cm) in the barrel (end-cap) region.

Hadronic calorimeters

There are three hadronic calorimeters at ATLAS: the Tile calorimeter, LAr hadronic end-cap (HEC) calorimeter and LAr forward calorimeter.

The tile calorimeter is placed directly outside the EM calorimeter envelope. Its barrel covers the region $|\eta| < 1.0$, and its two extended barrels the range $0.8 < |\eta| < 1.7$. The tile Calorimeter is a sampling calorimeter that makes use of steel as the absorber material and scintillating plates read out by wavelength shifting (WLS) fibers as the active medium. The calorimeter has quite high granularity - it consists of towers which have size 0.1×0.1 in $\Delta\eta$ and $\Delta\phi$. It has also

very quick response which makes it an ideal trigger device. The barrel and extended barrels are divided azimuthally into 64 modules. Radially, the tile calorimeter extends from an inner radius of 2.28 m to an outer radius of 4.25 m. It is segmented in depth in three layers.

The LAr HEC is in the endcaps and uses copper plates in liquid argon to stop hadrons. It consists of two independent wheels per end-cap, located directly behind the end-cap electromagnetic calorimeter and sharing the same LAr cryostats. To reduce the drop in material density at the transition between the end-cap and the forward calorimeter (around $|\eta| = 3.1$), the HEC extends out to $|\eta| = 3.2$, thereby overlapping with the forward calorimeter. Similarly, the HEC η range also slightly overlaps that of the Tile calorimeter ($|\eta| < 1.7$) by extending to $|\eta| = 1.5$.

The forward calorimeter (FCal) is located very close to the beampipe to cover particles with large pseudorapidity. It is made of copper and tungsten. It is integrated into the end-cap cryostats, as this provides clear benefits in terms of uniformity of the calorimetric coverage as well as reduced radiation background levels in the muon spectrometer. The FCal is approximately 10 interaction lengths deep, and consists of three modules in each end-cap: the first, made of copper, is optimised for electromagnetic measurements, while the other two, made of tungsten, measure predominantly the energy of hadronic interactions.

2.2.4 Muon spectrometer

The only detectable particles which usually traverse through the whole ATLAS are muons because they are minimum ionizing particles (MIP). Therefore, there is an outer envelope of muon spectrometers which measures their momenta with high precision. This is very important, because a typical trigger for a hadron collider like LHC would often include the existence of at least one high-energetic muon.

The muon spectrometry is based on the magnetic deflection of muon tracks in the large superconducting air-core toroid magnets, instrumented with separate trigger and high-precision tracking chambers. Over the range $|\eta| <$1.4, magnetic bending is provided by the large barrel toroid. For $1.6 < |\eta| < 2.7$, muon tracks are bent by two smaller end-cap magnets inserted into both ends of the barrel toroid. Over $1.4 < |\eta| < 1.6$, usually referred to as the transition region, magnetic deflection is provided by a combination of barrel and end-cap fields. This magnet configuration provides a field which is mostly orthogonal to the muon trajectories, while minimising the degradation of resolution due to multiple scattering.

In the barrel region, tracks are measured in chambers arranged in three cylindrical layers around the beam axis; in the transition and end-cap regions, the chambers are installed in planes perpendicular to the beam, also in three layers.

Over most of the η-range, a precision measurement of the track coordinates in the principal bending direction of the magnetic field is provided by Monitored Drift Tubes (MDTs). The mechanical isolation in the drift tubes of each sense wire from its neighbours guarantees a robust and reliable operation. At large pseudorapidities, Cathode Strip Chambers (CSCs, which are multiwire proportional chambers with cathodes segmented into strips) with higher granularity are used in the innermost plane over $2 < |\eta| < 2.7$, to withstand the demanding rate and background conditions.

The trigger system covers the pseudorapidity range $|\eta| < 2.4$. Resistive Plate Chambers (RPCs) are used in the barrel and Thin Gap Chambers (TGCs) in the end-cap regions. The trigger chambers for the muon spectrometer serve a threefold purpose: provide bunch-crossing identification, provide well-defined p_T thresholds, and measure the muon coordinate in the direction orthogonal to that determined by the precision-tracking chambers.

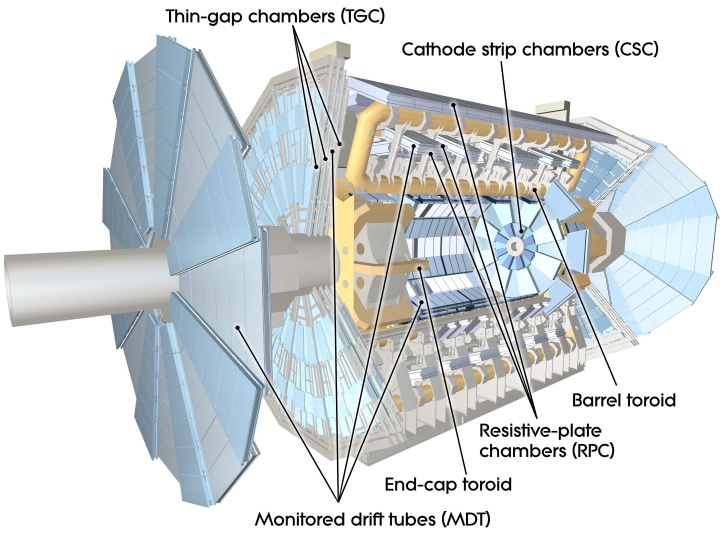

Figure 2.7: Scheme of the ATLAS muon spectrometer. Figure is from [67].

2.2.5 Magnets

The whole ATLAS is set in a very strong magnetic field which is used to bend the tracks of charged particles. The field is generated by two systems of magnets.

The first one is a solenoid magnet which is located between the inner detector and the Calorimeters. It is aligned with the beam axis and provides a 2T axial magnetic field for the inner detector while minimising the radiative thickness in front of the barrel electromagnetic calorimeter.

The second system is composed of the toroid magnets which are on the perimeter of the whole ATLAS detector, together with the muon chambers. The barrel toroid (8 coils with air core) is designed to provide 0.5 T. The endcap toroids are essentially large cryostats and should provide a field of 1 T.

2.2.6 Trigger and Data Acquisition

When running at the full design luminosity of 1×10^{34} cm^{-2}s^{-1}, there will be a bunch crossing every 25 ns and each crossing will bring more than 20 *pp* collisions. Not only such a huge flux of information ($O(10^9)$ Hz) is impossible to store and analyze, but only very few collisions are actually interesting for the new physics searches, because most of the LHC interaction are low energy soft QCD processes ("minimum bias"[3]).

In fact, the ATLAS physics program is like looking for a needle in a haystack. To be successful in this task, ATLAS employs a three level trigger to choose the potentially interesting events. That is not a trivial task - when running with the 25 ns bunch separation, the next bunch crossing happens before the products of the collisions from the previous crossing are able to reach the edge of the detector.

[3]Events selected with minimal trigger requirements are called *minimum bias*. It is obvious that this definition is experiment dependent as the notion of minimal trigger may vary across different experiments. In ATLAS, the minimal trigger is a hit it the scintillator placed on both ends of the inner detector – so-called Minimum Bias Trigger Scintillator (MBTS).

Level 1

The Level 1 (L1) trigger searches for high transverse-momentum muons, electrons, photons, jets, and τ- leptons decaying into hadrons ("τ jets"), as well as for events with large missing and total transverse energy. Its selection is based on information from a subset of detectors. High p_T muons are identified using trigger chambers in the barrel and end-cap regions of the muon spectrometer.

Calorimeter selections are based on reduced-granularity information from all the calorimeters. The transverse momentum of objects selected by the L1 trigger is compared to the programmable trigger thresholds. Some triggers require also the isolation threshold: the transverse energy deposited in the calorimeter around the candidate object must be less than a given threshold. Results from the L1 muon and calorimeter triggers are processed by the central trigger processor (CTP), which implements a trigger "menu" made up of combinations of trigger selections. The CTP receives the information from the calorimeter and muon triggers that consists of multiplicities of various passed thresholds for electrons/photons, jets, τ jets and muons and the flags indicating which thresholds were passed for the missing energy, total transverse energy and total transverse jet energy. Some input is also provided from the special triggers like minimum bias scintillator or beam pick-up monitors. Finally, the CTP is provided the information about the beam structure, i.e. which bunch crossings are "filled" (i.e. contain the beam) and "paired" (the corresponding bunch crossing is filled at both beams, so collisions are possible) and which bunch crossings are empty.

In the next step, CTP uses look-up tables to form trigger conditions from the input signals. Such a condition could be, that a multiplicity of a particular muon threshold is larger than one, i.e. at least 2 muons in the event have passed the threshold. For such an event the trigger conditions would be set true. Further condition can be whether the event happened in the filled and paired bunch. In total, there can be up to 256 trigger conditions at any time that are combined to form up to 256 trigger items. Every condition may contribute to every trigger item.

Pre-scaling[4] of trigger menu items is also available, allowing optimal use of the bandwidth as luminosity and background conditions change. Prescales can be changed during the run on the *lumiblock*[5] boundaries. Events passing the L1 trigger selection are transferred to the next stages of the detector-specific electronics and subsequently to the data acquisition system.

In each event, the L1 trigger also defines one or more Regions-of-Interest (RoIs), i.e. the geographical coordinates in η and ϕ, of those regions within the detector where its selection process has identified interesting features (fig. 2.8). The RoI data include information on the type of feature identified and the criteria passed, e.g. a threshold. This information is subsequently used by the high-level trigger. The size of the RoI depends on the object it stores, e.g. it is larger for jets than for photons.

L1 trigger needs about 2.5 μs (compare to 25 ns, which is the time separating the bunches) to reach its decision and then the information is passed to the high-level trigger. The output rate of the L1 trigger has hardware limitation of 75 kHz (compared to $O(20-40)$ MHz of the input collision rate).

[4]Prescale of n means that only one out of n times the trigger accept decision is true the event is passed further, while the event gets rejected otherwise. The net effect of prescale n is decreasing the output rate of a given trigger n times.

[5]Luminosity block (also lumiblock, LB) is the subset of a run during which data taking conditions are assumed to be constant. The length of a lumiblock was 2 minutes in 2010 and 1 minute in 2011.

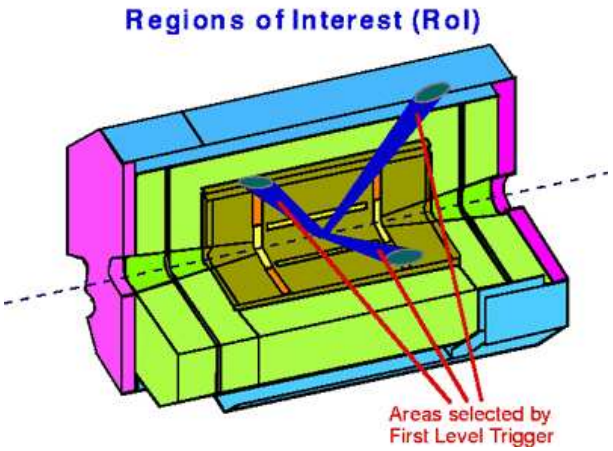

Figure 2.8: Example how the Regions of interest selected by L1 Trigger may look like. Figure is from [64].

High-level trigger

The high-level trigger (HLT) is composed of Level 2 (L2) and Event Filter (EF), both of which are software trigger systems run on a large processor farm adjacent to the ATLAS experimental cavern to prevent any unnecessary delays from signal transport.

The L2 uses full granularity information from the detectors, but only within the RoI's selected by the L1. They account for 2-6% of the total detector volume. The L2 uses fast algorithms and simplified selections to reduce the trigger rate down to 3.5 kHz. Unlike L1, the L2 also uses information from the inner detector to perform fast tracking. The processing of one event takes on average 40 ms.

The events accepted by the L2 are passed to Event Builder that assembles all the event fragments and passes the full event information to the last stage of the trigger selection: the Event Filter. Because it has access to the full detector information and also enough time for execution, the EF runs almost the same algorithms as used during offline reconstruction and also the object selection is very similar to the one used offline. The EF reduces the output rate to 300–400 Hz while spending on average 4 s on every event.

The events that pass the trigger selection are written to the disk for reconstruction and analysis. The average size of the event from pp collisions is approximately 1.3 MB.

There are about 500 triggers defined in the current trigger menu.

Trigger nomenclature

The trigger menu is composed of different classes of triggers:

Single object triggers are used for final states with at least one characteristic object. For example a single muon trigger with the p_T threshold of 6 GeV, referred to as mu6

Multiple object triggers are used for the final states with two or more characteristic objects of the same type. The multiplicity is indicating by a number in the trigger name – e.g. 2mu6 trigger requires presence of at least 2 muons passing the 6 GeV threshold

Combined triggers are used for final states with two or more characteristic objects of a different type. For example trigger requiring a muon passing 13 GeV p_T threshold and at

least 20 GeV of missing E_T for selection of $W \to \mu\nu$ events would be denoted mu13_xe20

Topological triggers are used for final states that require information from two or more RoI's. For example electron-muon trigger that applies cut also on the distance and invariant mass of the lepton pair.

When referring to a particular level of trigger, the level (L1, L2 or EF) appears as a prefix, so L1_TAU9 refers to the L1 trigger item with 9 GeV threshold, while L2_tau12 refers to the L2 item with a 12 GeV threshold. Names without a prefix are used to refer to the whole chain. The trigger rates can be controlled not only by different transverse momentum cuts but also by changing the object selection cuts (for example the size of the deposit in the calorimeter) at HLT. The selectivity of a set of cuts is represented by the terms loose, medium and tight that are appended to the trigger name: e.g. e10_medium. The loose selection has the highest efficiency (w.r.t. to the objects that can be reconstructed and selected using the most refined offline algorithms) but also the highest rate. The tight selection is opposite (lowest efficiency and lowest rates). More information about the ATLAS trigger design and performance can be found in [63, 68].

2.3 ATLAS detector software

The algorithms that are used to reconstruct the data and prepare the physics objects for the analysis are summarized in section 2.3.1. The algorithms that are running online to select interesting events are described in section 2.3.2.

Besides those two important categories of software, there are many other algorithms to provide detailed simulation of how various events look like inside the ATLAS detector [69]. Finally, there is a lot of support software packages to control and monitor detector status, performance of the other online and offline algorithms, etc. Most of the ATLAS software is made in the C++ based framework called Athena [70]. The detailed overview of the ATLAS algorithms and their performance is available in [71].

2.3.1 Offline reconstruction and identification

The ATLAS software is used to reconstruct the following physics analysis objects from data: muons, electrons, photons, hadronic taus, jets and missing transverse energy. Chapters 3 and 4 will present analyses using reconstructed muons, electrons and hadronic taus: so those objects will be introduced in this section. Interested reader is referred to [63, 71] for more details about the ATLAS offline reconstruction and identification.

Muons

The ATLAS detects and measures muons in the muon spectrometer and also exploits the measurements in the inner detector and the calorimeters to improve the muon identification efficiency and momentum resolution. Muon measurements are a combination of accurate measurements in the muon spectrometer and in the inner detector. The muon spectrometer also efficiently triggers on muons over a wide range of energies and over $|\eta| < 2.4$, as described in detail in section 2.3.2. The inner detector provides the best measurement at low to intermediate momenta, whereas the muon spectrometer takes over above 30 GeV. The toroidal field guarantees excellent momentum resolution even at the highest values of η.

Muons with momenta ranging from approximately 3 GeV to 3 TeV are identified and measured with optimal acceptance and efficiency through the use of a combination of three track reconstruction strategies (see [63] for a description of the tracking software):

Stand-alone muon track reconstruction based solely on the muon spectrometer data over the range $|\eta| < 2.7$ (defined by the spectrometer acceptance).

Combined combination of a muon-spectrometer track with an inner-detector track over the range $|\eta| < 2.5$(defined by the inner-detector acceptance).

Segment tag combination of an inner-detector track with a muon-spectrometer segment, i.e. a straight-line track, in an inner muon station.

The muon-spectrometer track parameters are determined at the inner muon spectrometer stations, which yield the first set of measurements in the muon spectrometer. The track is then propagated back to the interaction point and the momentum is corrected for the energy loss in the calorimeters (and in the inner detector). The energy lost by dE/dX in the calorimeters is estimated by an algorithm, which uses either the parametrised expected energy loss or the measured calorimeter energy. The measured energy is used only if it exceeds significantly the most probable energy loss and if the muon track is isolated.

The combination of the stand-alone tracks reconstructed in the muon spectrometer with tracks reconstructed in the inner detector is performed in the region $|\eta| < 2.5$, which corresponds to the geometrical acceptance of the inner detector. This combination considerably improves the momentum resolution for tracks with momenta below 100 GeV, but also suppresses to a certain extent backgrounds from pion punch-through and from pion or kaon decays in flight.

Electrons

For the reconstruction of electrons and photons, a seed cluster is taken from the electromagnetic calorimeter and a loosely matching track is searched for among all reconstructed tracks. Additionally, the candidate is flagged if it matches a photon conversion reconstructed in the inner detector. Electron and photon candidates are thus separated reasonably cleanly, by requiring the electrons to have an associated track but no associated conversion. In contrast, the photons are defined as having no matched track, or as having been matched to a reconstructed conversion.

For all electron candidates, shower-shape variables (lateral and longitudinal shower profiles, etc.) are calculated using the fine granularity of the electromagnetic calorimeter, and typically more than 50 calorimeter cells are summed to collect the full cluster energy. Additionally, combined reconstruction properties, such as the ratio of energy (calorimeter) to momentum (inner detector), the difference between the coordinates η and ϕ reconstructed by the cluster and the track extrapolated into the calorimeter, and the ratio of high-threshold transition radiation hits to low-threshold hits on the track in the TRT, are used to identify electrons.

The energy of electrons is obtained from the energy measured in the calorimeter. The η and ϕ directions are, however, more precisely determined using the associated track.

The standard identification for isolated electrons is based on cuts on the shower shapes, on information from the reconstructed track and on the combined reconstruction. Three sets of cuts have been studied depending on the signal efficiency and background rejection:

loose cuts consisting of simple shower-shape cuts (longitudinal leakage, shower shape in the middle layer of the electromagnetic calorimeter) and very loose matching cuts between reconstructed track and calorimeter cluster

medium cuts which add shower-shape cuts using the important information contained in the first layer of the electromagnetic calorimeter and track-quality cuts

tight cuts which tighten the track-matching criteria and the cut on the energy-to-momentum ratio. These cuts also explicitly require the presence of a innermost pixel layer hit on the track (to further reject photon conversions) and a high ratio between high-threshold and low-threshold hits in the TRT detector (to further reject the background from charged hadrons)

Hadronic taus

Hadronic decays of τ leptons play an important role at the LHC, especially as probes for new phenomena spanning a wide range of theoretical models.

In general, hadronically decaying τ leptons are reconstructed by matching narrow calorimeter clusters with a small number of tracks. Specific analyses may require exactly one or three tracks with total charge consistent with the charge of a τ lepton, and, if more than one, the tracks may be required to be quite collimated and to be consistent with originating from a common secondary vertex. The visible reconstructed energy of the hadronically decaying τ lepton is concentrated in a narrow cone around the leading (highest-p_T) track (typically a cone of $\Delta R = 0.2$ is sufficient to collect this energy).

Several key variables, which are characteristic of the properties of hadronic τ decays, are used for the purpose of identification [72].

Electromagnetic radius: Transverse energy weighted shower width in the electromagnetic (EM) calorimeter:

$$\mathcal{R}_{\mathrm{EM}} = \frac{\sum_{i\in\{\mathrm{EM}\ 0-2\}}^{\Delta R_i<0.4} E_{\mathrm{T},i}^{\mathrm{EM}} \Delta R_i}{\sum_{i\in\{\mathrm{EM}\ 0-2\}}^{\Delta R_i<0.4} E_{\mathrm{T},i}^{\mathrm{EM}}} ,$$

where i runs over cells in the first 3 layers of the EM calorimeter associated to the tau candidate. ΔR_i is defined between a calorimeter cell and the tau jet axis (which itself is a barycenter of the calorimeter cells associated to the tau candidate).

Calorimetric radius: Transverse energy weighted shower width in the electromagnetic and hadronic calorimeter:

$$\mathcal{R}_{\mathrm{calo}} = \frac{\sum_{i\in\{\mathrm{all}\}}^{\Delta R_i<0.4} E_{\mathrm{T},i}^{\mathrm{EM}} \Delta R_i}{\sum_{i\in\{\mathrm{all}\}}^{\Delta R_i<0.4} E_{\mathrm{T},i}^{\mathrm{EM}}} ,$$

where i runs over cells in all the calorimeter layers associated to the tau candidate. ΔR_i is defined between a calorimeter cell and the tau jet axis (which itself is a barycenter of the calorimeter cells associated to the tau candidate).

Track radius: Transverse momentum weighted track width:

$$\mathcal{R}_{\mathrm{track}} = \frac{\sum_{i}^{\Delta R_i<0.4} p_{\mathrm{T},i}^{\mathrm{EM}} \Delta R_i}{\sum_{i}^{\Delta R_i<0.4} p_{\mathrm{T},i}^{\mathrm{EM}}} ,$$

where i runs over the tracks associated to the tau candidate within $\Delta R_i < 0.4$. Distance ΔR_i is defined relative to the tau jet axis (therefore also single track candidates can acquire non-zero values of track radius) and $p_{\mathrm{T},i}$ is the track transverse momentum.

Track spread: Transverse momentum weighted track spread:

$$\mathcal{W}_{\text{track}} = \frac{\sum_i^{\Delta R_i<0.4} p_{\text{T},i}^{\text{EM}} \Delta R_i^2}{\sum_i^{\Delta R_i<0.4} p_{\text{T},i}^{\text{EM}}} ,$$

where i runs over the tracks associated to the tau candidate within $\Delta R_i < 0.4$. Distance ΔR_i is defined relative to the tau jet axis (therefore also single track candidates can acquire non-zero values of track radius) and $p_{\text{T},i}$ is the track transverse momentum.

Centrality fraction: Fraction of transverse energy in the core ($\Delta R < 0.1$) of the tau candidate

$$f_{\text{core}} = \frac{\sum_{i\in\{\text{all}\}}^{\Delta R_i<0.1} E_{\text{T},i}^{\text{EM}}}{\sum_{i\in\{\text{all}\}}^{\Delta R_i<0.4} E_{\text{T},i}} ,$$

where i runs over all cells associated to the tau candidate. ΔR_i is defined between a calorimeter cell and the tau jet axis.

Leading track momentum fraction:

$$f_{\text{track}} = \frac{p_{T.1}^{\text{track}}}{p_T^{\tau}}$$

where $p_{T,1}^{\text{track}}$ is the transverse momentum of the leading core track of the tau candidate and p_T^{τ} is the total transverse momentum of the tau candidate.

Both traditional cut-based selections and multi-variate discrimination techniques (likelihood, boosted decision trees) are applied to this set of identification variables.

2.3.2 Online reconstruction and identification

The main ideas and concepts of the ATLAS trigger have been already described in section 2.2.6. This section will give brief overview of how we can reconstruct an electron, muon and a hadronic tau within a very short time and use it to select events for future analysis. Additional details as well as other ATLAS trigger algorithms are described in [63, 68].

Muon trigger

The L1 muon trigger system is a hardware-based system to process input data from fast muon trigger detectors. Muons are triggered at L1 using the RPC system in the barrel region ($|\eta| < 1.05$) and the TGC system in the end-cap regions ($1.05 < |\eta| < 2.4$). The RPC and TGC systems provide rough measurements of muon candidate p_T, η, and ϕ. Muon candidates are identified by forming coincidences between the muon planes. The geometrical coverage of the trigger in the end-caps is close to 99%. In the barrel the coverage is reduced to roughly 80% due to a crack around $\eta = 0$, the feet and rib support structures for the ATLAS detector and two small elevators in the bottom part of the spectrometer.

In order to form coincidences, hits are required to lie within parametrized geometrical muon roads. A road represents an envelope containing the trajectories, from the nominal interaction point, of muons of either charge with a p_T above a given threshold. There are six programmable p_T thresholds at L1 which are divided into two sets: three low-p_T thresholds to cover values up to 10 GeV, and three high-p_T thresholds to cover p_T greater than 10 GeV.

The muon HLT makes use of the information from the MDT chambers that provide precision hits in η in addition to the L1 trigger chambers. The CSC that form the innermost muon layer in the region $2 < |\eta| < 2.7$, were not used in the HLT during 2010 data-taking period, but were used in 2011.

At L2, each L1 muon candidate is refined by including the precision data from the MDT's in the RoI defined by the L1 candidate. For the first time the L2 algorithm combines the tracks reconstructed in the spectrometer with the inner detector tracks to form muon candidate with refined track parameter resolution. Finally, tracking and calorimeter information is used to identify isolated muons.

At the EF, the muon reconstruction starts from the RoI identified by L1 and L2, reconstructing segments and tracks using information from the trigger and precision chambers. There are three different reconstruction strategies used in the EF that are analogical to the offline reconstruction: MS-only (similarly to the offline standalone muons, only muon spectrometer information is used to determine the muon track parameters), Combined muon and Inside-Out (similarly to the segment tag muons, the reconstruction starts with the inner detector track and extrapolated to the MS). Only combined and and inside-out muons are used for main physics trigger and offline reconstruction; MS-only muons are used only by specialized triggers.

Electron trigger

Electrons and photons are reconstructed in the trigger system in the region $|\eta| < 2.5$. At L1 RoI's are shared between electron and tau triggers. The electron/photon L1 trigger algorithm identifies an Region of Interest as a 2×2 trigger tower[6] cluster in the electromagnetic calorimeter for which the transverse energy sum from at least one of the four possible pairs of nearest neighbour towers (1×2 or 2×1) exceeds a pre-defined threshold (fig. 2.9) Isolation-veto thresholds can be set for the 12-tower surrounding ring in the electromagnetic calorimeter, as well as for hadronic tower sums in a central 2×2 core behind the cluster and the 12-tower hadronic ring around it.

For each identified electromagnetic object, RoI's are formed containing the η and ϕ directions and the transverse energy thresholds that have been passed, e.g. EM5, EM10, as specified by the L1 trigger menu.

The L2 electron algorithm performs clustering withing an RoI of dimension $\Delta\eta \times \Delta\phi = 0.4 \times 0.4$. The algorithm relies on the fact that most of the energy from an electron or photon is deposited in the second layer of the EM calorimeter. the L2 electron selections employ also fast track reconstruction.

The EF also performs calorimeter cluster and track reconstruction, but uses the algorithms similar to the offline reconstruction.

At L2 and the EF a calorimeter-based selection is made, based on cluster E_T and cluster shape parameters and three sets of reference cuts are defined with increasing power to reject background: loose, medium, and tight. They use similar selection as their offline counterparts.

Tau trigger

At Level 1, the tau trigger uses the electromagnetic and hadronic calorimeters to find transverse energy deposits that pass the threshold (during 2010 the lowest threshold was 5 GeV). As mentioned above, the RoI finding algorithm is shared between electron and the tau trigger, only the thresholds are different and electron trigger does not use hadronic calorimeter. The size of

[6] At L1, the decision is not based on the full granularity but rather on the information from analogue sums of calorimeter elements within projective regions called trigger towers. The size of a tower is approx. $\Delta\eta \times \Delta\phi = 0.1 \times 0.1$.

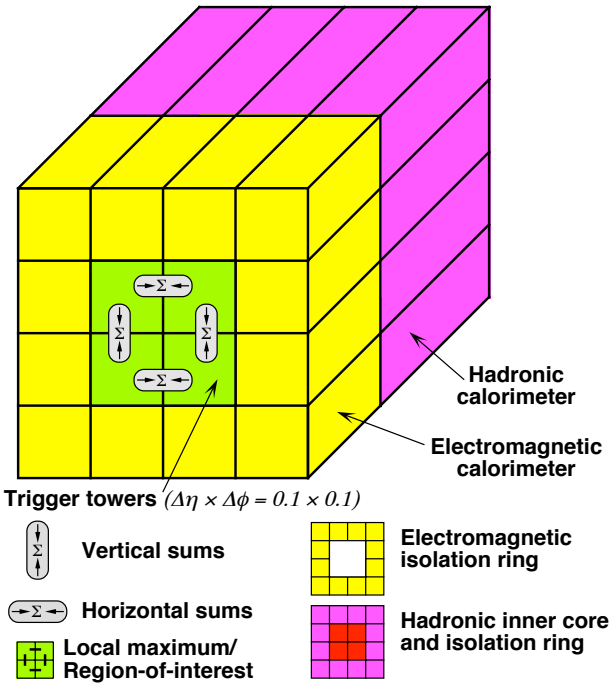

Figure 2.9: Building blocks of L1 e/γ and tau algorithms with the sums to be compared to the programmable thresholds.

the tau RoI is 0.4×0.4 in $\phi \times \eta$ space. At L2, full detector granularity inside the RoI is used and several selection criteria are applied using tracking and calorimeter based information. It takes advantage of calorimeter cluster confinement and low track multiplicity to discriminate taus from the QCD background. Exploiting the same characteristics, the Event Filter uses different selection criteria for 1-prong and multiprong decays in more refined algorithms which are similar to the offline reconstruction algorithms, with the time constraint of a few seconds. Note that unlike L2, the Event Filter can access the complete detector information in the full detail. The L2 and EF are together referred to as High Level Trigger (HLT). The ATLAS trigger system is described in detail in [63]. The EF performance at the tau trigger is presented in details in [73] for the tau trigger signatures implemented at the start of LHC physics run.

At the EF, the variables used for the trigger selection are the same as in the offline reconstruction. At L2, there is an additional variable used for the trigger decision, namely $\sum p_T^{(\mathrm{iso})} / \sum p_T^{(\mathrm{core})}$ that is exploiting the track isolation.

All tracks which have $\Delta R < 0.1$ from the leading track (track with highest p_T) are *core tracks*, all tracks with $0.1 < \Delta R < 0.3$ are *isolation tracks*. A variable defined as sum of the p_T of isolation tracks divided by the sum of p_T of core tracks is called $\sum p_T^{(\mathrm{iso})} / \sum p_T^{(\mathrm{core})}$ and is doing most of the QCD background rejection at L2.

Chapter 3

The Search for Low Mass Higgs Boson

As it is shown in chapter 1, the *Ideal Higgs Scenario* is an interesting realization of the NMMSM that itself is an attractive extension of the Standard Model. The most important signature of that model is the existence of the light pseudoscalar a_1, therefore detection or exclusion of such a particle can vastly improve our knowledge about the feasibility of the Ideal Higgs Scenario. The theoretically most favoured mass region is 8.8 GeV $< \mathrm{m}(a_1) <$ 10.5 GeV (see section 1.3.3).

There are 2 classes of analyses looking for the a_1 depending on its production: being the lightest of all the Higgs bosons and having considerable coupling to other Higgs bosons, it can be produced either directly, or via decay of the heavier Higgs boson(s). The a_1 then decays to a fermion-antifermion pair with the preference of heavy fermions. If the a_1 mass is larger than 2 m_τ and smaller than 2 m_B, the dominant decay is to the τ pair with the branching ratio 0.7-0.9 depending on the a_1 mass and $\tan\beta$. The full decay spectrum of a_1 is depicted in fig. 1.8.

The analyses searching for indirectly produced a_1 can be divided into further two categories. The analyses of the first type look for the decay of the lightest scalar boson h_1 to the a_1 pair that decays to the pairs of μ's or τ's [74, 75]. The analyses of the second type are trying to detect $H^\pm \to a_1 W^\pm$ events [76]. None of those has found any evidence of a_1.

The direct production searches have so far focused on the gluon fusion. Due to the lightness of a_1, the cross-section of $gg \to a_1$ is greatly enhanced compared to the gluon fusion production of the Standard Model Higgs boson with a mass greater then 115 GeV. The cross-section of the direct a_1 production in 7 TeV pp collisions is presented in fig. 3.1. The ATLAS analysis using 2010 data and searching for the $gg \to a_1 \to \mu\mu$ process saw no evidence of a_1 in the mass ranges 6–9 GeV and 11–12 GeV [77].

This chapter presents the first search for the direct production of a_1 in the τ channel using 2011 ATLAS data. The main advantage of the τ channel, compared to the μ channel, is a much larger branching fraction. Therefore, the decays of Υ resonances that form major background for the $a_1 \to \mu\mu$ searches are much less important in the $a_1 \to \tau\tau$ channel. Because of this, the analysis is also possible in the mass region directly around Υ resonances (9-11 GeV) that was excluded from analysis [77]. The disadvantage of the τ channel is the presence of neutrinos in the final state, making the detection of the a_1 more challenging.

3.1 Signal process

Unlike other charged leptons, the τ's are unstable particles with the lifetime of 2.9×10^{-13} s [18]. The reconstruction and identification of the hadronic τ decays is not reliable in the momentum

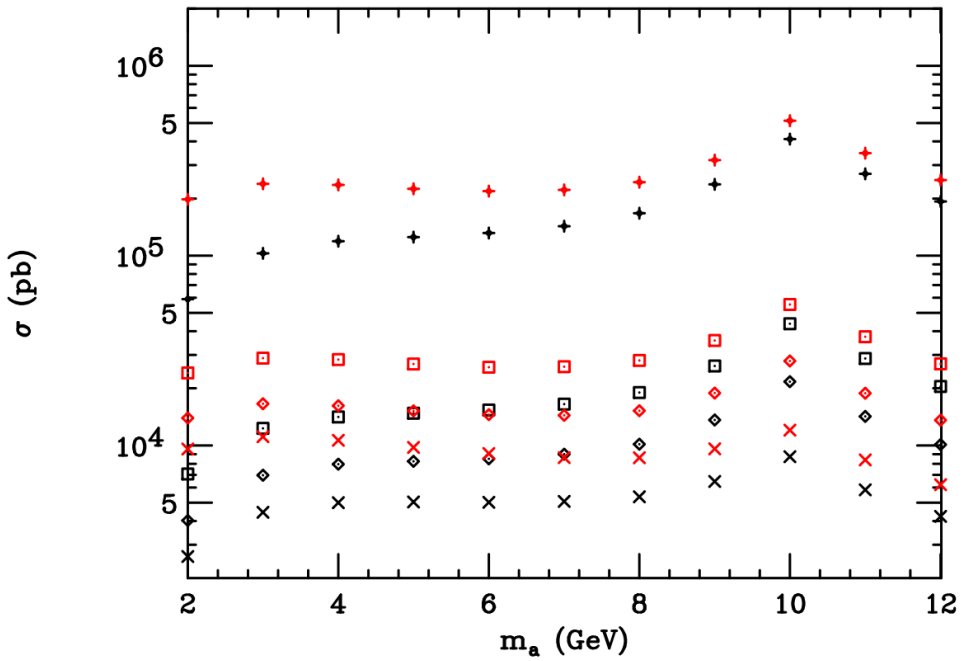

Figure 3.1: The cross-section of the production of a_1 particle via gluon fusion as a function of its mass. The four sets of points correspond to the $\tan\beta = 1$, 2, 3 and 10 from bottom to the top. For each m_a and $\tan\beta$ value, two points are plotted: cross-section with (higher point) and without (lower point) resolvable parton final state contribution. Note that the cross-section on this plot corresponds to the generic 2HDM with light CP-odd Higgs boson. To obtain value for the NMSSM, one should multiply the values in this plot by $(\cos\theta_A)^2$ (cf. (1.36)). The plot is from [50].

range of the a_1 decay products due to the low calorimeter resolution and huge QCD background. Therefore, this analysis focused on events where both τ leptons decay leptonically. There are three possible final states: ee, $\mu\mu$ and $e\mu$. Only the last one was studied because its branching fraction is twice the branching fraction of the same flavour decays. The $e\mu$ final state also offer better suppression of quarkonia decays: only $\Upsilon \to \tau\tau$ events can have this final state. The diagram of the signal process is shown in fig. 3.2.

The quark loop in the gluon fusion is composed mostly of b quarks, because coupling of a_1 to the down-type quarks is much enhanced [46]. There are 6 leptons in the final state, but only two of them are visible in the ATLAS detector. The mass constructed from electron and muon (so-called *visible* or *di-lepton mass*) is therefore only a fraction of the original a_1 mass.

3.2 Background processes

3.2.1 Real e and μ in the final state

There are several Standard Model processes that can produce electron and muon in the final state and contribute as a background to the search. Those are events where a tau pair is produced (either in the decay of a heavier resonance or through a Drell-Yan process) and both taus decay leptonically or processes where an electron and a muon are produced in a decay cascade of other particles. The particles that can decay to a τ pair are $\Upsilon(1S)$, $\Upsilon(2S)$, $\Upsilon(3S)$, Z boson and the

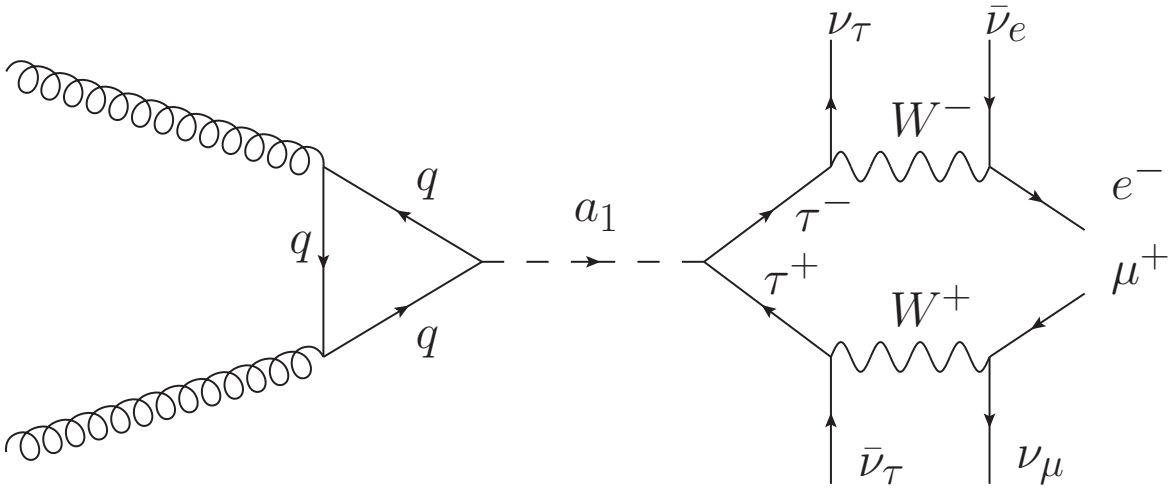

Figure 3.2: The Feynman diagram of the signal process when gluon fusion creates a_1 that decays to τ pair decaying to $e\mu$ leptons.

photon.

The Υ resonances are bound states of the $b\bar{b}$ system (bottomium). There are several allowed energy levels for this $b\bar{b}$ system (although all of them are only meta-stable). Therefore the whole bottomium system can be with some approximation described by non-relativistic QCD (NRQCD) [78]. The whole family of bottomium resonances is shown in fig. 3.3. The Υ resonances are special, because a large fraction of them decays to a $\ell^+\ell^-$ pairs, while all the other $b\bar{b}$ resonances decay almost exclusively to hadrons [18]. Nevertheless, only those Υ's that are below $B\bar{B}$ threshold (1S,2S and 3S) decays to lepton pairs via $b\bar{b}$ annihilation (fig. 3.4(a)). The higher Υ resonances decay almost all the time to the $B\bar{B}$ meson pair (fig. 3.4(b)) [18].

The Υ resonances share many characteristics with the signal process: they have similar mass and they can also decay to a tau lepton pair. Therefore a good estimate of the Υ yield is necessary for this analysis. That is discussed in section 3.8.1.

When quark and antiquark from different protons in the beam annihilate, a virtual photon or Z boson can be created, and decay subsequently to a pair of oppositely-charged leptons. This is called Drell-Yan process [79] and its Feynman diagram is shown in fig. 3.4(c). The mass spectrum of such events is continuous so some of them can resemble the decay of 10 GeV neutral Higgs boson.

One of the most important processes that has electron and muon in its decay cascade is $t\bar{t}$ production. It is shown in fig. 3.4(d) where electron and muon are originating from decays of different W bosons. Such events have oppositely-charged electron and muon in the final state. Because the energy of $t\bar{t}$ decay is split between W's and b's, the di-lepton mass constructed from electron and muon has wide distribution with long tails that extend all the way to the mass region relevant for this analysis.

There are, however, additional sources of leptons in $t\bar{t}$ events. The electron and muon can be also produced in the semi-leptonic decay of the B hadrons created after b quark hadronization (fig. 3.4(e)). It is also possible that a charm meson created in the bottom meson semi-leptonic decay also decay semi-leptonically, thus producing oppositely-charged lepton pair in a decay of single particle. The diagram of this process is in fig. 3.4(f).

The bottom and charm hadrons are produced also independently of $t\bar{t}$ events and via decays like in figs. 3.4(e) and 3.4(f) they can produce electron and muon in the final state as well.

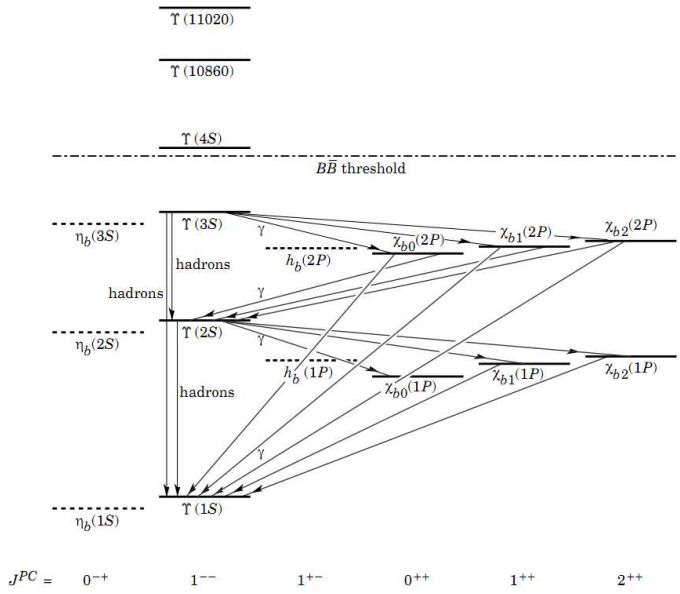

Figure 3.3: Overview of the bottomium resonances. The vertical axis corresponds to the mass of the bottomium states. Picture is from [15].

The largest fraction of the background is prompt $b\bar{b}$ and di-jet events. Finally, the bottom or charm hadrons can be produced in decays of other heavier particles, e.g. $Z \to b\bar{b}$, $W \to c\bar{s}$ or $\Upsilon(4S) \to B\bar{B}$.

3.2.2 Fake electron and/or muon in the final state

As described in chapter 2, the electron is reconstructed by matching the energy cluster in the electromagnetic calorimeter to a track reconstructed in the Inner detector and combined muon by matching tracks reconstructed in the Inner detector and in the Muon spectrometer. However, given the large multiplicity of tracks (consequence of multiple interactions per bunch crossing), it is possible to fake either lepton by tracks and calorimeter deposits that just happen to look like a real electron or muon. The example of such events are processes where there is a real high-p_T muon coming from a semileptonic heavy flavour or W decay and a narrow deposit in the EM calorimeter from a photon that can be matched to a track made by some different particle.

3.3 Data

The analysis uses 7 TeV proton-proton LHC collisions collected by the ATLAS detector between March and July 2011. Only the lumiblocks (see section 2.2.6) passing the criteria on the data quality were considered. The events were selected using combined electron and muon trigger e10_medium_mu6. It requires that both e10_medium and mu6 triggers fire at the same time. For more detailed description of the ATLAS trigger read the section 2.2.6. The total integrated luminosity used in this analysis is 1.01 fb^{-1}.

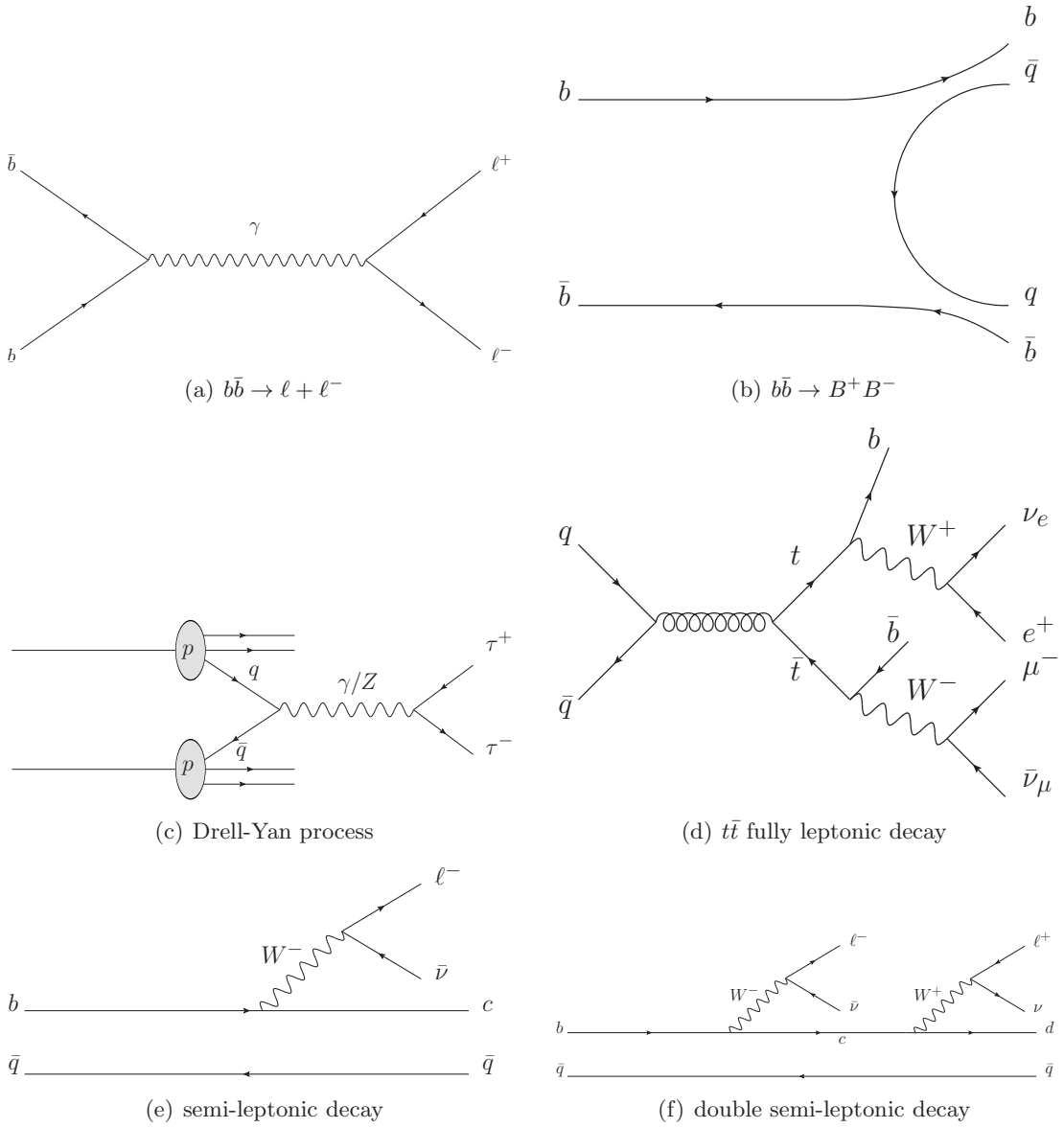

(a) $b\bar{b} \to \ell + \ell^-$

(b) $b\bar{b} \to B^+B^-$

(c) Drell-Yan process

(d) $t\bar{t}$ fully leptonic decay

(e) semi-leptonic decay

(f) double semi-leptonic decay

Figure 3.4: Feynman diagrams of Standard Model processes producing oppositely-charged electron and muon in the final state.

3.4 Monte Carlo

Several Monte Carlo samples were used in this analysis to get an estimate of signal and background yields. The signal was generated with MC@NLO [80] simulating gluon fusion to CP-odd Higgs boson whose mass was set to be 9, 10 and 10.5 GeV. The decay width was set to 0.009 GeV in all of them [50]. The Higgs boson was forced to decay to τ lepton pairs. The subsequent τ lepton flight from primary vertex and its decay were simulated by HERWIG [81] and TAUOLA [82], respectively, while underlying event was simulated by JIMMY [81]. TAUOLA also took care of the correct polarization of the tau leptons. The fragmentation and hadronization was also simulated by HERWIG. The same chain of generators was also used to simulate $t\bar{t}$ background. Only the non fully hadronic decay modes (branching fraction 0.543) were considered.

QCD dijets, Υ, $b\bar{b}$ and low mass (M $<$ 10 GeV) Drell-Yan pairs production was simulated by

Pythia [83] and finally W and Z production associated with jets was generated by ALPGEN [84]. TAUOLA was used to handle tau decays in all samples. All generators were also interfaced to PHOTOS to simulate the effect of final state QED radiation. The Monte Carlo samples were produced with so-called MC10 tune [85, 86] – a special tune using knowledge obtained from 2010 ATLAS data to properly simulate minimum bias and underlying event at 7 TeV pp collisions.

No simulation was made of events when W, Z or heavy Υ (4S, 5S) decays to bottom or charm hadrons. The $Z \to q\bar{q}$ events behave similarly to the regular dijet events, so one may expect that the most important contribution will be coming from $Z \to b\bar{b}$ events because those have the highest probability to produce electron and muon, either in a decayu of two different bottom hadrons or in a decay of a single B hadron. Nevertheless, the branching fraction of $Z \to b\bar{b} \to e\mu$ is roughly the same as the branching fraction $Z \to \tau\tau \to e\mu$ (0.001), so the effect of those two processes should be comparable. And because the amount of $Z \to \tau\tau$ events passing the event selection is close to zero, also the effect of $Z \to q\bar{q}$ backround is negligible. Out of the events of the type $W \to qq'$, the largest contribution will be from $W \to cs \to \mu X$ events, where X is either a real electron or something that can fake an electron. Those events will, however, have both same sign and opposite sign leptons in the final state and will contribute to both isolated and anti-isolated events - therefore they can be included in the "QCD" backround that is estimated from data (see section 3.8.2 that explains how the backround is estimated from data and how the isolation is applied). Finally, to produce (prompt) $\Upsilon(4S)$, the $b\bar{b}$ pair that has enough energy to directly hadronize to $B\bar{B}$ pair, must be created in pp collision. Therefore, there is only a little difference in events where $B\bar{B}$ meson pair is produced directly from $b\bar{b}$ quarks or via extremely short-lived [18] $\Upsilon(4S)$ resonance. Also the production of $\Upsilon(4S)$ is negligible compared to the lower Υ resonances like 1S, 2S or 3S [87] (fig. 3.5).

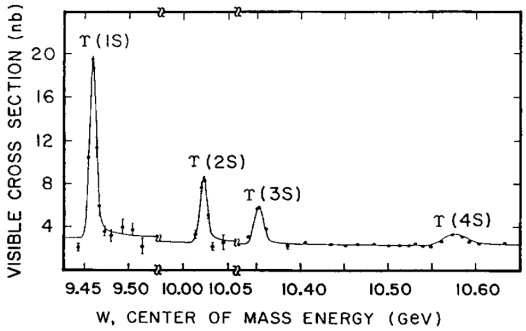

Figure 3.5: The visible cross-section of the various Υ resonances at the CLEO experiment. Figure is from [87].

After the event generation step, all events are passed through the full simulation of the ATLAS detector based on GEANT4 and mixed with the additional pp collisions simulated by Pythia in order to account for the pile-up. Finally, the simulated events are reconstructed using the same procedure as for real data. As described in chapter 4, the number of pile-up events is Poisson-distributed with a mean μ. However, the distribution of average number of collisions μ is different in data and Monte Carlo (fig. 3.6), therefore simulated events are re-weighted to match the distribution in data. Fig. 3.7 show the μ distribution after reweighing.

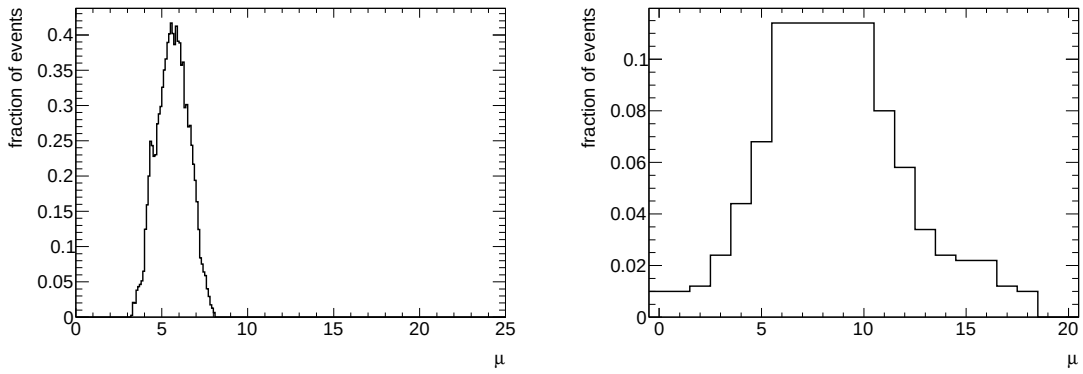

(a) data (b) Monte Carlo

Figure 3.6: Distribution of the average number of interactions per event (μ) in data and simulation.

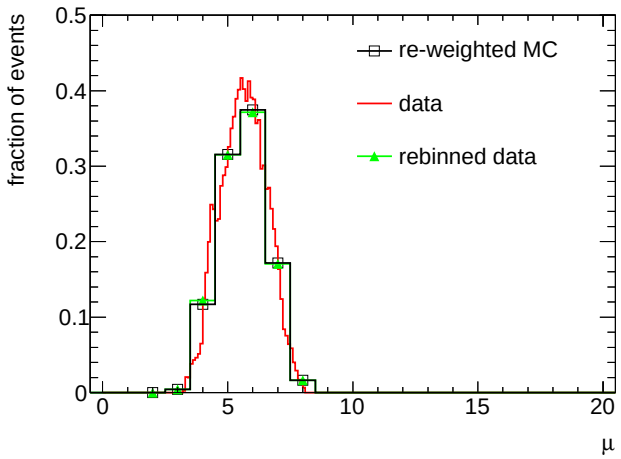

Figure 3.7: Comparison of the distribution of the average number of interactions per event (μ) in data (red) and simulation after reweighing (black). The histogram for data is scaled up by 10 because it has 10 times more bins. For more straightforward comparison, data histogram has been re-binned to the same bin size as histogram for simulated events. This is plotted in green.

3.5 Event preselection

3.5.1 Object pre-selection

Before looking for physics objects, all events are required to have at least one good reconstructed vertex to reject non-collision backgrounds[1]. Afterwards, the electron and muons are selected from the reconstructed objects.

Muon selection

The muons are reconstructed using algorithm described in detail in section 2.3.1. Following requirements must be passed in order for muon to be accepted:

[1]Due to the trigger design, which does read-out only when the proton bunches are supposed to collide, this background is negligibly small.

- Track reconstructed in muon spectrometer and inner detector are matched: muon is *combined*
- Charge is equal to 1 or -1
- $|\eta| < 2.5$ (acceptance of the inner detector)
- $p_T > 6$ GeV (to guarantee good trigger efficiency)
- longitudinal distance between combined track and primary vertex is less than 1 cm to reject cosmic muons
- The track in the inner detector satisfies series of quality cuts on the numbers of hits present in the various tracking subdetectors [88]

Electron selection

Electron candidates are reconstructed using a cluster based algorithm described in the section 2.3.1 and must pass following requirements:

- Electron candidate is passing set of quality cuts including stringent requirement on the matching between extrapolated inner detector track and the calorimeter cluster [88]
- Charge is equal to 1 or -1
- $|\eta| < 1.37$ or $1.52 < |\eta| < 2.47$ (the transition region between barrel and endcap calorimeters is excluded from the analysis)
- $p_T > 10$ GeV (to guarantee good trigger efficiency)
- ΔR to all muons selected in previous step is larger than 0.2

LAr hole treatment

During run 180614 several frontend boards in the Liquid Argon calorimeter stopped working, making part of the calorimeter effectively dead as no data could have been read out from that region. The inactive part of calorimeter is referred to as "LAr hole". The calorimeter problem has influence on the reconstruction of electrons and jets so it is important also this analysis. This failure happened at an early stage of 2011 data-taking, so most of the data used in this analysis are affected by this problem. Only 161.2 pb^{-1} out of 1010 pb^{-1} selected for this analysis do not suffer from the LAr hole. To correct for this problem, the following procedure was applied for selected electrons

- if the event is in data taken after the run 180614 (included) and the electron is in $-0.1 < \eta < 1.55$ and $-0.888 < \phi < -0.492$, the whole event is rejected
- if the event is simulated and the electron is in $-0.1 < \eta < 1.55$ and $-0.888 < \phi < -0.492$, the event is assigned the weight of 161.2/1010

p_T region	10 GeV—15 GeV	15 GeV—30 GeV	30 GeV—100 GeV
$\|\eta\| < 0.8$	0.9707 ± 0.0113	0.9884 ± 0.0010	0.9897 ± 0.0005
$0.8 < \|\eta\| < 1.37$	0.9530 ± 0.0092	0.9852 ± 0.0011	0.9899 ± 0.0005
$1.37 < \|\eta\| < 1.52$	1.0148 ± 0.0464	0.9918 ± 0.0070	0.9746 ± 0.0038
$1.52 < \|\eta\| < 2.01$	0.9802 ± 0.0129	0.9906 ± 0.0017	0.9879 ± 0.0009
$2.01 < \|\eta\| < 2.47$	0.9919 ± 0.0108	0.9799 ± 0.0030	0.9799 ± 0.0018

Table 3.1: The scale factors applied to the simulated events to correct for the e10_medium efficiency.

3.6 Corrections to the reconstructed events

3.6.1 Trigger Efficiency

Electron trigger

Monte Carlo models of signal and background events production might not well reproduce data and also detector simulation might be incomplete, therefore it is necessary to correct the trigger simulation by determining the trigger efficiency from data. The trigger efficiency is essentially the ratio of triggered events containing the relevant physics object (in this case an electron) to all events containing that object.

One method to determine the trigger efficiency from data is called *tag-and-probe*. The key to determine the trigger efficiency with this method is to find a data sample that was not selected by the studied trigger, but by an independent trigger ("tag") and check the efficiency of the trigger there ("probe").

For the determination of e10_medium efficiency, $Z \to ee$ events were used. The events were selected with e20_medium trigger that was unprescaled for the large part of the data taken between April and July 2011. As a next step, the events compatible with the $Z \to ee$ decays were selected: electrons with opposite charge, well separated ($\Delta R > 0.8$) and with an invariant mass from interval (80 GeV, 100 GeV). Both electrons were also required to be isolated in the calorimeter and to pass the same identification criteria as required in section 3.5.1. Finally, one of them had to be matched to the electron trigger object firing e20_medium trigger. The matching was done requiring a distance $\Delta R < 0.15$.

In all those events, there was an isolated electron passing tight identification criteria, whose presence was in no way influenced by the e10_medium trigger, so it was possible to probe in an unbiased way whether events fire also e10_medium trigger and whether the trigger object firing that trigger can be matched to the reconstructed and identified electron. In this way an efficiency map in transverse momentum and pseudorapidity was created.

In the Monte Carlo, the trigger efficiency determination is much simpler, because the events rejected by the trigger are present. The efficiency map can be constructed by selecting events with isolated, tightly identified electrons, and counting how many of them are passing e10_medium trigger.

Finally, by comparison of the efficiency maps for data and Monte Carlo, the (p_T, η)-dependent scale factors were obtained and applied as a correction to all Monte Carlo samples. The average correction factor was 0.98, meaning that Monte Carlo slightly (by 2 %) overestimates the trigger efficiency. The scale factors that were applied to the simulated data are in tab. 3.1.

Muon trigger

The efficiency of the muon trigger has also been determined from data with the tag-and-probe method. However, due to very high prescales applied on EF_mu6 trigger in 2011, the procedure outlined above has been somehow modified. If the lowest unprescaled single muon trigger in the studied period was EF_mu18 is used for selecting the tag events, there is only handful of probes passing EF_mu6 (bulk of the events are rejected by the prescaling), so the efficiency determination is not reliable due to very low amount of passing events.

The other unprescaled muon triggers running in the 2011 included EF_2mu10 and EF_3mu6. The first trigger means that trigger EF_mu10 is fired twice by different objects in one event, the latter accepts events with three objects passing EF_mu6. Therefore the first was used to select events in which *three* reconstructed muons were requested. All of them must have been combined and passing all the muon selection criteria defined in section 3.5.1. On top of this, the muons were required to be isolated in the same way as it is applied in the later event selection stage (see section 3.7.1 for details). All muons were also required to be separated at least by $\Delta R > 0.4$ and two of them had to match the EF_mu10 trigger objects within $\Delta R < 0.15$. This left the third muon for probing by EF_mu6 trigger.

The trigger EF_3mu6 is composed of three independent EF_mu6 triggers. The probability that event will be accepted by EF_3mu6 can be written as

$$p(\text{3mu6}) = p(\text{mu6}) \times p(\text{mu6}) \times p(\text{mu6}) \ .$$

Having three muons in the event, all 3 of them are required to match EF_mu6 objects in case the tag event fires EF_3mu6 trigger. Because two of the muons have been selected by EF_mu10 trigger the probability is modified to

$$p(\text{3mu6}|\text{2mu10}) = p(\text{mu6}|\text{mu10}) \times p(\text{mu6}|\text{mu10}) \times p(\text{mu6})$$

where $p(\text{mu6}|\text{mu10})$ denotes the probability that an object passes EF_mu6 trigger given that has passed the EF_mu10 trigger. This trigger is designed in a way that this probability is 1. So finally we came to the conclusion, that the efficiency of EF_3mu6 trigger obtained with tag-and-probe is equal to the desired efficiency of the EF_mu6 trigger

$$p(\text{3mu6}|\text{2mu10}) = p(\text{mu6}) \ .$$

In the Monte Carlo, the efficiency was obtained in the same way as for electrons. Finally, the trigger scale factors were determined. They were distributed around 0.9 meaning that also muon trigger overestimates the real efficiency in the simulation. Fig. 3.8 shows the efficiency of the EF_mu6 trigger with respect to the combined offline muons in data and in the simulation as a function of its transverse momentum and tab. 3.2 shows the muon trigger scale factors.

Finally, the scale factors obtained for electron and muon trigger are multiplied to get the scale factor for the e10_medium_mu6 trigger.

3.6.2 Reconstruction and Identification Corrections

Electrons

As mentioned in section 2.3.1, the transverse momentum of the electron is determined from the energy it deposits in the calorimeter. ATLAS calorimeters are non-compensating, so the detector response must be calibrated in order to obtain the correct energy measurement. This calibration has been first derived from the test beams before the ATLAS detector was operational. The

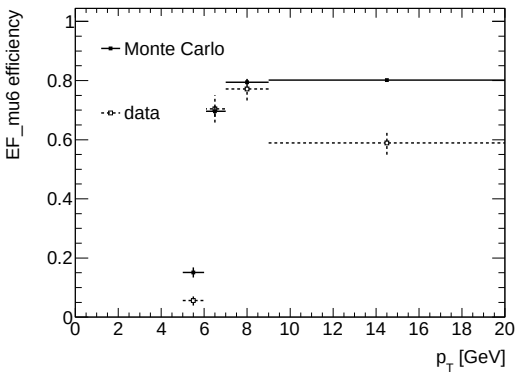

Figure 3.8: The efficiency of the EF_mu6 trigger determined via tag-and-probe method in data and in the Monte Carlo. The efficiency is calculated with respect to the offline combined muons passing the selection listed in section 3.5.1.

p_T region	6 GeV—7 GeV	7 GeV—9 GeV	9 GeV—20 GeV
$\|\eta\| < 0.5$	0.91 ± 0.18	1.04 ± 0.15	0.77 ± 0.08
$0.5 < \|\eta\| < 1.0$	1.01 ± 0.13	0.89 ± 0.11	0.63 ± 0.08
$1.0 < \|\eta\| < 1.5$	0.78 ± 0.12	1.11 ± 0.10	0.84 ± 0.08
$1.5 < \|\eta\| < 2.5$	1.09 ± 0.12	0.98 ± 0.08	0.70 ± 0.05

Table 3.2: The scale factors applied to the simulated events to correct for the mu6 efficiency.

calibration was then also derived from the cosmic events and finally from data (using "standard candles" like $Z \to ee$ events). The electron energy scale corrections to Monte Carlo have been derived from 2010 data and applied at cell level in Monte Carlo production. Residual correction factors were determined in 26 pseudorapidity bins from $Z \to ee$ events in 2011 data and applied to all data in this analysis in order to match Monte Carlo generated with slightly older calibration. The correction depends on η and the typical value of this residual correction is by 0.3% up or down. The typical uncertainty of the correction is 0.0008, i.e. the value of the energy scale correction varies between 0.22% and 0.38%.

Since the Monte Carlo does not reproduce the electron energy resolution in data, a smearing procedure was also applied to the simulated electrons. The details about the energy scale and resolution corrections can be found in [89]. The typical scale of the η dependent resolution correction is 1.5±0.5%.

Similarly as with the trigger, the reconstruction and identification efficiency is not perfectly reproduced in simulation, so the scale factors were calculated from the comparison of efficiency in data and Monte Carlo. The efficiency in data has been determined with the tag-and-probe method using $Z \to ee$ events in the same way as described above, and also $W \to e\nu$ events. In the latter case, the "tag" were the events selected by missing E_T trigger that had an electron candidate. The details about the electron efficiency measurements and correction factors determination can be found in [89]. The reconstruction efficiency scale factor for the electron with $E_T < 15$ GeV (bulk of electrons in this analysis) is 1 (i.e. no correction necessary) with the uncertainty of 0.02. The identification efficiency correction is also η dependent and its value is 0.95±0.08.

Muons

The muon transverse momentum is measured from the curvature of the track. However, the resolution of this momentum measurement might not be correctly simulated. Therefore the resolution was determined using external constraints from the analysis of toroid-off data and the dimuon mass resolution at the Z pole [90]. Consequently, a momentum smearing was applied on the Monte Carlo events. The typical value of the smearing is 0.7–1.5%.

The muon reconstruction and identification efficiency was measured from $Z \to \mu\mu$ events using tag-and-probe in the same way as for electrons. By comparing to the efficiency obtained from Monte Carlo, a set of scale factors was determined that was used to correct the simulated events. More details about the method of determining the muon efficiency can be found in [91]. The residual corrections to the muon efficiency and resolution derived from 2011 data are in fig. 3.9. The typical value of the momentum and pseudorapidity dependent scale factor is 0.99±0.003.

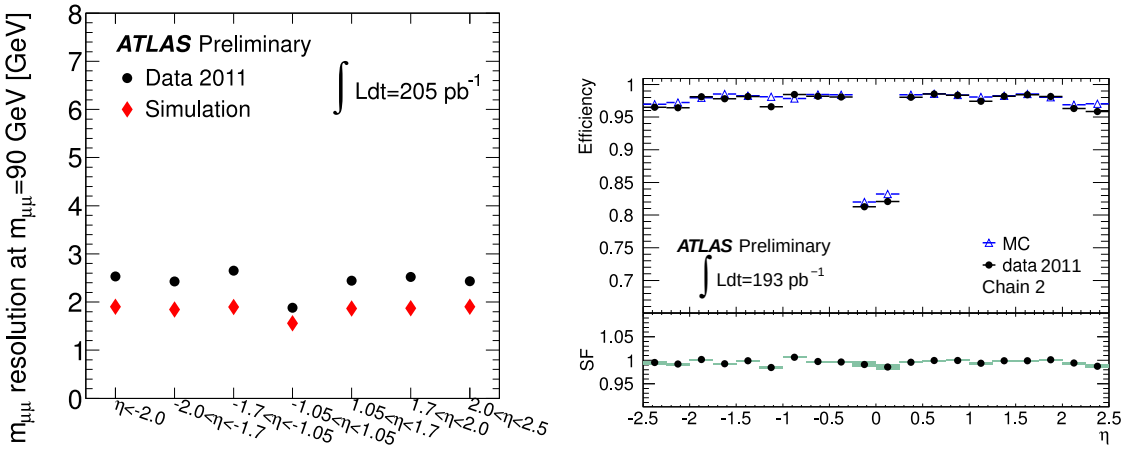

(a) resolution (b) efficiency

Figure 3.9: Experimental and simulated dimuon mass resolution in different η regions (fig. 3.9(a)) and the efficiency of the combined muon reconstruction with respect to the Inner tracking efficiency as a function of η (fig. 3.9(b)). The panel at the bottom of the fig. 3.9(b) shows the ratio of predicted and measured efficiencies.

3.7 Selected Events

The combined trigger and object selection requirements reject large portion of events in data. To find signal in the events passing the pre-selection outlined in section 3.5.1, a simple cut-based analysis was applied. First step was to identify the variables that can distinguish between signal and background:

- Angular distance $\Delta R = \sqrt{(\Delta\phi)^2 + (\Delta\eta)^2}$ between electron and muon
- Dilepton mass, defined as the reconstructed mass of the electron and muon pair: $M_{\text{lep}} = \sqrt{(E_e + E_\mu)^2 - |\vec{p_e} + \vec{p_\mu}|^2}$

The spectrum of invariant mass of eμ pairs after selecting exactly one electron and muon with all the efficiency, energy scale and resolution corrections is presented in fig. 3.10.

There are two distinct features in the spectrum. Those can be better understood from fig. 3.11 showing the difference in a direction of the electron and the muon ΔR and its correlation with the mass of the pair. Fig. 3.11 presents that bulk of the preselected events falls into either of the 2 event categories:

- The events where electron and muon are back-to-back in the transverse plane. Those are events where either a heavy resonance decayed to a lepton pair (a small fraction) or dijet events where one jet has electron among the decay products of its hadrons and the other has muon among its decay product (most of back-to-back events). Because the transverse momenta carried by the electron and the muon inside different jets produced directly in pp collision are random and uncorrelated, the distribution of the mass follow exponential distribution with a turn-on caused by trigger cuts.

- The events where electron and muon are close to each other. Those are events which are coming from a decay of a single, highly boosted particle. The prime example are the B^+ and B^0 hadrons that, when decaying semi-leptonically, can produce both electron and muon in their decay cascades [18]. The momenta of electrons and muons in this case are highly correlated and events of those type form a sharp peak at around 3 GeV.

Fig. 3.12 shows the mass distribution of the eμ pairs originating in decays of tau lepton pairs produced by the signal a_1 particle as well as their distance in terms of ΔR. We can see that trigger selection restricts us to look only on events with highly boosted a_1's where electron and muon are going close to each other (cf. fig. 3.21(d) in section 3.7.2).

It is therefore clear that requiring a small distance between electron and muon will help separate signal from background. Fig. 3.13 shows the efficiency of an upper ΔR cut as a function of this cut for simulated signal events as well as for the data. In this analysis, the cut has been set to $\Delta R < 0.4$ because its efficiency for signal is still high (70 %), and its efficiency for data is quite small (10 %) as most of the events where electron and muons were produced inside different jets are indeed rejected. The size of separation was chosen to be 0.4, because this is also the distance parameter in the ATLAS anti-k$_T$ jet clustering algorithm, so if two jets are produced closer to each other than this cut, they will be most probably reconstructed as a single object anyway.

The data with the superimposed signal shape after the ΔR cut are presented in fig. 3.14 showing us that the separation between the peak in data and expected signal is very small. This means that understanding the nature of this peak is a crucial aspect of this analysis.

Fig. 3.15 shows the data compared to an inclusive Pythia simulation of jet events. One can see that this simulation describes reasonably well the data within the statistical error. Because the generator information is stored in the simulated events, it is possible to check what was the origin of the reconstructed electrons and muons in fig. 3.15. It turns out that more than 99 % of reconstructed electrons and muons can be matched to a true generated leptons that originate in decays of bottom and charm hadrons. This suggests a decay chain like $B \to e + D + X \to e + \mu + Y + X$ that should have branching fraction around 1 %. The flavour composition of the simulated dijet events is in fig. 3.16. It shows that the first narrow peak is formed almost exclusively by the decays of the single B hadrons, while the broad second peak is composed from $b\bar{b}$ and other dijets.

Because the simulated statistics of the inclusive dijet sample was small, compared to the analyzed data, a dedicated simulated sample of $b\bar{b}$ events was studied. Fig. 3.17(a) shows the mass of electron muon pairs for all generated events that have exactly one electron and muon in the final state together with the overlayed distributions of the events where both leptons could have been matched to a single b quark, and the events where both leptons were matched to a

different b-quarks. The plot clearly emulates the double-peak structure seen in data and shows that contents of the first peak are events with single boosted b-hadron decaying to collimated pair of leptons, while the other peak is populated by events where leptons are coming from decays of different particles. The similarity to data is even more obvious when the mass is plotted from reconstructed electrons and muons passing the trigger (fig. 3.17(b)). The plot shows that bulk of the first plot can be described as single b-hadrons decaying in a double-leptonic way. In the second peak we can see a deficiency in the Monte Carlo shape. This means that there are more flavours than just $b\bar{b}$ populating the second peak as it has already been shown in fig. 3.16.

Figs. 3.16 and 3.17 show that the structure of the data is qualitatively understood. However, the normalization is not: at all those figures the simulated events were normalized according to the number of entries in data. Moreover, the amount of analyzed data (5 million events after the trigger) makes it technically impossible to simulate corresponding dijet and $b\bar{b}$ Monte Carlo sample. Therefore the effect of QCD background is estimated directly from the data as it shown in section 3.8.2.

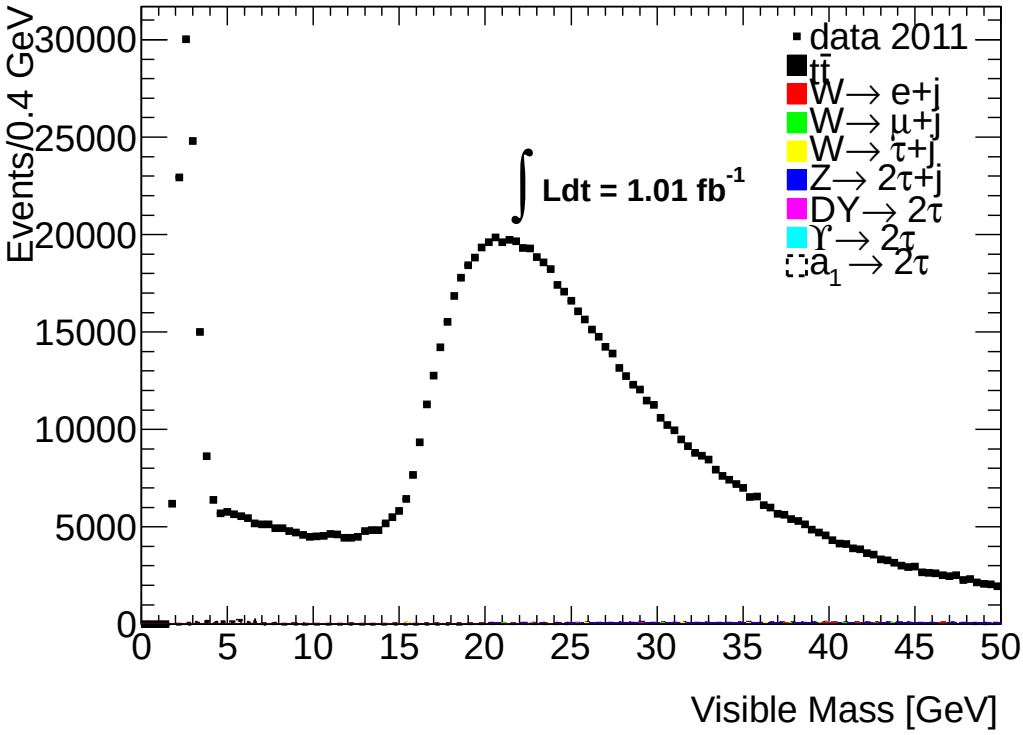

(a) linear scale

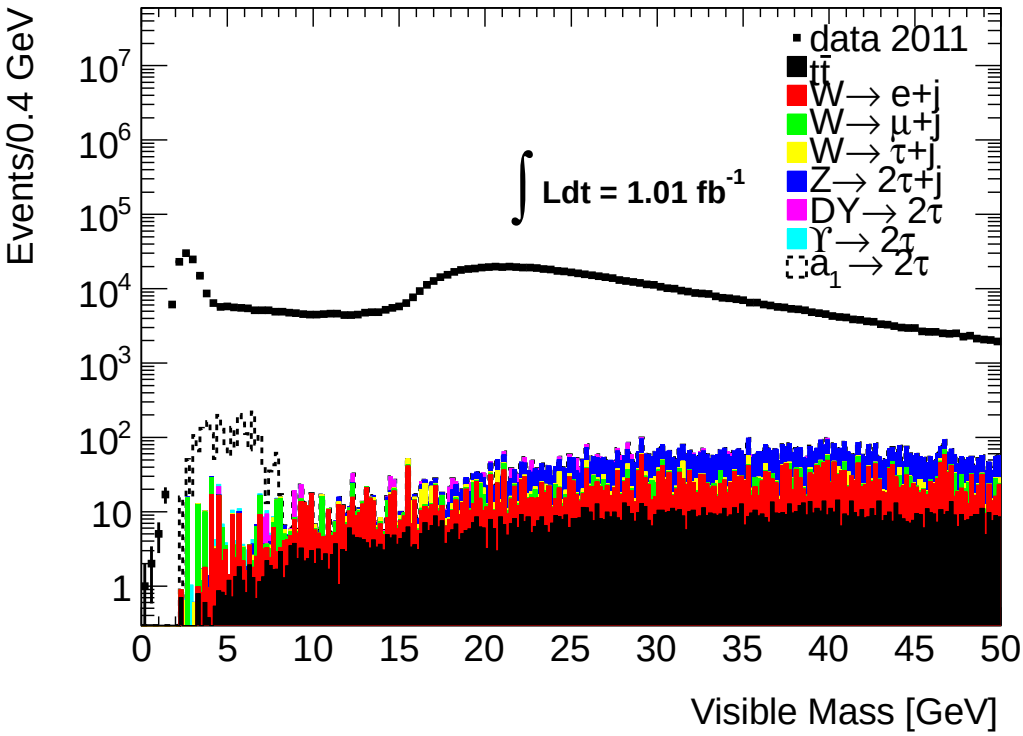

(b) logarithmic scale

Figure 3.10: Invariant mass of eμ pairs after the object pre-selection (see text for details). Fig. 3.10(a) shows the full spectrum, while the fig. 3.10(b) presents the same picture in logarithmic scale to better show the expected contribution from electroweak processes and $t\bar{t}$ production. The signal events are stacked on top of the simulated backgrounds and scaled up to cross-section of 70 nb (i.e. 10 times more than discussed in the text later).

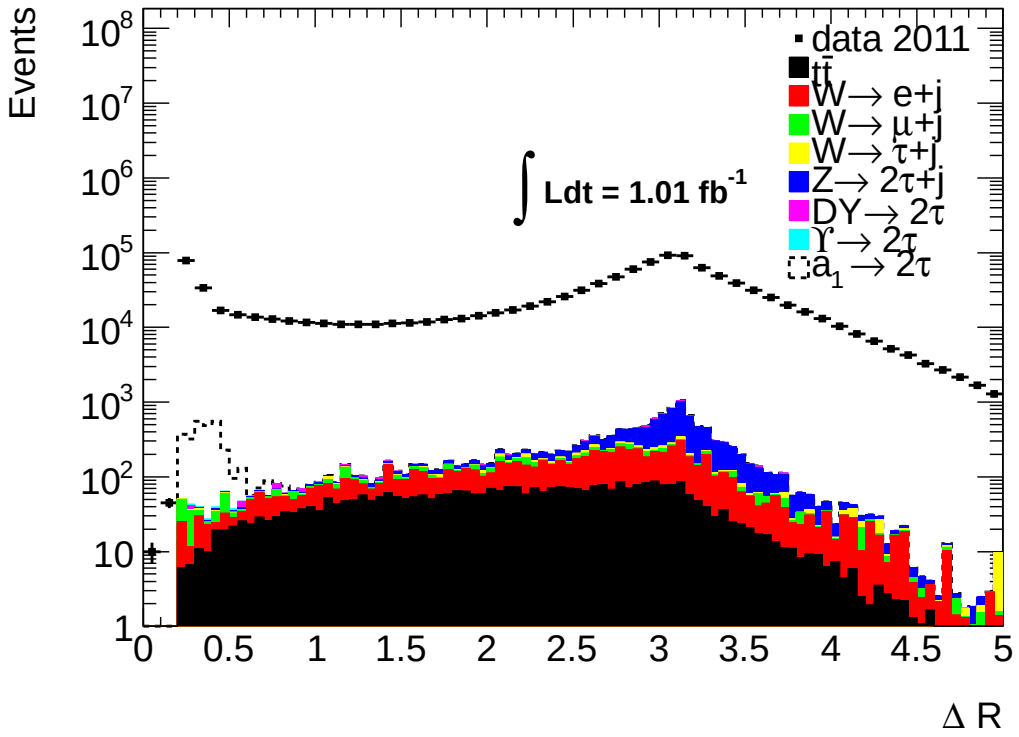

(a) distance of e and μ

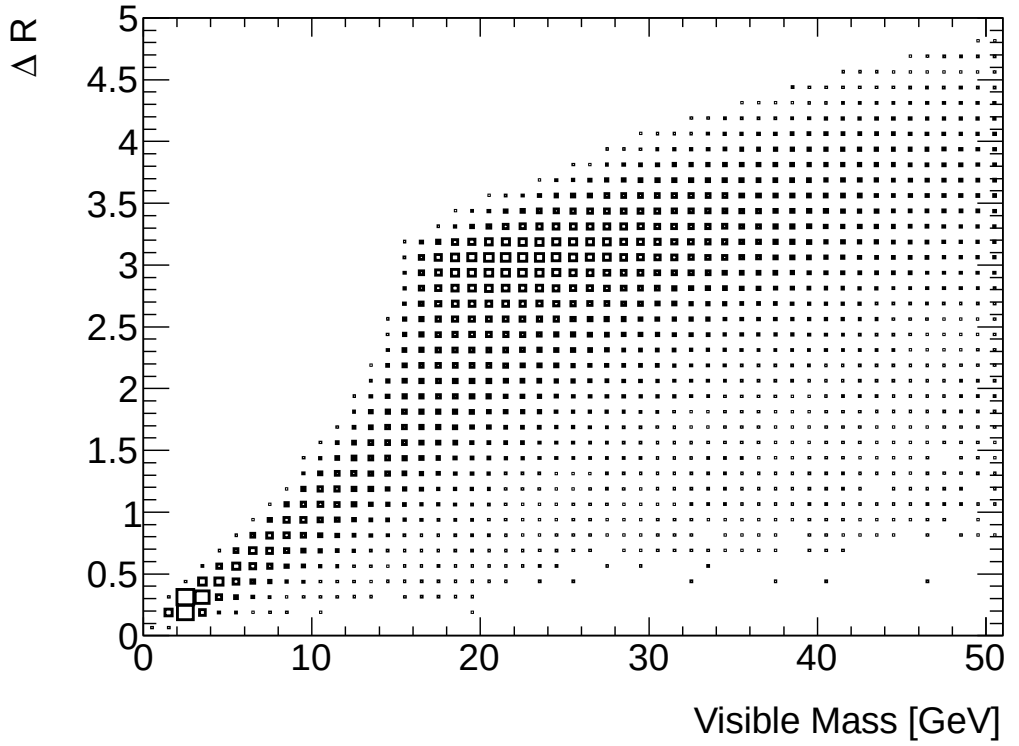

(b) correlation between ΔR and mass

Figure 3.11: Distance ΔR of electrons and muons in data and Monte Carlo (fig. 3.11(a) and its correlation with the mass of electron-muon pair in data (fig. 3.11(b)). The signal events are stacked on top of the simulated backgrounds at fig. 3.11(a) and scaled up to cross-section of 70 nb (i.e. 10 times more than discussed in the text later).

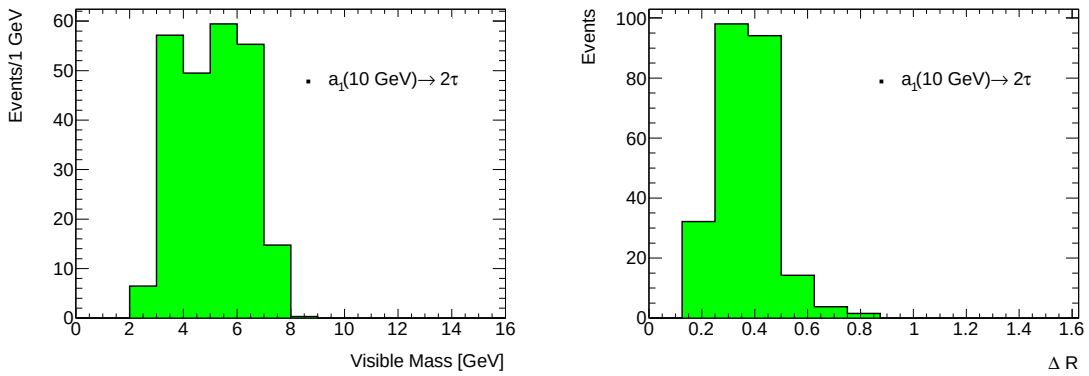

(a) The mass of e and μ from a_1 decays

(b) ΔR between e and μ from a_1 decays

Figure 3.12: Mass of electron-muon pair from signal particle decays (fig. 3.12(a)) and the angular distance of electron and muon in those events (fig. 3.12(b)).

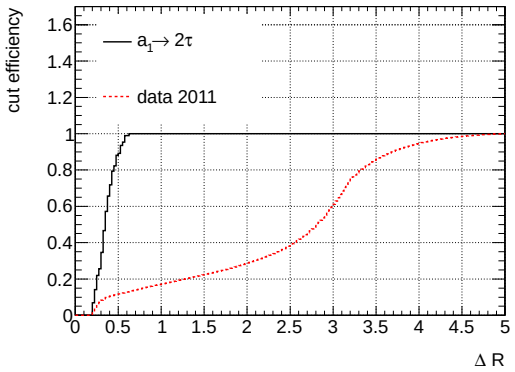

Figure 3.13: The efficiency of upper ΔR cut as a function of the cut value for the simulated signal events and for data.

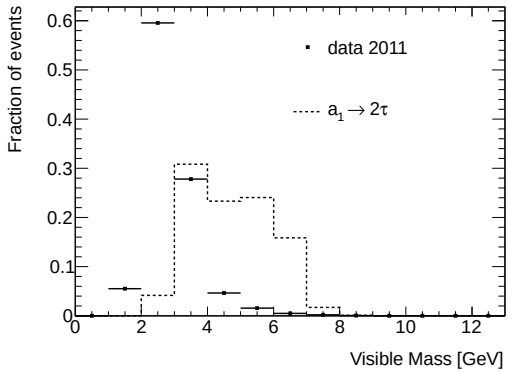

Figure 3.14: The comparison of the distribution of visible mass in the data after the cut of $\Delta R < 0.4$ and in the signal Monte Carlo. The distributions have been normalized to 1.

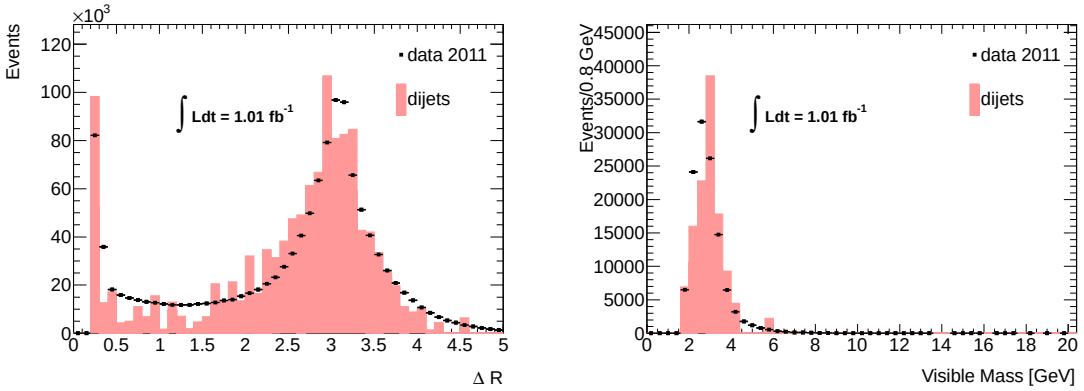

(a) ΔR between e and μ (b) Mass distribution after ΔR cut

Figure 3.15: The comparison of the data and inclusive dijet simulation. The fig. 3.15(a) presents the angular distance between electron and muon while fig. 3.15(b) shows the mass distribution after the ΔR cut. The content of the histogram with dijet simulation has been normalized to the data.

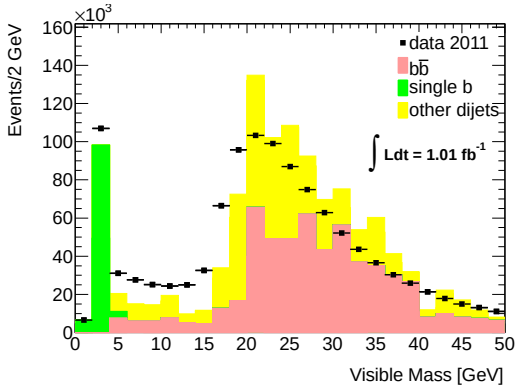

Figure 3.16: The composition of the dijet events compared to the data. The first peak is completely dominated by the decays of a single B hadrons, while the second peak is populated by both $b\bar{b}$ and other dijets.

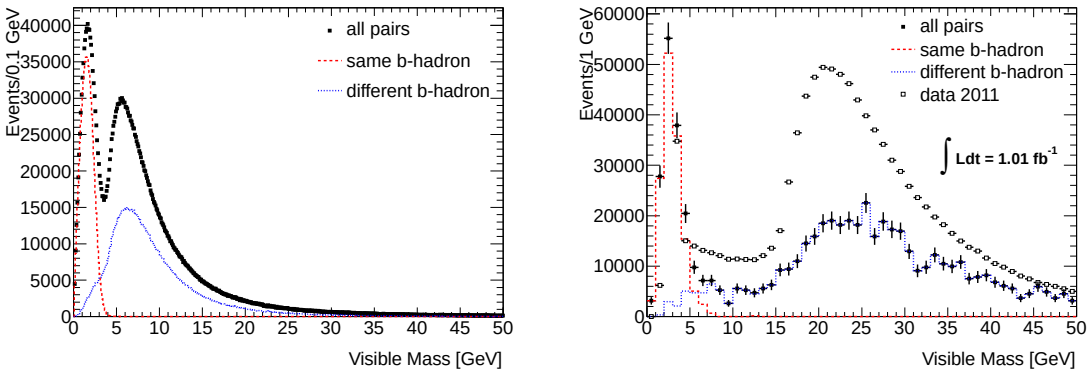

(a) Generated mass of e and μ pair (b) Reconstructed mass of eμ pairs after the trigger

Figure 3.17: Mass of electron-muon pair in the simulated production of $b\bar{b}$ quark pairs. The fig. 3.17(a) shows the mass on the generator level, while the fig. 3.17(b) shows the mass obtained from the reconstructed events passing the trigger. The Monte Carlo histograms in fig. 3.17(b) have been normalized to the first peak.

3.7.1 Effect of isolation

The decay of a_1 is characterized by the presence of an electron, a muon and the missing energy from the neutrinos, while the decays of B hadrons contain additional particles on top of the electron and muon. Therefore, requiring that the lepton is isolated should help to further suppress the background. There are two types of isolation cuts that can be applied based on:

- the sum of transverse momenta of the tracks in the pseudo-cone with radius R=0.2[2] around the lepton track (excluding the lepton track itself) called $p_T^{(iso20)}$
- the sum of transverse energy deposited in a pseudo cone with radius R=0.2 around the electron cluster/extrapolated muon track (excluding the energy of the lepton cluster itself) called $E_T^{(iso20)}$

The isolation cut is applied as a relative constraint and the actual variables on which the cut is applied are $\frac{p_T^{(iso20)}}{p_T}$ and $\frac{E_T^{(iso20)}}{E_T}$. The values of cuts have been chosen such that most of the a_1 decays pass (due to the presence of additional collisions in the event they are not perfectly isolated). The distribution of isolation in a_1 events compared to isolation in data and in $b\bar{b}$ simulation is shown in fig. 3.18.

The distributions of isolation variables show that only tracking isolation can offer distinction between signal and data: the calorimeter isolation of signal events is very similar to those expected for background and observed in data. The reason for this is the low momentum of electrons and muons (calorimeter resolution increases with momentum) and pile-up. Therefore only tracking isolation is applied. The cut values are

- For electrons: $\frac{p_T^{(iso20)}}{p_T} < 0.02$
- For muons: $\frac{p_T^{(iso20)}}{p_T} < 0.02$

3.7.2 Lepton mass window cut

The previous sections shows that the spectrum of selected event is dominated by decays of boosted B hadrons that share many characteristics with the signal. On the other hand, the dilepton mass is always bound from above by the mass of the parent particle, so almost all eμ pairs coming from decay of a single boosted b-hadrons are reconstructed with mass smaller than 6 GeV, while the eμ pairs from a_1 decays tend to have greater mass (fig. 3.14). The setting of the mass window has very direct influence on the significance of the result, so the number of expected signal and background events have been calculated for different values of the mass cut. The background has been calculated from data using the method described in section 3.8.2. The result of this is shown in fig. 3.19. The lower mass cut value of 5.5 GeV was chosen because this value provides high significance that is also quite stable around this cut value. In addition, an upper cut of $M(e\mu)$ <11 GeV is used to exclude some of the remaining $t\bar{t}$ events from the background estimation while it leaves the signal distribution untouched.

The full analysis cut-flow

To summarize the previous sections, here is the full list of cuts used for event selection:

[2]Region in a detector whose coordinates ϕ' and η' fulfill the relation $\Delta R' = \sqrt{(\phi' - \phi_0)^2 + (\eta' - \eta_0)^2} < R$ where ϕ_0 and η_0 are directional coordinates of the track for which the isolation is being calculated.

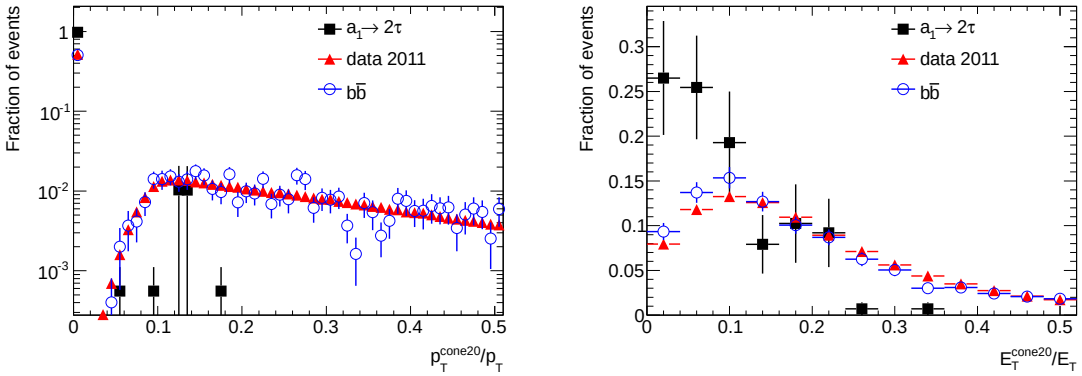

(a) Electron tracking isolation

(b) Electron calorimeter isolation

(c) Muon tracking isolation

(d) Muon calorimeter isolation

Figure 3.18: The isolation variables for electron and muon. The figs. 3.18(a) and 3.18(b) show the relative isolation of electron in tracker and calorimeter, respectively. The figs. 3.18(c) and 3.18(d) show the same distributions for the muon. On each plot there are three overlayed distributions: signal $a_1 \to \tau\tau$ events together with the data and simulated $b\bar{b}$ events. All distributions have been normalized to unity prior to the plotting.

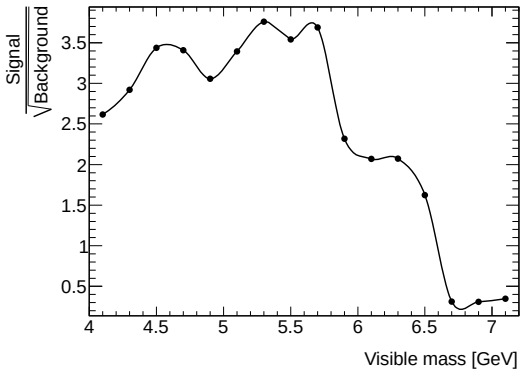

Figure 3.19: The significance of signal calculated as ratio of number signal events to the square root of the number of expected background events. Significance is shown as a function of lepton mass cut. The number of signal events is based on Monte Carlo simulations, while the number of background events have been calculated from data for every value of lepton mass cut.

- e10_medium_mu6 trigger
- exactly one electron and muon passing the criteria outlined in section 3.5.1
- electron and muon $\Delta R < 0.4$
- electron $\frac{p_T^{(iso20)}}{p_T} < 0.02$
- muon $\frac{p_T^{(iso20)}}{p_T} < 0.02$
- lepton mass 5.5 GeV $< M_{\text{lep}} <$ 11 GeV
- opposite charge

The cut-flow for simulated backgrounds from electroweak processes is in tab. 3.3. Note that those samples that did not pass ΔR and isolation cuts are not listed. The sum of the backgrounds in tab. 3.3 is compared to the cut-flow observed in data and the one expected for signal events in tab. 3.4. The pictorial representation of the cut flow, showing how the various cuts help to suppress background in the signal region and which fraction of signal is selected, is shown in fig. 3.20.

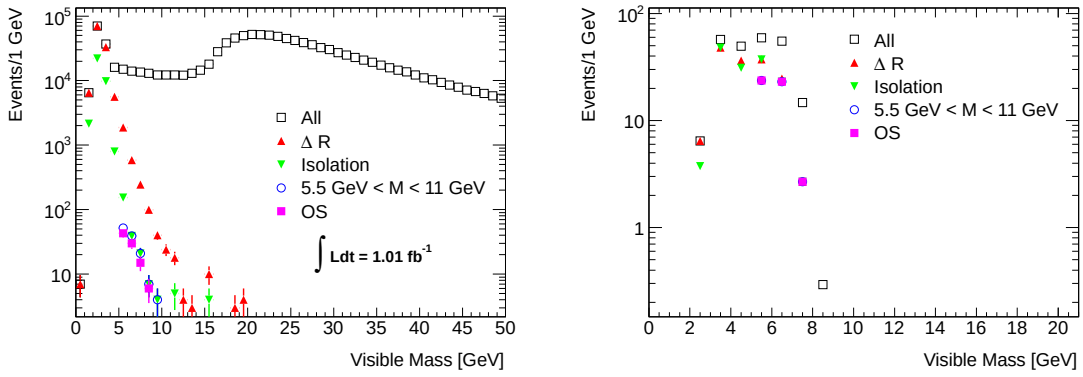

(a) data

(b) $a_1 \to \tau\tau$ Monte Carlo

Figure 3.20: Fig. 3.20(a) shows the distribution of dilepton mass in the data and how it changes after the successive application of the cuts from section 3.7.2. The legend indicates after which cut the distribution is being plotted. Note the logarithmic scale. Fig. 3.20(b) shows the same information for the simulated signal events.

Finally, the relative cut efficiency for data, signal and selected simulated backgrounds are compared in tab. 3.5. Note that the efficiency of the trigger cut is not included there, because the numerator is different in data and simulated events. In data, the numerator are all events that passed at least one electron or photon trigger, while in simulation the numerator are all generated events. Therefore the trigger efficiency in data appears somehow higher than in the simulation.

The number of simulated events has been scaled to the same integrated luminosity as data according to the sample cross-sections. Those are shown together with the luminosity corresponding to samples before rescaling in Tab. 3.6. Signal cross-section is a free parameter of this analysis. For simplicity, it was set to 7 nb so the integrated luminosity in the simulated signal

	$t\bar{t}$	$W \to \mu\nu$	$Z \to \tau\tau$	Drell-Yan (M<10 GeV)	$\Upsilon(1S) \to \tau\tau$	$\Upsilon(2S) \to \tau\tau$	$\Upsilon(3S) \to \tau\tau$
Total	90329 ± 0	10592444 ± 0	1084134 ± 0	3489416 ± 0	58070 ± 0	18339 ± 0	11098 ± 0
Pileup weight.	90116 ± 4	10564364 ± 260	1081276 ± 19	3480048 ± 128	57915 ± 4	18290 ± 1	11067 ± 1
Trigger	7952 ± 24	22542 ± 233	10950 ± 37	536 ± 31	26.9 ± 1.8	3.0 ± 0.3	1.3 ± 0.2
Good Vx	7952 ± 24	22530 ± 233	10949 ± 37	536 ± 31	26.9 ± 1.8	3.0 ± 0.3	1.3 ± 0.2
1 e + 1 μ	4142 ± 18	828 ± 45	5526 ± 26	272 ± 22	12.0 ± 1.2	1.4 ± 0.2	0.7 ± 0.1
$\Delta R < 0.4$	1.7 ± 26.8	55.8 ± 11.6	2.4 ± 0.6	3.5 ± 2.5	4.1 ± 0.7	0.6 ± 0.1	0.0 ± 0.0
μ isol.	18.9 ± 1.2	55.4 ± 11.6	1.5 ± 0.4	3.5 ± 2.5	4.1 ± 0.7	0.6 ± 0.1	0.0 ± 0.0
e isol.	17.3 ± 1.2	45.8 ± 10.5	1.5 ± 0.4	3.5 ± 2.5	3.8 ± 0.7	0.4 ± 0.1	0.0 ± 0.0
Mass window	8.3 ± 0.8	6.9 ± 4.1	0.0 ± 0.0	0.0 ± 0.0	0.5 ± 0.2	0.2 ± 0.1	0.0 ± 0.0
Opp. charge	8.3 ± 0.8	6.7 ± 4.0	0.0 ± 0.0	0.0 ± 0.0	0.5 ± 0.2	0.2 ± 0.1	0.0 ± 0.0

Table 3.3: The number of simulated events for various processes passing the analysis cuts. The number of events in Monte Carlo is scaled to the same integrated luminosity as in data. The errors are statistical.

	data	a_1 (9 GeV)	a_1 (10 GeV)	a_1 (10.5 GeV)	Sum of tab. 3.3
Total	135885682	33357 ± 0	42894 ± 0	47629 ± 0	10770279 ± 0
GRL	125230519	33358 ± 0	42894 ± 0	47630 ± 0	10770279 ± 0
Pileup weight.	125230519	33358 ± 1	42895 ± 1	47631 ± 2	10741753 ± 291
Trigger	4972004	515.1 ± 20.8	576.2 ± 25.7	675.9 ± 29.5	30525 ± 239
Good Vx	4972002	515.1 ± 20.8	576.2 ± 25.7	675.9 ± 29.5	30513 ± 239
1 e + 1 μ	1217204	217.8 ± 13.6	240.1 ± 16.6	296.6 ± 19.6	4984 ± 59
$\Delta R < 0.4$	118114	157.3 ± 11.6	153.1 ± 13.3	166.7 ± 14.7	98.7 ± 12.0
μ isol.	52852	151.3 ± 11.3	147.1 ± 13.0	165.6 ± 14.7	78.9 ± 11.9
e isol.	34985	143.7 ± 11.0	142.1 ± 12.8	161.1 ± 14.5	67.4 ± 10.9
Mass window	125	21.9 ± 4.3	51.0 ± 7.7	63.8 ± 9.1	15.8 ± 4.2
Opp. charge	98	21.9 ± 4.3	51.0 ± 7.7	63.8 ± 9.1	15.6 ± 4.1

Table 3.4: The number of events for data and various signal masses passing the analysis cuts. The last column shows the sum of events in tab. 3.3. The number of events in Monte Carlo is scaled to the same integrated luminosity as in data. The errors are statistical.

	data	$b\bar{b}$	di-jet	$t\bar{t}$	$\Upsilon(1S)$	a_1 (10 GeV)
Trigger	100%	100%	100%	100%	100%	100%
1 e + 1 μ	25%	34%	39%	54%	50%	52%
$\Delta R < 0.4$	10%	11%	9%	1%	34%	64%
μ isol.	45%	48%	54%	49%	100%	96%
e isol.	66%	44%	59%	92%	94%	97%
Mass window	0.4%	0.0%	0.0%	44%	12%	36%
Opp. charge	78%	N/A	N/A	100%	100%	100%

Table 3.5: The relative efficiencies of various cuts on data and selected simulated backgrounds. Note that no events were left in $b\bar{b}$ and di-jet sample after the mass window cut.

sample corresponded to the integrated luminosity in the data. The total number of expected signal events with that normalization is

$$N_{a_1} = 51.0 \pm 7.7 \text{ (stat.)} \tag{3.1}$$

Note the difference in the number of triggered events between Upsilon and signal although the mass of mother particle and production cross-section times branching ratio to tau pair are very similar. The reason for this is the difference in momentum of the a_1 and Υ resonances coming from the different production mechanism: a_1 is produced in a gluon fusion, while Υ is produced from quark-antiquark pair that fuses to a bound state. The distribution of the kinematic variables of Υ and a_1 and their decay products is in fig. 3.21. Similar distributions of a_1 and Υ expected transverse momenta have been confirmed also in the $a_1 \to \mu\mu$ search. [77].

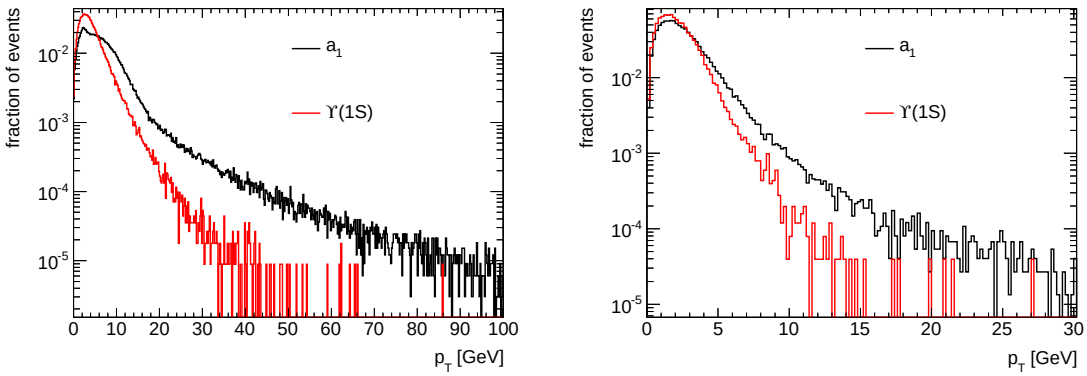

(a) transverse momentum of a mother particle

(b) leading e/μ p_T

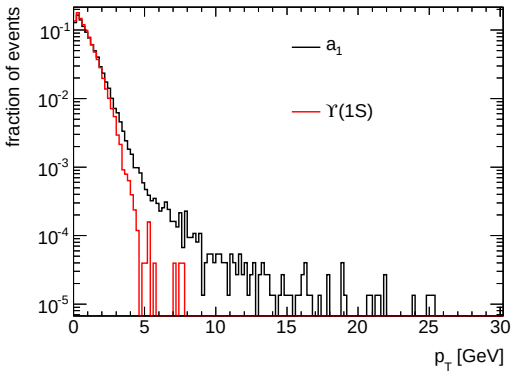

(c) sub-leading e/μ p_T

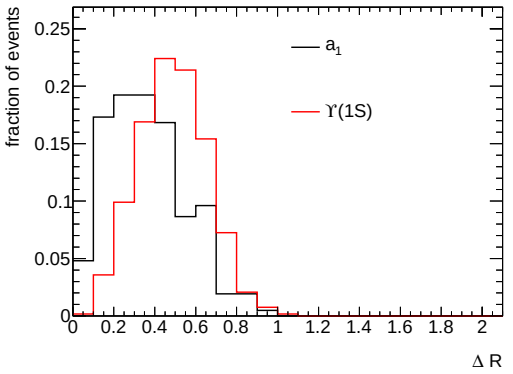

(d) distance of the lepton pair after p_T cut

Figure 3.21: The distribution of of p_T of the a_1 and $\Upsilon(1S)$ particle (fig. 3.21(a)), the transverse momentum of leading and sub-leading lepton from the τ decay (figs. 3.21(b) and 3.21(c)). Finally, the distance $\Delta R = \sqrt{(\Delta\phi)^2 + (\Delta\eta)^2}$ between the electron and muon after the transverse momentum cuts at 10 GeV and 6 GeV, respectively is shown in fig. 3.21(d).

3.8 Analysis details

3.8.1 Determination of the Υ cross-section and integrated luminosity

The production mechanism of Υ resonances is still not fully understood so the Monte Carlo modeling of Υ production is only approximate [78]. Therefore, measured $\Upsilon \to \mu\mu$ cross section [92]

sample	cross-section [pb]	total integrated luminosity in sample [pb^{-1}]	Generator
$a \to \tau\tau$, m$_a$=10 GeV	7000	1010	MC@NLO
$t\bar{t}$	89.4	12962	MC@NLO
W$\to e\nu$+jets	10486	416	ALPGEN
W$\to \mu\nu$+jets	10483	417	ALPGEN
W$\to \tau\nu$+jets	10481	411	ALPGEN
Z$\to ee$+jets	1072	7915	ALPGEN
Z$\to \mu\mu$+jets	1072	7919	ALPGEN
Z$\to \tau\tau$+jets	1073	7921	ALPGEN
Drell-Yan $\to \tau\tau$	345	579	Pythia
Υ(1S)$\to \tau\tau$	7373	8699	Pythia
Υ(2S)$\to \tau\tau$	1912	27544	Pythia
Υ(3S)$\to \tau\tau$	1034	44150	Pythia

Table 3.6: The cross-sections assumed for Monte Carlo samples as well as total integrated luminosity contained in the samples. The cross-section of Υ decay was calculated from measured $\Upsilon \to \mu^+\mu^-$ cross-section [92] (see section 3.8.1 for details). All other cross-sections are calculated to NNLO.

has been used for correction. CMS [92] provides differential cross section as a function of Υ transverse momentum for rapidities smaller than 2. Unfortunately, due to small integrated luminosity used in that measurement, the results are available only up to 30 GeV. In this analysis, however, the trigger selection imposes quite hard cuts compared to the Υ mass, meaning that only events with Υ's produced with large transverse momentum can pass the trigger cuts. Therefore, the measured $\Upsilon \to \mu\mu$ cross section has been rescaled by BR($\Upsilon \to \tau\tau$)/BR($\Upsilon \to \mu\mu$)=1.008, fitted with exponential and extrapolated to the larger momentum values (fig. 3.22).

Because only a fraction of Υ events is decaying within the detector active volume and even smaller fraction of those is able to pass the trigger, some kinematic cuts were applied at the generator level to save CPU time by not simulating events that have no chance of passing the trigger.

In order to evaluate the acceptance of the generator-level cuts, a samples of 1 million events per Υ resonance were generated without applying any of the cuts. Those unbiased samples were used to calculate the efficiency of those generator fiducial cuts in momentum bins inspired by the cross-section measurement in [92]. The acceptances are shown in fig. 3.23. Those acceptances were applied to samples with fully simulated Υ decays to obtain the original distribution of events before the generator cuts were applied. The next step is to calculate how many of those events have rapidity less than 2 and transverse momentum less than 30 GeV. This number was then divided by the measured cross-section of $\Upsilon \to \mu\mu$ in this kinematic range multiplied by BR($\Upsilon \to \tau\tau$)/BR($\Upsilon \to \mu\mu$)=1.008 to get the total integrated luminosity contained in the given sample. Those numbers are summarized in tab. 3.7. Finally, the events were reweighed depending on their p_T to make momentum distribution in Monte Carlo match the measured distribution in the data (fig. 3.24).

To conclude, the generated Υ distributions (corrected with the data from $\Upsilon \to \mu\mu$ events) showed that Υ decays have much smaller acceptance due to the trigger and therefore they do not form major background for the a_1 search with the integrated luminosity used in this analysis. This conclusion is far from obvious. Given the very similar masses, decay modes and integral cross-sections, it is natural to expect that the contribution from the Υ events would form a

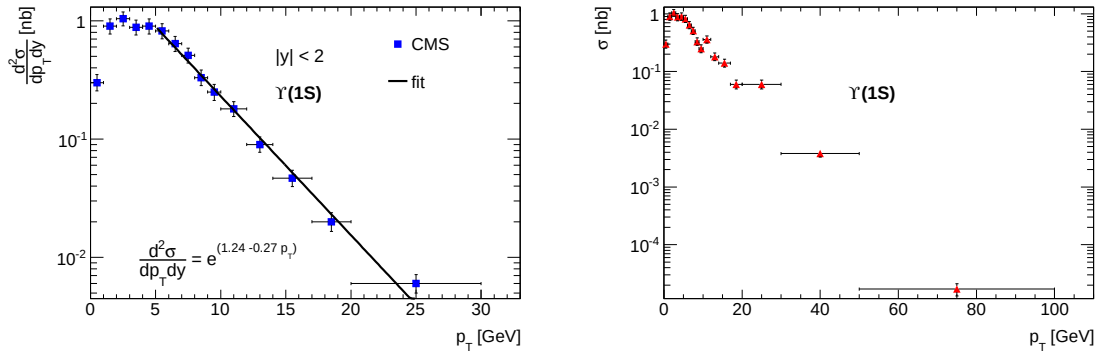

(a) $\Upsilon(1S)$

(b) $\Upsilon(1S)$

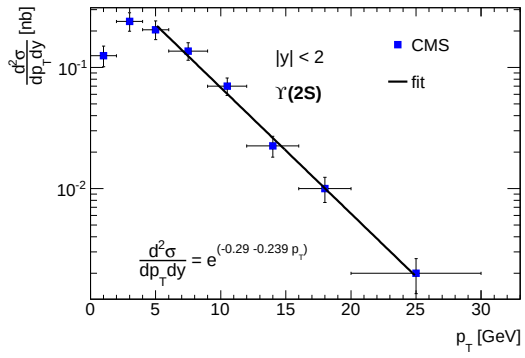

(c) $\Upsilon(2S)$

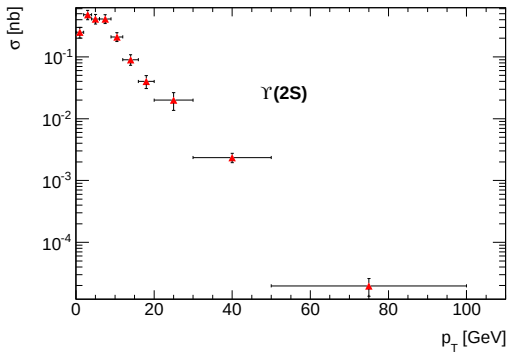

(d) $\Upsilon(2S)$

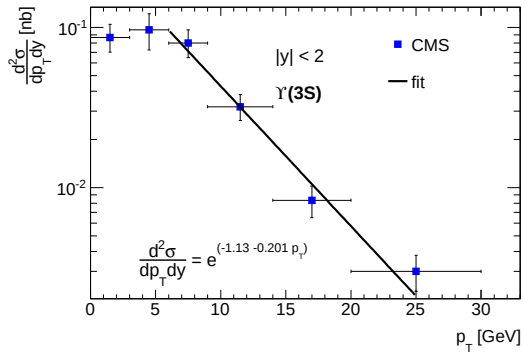

(e) $\Upsilon(3S)$

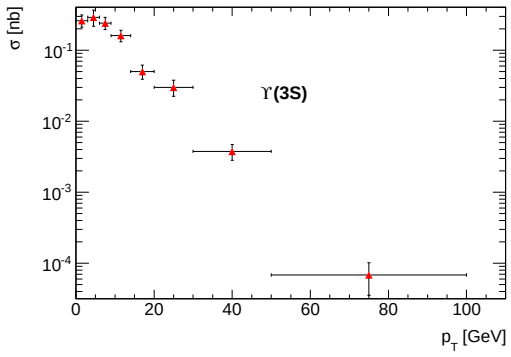

(f) $\Upsilon(3S)$

Figure 3.22: Differential cross-section of 3 Υ resonances decaying to τ lepton pair (figs. 3.22(a), 3.22(c) and 3.22(e)). The squares are measured values with experimental errors as taken from [92]. The fit is shown as a black line together with its parameters. Figures 3.22(b), 3.22(d) and 3.22(f) show the integral cross-section of 3 Υ resonances decaying to τ lepton pair for different momentum intervals. The values below 30 GeV correspond to measured values in [92], while the values above it are extrapolation using fits shown on figs. 3.22(a), 3.22(c) and 3.22(e). The errors below 30 GeV are experimental, the ones above 30 GeV come from the fit uncertainty.

major backround for the a_1 search. However, the careful data driven approach in this section showed that this is not the case because of the different a_1 and Υ production mechanisms and thus different p_T distributions.

	$\Upsilon(1S) \to \tau\tau$	$\Upsilon(2S) \to \tau\tau$	$\Upsilon(3S) \to \tau\tau$
events in full simulation	499945	499938	499945
generated events in $p_T < 30$ GeV and $\|y\| < 2$	59.64×10^6	52.67×10^6	45.64×10^6
$\sigma_{\Upsilon\to\tau\tau}(p_T < 30$ GeV; $\|y\| < 2)$ [nb]	7.37	1.9	1.02
total luminosity [pb^{-1}]	8699	27544	44150

Table 3.7: The Upsilon sample luminosity summary. Starting from the number of events in the fully simulated sample on the first line, applying acceptance corrections from fig. 3.23 to get the number of generated events before the generator cuts and finally calculating the integrated luminosity from the measured cross-section.

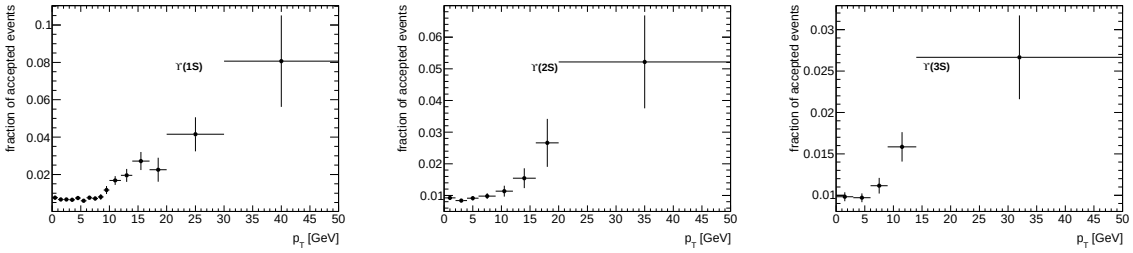

(a) $\Upsilon(1S)$ (b) $\Upsilon(2S)$ (c) $\Upsilon(3S)$

Figure 3.23: The acceptance of the generator filter cuts for three Υ resonances.

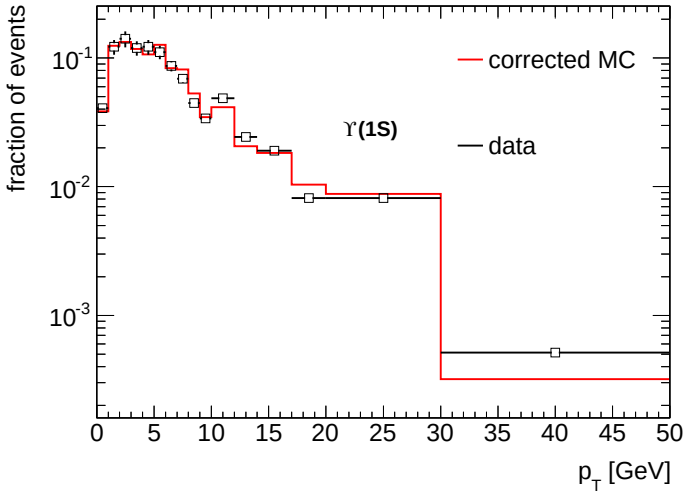

Figure 3.24: The simulated transverse momentum of $\Upsilon(1S)$ after all corrections applied in section 3.8.1 compared to the measured $\Upsilon(1S)$ p_T distribution from [92].

3.8.2 Background estimation

Previous section showed that most of the background for $a_1 \to \tau\tau \to e\mu$ is coming from the decays of boosted b-hadrons and other QCD processes producing real electrons and muons. Such a background is difficult to simulate because QCD at this energy range is not described by the perturbative QCD theory and also, due to its cross section it is technically difficult to simulate enough events to describe data. Therefore, the background needs to be estimated from data using the methods described in the next paragraphs.

ABCD method

The decays of boosted B hadrons share many characteristics with the signal events, making the data-driven estimation very challenging. A method called "ABCD" has been used. It assumes the existence of (at least) 2 uncorrelated variables that distinguish signal from background. The variables that provide some distinction between signal and background have been presented in section 3.7. The goal is to use those variables to define control regions (by removing or reverting cuts on those variables) which are signal-free yet as much similar to the background in the signal region as possible. The angular distance ΔR is used to reject di-jet background so it is not very useful for background estimation as the events rejected by this cut are quite different from those that are accepted by this cut. Similarly the cut on the lepton mass is also directly affecting the kinematics, so it is not useful to define a control regions with signal-like, yet signal-free events.

In order to select signal free control regions, a so-called anti-isolation region is also defined. This means that cuts on isolation are reversed and somehow increased to make sure that signal events are rejected. The cut values for anti-isolation are

- For electrons: $\frac{p_T^{(iso20)}}{p_T} > 0.05$
- For muons: $\frac{p_T^{(iso20)}}{p_T} > 0.05$

No signal event is passing this selection. The distributions of the mass of eμ pairs after the isolation on both leptons and before the mass window cut is shown in fig. 3.26(a). Many data events have been rejected but the peak from single B hadrons decays is still present. Fig. 3.26(a) shows also the distributions of the events with the same sign and opposite sign leptons. The peak is composed mostly from opposite sign events, while the same sign event contribute only a small fraction. Fig. 3.26(b) shows the distributions of eμ pair mass obtained from the data for the events passing reversed isolation cuts (so-called anti-isolated events) and again, no mass cut was applied. This is compared to the shape of the mass constructed from pair of isolated leptons. The distribution of single b-hadron lepton mass is different for isolated and anti-isolated events because the electron and muon are not the sole decay products of B hadron and isolation requirement influences how the B hadron momentum is divided among its decay product and thus the mass reconstructed from electrons and muons. The different shape of isolated and anti-isolated data is an additional motivation for the dilepton mass cut - to reject the bulk of single B hadron events for that cannot be estimated from data with the ABCD method.

Moreover, due to requirement of electrons and muons being close to each other, the isolation requirements on different leptons are also not independent: if electron and muon are closer to each other than $\Delta R = 0.4$, the isolation cones that have radius equal to 0.2 necessarily do overlap. Therefore, requiring small sum of the track momenta around one lepton affects the sum of the tracks calculated around the other lepton, therefore using electron and muon (anti)isolation as independent variables for background estimation is noy good. The plot of correlation between the electron and muon tracking isolation is presented in fig. 3.25. The Pearson product-moment correlation coefficient[3] of the two distributions is 0.3, meaning weak but existing correlation.

Therefore in the end the selected variable pair was charge product and isolation. Using them, 4 major regions can be defined in the phase-space based on passing/failing cuts on isolation and charge product as it is depicted in fig. 3.27. The regions are defined as follows:

[3]Pearson's correlation coefficient between two variables is defined as the covariance divided by the product of the standard deviations: $\rho_{X,Y} = \frac{\mathrm{cov}(X,Y)}{\sigma_X \sigma_Y}$. The value of 0 is no correlation, while the value of (-)1 means full (anti)correlation.

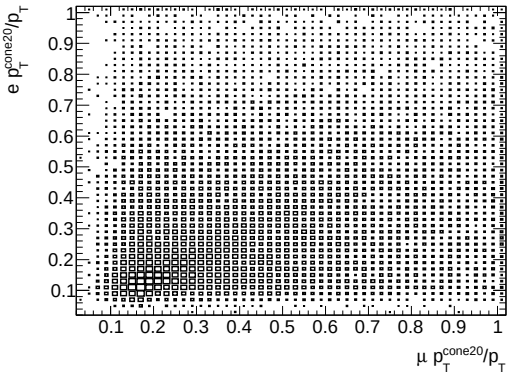

Figure 3.25: The correlation of electron (vertical axis) and muon (horizontal axis) relative tracking isolation in data. Note that dominating part of the distribution that is below 0.02 in both variables has been excluded from the plot.

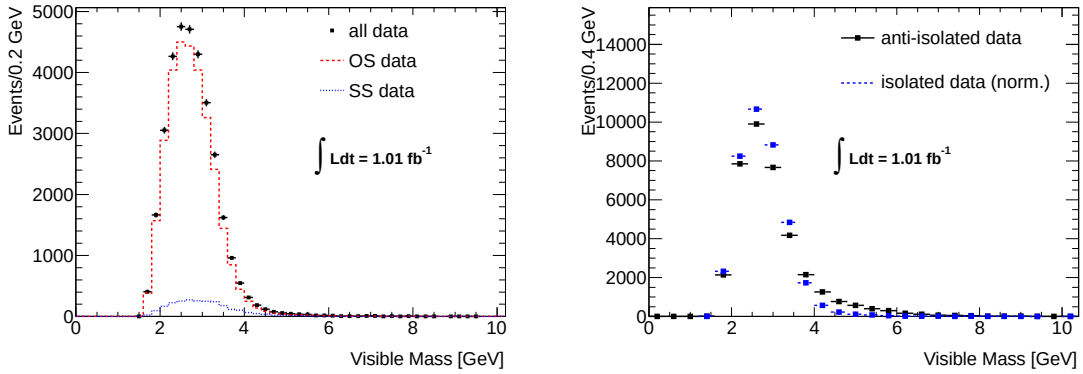

(a) events passing isolation cuts

(b) events passing reverse isolation cuts

Figure 3.26: The mass of electron-muon pairs in events passing the cuts on tracking and calorimeter isolation (fig. 3.26(a)) and in events failing all isolation cuts simultaneously (anti-isolated events depicted at fig. 3.26(b)). Both plots show data (only in fig. 3.26(b) the number of isolated events is rescaled to match anti-isolated ones in order to compare shapes).

Region A: Electron and muon have opposite signs and both pass all isolation cuts

Region B: Electron and muon have same signs and both pass all isolation cuts

Region C: Electron and muon have opposite signs and both fail all isolation cuts

Region D: Electron and muon have same signs and both fail all isolation cuts

One should note, however, that those regions do not cover the whole phase-space. For example events with one isolated and one anti-isolated lepton are not included in any of the ABCD regions. It is clear that almost all signal events end up in region A.

Fig. 3.28 shows the distribution of the isolation variables for the same sign and opposite sign events. The distributions are of electron isolation are indeed compatible within 2 sigma based on the Kolmogorov-Smirnov test. Fig. 3.28(c) shows the ratio of same sign and opposite sign events in the isolated and antiisolated events. The expected background from the electroweak events (tab. 3.3) is subtracted. It is important to check that also key observables do not change between the regions. Fig. 3.29 show the shapes of mass distributions of the same and oppositely

signed electron-muon pairs. The compatibility is very good (p-value of Kolmogorov-Smirnov test is 0.8). The distributions in figs. 3.28 and 3.29 show that the ratio of isolated and anti-isolated events is same for same-sign and opposite-sign events and we can write formula for the expected number of QCD events in region A:

$$N_A^{QCD} = N_B \times \frac{N_C}{N_D} \tag{3.2}$$

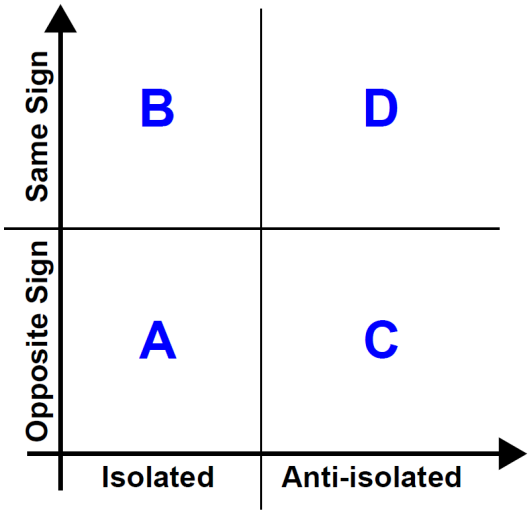

Figure 3.27: The scheme of definition of the various regions within the ABCD method.

The number of events observed in data and non-QCD backgrounds in different regions is given in tab. 3.8. Inserting them into the formula 3.2, we obtain the estimate for the number of QCD events in the signal region

$$N_A^{QCD} = 78.6 \pm 16.4 \text{ (stat.)}$$

The contribution from the electroweak processes can be obtained from tab. 3.3:

$$N_A^{t\bar{t}} = 8.3 \pm 0.8 \text{ (stat.)} \qquad N_A^{W\to\ell\nu} = 6.7 \pm 4.0 \text{ (stat.)}$$

Finally, the Υ events are signal like in a sense that they are opposite sign and isolated, so their expected contribution should be added as well.

$$N_A^{\Upsilon} = 0.7 \pm 0.3 \text{ (stat.)} \ \pm 0.3 \text{ (sys.)}$$

This leads us to total estimate of background events in the signal region A:

$$N_A^{BG} = 94.3 \pm 21.9 \text{ (stat.)} \tag{3.3}$$

Finally, the comparison of the mass distribution of data and estimated background and signal is shown in fig. 3.30 where opposite-sign anti-isolated events were used as a shape template for the QCD events and the distribution was normalized to give the expected output of 78 events. The plot shows also total (statistical and systematic) uncertainty on the signal and background estimation. Overall, there is very good agreement between data and estimated background thus providing confidence to the procedure presented in this section.

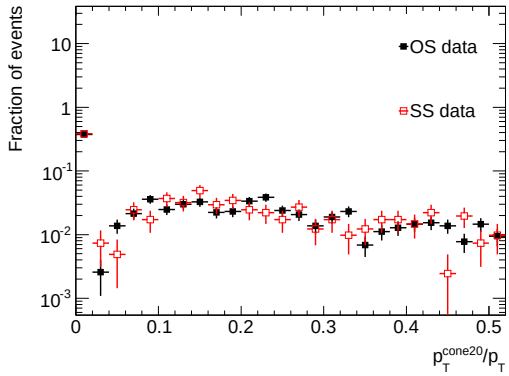

(a) Electron tracking isolation

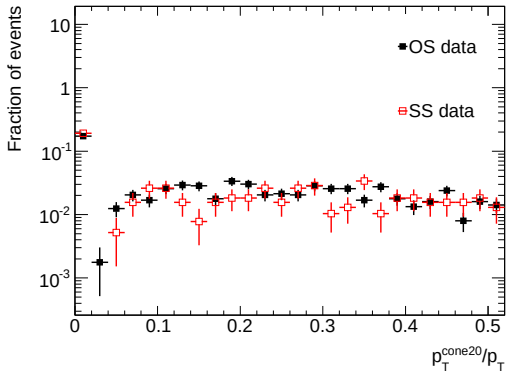

(b) Muon tracking isolation

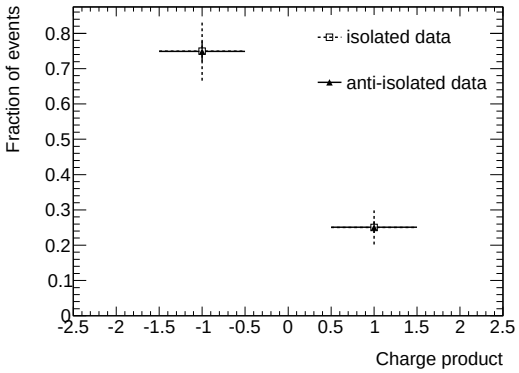

(c) Charge product

Figure 3.28: The isolation variables for electron and muon passing all the cuts as defined in section 3.7.2 with the exception of isolation and charge product. Fig. 3.28(a) shows the relative isolation of electron in tracker. Fig. 3.28(b) shows the same distributions for the muon. On each plot there are two overlayed distributions: data with the opposite sign and same sign electron-muon pair. Finally, fig. 3.28(c) shows the ratio between same charge and opposite charge events in the isolated and anti-isolated data after the subtraction of the expected background from EW processes from the isolated opposite sign events.

3.8.3 Systematical Uncertainty

The contribution of the electroweak background is estimated from the Monte Carlo. There are several uncertainties on the Monte Carlo predictions:

- The cross-section assigned to the simulated samples
- The luminosity
- Trigger efficiency
- Electron reconstruction and identification
- Muon reconstruction and identification
- Electron energy scale
- Muon momentum resolution

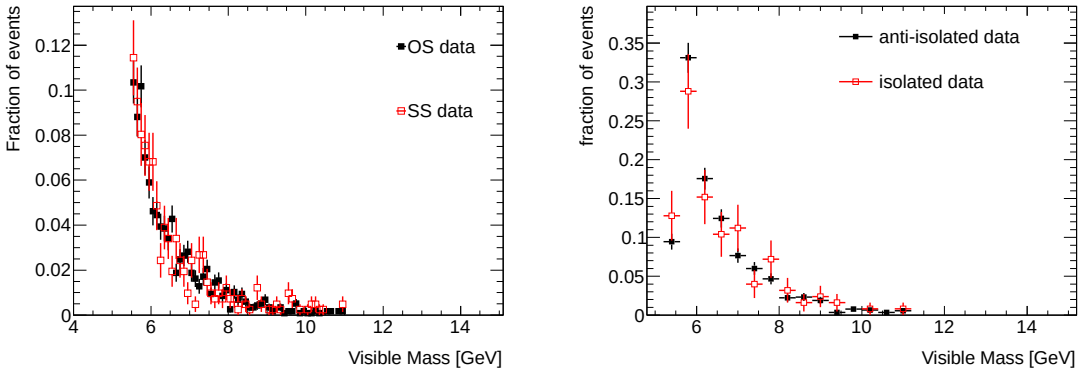

(a) no isolation cut (b) no charge cut

Figure 3.29: The distribution of the mass of the electron-muon pair for opposite and same sign events without isolation in the mass window of 5.5–11 GeV (fig. 3.29(a)) and for isolated and antiisolated events without applying the charge cut (fig. 3.29(b)).

	region A	region B	region C	region D
data	98	27	674	226
$t\bar{t}$	8.3	0.0	2.2	0.1
$W \to \ell\nu$	6.7	1.0	0.9	0.0
$\Upsilon \to \tau\tau$	0.7	0.0	0.0	0.0
$a_1 \to \tau\tau$	51.0	0.0	0.0	0.0

Table 3.8: The number of events in 4 different regions defined in text for data, simulated background and signal.

The signal events estimation has the same uncertainty with the exception of the first one. Rather than being uncertain about the total cross-section, the signal events have uncertain acceptance arising from the Monte Carlo modeling.

There is also systematic uncertainty in the data: Electron energy scale and the background estimation with ABCD method. The uncertainty on the electron energy scale does not affect the amount of QCD estimated from data, because this method uses ratio of events. On the other hand, the amount of data events observed in signal region is obviously not affected by the uncertainty on the QCD background estimation.

3.8.4 Luminosity

Evaluation of the luminosity scale was performed using several luminosity-sensitive detectors, and comparisons of the long-term stability and accuracy of this calibration applied to the 2011 data were made. A relative luminosity uncertainty of 3.7 % was obtained [93].

Background cross-section

The cross-section used for the simulated electroweak background processes have been taken from NNLO calculations. The main contributions to the background are coming from $t\bar{t}$ and $W \to \mu\nu$+jet processes. The $t\bar{t}$ cross-section used in this analysis is [94]

$$\sigma_{t\bar{t}} = 164.57^{+11.45}_{-15.78} \text{ pb}$$

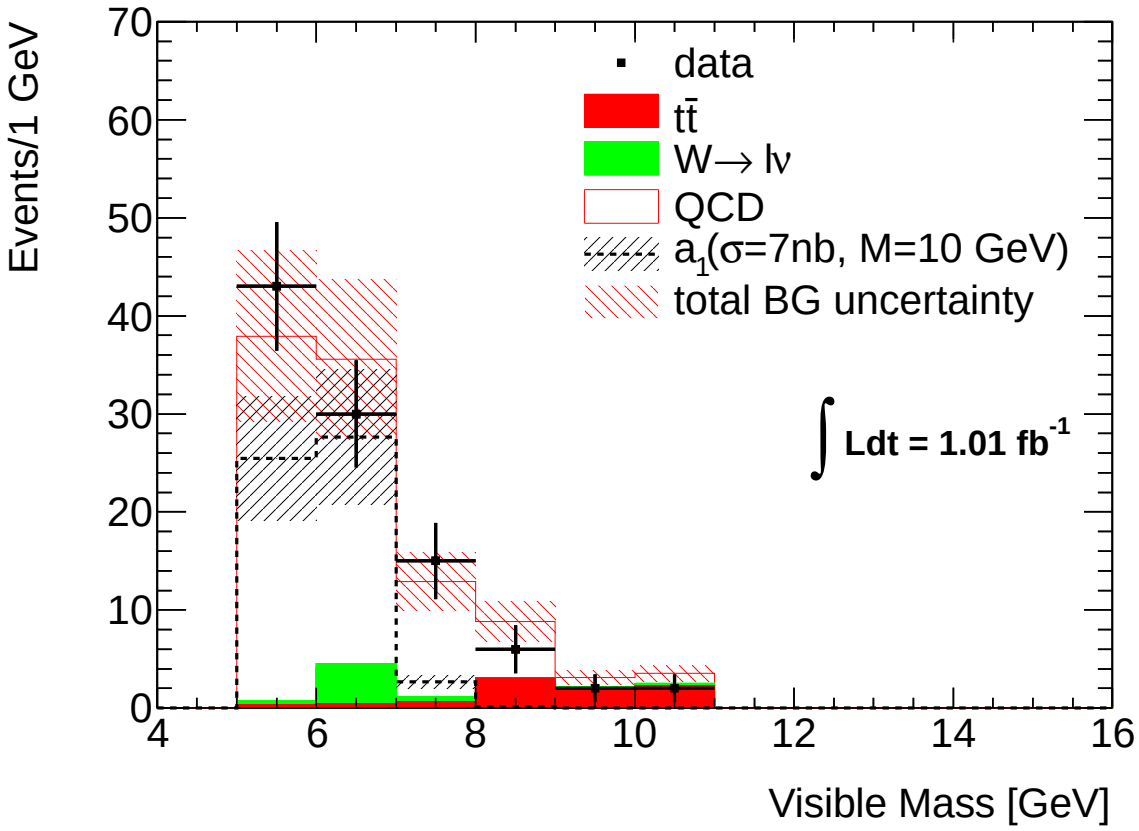

Figure 3.30: The distribution of the visible mass of the a_1 candidate particle for data and estimated backgrounds after all cuts. Contribution for $t\bar{t}$ and $W \to \ell\nu$ is based on MC simulation and scaled to the integrated luminosity in data while contribution from QCD events has been derived from data using ABCD method. All background contributions are stacked on top of each other. Finally, the expected distribution for signal is overlayed in dotted line. The plot also show the total (statistical and systematic) uncertainty on expected signal events (black pattern) as well as the total uncertainty on the expected background (red pattern).

yielding the uncertainty of 9.6 %. The inclusive $W \to \ell\nu$ cross-section at NNLO was taken as [95]

$$\sigma_{W\to\ell\nu} = 10.46 \pm 0.52 \text{ nb}$$

yielding uncertainty of 5.0 %.

The cross-section for the Υ resonances have been extrapolated from the measured values. The uncertainty of the fit is dependent on the uncertainty of the experimental input and distance from the measured values. The highest uncertainty on the extrapolated cross-section (50 %) out of all 3 extrapolations is used as systematical uncertainty for Υ events.

3.8.5 Signal acceptance

The sources of uncertainty on the signal acceptance arise from the modeling of initial and final state radiation, the choice of parton density functions, the choice of α_S and also from the (lack of) knowledge of the effects beyond Next-to-Leading order. This uncertainty was discussed in [77] where the value was obtained by comparing MC@NLO and PYTHIA simulations due to

the lack of other NLO simulations of signal. For the 10 GeV a_1 it has been set to 20 %. Note that this value is a conservative upper estimate of the uncertainty.

3.8.6 Trigger efficiency

The uncertainty on the trigger efficiency arises from the difference in the performance of the trigger on the simulated events and on the data, as it is discussed in section 3.6.1. The scale factors on electron and muon trigger have been varied within 1 σ of their respective errors to see the effect of changing trigger efficiency on the signal and background yield. The highest observed difference is quoted as the systematic uncertainty. The uncertainty on the trigger efficiency is 2.0 %.

3.8.7 Electron reconstruction and identification

In section 3.6.2 it is described how scale factors for the electron reconstruction and identification efficiency are determined. Those scale factors are varied within their uncertainty to obtain their influence on the event yield. It is 7.8 % for signal and 4.1% for the background.

3.8.8 Muon reconstruction and identification

In section 3.6.2 it is described how scale factors for the muon reconstruction and identification efficiency are determined. Those scale factors are varied within their uncertainty to obtain their influence on the event yield. It is 0.9 %.

3.8.9 Electron Energy Scale and resolution

In section 3.6.2 it was shown that the electron energy scale in the data must be corrected in order to match the scale used for simulation. The correction factors are varied within their uncertainty to obtain the effect of electron energy scale on the data yield. Similarly, the energy resolution is not correctly reproduced in the Monte Carlo, so a smearing is applied and again, it is varied within 1 σ of its uncertainty to calculate the systematical effect. The uncertainty on the electron energy scale in data is 2.2 %, and the uncertainty on the energy scale resolution in the Monte Carlo is 0.01 %.

3.8.10 Muon Momentum Resolution

The muon momentum resolution has to be smeared in the Monte Carlo to match the experimental resolution. To check the systematical effect of the smearing, the resolution in the Inner Detector and Muon Spectrometer has been varied by 1 σ in both directions. The maximal effect was 2.8 % that is used as the systematical uncertainty.

3.8.11 ABCD background method estimation

The ABCD method relies on the fact that the variables are uncorrelated. This is, however, difficult to reach in practice and there is always some residual correlation between the variables. To evaluate that effect for this analysis, the anti-isolation cut, designed to select same sign and opposite sign background, have been varied between 0.02 and 0.06 (the value used for the background determination is 0.05 - see section 3.8.2) and the effect on the predicted number of background events has been evaluated. The highest deviation from the original value used in section 3.8.2 is 2.5 % that is also used as the systematical uncertainty.

3.8.12 Summary

Tab. 3.9 summarizes different contributions to the systematical error for signal, background and data.

uncertainty source	signal	$t\bar{t}$	$W \to \mu\nu$	$\Upsilon \to \tau\tau$	QCD	data
luminosity	3.7%	3.7%	3.7%	3.7%	-	-
cross-section	-	9.6%	5.0%	50%	-	
signal acceptance	20%	-	-	-	-	-
trigger	2.0%	2.0%	2.0%	2.0%	-	-
electron reconstruction and identification	7.8%	4.1%	4.1%	7.8%	-	-
muon reconstruction and identification	0.9%	0.9%	0.9%	0.9%	-	-
electron energy scale	-	-	-	-	-	2.2%
electron energy resolution	0.01%	0.01%	0.01%	0.01%	-	-
muon momentum resolution	2.5%	2.5%	2.5 %	2.5%	-	-
ABCD method	-	-	-	-	2.5%	-
TOTAL	22.0 %	11.6%	8.2%	50.8%	2.5%	2.2%

Table 3.9: The systematical uncertainties from various sources and their effect on signal, simulated background and and background estimated from the data as well as uncertainty on the observed amount of date in the signal region. In the last line they are all added together.

3.8.13 Results with systematical errors

After calculating the systematical errors it is possible to write complete results on the number of expected and observed events:

$$\begin{aligned} N^{\text{obs}} &= 98.0 \pm 2.2 \text{ (sys.)} \\ N^{\text{exp}}_{BG} &= 94.3 \pm 21.9 \text{ (stat.)} \pm 3.4 \text{ (sys.)} \end{aligned}$$

where N^{obs} is the number of observed events in the signal region, and N^{exp}_{BG} is total number of expected backround events there. Finally, the signal expectations for various masses are:

$$\begin{aligned} N^{\text{exp}}_{a_1(9000)} &= 21.9 \pm 4.3 \text{ (stat.)} \pm 4.5 \text{ (sys.)} \\ N^{\text{exp}}_{a_1(10000)} &= 51.0 \pm 7.7 \text{ (stat.)} \pm 10.5 \text{ (sys.)} \\ N^{\text{exp}}_{a_1(10500)} &= 63.8 \pm 9.1 \text{ (stat.)} \pm 13.1 \text{ (sys.)} \end{aligned}$$

where the number is expected a_1 mass in MeV. Note that all mass points assumed the cross-section of 7 nb.

3.9 Limit calculation

Section 3.8.2 shows that QCD background for this analysis is difficult to describe and estimate. Also, due to very small acceptance of this analysis, the shape of the signal events distribution is

not very reliable. Therefore, to reduce the uncertainty coming from the wrong shape estimation, the limit on cross-section setting is treated as a counting experiment described by the following likelihood function:

$$\mathcal{L}(\sigma_{gg\to a_1\to\tau\tau}, L, \vec{\theta}) = \text{Pois}\left(N^{\text{obs}}|N^{\text{exp}}_{\text{tot}}(\vec{\theta})\right) \times G(L_0|L,\sigma_L) \times \prod_{j\in\text{syst.}} G(\theta_j|0,1) \tag{3.4}$$

The likelihood contains a Poisson term in the observed number of events N^{obs} with expectation value $N^{\text{exp}}_{\text{tot}}$ that is sum of contributions from signal and all backgrounds (estimated from data or Monte Carlo). Next term is a Gaussian with a mean equal to measured value of integrated luminosity and variance corresponding to the uncertainty with which the total luminosity has been measured. The likelihood also includes the nuisance parameters θ_j that characterize the systematic uncertainty. In our case

$$\begin{aligned} N^{\text{obs}} &= 98.0 \\ N^{\text{exp}}_{s+b} &= 151.7 \\ N^{\text{exp}}_{b} &= 95.7 \end{aligned}$$

This likelihood function was used to construct the test statistics $\tilde{q}_\sigma$ based on the one-sided profile likelihood ratio $\tilde{\lambda}(\sigma)$:

$$\tilde{\lambda}(\sigma) = \begin{cases} \dfrac{\mathcal{L}\left(\sigma,\hat{\hat{\theta}}(\sigma)\right)}{\mathcal{L}\left(\hat{\sigma},\hat{\theta}\right)} & \text{if} \quad \hat{\sigma} \geq 0 \\ \dfrac{\mathcal{L}\left(\sigma,\hat{\hat{\theta}}(\sigma)\right)}{\mathcal{L}\left(0,\hat{\hat{\theta}}(0)\right)} & \text{if} \quad \hat{\sigma} < 0 \end{cases} \tag{3.5}$$

where σ is the cross-section of the signal process. The single circumflex represents the maximum likelihood estimate (MLE) for a given parameter, while $\hat{\hat{\theta}}(\sigma)$ and $\hat{\hat{\theta}}(0)$ are MLE of θ parameters given cross-section equal to σ and 0, respectively. The test statistics $\tilde{q}_\sigma$ is given by

$$\tilde{q}_\sigma = \begin{cases} -2\ln\tilde{\lambda}(\sigma) & \text{if} \quad \hat{\sigma} \leq \sigma \\ 0 & \text{if} \quad \hat{\sigma} > \sigma \end{cases} \tag{3.6}$$

Having the test statistics, it is evaluated for tested σ and actual observed data to obtain $\tilde{q}_{\sigma,obs}$. This number provides a measure (in a yet unknown metric) of how likely the tested σ is, given the data. The next step is to use pdf of signal+background (eq. 3.4 with $\sigma_{a_1\to\tau\tau} > 0$) to generate toy Monte Carlo experiments to construct probability density function of the test statistics $\tilde{q}_\sigma$: $f(\tilde{q}_\sigma|\sigma,\hat{\hat{\theta}}(\sigma,obs))$. Note that conditional MLE for nuisance parameters is based on observed data. Nevertheless, the nuisance parameters are fixed only for generating the toy MC experiments but are allowed to float when the test statistic is evaluated.

With the constructed distribution of $\tilde{q}_\sigma$ for the signal+background hypothesis it is possible to calculate the p-value for a given σ:

$$p_\sigma = \int_{\tilde{q}_{\sigma,obs}}^{\infty} f(\tilde{q}_\sigma|\sigma,\hat{\hat{\theta}}(\sigma,obs))d\tilde{q}_\sigma \tag{3.7}$$

This definitions shows that p-value is a probability of obtaining data that are less compatible with the hypothesis (in this case signal+background) than observed data. Analogically, we can define a p-value for background only hypothesis, by replacing $\sigma \to 0$:

$$p_b = \int_{\tilde{q}_{\sigma,obs}}^{\infty} f(\tilde{q}_\sigma|0,\hat{\hat{\theta}}(0,obs))d\tilde{q}_\sigma \tag{3.8}$$

mass	observed upper limit	expected upper limit
9 GeV	29 nb	27±15 nb
10 GeV	12 nb	11± 5 nb
10.5 GeV	10 nb	10± 4 nb

Table 3.10: The upper 95% exclusion limits on the a_1 decaying to τ pair produced directly in gluon fusion as a function of the a_1 mass.

and calculate so-called CL_s:

$$CL_s = \frac{p_\sigma}{1 - p_b} \tag{3.9}$$

Finally, iterative numerical procedure is used to find for which value of σ the CL_s is 0.05; those cross-sections (and all greater) are excluded on 95 % confidence level based on observed data.

Next step is the calculation of the expected limit for background only hypothesis. This is done in this case by using the same pdf as for signal+background, only with σ=0, to generate pseudo-data for background only experiment. Then the whole procedure of setting the upper limit σ_{up} described above is repeated with background-only pseudo-data playing the role of observed data. This leads to a distribution of σ_{up}'s. Its median is the expected upper limit and the 68 % and 95 % bands of the σ_{up} distribution define the ±1 and ±2 sigma bands of the expected limit.

This is repeated for 3 simulated a_1 mass points and the CL_s for observed and expected limit on $gg \to a_1 \to \tau\tau$ cross-section for mass points 9, 10 and 10.5 GeV is shown in fig. 3.31.

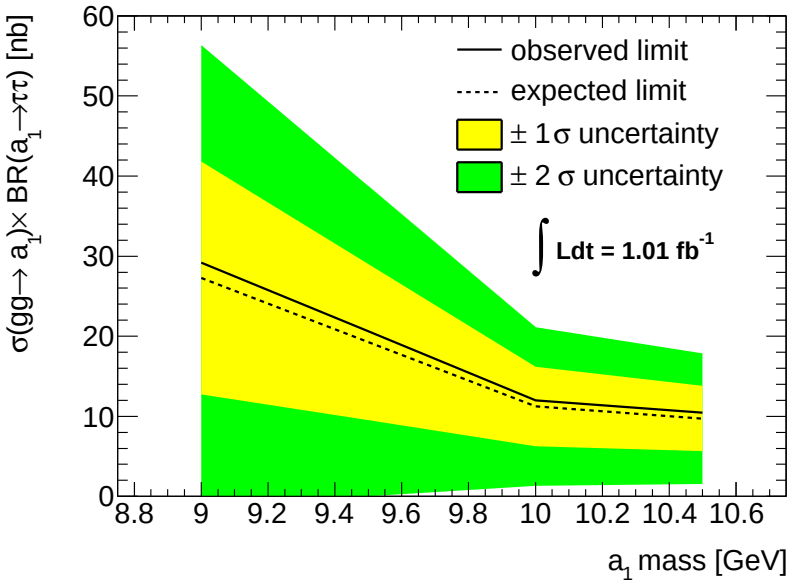

Figure 3.31: The expected and observed upper limit on cross-section as a function of a_1 mass. Solid line is observed limit at 3 points, dashed line is the expected limit for background only hypothesis and yellow and green bands correspond to 1 and 2 σ uncertainty.

The limits are also summarized in tab. 3.10.

3.10 Result interpretation

The result presented in section 3.9 is the limit on a production cross-section of a_1 times its branching fraction to a τ pair. The theory, on the other hand, provides the expected production cross-section as a function of $\tan\beta$ [50] and a branching fraction as a function of $\tan\beta$ [19]. The values obtained from figs. 1.8 and 3.1 taken from [50, 19] are summarized in tab. 3.11.

(a) m_{a_1}=9 GeV

m = 9 GeV	σ[nb]	BR
$\tan\beta = 10$	200	0.85
$\tan\beta = 3$	23	0.82
$\tan\beta = 2$	10	0.62
$\tan\beta = 1$	6	0.3

(b) m_{a_1}=10 GeV

m = 10 GeV	σ[nb]	BR
$\tan\beta = 10$	400	0.75
$\tan\beta = 3$	40	0.72
$\tan\beta = 2$	20	0.56
$\tan\beta = 1$	8	0.29

(c) m_{a_1}=10.5 GeV

m = 10.5 GeV	σ[nb]	BR
$\tan\beta = 10$	315	0.75
$\tan\beta = 3$	35	0.72
$\tan\beta = 2$	15	0.56
$\tan\beta = 1$	7	0.29

Table 3.11: a_1 production cross section $\sigma(gg \to a_1)$ ("σ" in the tables) and branching ratios to a tau lepton pair as a function of mass and $\tan\beta$.

Using information in tabs. 3.11 and 3.10, it is possible to plot predicted production cross-section as a function of $\tan\beta$ and compare it with the observed limit on the production cross-section. The latter is obtained by dividing the limit from section 3.9 by the branching fraction to τ's from tab. 3.11. The comparison of predicted and measured limits on $\sigma(gg \to a_1)$ as a function of $\tan\beta$ is shown in fig. 3.32 for the a_1 masses 9, 10 and 10.5 GeV. The cross-section prediction is valid for the 2-Higgs-doublet models of type II where $C_{ab\bar{b}} = C_{a\tau^+\tau^-} = \tan\beta$. The example of such a model is MSSM.

Fig. 3.32 shows that the measurement presented in this chapter puts severe limitations on $\tan\beta = C_{ab\bar{b}}$ which should be smaller than 2 (for $m_{a_1} = 10$ GeV and $m_{a_1} = 10.5$ GeV) or 4 (for $m_{a_1} = 9$ GeV), respectively. Compared to the $C_{ab\bar{b}}$ limits in [19], the limits on maximal $ab\bar{b}$ coupling have been somehow extended for $m_{a_1} \gtrsim 10$ GeV (fig. 3.33).

In the context of NMSSM we have $C_{ab\bar{b}} = C_{a\tau^+\tau^-} = \tan\beta\cos\theta_A$ (cf. section 1.3.3). Therefore for every $\tan\beta$ where the predicted cross-section is larger than observed limit, we can set a limit on maximal $\cos\theta_A$, remembering that $\sigma(gg \to a_1) \sim C^2_{ab\bar{b}} \sim \cos^2\theta_A$:

$$\text{Max } |\cos\theta_A| = \sqrt{\frac{\sigma_{\text{limit}}(gg \to a_1)}{\sigma_{\text{prediction}}(gg \to a_1)}}$$

The limits on maximal NMSSM mixing angle are shown in fig. 3.34(a) for various $\tan\beta$ values as a function of m_{a_1}. The limits should be compared with the values shown in fig. 1.9 that is for reader convenience repeated here as fig. 3.34(b).

Comparing figs. 3.34(a) and 3.34(b) we find that if $m_{a_1} \gtrsim 10$ GeV, the limits for $\tan\beta \geq 10$ (bottom three curves in fig. 3.34(b)) are improved with respect to the previous experiments. Previously, $|\cos\theta_A|$ has been practically unconstrained for $m_{a_1} \gtrsim 10$ GeV and $\tan\beta \geq 10$, while plot in fig. 3.34(a) sets limit for max $|\cos\theta_A|$ in this case to 0.2.

Finally, using $BR(a_1 \to \mu\mu)$ from fig. 1.8, it is possible to translate previous ATLAS result on $\sigma(gg \to a_1) \times BR(a_1 \to \mu\mu)$ [77] to a limit on $\sigma(gg \to a_1)$ as a function of $\tan\beta$. This can be compared with the limits on $\sigma(gg \to a_1)$ set by the analysis presented in this thesis in different mass points. This is done in fig. 3.35. It shows that the results presented in this chapter nicely complement the previous measurement and improve the limits for $m_{a_1} = 9$ GeV, where the sensitivity of $a_1 \to \mu\mu$ analysis was decreased due to the closely lying Υ resonances.

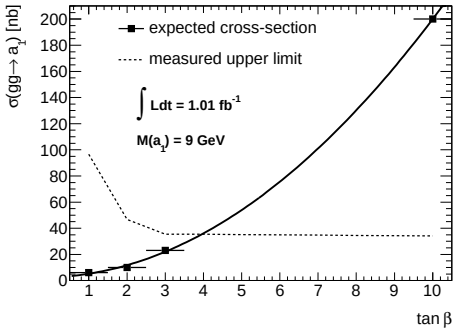

(a) $m_{a_1} = 9$ GeV

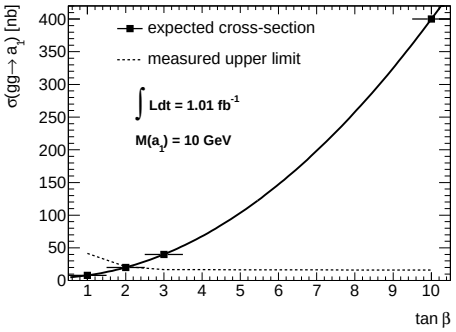

(b) $m_{a_1} = 10$ GeV

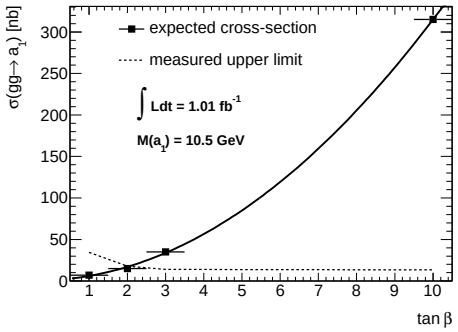

(c) $m_{a_1} = 10.5$ GeV

Figure 3.32: The predicted direct production cross-section as a function of $\tan\beta$ together with the observed upper limit on the direct production cross-section. The predicted values are fitted with the second order polynomial (the cross-section scales with $\tan^2\beta$ for small $\tan\beta$ [50]). The dotted line is linear interpolation between the values given at $\tan\beta = 1$, 2, 3 and 10.

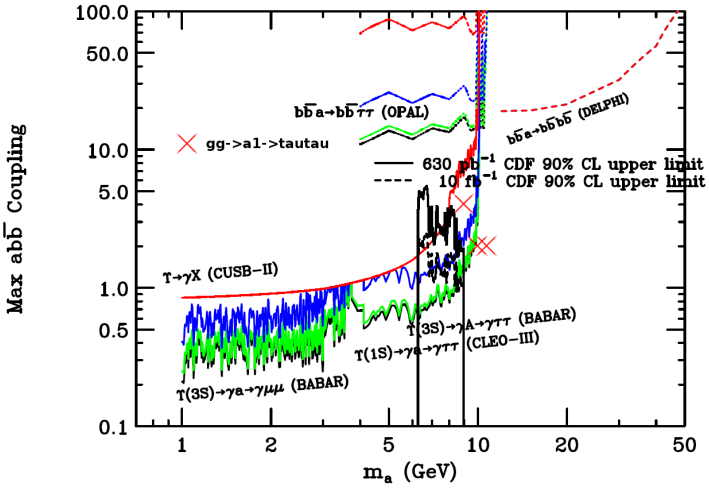

Figure 3.33: The published limits on $C_{ab\bar{b}}$ coupling from various experiments as appeared in [19]. The values are coming directly from the experiment and colours correspond to the $\tan\beta = 0.5$ (red), 1 (blue), 2 (green) and ≥ 3 (black). The red crosses are limits on $C_{ab\bar{b}}$ derived from search for $gg \to a_1 \to \tau^+\tau^-$ events for 2HDM type-II models where $\tan\beta = C_{ab\bar{b}} = C_{a\tau^+\tau^-}$.

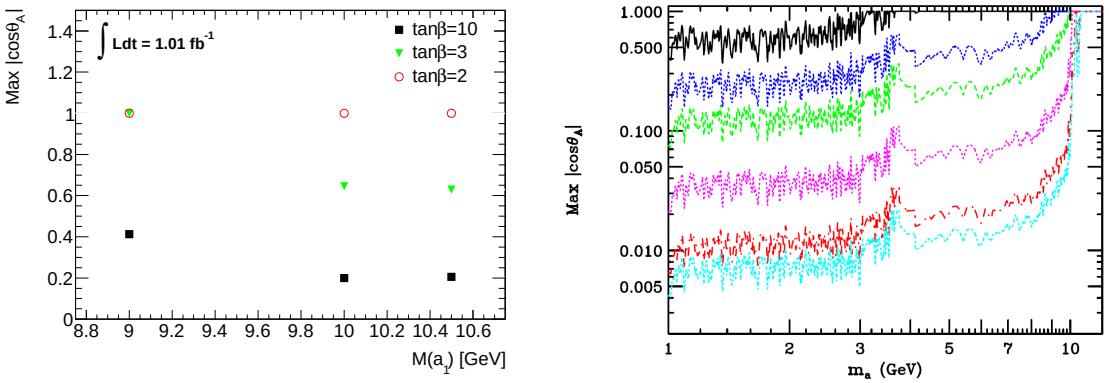

(a) limits from $a_1 \to \tau\tau$ analysis

(b) limits from [19]

Figure 3.34: The observed limits on maximal value of $\cos\theta_A$ at three different mass points and for 3 different $\tan\beta$ values are shown in fig. 3.34(a). The limits from previous experiments as presented in [19] are shown in fig. 3.34(b). The curves correspond to $\tan\beta = 1$ (upper curve), 1.7, 3, 10, 32 and 50 (lowest curve).

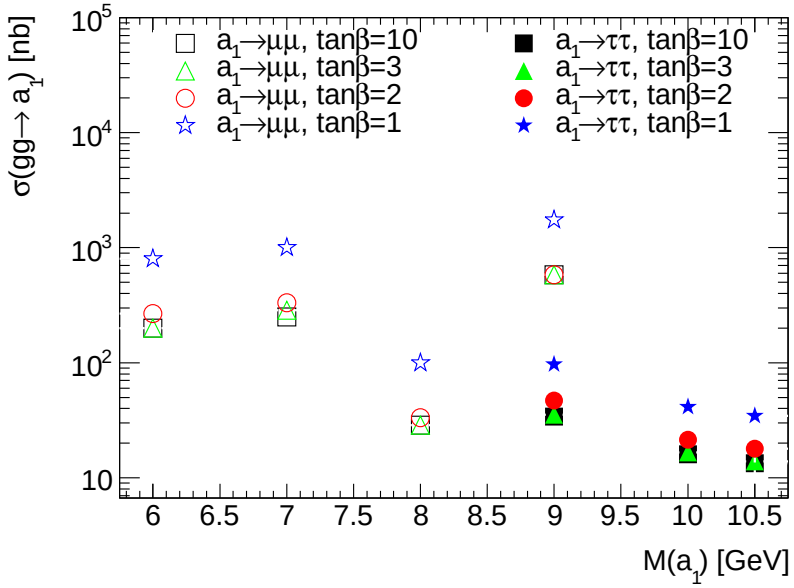

Figure 3.35: The summary of the limits on $\sigma(gg \to a_1)$ from $a_1 \to \mu\mu$ search [77] and $a_1 \to \tau\tau$ search (this thesis) as a function of $\tan\beta$.

3.11 Summary of new experimental constraints

The analysis presented in this thesis was designed to explore the mass region just below the $2m_B$ threshold, close to the Υ resonances, and managed to set new limits there. The primary reason why it is possible to obtain better limits than the previous experiments are 1) The direct production search does not suffer from the upper mass limit that prevents B-factories from setting limits above Υ mass and 2) The search in ditau channel is not limited by the small branching fraction and overwhelming Υ background, as it is the case for the dimuon channel.

Assuming $C_{ab\bar{b}} = C_{a\tau^+\tau^-} = \tan\beta$, a limit is set for masses $m_{a_1} \geq 9$ GeV. For the values $m_{a_1} \geq 10$ GeV the limits are stronger than those presented in [19].

The limit on cosine of NMSSM mixing angle $\cos\theta_A$ is also improved for $m_{a_1} \geq 10$ due to the stronger limits on $C_{ab\bar{b}} = \tan\beta\cos\theta_A$. The upper limits on $C_{ab\bar{b}}$ and $\cos\theta_A$ set by this analysis are summarized in tab. 3.12.

In order to see the effect on the Ideal Higgs Scenario, one should compare values in tabs. 1.6 and 3.12. We can see that the Ideal Higgs Scenario is already quite constrained by the LEP limits and no new constraints are brought there by the $gg \to a_1 \to \tau\tau$. So all Ideal Higgs scenarios discussed in [50, 19] are compatible with the ATLAS data. However, for $\tan\beta = 10$, the observed limit is worse than the current limit only by a little margin. Therefore possible future improvement of this analysis leading to more precise results and smaller limit might lead to the exclusion of some of the Ideal Higgs scenarios.

(a) m_{a_1}=9 GeV

m = 9 GeV	Max $C_{ab\bar{b}}$	Max $\lvert\cos\theta_A\rvert$
$\tan\beta = 10$		0.4
$\tan\beta = 3$	4	1.0
$\tan\beta = 2$		1.0

(b) m_{a_1}=10 GeV

m = 10 GeV	Max $C_{ab\bar{b}}$	Max $\lvert\cos\theta_A\rvert$
$\tan\beta = 10$		0.2
$\tan\beta = 3$	2	0.65
$\tan\beta = 2$		1

(c) m_{a_1}=10.5 GeV

m = 10.5 GeV	Max $C_{ab\bar{b}}$	Max $\lvert\cos\theta_A\rvert$
$\tan\beta = 10$		0.2
$\tan\beta = 3$	2	0.65
$\tan\beta = 2$		1

Table 3.12: The summary of the limits on the SUSY parameters derived from results of $a_1 \to \tau\tau$ search. The $C_{ab\bar{b}}$ limit is in 2HDM of type-II dependent only on a mass and not on $\tan\beta$.

3.12 Outlook and possible analysis improvements

The two largest sources of uncertainty of the result presented in this chapter are the statistical error of the QCD background estimation and the systematical error on the signal acceptance. The second uncertainty can be reduced by using more NLO Monte Carlo generators and different pdf's to study the $gg \to a_1$ process. The good candidate is PowHeg [96] that already has gluon fusion process implemented.

The statistical uncertainty can be made smaller by increasing the amount of analysed data - the full 2011 dataset contains over 5 fb^{-1} of data, while only the first 1 fb^{-1} has been used for this work. Moreover, as can be inferred from tab. 3.4, the amount of analyzed events can be increased significantly if a better trigger selection is used. This was the motivation for a trigger that uses topological combination of electron and muon to select events.

3.12.1 Topological electron muon trigger

Since most of the $a_1 \to \tau\tau \to e\mu$ events are at or below the p_T thresholds of combined electron-muon trigger (fig. 3.21), improving the trigger selection can significantly increase the number of expected signal events. Therefore, author of this thesis proposed, designed and developed the trigger that selects low-p_T electrons and muons and uses the topology of an event to reject background. It is the first topological trigger at ATLAS that combines trigger objects of different types (all previous used multiple objects of the same type).

The topological trigger selection starts at L2, where simultaneous presence of electron and muon trigger object that pass L2_e5_medium and L2_mu6 triggers is requested. Afterwards, the event must pass following cuts:

- electron-muon $\Delta R < 3$
- electron-muon $\Delta\phi < 1.5$
- 1.5 GeV $< M_{e\mu} <$ 10 GeV

At the EF, the event must pass EF_e5_medium and EF_mu6 and same requirements as at L2 with the addition of:

- electron-muon $\Delta R > 0.1$

Those cuts are inspired by the topology of the signal events and have indeed very high signal efficiency. At the same time, those cuts are able to reject many background events even if the p_T threshold is low. The comparison of efficiency and rates of various triggers is given in tab. 3.13. It shows the trigger efficiencies with respect to all simulated events and the efficiencies w.r.t. events with at least one reconstructed muon and electron. It also shows the trigger efficiency for events that pass the full offline selection as defined in section 3.7.2. Note that all the efficiencies in tab. 3.13 are normalized by e5_medium_mu6 efficiency to better present the effect of topological and momentum trigger cuts. Because the topology required by the trigger is looser than the analysis selection, the efficiency of trigger with respect to the events passing full offline selection is the same with and without topological selection. The rate column in tab. 3.13 shows that the rate of the topological trigger is almost the same as the rate of the lowest unprescaled combined electron-muon trigger (that was also used in the analysis presented in this chapter), but the efficiency is more than twice as high.

trigger	ε trigger	ε trigger + reco.	ε analysis	rate@1×10^{33} cm^{-2}s^{-1}
e5_medium_mu6	1.00	0.87	0.60	31 Hz
e5_medium_mu6_topo	0.85	0.81	0.60	6 Hz
e10_medium_mu6	0.42	0.40	0.27	5 Hz

Table 3.13: The efficiency of various triggers. The "ε trigger" is the fraction of true events passing the trigger. Next column, "ε trigger + reco." shows the fraction of true events having at least one reconstructed electron and muon that pass the trigger. Finally, the column "ε analysis" shows the efficiency for events passing the full analysis. The last column presents the output trigger rate for instantaneous luminosity of 1×10^{33} cm^{-2}s^{-1}.

The topological trigger was deployed online in July 2011, so it is not present in most of the data used in this analysis. However, it is present in the additional 4 fb^{-1} of data, meaning that it is possible to have twice as much data for analysis than from simple combined electron-muon trigger.

3.12.2 Outlook

With more data and improved trigger selection, it should be possible to reduce background uncertainty by a factor of 2-3 (more than 5 times higher amount of data and up to 100% more efficient trigger selection). At the same time, the signal acceptance uncertainty can be decreased to 5-10% if PowHeg will be used for comparison. Those two effects can result in a lower limit on the $gg \to a_1 \to \tau\tau$ cross section and possibly even constrain the Ideal Higgs Scenario even more than limits in tab. 1.6.

Chapter 4

Tau Trigger Performance Improvement

4.1 Introduction

The current experimental program of the ATLAS experiment contains many analyses which look for a τ lepton in the final state. This is motivated mostly by light Higgs boson searches (Branching ratio of light Higgs to taus is roughly 0.1, it is the second most abundant decay mode after $b\bar{b}$). For example, one of the very good channels to study the Ideal Higgs scenario is $h_1 \to a_1 a_1 \to 4\tau$. This analysis has so far not been done, because the production cross-section is much smaller than the direct a_1 production discussed in the previous chapter. However, with more than 5 fb^{-1} already recorded and about additional 10 fb^{-1} expected in 2012, the analysis of $h_1 \to a_1 a_1 \to 4\tau$ decays has become feasible. The high instantaneous luminosity expected in 2012 will force the single lepton trigger thresholds to be very high. In order not to harm the selection efficiency, a combined trigger, requesting several τ decays already at the trigger level, can be used. Without the τ trigger, only a very small fraction of $h_1 \to a_1 a_1 \to 4\tau$ can be recorded. For the similar reason, tau trigger is indispensable in the searches of the low mass SM Higgs and some SUSY searches with high branching ratio to τ leptons.

Being the heaviest lepton, τ can decay either to μ or electron ("leptonic τ") or to lighter hadrons ("hadronic τ") via a virtual W boson. Most of the τ leptons decay hadronically (65%). Due to charge conservation, there is always an odd number of charged hadrons possibly accompanied by neutral hadrons, forming together so-called τ jet. Finally, there is always at least one neutrino (two for leptonic modes) among the τ decay products because the first step in the cascade is mediated by the weak interaction.

The leptonic tau decays are triggered by muon and electron trigger, as it was shown in chapter 3. However the final states with at least one hadronic tau form a majority of decays, so it is desirable to be able to trigger on the hadronic tau decays as efficiently as possible.

The tau trigger is designed to select hadronic τ's, characterized by the presence of 1 or 3 $\pi^{\pm}$ accompanied by a neutrino and possibly neutral pions. This distinguishes τ jets from regular jets originating in quark or gluon decays, which typically have much larger particle multiplicities. Before producing hadrons, the tau lepton often decays into a short-lived resonance. Because of the small mass difference, the momentum of the resonance is very similar to that of mother particle. The resonance then decays mostly to pions: those can be spread more widely relative to the its direction, because the mass difference is larger there. Nevertheless, the mass differences involved in a tau jet are smaller than in a pure QCD jet so the tau decay products tend to be more collimated with respect to the direction of a mother particle, thus forming very narrow

jet. The details about the tau trigger design are in section 2.3.2.

The tau trigger has been successfully commissioned with 900 GeV and 7 TeV collisions ([97], [98]). Those data were collected with beams of smaller intensity, where the average number of collisions per event was smaller than one. Towards the end of 2010 data taking luminosity increased such that on average more than 2 collisions were observed in every event. This chapter presents the results of the evaluation of the effect of this real pileup on tau trigger together with optimization strategy based on Monte Carlo pile-up simulations.

Pile-up poses strong challenges to tau identification as it increases density of the energy deposits and tracks around thr true tau decay products and therefore makes taus more simular to QCD jets. A large fraction of author's time in 2009-2010 has been devoted to analysis of data and simulation of events with more than one interaction per event in order to prepare a strategy for 2011 and 2012 where pileup will reach values up to 15-20 interactions per event.

4.2 Monte Carlo and data samples

4.2.1 Monte Carlo

The simulated signal and background samples are listed in tabs. 4.1 and 4.2, respectively. All MC samples were generated with Pythia6 [83], simulated with the most detailed knowledge of the detector geometry and reconstructed using the same algorithms as for the data.

description	cross-section [nb]	n. of events
$W \to \tau\nu$, all tau decays, $\mu = 1$	8.92	200k
$W \to \tau\nu$, all tau decays, $\mu = 6$	8.92	150k
MSSM $A \to \tau\tau$, $m_A = 800$ GeV, all tau decays, $\mu = 1$	1.6×10^{-6}	50k
MSSM $A \to \tau\tau$, $m_A = 800$ GeV, all tau decays, $\mu = 6$	1.6×10^{-6}	50k

Table 4.1: List of signal MC samples. The description shows also the average number of collisions per event (μ), number of the minimum bias collisions is equal to $\mu - 1$.

description	cross-section [μb]	n. of events
$pp \to$ all (non-diffractive only), "minimum bias", μ=1	58450	20M
$pp \to$ all (non-diffractive only), "minimum bias", μ=6	58450	1M
$pp \to jj$, "J0", 8 GeV $< p_T^{truth} <$ 17 GeV, μ=1	9585	400k
$pp \to jj$, "J0", 8 GeV $< p_T^{truth} <$ 17 GeV, μ=6	9585	400k
$pp \to jj$, "J1", 17 GeV $< p_T^{truth} <$ 35 GeV, μ=1	679.4	400k
$pp \to jj$, "J1", 17 GeV $< p_T^{truth} <$ 35 GeV, μ=6	679.4	400k
$pp \to jj$, "J2", 35 GeV $< p_T^{truth} <$ 70 GeV, μ=1	40.88	400k
$pp \to jj$, "J2", 35 GeV $< p_T^{truth} <$ 70 GeV, μ=6	40.88	400k
$pp \to jj$, "J3", 70 GeV $< p_T^{truth} <$ 140 GeV, μ=1	2.194	400k
$pp \to jj$, "J3", 70 GeV $< p_T^{truth} <$ 140 GeV, μ=6	2.194	400k

Table 4.2: List of background MC samples. The description shows also the average number of collisions per event (μ), number of the minimum bias collisions is equal to μ -1. There were different momentum cuts applied during hard scattering at parton level (p_T^{truth}).

4.2.2 Data

The data collected in 2010 were compared with the MC predictions for the pile-up performance. The early data, collected in the periods A-C (March 30 - June 5, 2010) were used as a sample with low or no pile-up (Average number of collisions per bunch crossing (BC) was below 1 in those data). On the other hand, the data collected in period I (October 24-29, 2010) were used as a pile-up sample: the average number of collisions per bunch crossing in these data is above 2.

4.2.3 Event and objects preselection

Data

In order to have meaningful performance comparison, only the events which fired the L1_TAU5 chain were selected. Because this chain only cuts on the L1 energy higher than 5 GeV, it was possible to study unbiased distributions of variables which were being cut on in other, more restrictive chains. The total luminosity is 14.6 nb^{-1} for no pile-up data and 748 μb^{-1} for pile-up data. The total number of events passing this selection from period I was 132 034 (out of 47 millions). From periods A to C 2 586 768 events were used.

For every trigger object, the same RoI identification number was required at L1, L2 and EF. When offline and EF performance was compared, reconstructed τ candidate was matched to the most energetic EF τ candidate within $\Delta R = \sqrt{\Delta\phi^2 + \Delta\eta^2} < 0.3$.

Monte Carlo

All events were required to have passed the same collision criteria as data, i.e. passing L1_TAU5 requirement. This selection was more than 99% efficient for all MC samples.

Finally, matching to truth was required for τ candidates in signal samples: a trigger or offline reconstructed object was considered only if hadronically decaying τ lepton was found within $\Delta R < 0.2$. Also, only the true τ leptons decaying within the detector pseudorapidity acceptance of $|\eta| < 2.5$ were considered for matching.

The trigger objects at L1, L2 and EF were matched to each other and to offline in the same way as for data.

4.3 Pile-up at ATLAS

The different sources of pile-up are discussed in detail in [23]. The trigger performance is affected mostly by pile-up coming from multiple pp interactions per event: so-called *in-time* pile-up[1]. However, we are interested only in such collisions which can trigger the detector read-out (minimum bias interactions), therefore we would like to calculate the mean number of minimum bias interactions per event. This is very straightforward. The mean number of minimum bias collisions per second is defined as $\mathcal{L}\cdot\sigma_{\text{MB}}$, where $\mathcal{L}$ is the instantaneous luminosity and σ_{MB} is the minimum bias cross-section at LHC centre-of-mass energy (7TeV [57]). Next piece of information is the frequency of bunch crossings inside ATLAS. This is proportional to the number of colliding bunches n_{bunch} and the LHC frequency f_{LHC} (number of cycles per second) which is 11245 Hz. The number of minimum bias collisions per bunch crossing n_{BC} is

[1]The other pile-up is so-called *out-of-time* pile-up whose main (but not the only) source are events happening very shortly before or after the triggered events. This started to happen when the bunch trains are introduced where events are separated by 150 ns or less.

given by the ratio of the number of collisions per second and number of bunch crossings per second:

$$n_{\mathrm{MB}}^{(\mathrm{BC})} = \frac{\mathcal{L} \cdot \sigma_{\mathrm{MB}}}{f_{\mathrm{LHC}} \cdot n_{\mathrm{bunch}}} \tag{4.1}$$

Instantaneous luminosity and minimum bias cross-section are not easy to measure, however their product is just the interaction rate f_{int}, which is quite easy to obtain from data. Then the formula becomes very simple:

$$n_{\mathrm{MB}}^{(\mathrm{BC})} = \frac{f_{\mathrm{int}}}{f_{\mathrm{LHC}} \cdot n_{\mathrm{bunch}}}$$

As the probability of having an additional $(n+1)$th collision in the event with n collisions already in place is independent of n (the protons in bunch are independent), the number of collisions per event follows binomial distribution. However, because the probability of a *single* proton in a bunch to collide is extremely small and the number of protons in a bunch is huge $(10^{11} - 10^{12})$, one can very well approximate this probability by the Poisson distribution with a mean $n_{\mathrm{MB}}^{(\mathrm{BC})}$. Therefore, the probability of having *exactly* k collisions in an event is equal to

$$\left(n_{\mathrm{MB}}^{(\mathrm{BC})}\right)^{k} \cdot \frac{e^{-n_{\mathrm{MB}}^{(\mathrm{BC})}}}{k!} \tag{4.2}$$

The ATLAS Run Query web interface[2] calculates both $n_{\mathrm{MB}}^{(\mathrm{BC})}$ and the probabilities of having k or more events using the formulas (4.1) and (4.2).

From (4.1) one can easily infer how the level of pile-up can be influenced. There are 2 constants (LHC frequency and cross-section) and 2 variables which depend on the machine settings (instantaneous luminosity and number of colliding bunches). However, they are not independent: $\mathcal{L}$ is proportional to n_{bunch} and the bunch intensity. As the quotient of luminosity and number of bunches enter the formula, in the end it is only the bunch intensity which influences the number of in-time minimum bias collisions per bunch crossing. The bunch intensity is proportional to the number of protons per bunch and inversely proportional to the beam cross-section. The latter can be decreased (and so the bunch intensity increased) by so-called "squeezing" of the beam, which happened for the first time during run 153565 (LHC fill 1058). The effect of squeezing can be nicely seen in fig. 4.1(a).

Due to its long duration (almost 42 hours), this run was the first to record a considerable number of events with pile-up. One of these events is shown in fig. 4.1(b). To evaluate the effect of pile-up, events with multiple interactions were extracted from data. The event had to have at least 2 good vertices to be considered as pile-up event. The good vertex needed to pass following criteria:

- There were at least 8 tracks associated to this vertex.
- The fraction of outliers (defined as a track with weight less than 0.001) is less than 1/4

On top of this, any additional vertex in the event was required to have less than 4 tracks, allowing to select very clean pile-up sample. In this way 89335 pileup events were selected out of the original 21 million events recorded in this stream. The first check one may do is to compare the number of pile-up events with the predictions. The average interaction rate (defined as rate

[2] http://atlas-runquery.cern.ch/

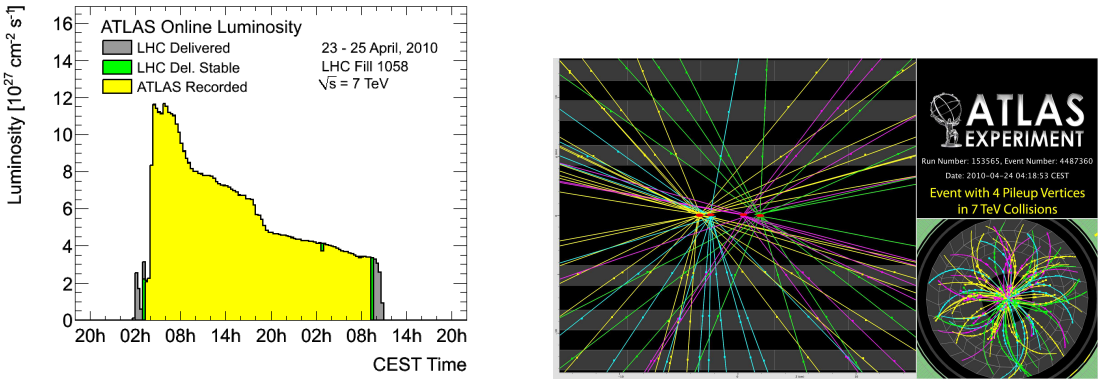

(a) ATLAS run 153565

(b) Pile-up event in run 153565

Figure 4.1: Fig. 4.1(a) shows the instantaneous luminosity as a function of time during run 153565 (fill 1058). Two-step squeeze is clearly visible in the very beginning of the run as well as roughly 6 times increase in instantaneous luminosity due to squeeze. The right plot 4.1(b) shows an event with 4 vertices reconstructed from run 153565.

of L1_MBTS_1_1[3] that is placed before prescaling) during run 153565 can be retrieved from the database. The number of colliding bunches can be found in the ATLAS Run Query by checking the Bunch Group configuration. The interaction rate, number of colliding bunches and resulting mean number of minimum bias collisions can be found in tab. 4.3

average interaction rate	289 Hz
number of colliding bunches	2
mean number of MB collisions per bunch crossing	0.0129
probability of one MB collision in a bunch crossing	1.27×10^{-2}
probability of two MB collision in a bunch crossing	8.15×10^{-5}
ratio of events with pile-up to events without pile-up	6.43×10^{-3}

Table 4.3: The pile-up properties of run 153565. The probabilities were calculated assuming Poisson distribution with the mean equal to the mean number of collisions per bunch crossing. Events without pile-up are events with exactly one minimum bias (MB) collision.

As a cross-check, one can take the number of events with 2 good vertices in the sample of pile-up events (total 88 162) and compare to the number of events with one good vertex obtained from the whole run (total 13 635 342). The ratio of those two numbers is 6.47×10^{-3} which is in a good agreement with the number given in tab. 4.3.

4.4 Pile-up in 2010 data

During the LHC run in 2010 gradually both in-time and out-of-time pile-up[4] has occurred. The beam intensity necessary for producing in-time pile-up in every event has been reached in later periods, that is why the last data taking period has been used as an example of data with pile-up. On the other hand, during the LHC start-up, most of the events did not have any

[3]This L1 minimum bias trigger requires at least one hit in forward and backward side of the minimum bias scintillator.

[4]The definition and description of different pile-up types can be find in section 4.3

collision at all: this data has been used as reference for no pile-up. The event selection criteria are discussed in section 4.2.3.

The effect of in-time pile-up in data is the same as predicted by Monte Carlo (cf. section 4.5 for variable definitions and MC results). Fig. 4.2 shows a comparison between the energy and shape HLT variables obtained for events with one and four and more vertices. This is consistently observed also in Monte Carlo simulations — see section 4.5.1: the shape variables become wider and energy distribution shifts to higher values.

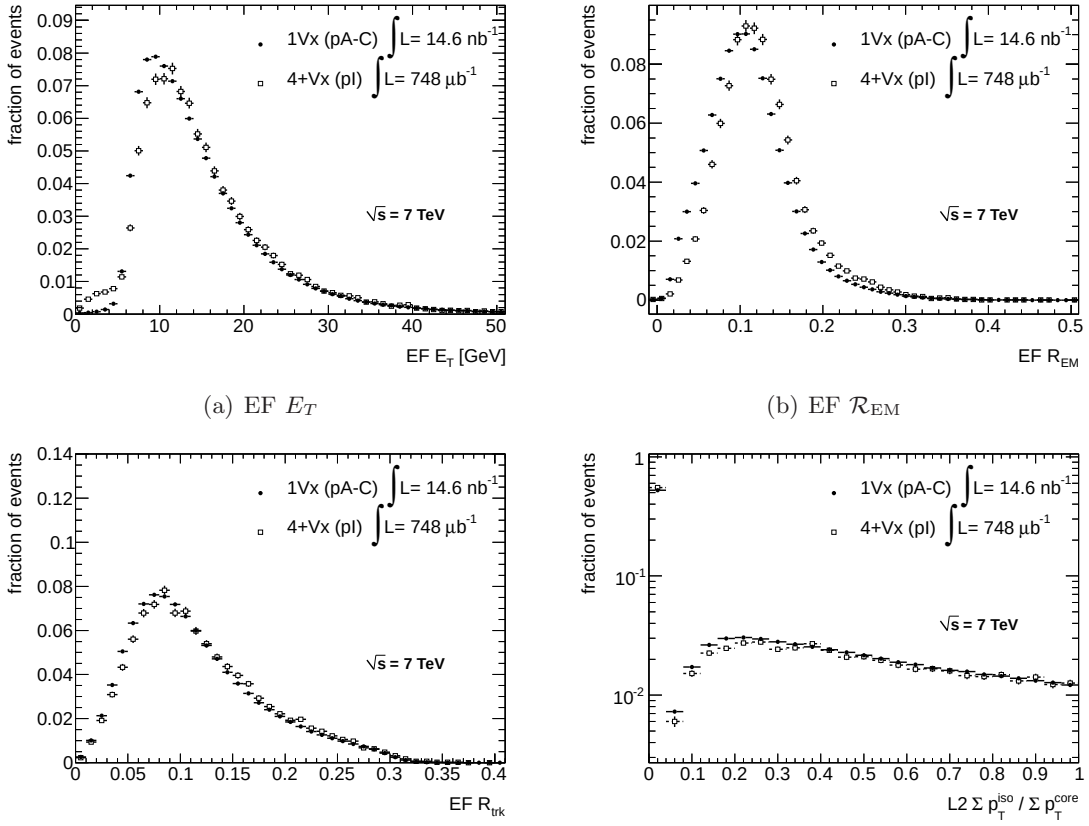

(a) EF E_T

(b) EF $\mathcal{R}_{\mathrm{EM}}$

(c) EF $\mathcal{R}_{\mathrm{trk}}$

(d) L2 $\sum p_T^{(\mathrm{iso})} / \sum p_T^{(\mathrm{core})}$

Figure 4.2: Comparison of data events with exactly 1 vertex from periods A to C ("pA-C") with events having 4 and more vertices from period I ("pI"). The τ candidates become wider and more energetic, as observed in Monte Carlo (cf. section 4.5 for variable definitions and MC distributions).

The data from period I, however, contain something which is not included in MC samples used in this study: out-of-time pile-up caused by bunches being close to each other in so-called bunch trains. The effect of out-of-time pile-up in the 2010 run can be examined in 2 ways. The first is to compare data with and without bunch trains. This is done in fig. 4.3 which compares event with the same number of vertices (thus eliminating the difference caused by in-time pile-up) between the early periods A-C and period I. No difference beyond statistical fluctuations is observed. The second way to examine the effect of out-of-time pile-up is to compare events taken in different bunches, namely the ones from the front of the train (which should have no out-of-time pile-up) with the ones taken in the last (eighth) bunch of the train (bunch no. 7) which should have maximal out-of-time pile-up from the remnants of all previous bunches. Such a comparison is presented in fig. 4.4. Once again, no systematic difference is seen, meaning that out-of-time pile-up in 2010 had a negligible effect on the tau trigger. This can be deduced

also from fig. 4.5 that shows the dependence of the rate on the position in bunch train. The differences between runs are larger than the effect of the different position in a bunch train so all the difference in rates is dominated by the non-uniformity of bunches in a fill.

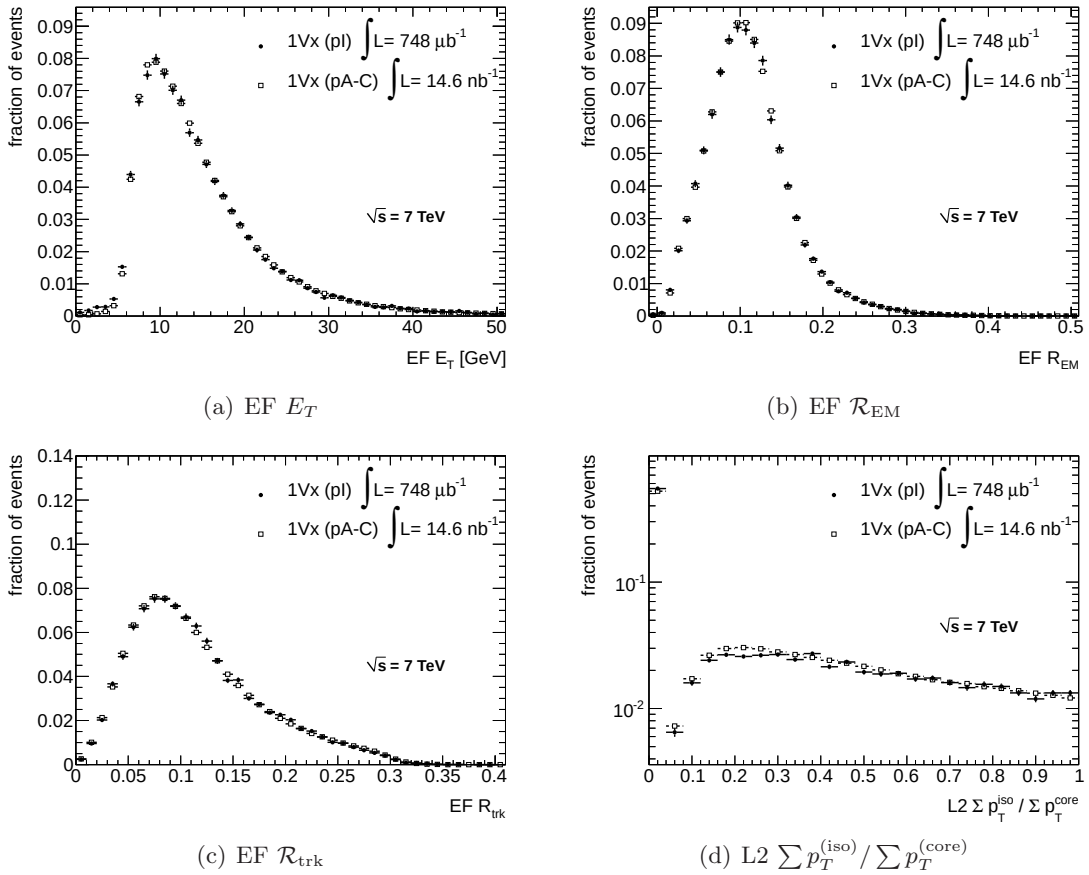

(a) EF E_T (b) EF $\mathcal{R}_{\mathrm{EM}}$

(c) EF $\mathcal{R}_{\mathrm{trk}}$ (d) L2 $\sum p_T^{(\mathrm{iso})} / \sum p_T^{(\mathrm{core})}$

Figure 4.3: Comparison of data events with exactly 1 vertex from periods A to C ("pA-C") with events with exactly 1 vertex from period I ("pI"). No difference which might have been attributed to out-of-time pile-up is visible. The meaning of variables is explained in section 4.5.

Now, in 2011 and certainly in 2012 we expect a much higher pile-up. In fact, as it turns out now (one year after the study presented in this chapter was done), the average pile-up in the first half of 2011 data is more like "4+Vx" events. In the second half of 2011, the average μ was around 10, increasing to 15 in the final weeks of data taking. In 2012, the LHC is expected to regularly deliver proton beams with $\mu > 20$. Therefore, we now move to higher statistics simulation to study with signal and background how the trigger selection can be improved.

4.5 Tau observables and pileup

4.5.1 Effect of in-time pile-up on selected HLT observables

There are several variables used for the tau selection at HLT as described in section 2.3.2. The baseline for trigger selection is the energy cut because the τ's coming from decays of heavy particles like Higgs boson are harder than the bulk of background processes. The pile-up brings additional energy to the event which is randomly deposited in the detector and so it can increase the energy of the tau candidate clusters. This is shown in fig. 4.6 where distributions of the

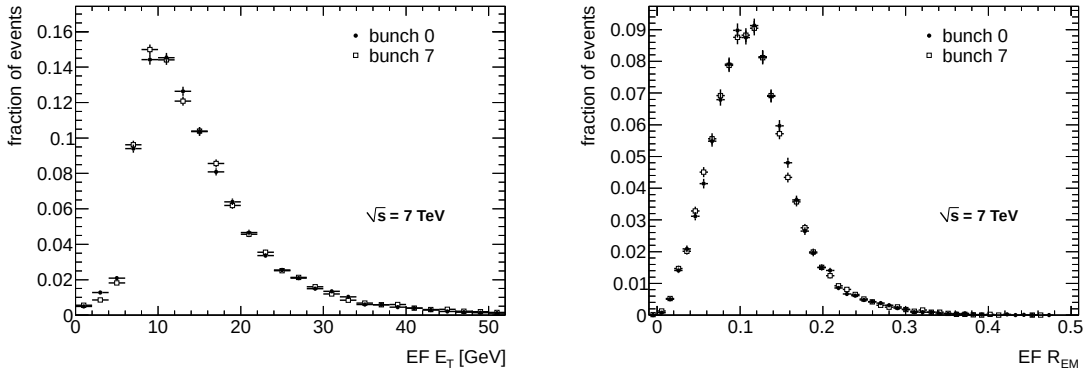

(a) EF E_T (b) EF $\mathcal{R}_{\mathrm{EM}}$

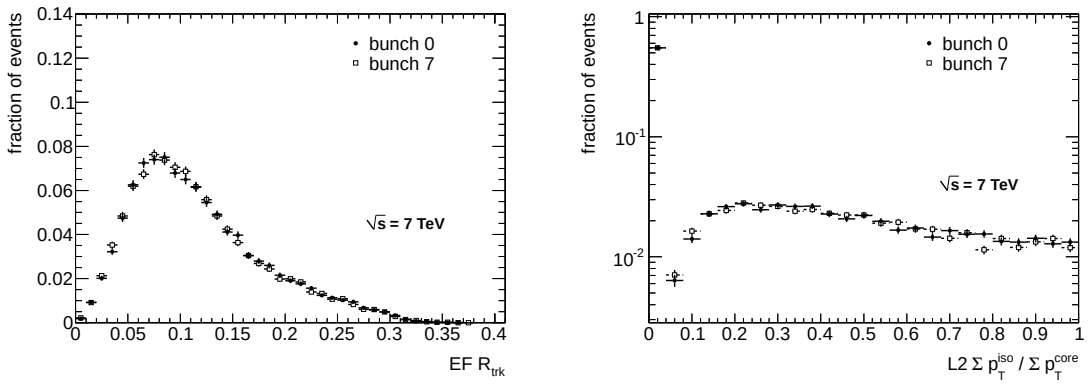

(c) EF $\mathcal{R}_{\mathrm{trk}}$ (d) L2 $\sum p_T^{(\mathrm{iso})} / \sum p_T^{(\mathrm{core})}$

Figure 4.4: Comparison of data events recorded in the first bunch of the train ("bunch 0") with the events recorded in the last bunch ("bunch 7") during period I. No difference which might have been attributed to out-of-time pile-up is visible. See section 4.5 for the variable definition.

transverse energy reconstructed at EF are compared between scenarios with and without pile-up. Note that two effects can be observed there: a small shift of the E_T towards higher values of transverse energy and wider E_T distribution.

The existence of E_T "turn-on" is caused in the first place by the requirement of 5 GeV at L1 (implicitly contained in EF_tauNoCut requirement: without it, the distribution would be exponentially falling from the maximum at zero) and the E_T distribution shift is caused by different sizes of cones used for energy calculation: it is 0.2×0.2 for L1 and 0.4×0.4 for EF. The outer region is more affected by random pile-up energy deposits than the core region (assuming random distribution of pile-up contribution, the outer region has 3 times the area of the core). In the E_T distributions for the background QCD dijets the less steep rise of the transverse energy values with pile-up is very prominent. The QCD jets tend to be wide objects spreading over the whole 0.4×0.4 window of EF even without pile-up: this results in quite sharp turn-on. However, with the additional pile-up contribution, it is possible that some of the jets which would have been rejected at L1, are accepted and sent to HLT. Nevertheless, those jets tend to be small and not so wide, so the reconstructed EF transverse energy is also smaller so the E_T distribution turn-on becomes less steep.

The presence of pile-up also increases the number of reconstructed tracks (fig. 4.7) and

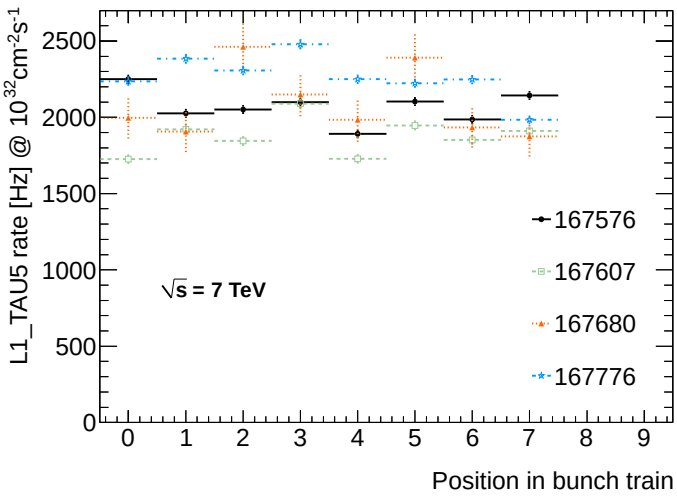

Figure 4.5: Average partial rate of L1_TAU5 (before prescale) as a function of position in a bunch train. The rates from different run were normalized to the same inst. luminosity of 10^{32} cm^{-2}s^{-1}. Events from bunch trains shorter than 8 bunches were excluded from the plot. The plotted error is statistical only. The total rate of L1_TAU5 in a given run is always an integral over all bins.

vertices[5] (fig. 4.8).

In order to obtain a better signal efficiency, some additional cuts are applied besides energy threshold to reject pure QCD interactions which are the main background for hadronic τ's. The tau lepton decays to few highly collimated hadrons, while quarks and gluons tend to form large jets with many particles. Therefore, the narrowness of the jet is the main feature exploited by tau trigger and there are several variables both at L2 and EF that measure the width of the jet using inputs from the tracking detector and the calorimeter.

The shape variables depend on the τ candidate transverse energy [99] and as shown in fig. 4.6, pile-up changes the energy distribution. Therefore, in order to have fair comparison, the shape variables are plotted only for candidates with transverse energy 15 GeV $< E_T <$ 40 GeV.

The width of the jet in the calorimeter is measured by a variable called *EM radius* defined in section 2.3.1. It is used both at EF and L2. Events with pile-up have additional energy deposits in the calorimeter coming from the minimum bias collisions (in-time pile-up) and from previous events (out-of-time pile-up). Some of them are inevitably placed in the same area as candidate tau jet. Those near, yet off-axis energy clusters not coming from the primary interaction make the candidate jet look wider. This is illustrated in fig. 4.9 that shows the shift in distributions of $\mathcal{R}_{\mathrm{EM}}$ at EF when pile-up is present.

One can easily extend the definition of $\mathcal{R}_{\mathrm{EM}}$ to include also energy deposited in hadronic calorimeter to get variable called *calorimetric radius* ($\mathcal{R}_{\mathrm{calo}}$) which has been defined in section 2.3.1. Although this variable has similar performance as $\mathcal{R}_{\mathrm{EM}}$, it should be more stable against pile-up. This effect can be caused by the fact that hadrons from minimum bias tend to be quite soft and not all of them reach the hadronic calorimeter. The calorimeter radius distribution is depicted in fig. 4.10.

Another useful property for selecting τ jets is the isolation in calorimeter. Then it is possible to use a variable called *centrality fraction* f_{core} defined in section 2.3.1. The idea behind this variables is that τ jets should deposit most of their energy in the core region while the isolation

[5]This applies only to offline reconstruction. There is never more than one vertex reconstructed at EF available at tau trigger, cf. discussion in section 4.5.2.

region would be relatively empty. Pile-up affects both the core and the isolation region and tend to smear the difference between them, thus making isolation variables less useful. The effect of pile-up on the centrality fraction distribution at EF is shown in fig. 4.11.

The data from the inner detector can be used to construct variables similar to those discussed above, based on the tracks instead of on the calorimeter cells. The size of the τ jet can be quantified by the *tracking radius* ($\mathcal{R}_{\text{trk}}$) (see section 2.3.1 for full definition). Tracking radius is much more stable against pile-up than the calorimeter based variables. When tracks from τ candidates are reconstructed, a vertex constraint is applied demanding that all tracks originate from the same region and most of the pile-up tracks from different vertices do not pass that constraint. The effect of pile-up on the distributions of $\mathcal{R}_{\text{trk}}$ for signal and background is shown in fig. 4.12.

Finally, one can exploit τ jet isolation with tracks in the similar way as f_{core} does with the cells in the calorimeter using the variable $\sum p_T^{(\text{iso})} / \sum p_T^{(\text{core})}$ defined in section 2.3.2. The track isolation is also quite stable against pile-up: although there is no explicit vertex constraint at L2, the requirement of track proximity in $\phi \times \eta$ space selects only tracks which originates close to each other and thus ignores tracks not coming from the tau decays. Also, the lower p_T track is quite high at L2 (1.5 GeV), so a lot of soft tracks from pile-up are not considered. The distribution of $\sum p_T^{(\text{iso})} / \sum p_T^{(\text{core})}$ is presented in fig. 4.13.

This is by far not exhaustive list of the variables used for selection and identification of hadronic τ leptons, this can be found together with more rigorous definitions in [72, 23, 99].

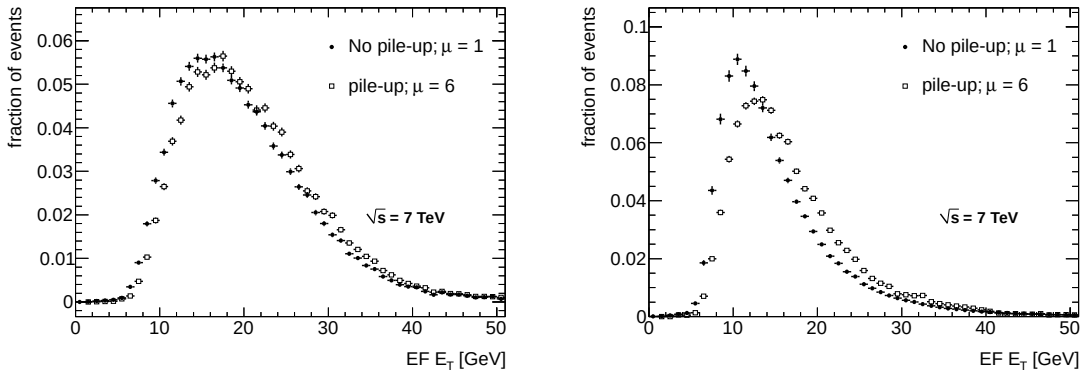

(a) τ candidates from W$\rightarrow \tau\nu$

(b) τ candidates from QCD dijets

Figure 4.6: Transverse energy reconstructed at EF with and without pile-up. Fig. 4.6(a) shows the distribution for signal events, fig. 4.6(b) for background events.

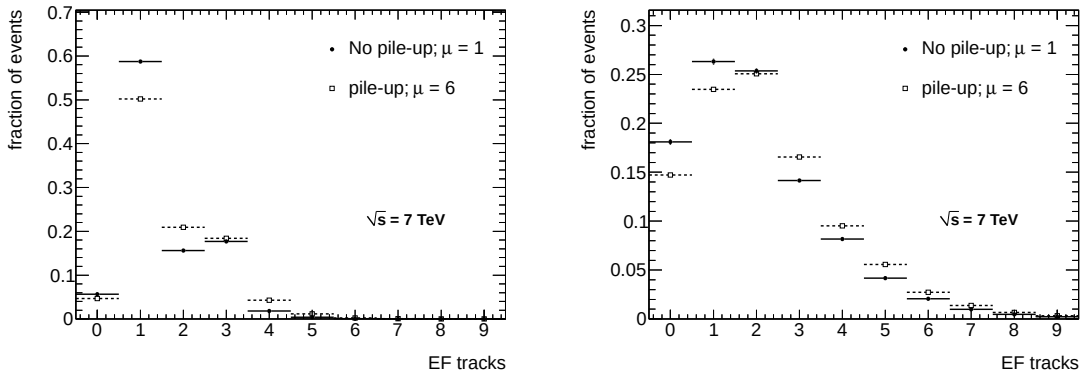

(a) τ candidates from W$\rightarrow \tau\nu$ (b) τ candidates from QCD dijets

Figure 4.7: Number of "loose tracks" ([73]) attached to a τ candidate at EF with and without pile-up. Fig. 4.7(a) shows the distribution for signal events, fig. 4.7(b) for background events.

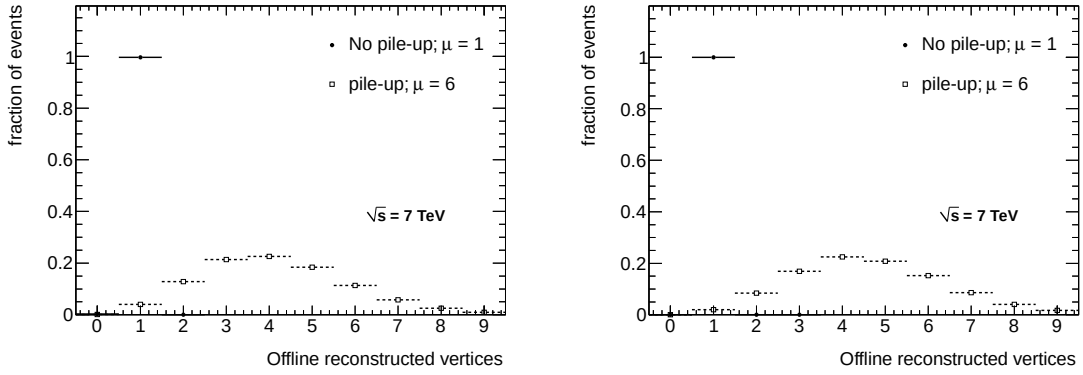

(a) τ candidates from W$\rightarrow \tau\nu$ (b) τ candidates from QCD dijets

Figure 4.8: Number of vertices reconstructed during offline processing in events with and without pile-up containing at least one τ candidate. Fig. 4.8(a) shows the distribution for signal events, fig. 4.8(b) for background events.

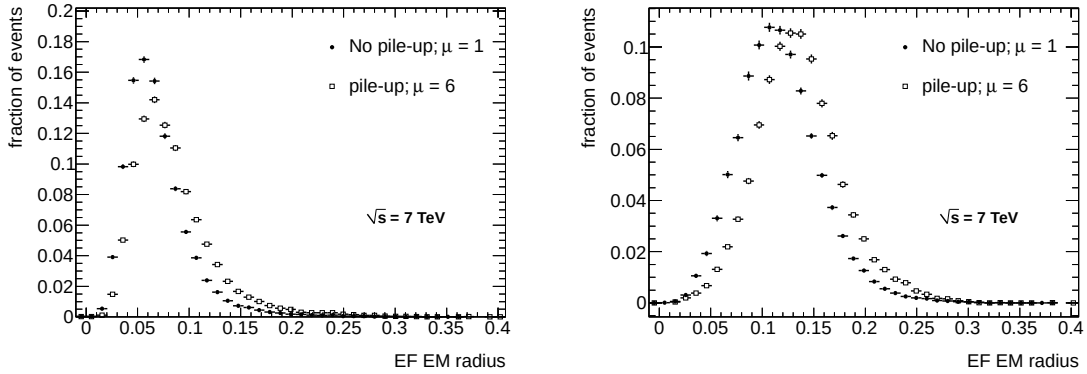

(a) τ candidates from W$\rightarrow \tau\nu$ (b) τ candidates from QCD dijets

Figure 4.9: EM radius reconstructed at EF with and without pile-up. Fig. 4.9(a) shows the distribution for signal events, fig. 4.9(b) for background events in the range 15 GeV $< E_T <$ 40 GeV.

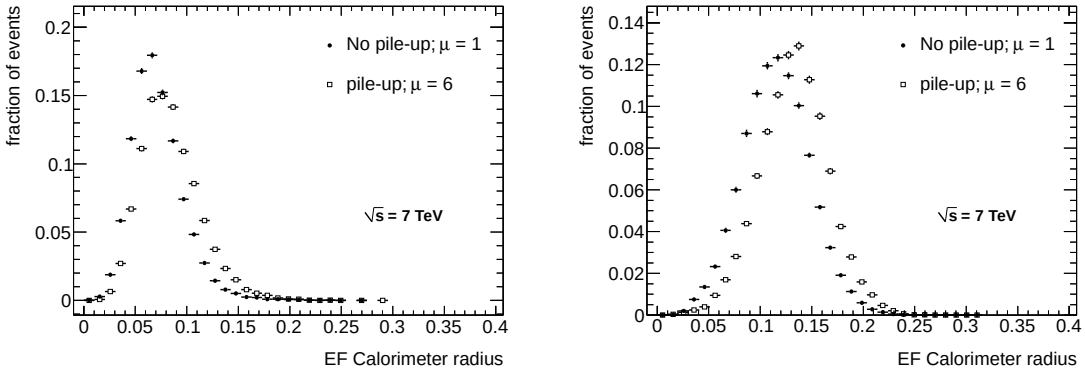

(a) τ candidates from W$\rightarrow \tau\nu$ (b) τ candidates from QCD dijets

Figure 4.10: Calorimeter radius reconstructed at EF with and without pile-up. Fig. 4.10(a) shows the distribution for signal events, fig. 4.10(b) for background events in the range 15 GeV $< E_T <$ 40 GeV.

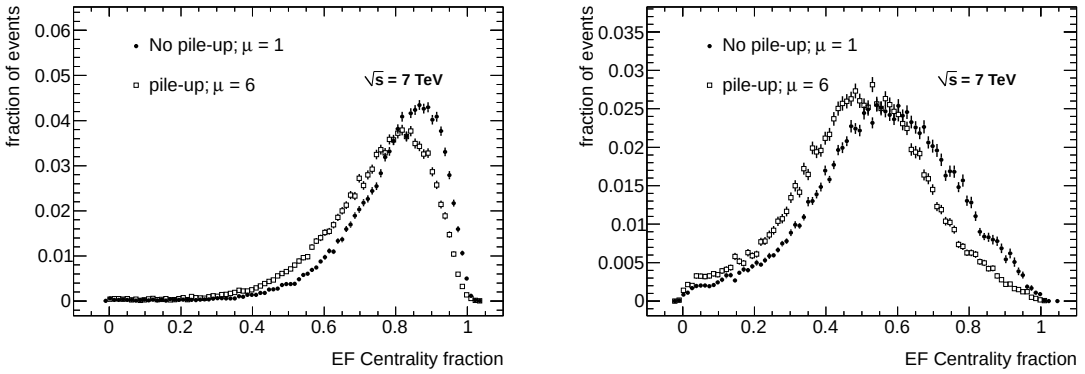

(a) τ candidates from W$\rightarrow \tau\nu$ (b) τ candidates from QCD dijets

Figure 4.11: Centrality fraction reconstructed at EF with and without pile-up. Fig. 4.11(a) shows the distribution for signal events, fig. 4.11(b) for background events in the range 15 GeV $< E_T <$ 40 GeV.

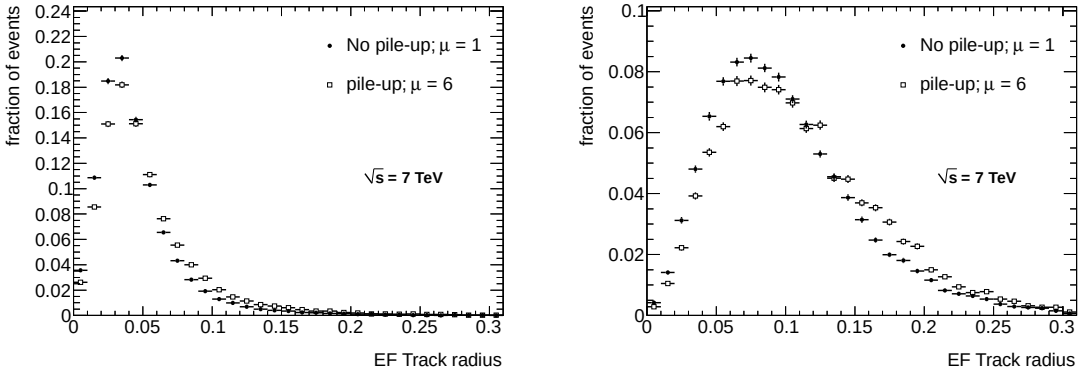

(a) τ candidates from W$\rightarrow \tau\nu$ (b) τ candidates from QCD dijets

Figure 4.12: Track radius reconstructed at EF with and without pile-up. Fig. 4.12(a) shows the distribution for signal events, fig. 4.12(b) for background events in the range 15 GeV $< E_T <$ 40 GeV.

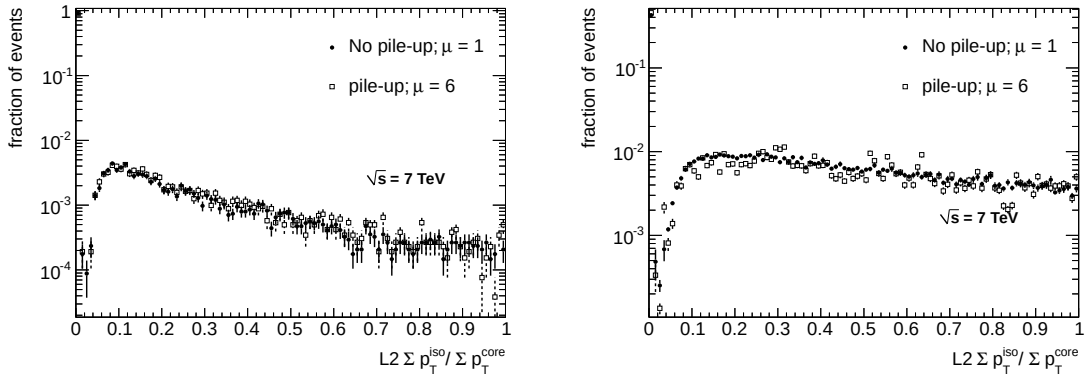

(a) τ candidates from W$\rightarrow \tau\nu$ (b) τ candidates from QCD dijets

Figure 4.13: $\sum p_T^{(\mathrm{iso})} / \sum p_T^{(\mathrm{core})}$ reconstructed at L2 with and without pile-up. Fig. 4.13(a) shows the distribution for signal events, fig. 4.13(b) for background events in the range 15 GeV $< E_T <$ 40 GeV.

4.5.2 EF and Offline

The variables used for tau identification in the offline analysis are the same as the ones used at EF for selecting tau candidates and it is desirable to check that the values of these observables are similar for EF and offline. This section shows that pile-up affects the offline-reconstructed variables in a similar way it affects EF, however, the effect is less pronounced. This leads to a slightly decreased trigger efficiency with respect to the offline reconstruction with pile-up. Fig. 4.14 shows the comparison of the distributions of $\mathcal{R}_{\text{calo}}$. There is a noticeable shift in the EF distributions towards more energetic and wider τ candidates, different from the from offline distributions with pile-up present. For events without pile-up the EF and offline distributions lie on top of each other.

The difference can be caused by various aspects: from the difference in algorithms used at EF and offline reconstruction and/or from different inputs. First, tau offline reconstruction uses the anti-k_T algorithm to reconstruct tau jets from cells, while there is no jet reconstruction at EF. Both offline and EF are reconstructing topo clusters out of the cells. However, EF uses only the cells inside the RoI, while offline uses the cells from the whole calorimeter which leads to a difference at the edges of the RoI. Also, the noise treatment is different because offline the most up-to-date calibration which is not known at the time of triggering. This can lead to a different cell lists at EF and offline, affecting the τ direction reconstruction.

Secondly the EF cell E_T is calculated by the calorimeter read-out electronics, while during offline reconstruction the energy is recalculated from raw cell signals, with the most up-to-date calibration, thus providing more precise result. Yet another source of difference in the E_T calculation between EF and offline reconstruction is the different cell list. The changes in the reconstructed energy as a function of the number of offline reconstructed vertices are shown in figs. 4.15 and 4.16.

After the study presented in this chapter has been concluded, the first efforts for a treatment of a pile-up noise had been conducted in ATLAS both in the offline reconstruction and on the trigger level[6]. However, in the samples used at this study, there is no correction for pile-up noise applied neither in data nor in the Monte Carlo samples. The exception is offline reconstruction of MC samples with pile-up: there the default unoptimized correction is applied - but its effect is very small as it is shown in figs. 4.15 and 4.16.

A mismatch in the energy calculation can also affect the distributions of $\mathcal{R}_{\text{trk}}$ because the axis, to which the track distance is calculated, is determined as the barycenter of the energy of the cells belonging to the τ candidate. However, also the tracking algorithm is different - during offline processing, the full vertexing is being done, while at EF, only one vertex is reconstructed from the tracks in the RoI, leading to a biased track-to-vertex association and more parasitic tracks being included in the τ object at EF. This is presented in figs 4.17 and 4.18 that show the number of fake tracks[7] per offline or EF object as a function of momentum or pseudorapidity for 3 different scenarios. The first one are events with no-pileup. The second (third) are events which have at least 4 (7) reconstructed vertices selected from the pile-up sample. Without pile-up, the fake rate (and also tracking efficiency) is smaller at EF, but with an increased number of collisions in an event, the number of fake tracks is increasing faster at EF than at offline. The fake tracks induced by pile-up are mostly soft (below 2 GeV) and have no particular dependence on pseudorapidity.

As seen in fig. 4.17, the lower cut on the track associated with the reconstructed τ object is 1 GeV [99] and most of the "additional" (compared to no pile-up) fake tracks are in the

[6]Pile-up noise is being treated with by applying an additional correction to the calorimeter energy calibration.

[7]Fake track is a reconstructed track which could not be matched to a true charged τ decay product within $\Delta R < 0.1$.

1-2 GeV momentum region. One can be therefore inclined to increase the lower cut to e.g. 2 GeV. However, although this makes track-based variables more stable against pile-up, it also decreases the discrimination power of such variables (the difference between QCD and τ jets is smaller when looking only on tracks with 2 GeV and more).

Altogether, pile-up exploits and magnifies the existing differences between the EF and offline event reconstruction. Those differences will increase as a function of pile-up and will form a significant part of trigger systematic error in the 2011 LHC run. This note does not address this but rather the change of the trigger variables and how to optimize the selection.

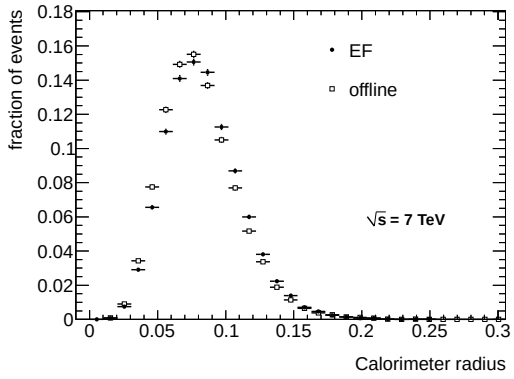

(a) W→ $\tau\nu$ with pile-up

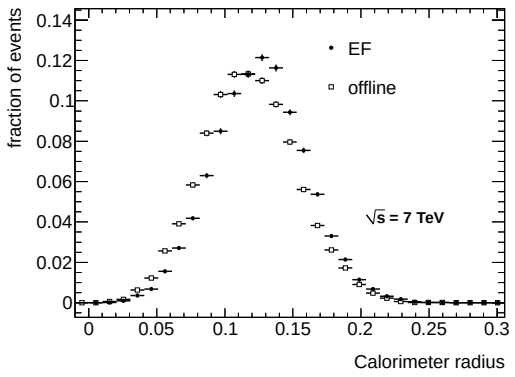

(b) QCD dijets with pile-up

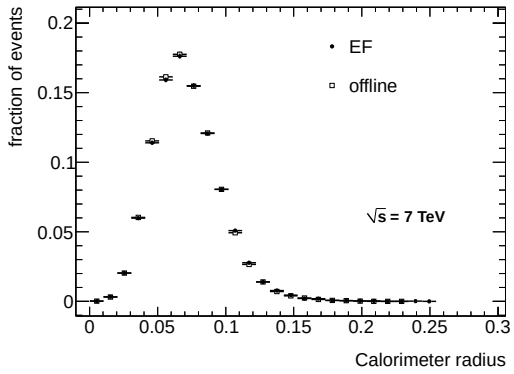

(c) W→ $\tau\nu$ without pile-up

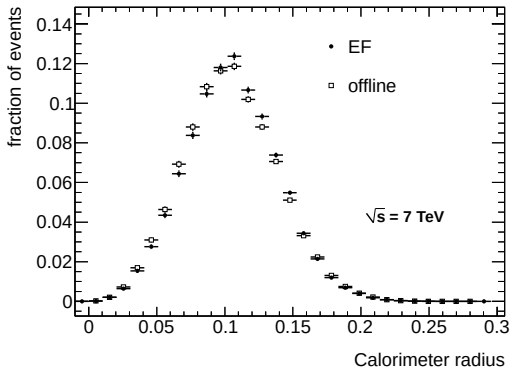

(d) QCD dijets without pile-up

Figure 4.14: Calorimeter radius reconstructed at EF and offline with and without pile-up. Figs. 4.14(a) and 4.14(c) show the distribution for signal events, Figs. 4.14(b) and 4.14(d) show the background events.

4.5.3 Effect of additional collisions on tau trigger performance

The previous section showed that distributions of the variables used for the trigger selection change due to pile-up and so it is important to check how the trigger performance would be affected. As the τ candidates become more energetic and the shower shapes wider, one can expect two competing effects: increase in trigger acceptance due to more candidates passing energy threshold, but also decrease caused by failed shape cuts on the narrowness and isolation. This results in a decrease in the signal acceptance (i.e. more signal events are rejected in events with pile-up) and an increase in the trigger rate (i.e. more background events are allowed to pass). It is caused by

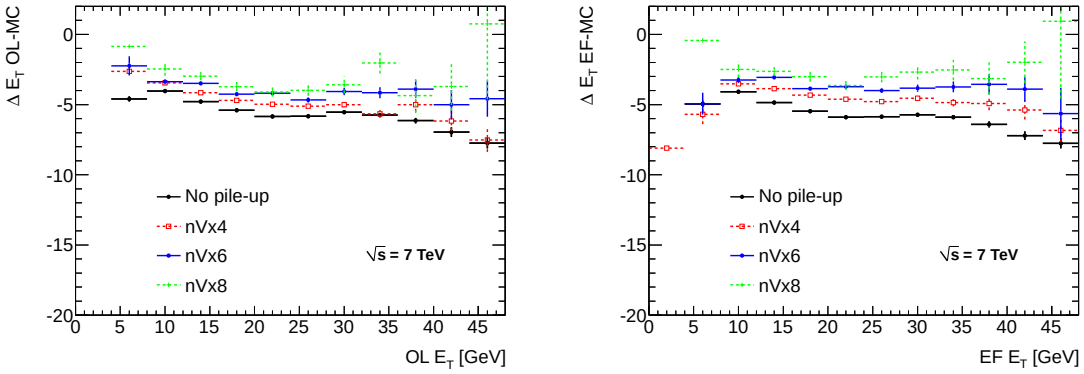

(a) Offline (b) Event filter

Figure 4.15: Difference between reconstructed transverse energy and true visible transverse momentum as a function of reconstructed momentum for different amount of vertices in the $W \to \tau\nu$ sample. There is a systematic increase of 0.3 GeV per vertex for offline and 0.4 GeV per vertex for EF. The reconstructed energy is at EM scale.

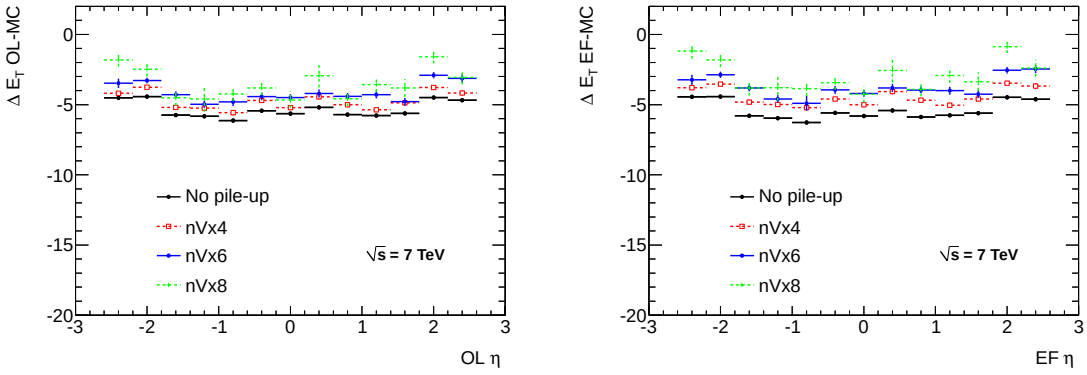

(a) Offline (b) Event filter

Figure 4.16: Difference between reconstructed transverse energy and true visible transverse momentum as a function of reconstructed pseudorapidity for different amount of vertices in the $W \to \tau\nu$ sample. There is a systematic increase of 0.3 GeV per vertex for offline and 0.4 GeV per vertex for EF. The increase does not seem to depend on pseudorapidity. The reconstructed energy is at EM scale.

- Upwards shift in all energies. This is documented and discussed in fig. 4.6. Because the QCD background E_T distribution is steeper than the signal τ's from weak boson decays, more background passed the E_T threshold.
- The pile-up energy is flatly distributed over the calorimeter. This results in a relative increase of energy in the outer cone with respect to the core region compared to the situation without pile-up. Consequently, all shape variables which are energy weighted, become larger as there is now more energy outside the core. The shift is largest for narrow topologies which tend to have all energy concentrated in the core and only negligible deposits outside.

The result of both effects is that the separation between signal and background is smaller.

The rate increase, however, is not caused by QCD jets becoming more "tau-like" (actually, the opposite is true because QCD jets also became wider), but because of higher chance of

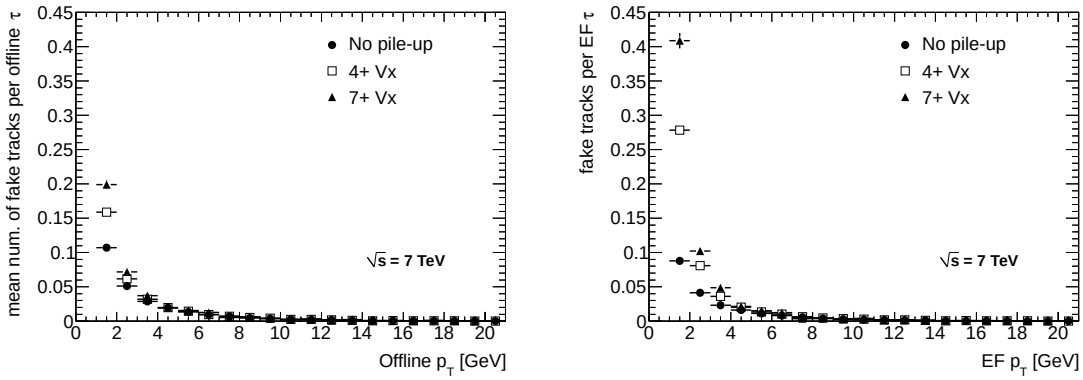

(a) Offline (b) Event filter

Figure 4.17: Average number of fake tracks associated to the offline or event filter τ object as a function of the fake track momentum for no pile-up and 2 different pile-up scenarios. There is a significant difference in stability between the EF and offline tracking. The events are from $W \to \tau\nu$ sample.

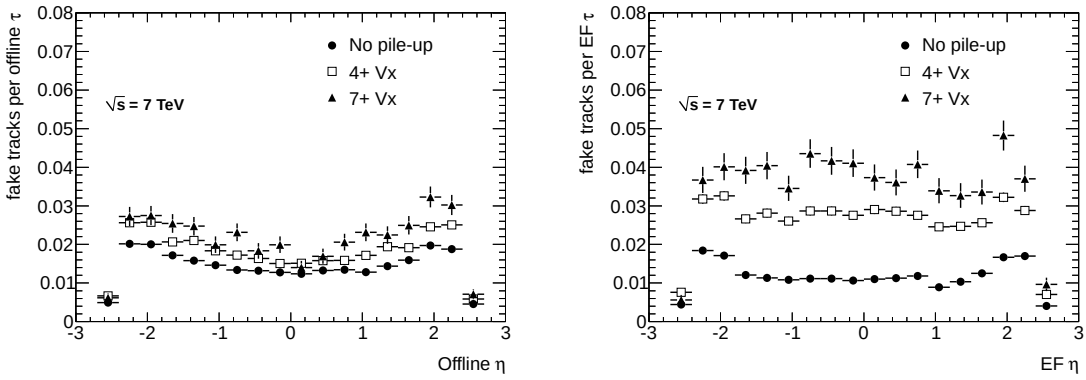

(a) Offline (b) Event filter

Figure 4.18: Average number of fake tracks associated to the offline or event filter τ object as a function of the fake track pseudorapidity for no pile-up and 2 different pile-up scenarios. There is a significant difference in stability between the EF and offline tracking but it is not dependent on η. The events are from the $W \to \tau\nu$ sample.

producing QCD jet by having more collisions per event. Therefore, although chance that trigger would accept a QCD jet is mostly decreased with pile-up[8], the average amount of jets in an event is higher so also the chance of event to be accepted is in the end increased with respect to events without pile-up. This is the cause of the trigger rate increase. Tabs. 4.5 through 4.8 present trigger acceptance for various signal and background MC samples, with and without pile-up.

Four trigger chains are selected as performance benchmarks: tau16_loose, tau16_medium, tau29_loose and tau50_medium. The numbers in the name correspond to the transverse energy thresholds required at EF.

Similar to section 4.5.2, two pile-up scenarios are considered: events with 4 and more (7 and more) vertices, denoted in plots as "4+ Vx" ("7+ Vx"). The second set is a subset of the first one and both are subsets of the sample listed in tabs. 4.1 and 4.2. The cuts defining the studied

[8]Except for the very soft jets that get energy boost from pile-up and can then pass the trigger E_T cuts.

chains are listed in tab. 4.4.

The causes of signal efficiency loss have been already discussed in the previous sections. Also, due to the increasing difference between the EF and offline reconstructed objects one can expect a decreased trigger efficiency with respect to the offline reconstructed objects. Tabs. 4.9 and 4.10 show the efficiency with respect to the offline objects identified by the tau selection criteria as loose or medium, respectively [99]. The efficiency change as a function of the offline transverse energy is shown in fig. 4.19. Note, that in the lowest energy bins the efficiency is actually increased due pile-up effects. These are events which narrowly missed the energy cut without pile-up, but are passing with pile-up due to additional energy and the fact that on average the increase of the EF E_T is larger than the offline one (fig. 4.15).

Tab. 4.11 shows the trigger rates for events with and without pile-up. The rates are given for two luminosity scenarios with the the pile-up conditions (assuming the LHC machine parameter settings for the 2011 run) and one scenario without pile-up. Tab. 4.11 shows that the L1 rate increases slightly faster than luminosity. At the HLT, the rates of triggers with E_T threshold of 16 GeV are increasing more slowly than the luminosity. The chain with threshold of 29 GeV is increasing slightly faster than luminosity, however. The rate of EF items is increasing more slowly with the luminosity than that of L2 items.

It is possible to compare this rate predictions made about a year before the actual pile-up appeared with data. The numbers in tab. 4.11 somehow overestimate the actual rate for the given instantaneous luminosity, but one should have in mind, that 1) the cross-section used for the rate calculation is from Pythia, that tends have higher predictions on low-p_T jet cross-sections that is actually observed in ATLAS [100] and 2) no correction factors have been applied to the trigger efficiency to correct for the imperfect trigger simulation. With these consideration the rates predicted by tab. 4.11 are compatible with those observed in data.

The right three columns of tab. 4.11 shows the change in signal rate. It is increasing more slowly than the total rate, so signal-to-background ratio is dropping by about 1/3 when going from the 1 Vx scenario to 4+ Vx scenario. This is caused by the concurrent drop in signal efficiency and increase in minimum bias event acceptance as discussed above. This trend is observed also for higher pile-up, although for tau29, which accepts only tails of W$\rightarrow \tau\nu$ distribution, the dependence on the number of additional collisions is quite weak: both signal and background rate increase roughly with the same pace.

Tab 4.11 can be also used to estimate the effect of pile-up on the results from physics analysis. For example, analyses using trigger EF_tau29_loose would collect 6.2 times more events during the same time in scenario "4+ Vx" as in scenario "1 Vx". However, the number of signal events would increase only by a factor of 4.8. Therefore the ratio of signal/$\sqrt{\text{background}}$ would change by a factor of $(4.8/6.2) \times \sqrt{6.2} = 1.9$. The significance of a result increases only three quarters as much as it would do if the same amount of data without pile-up would be used.

Finally, tab. 4.11 can be used to calculate the relative rate between L1/L2 and L2/EF changes with pile-up. The HLT rejection is increasing with pile-up for all chains as a monotonous function of pile-up.

	tau16_loose		tau16_medium		tau29_loose		tau50_medium	
	1 Trk	> 1 Trk	1 Trk	> 1 Trk	1 Trk	> 1 Trk	1 Trk	> 1 Trk
EF $\mathcal{R}_{\mathrm{EM}}$	< 0.094	< 0.106	< 0.080	< 0.092	< 0.072	< 0.088	< 0.05	< 0.07
EF $\mathcal{R}_{\mathrm{trk}}$	< 0.096	< 0.082	< 0.076	< 0.062	< 0.062	< 0.050	< 0.03	< 0.03
EF E_T	> 16	> 16	> 16	> 16	> 29	> 29	> 50	> 50
L2 $\mathcal{R}_{\mathrm{EM}}$	< 0.0162		< 0.0124		< 0.013		< 0.009	
L2 $\frac{\sum p_T^{(\mathrm{iso})}}{\sum p_T^{(\mathrm{core})}}$	< 0.1		< 0.1		< 0.1		< 0.05	
L2 $\mathrm{N}_{\mathrm{trk}}^{(\mathrm{core})}$	1-100		1-7		1-4		1-7	
L2 $E_T^{(\mathrm{nar})}$	> 7.7		> 9.0		> 13.9		> 35	

Table 4.4: Cuts on HLT variables for four different trigger items. Note, that single prong are all candidates with exactly one track at EF, while multiprongs have more tracks. The transverse energy cut at L2 and EF is in GeV.

trigger	sample	1 Vx	4+ Vx	7+ Vx
L1_TAU6 (seeding tau16_loose and tau16_medium)	Minimum Bias	4.9×10^{-3}	0.035	0.047
	QCD jets J0	0.012	0.046	0.065
	QCD jets J1	0.17	0.20	0.22
	QCD jets J2	0.71	0.72	0.73
	QCD jets J3	0.98	0.98	0.98
L1_TAU11 (seeding tau29_loose)	Minimum Bias	1.0×10^{-3}	6.8×10^{-3}	9.4×10^{-3}
	QCD jets J0	-	7.0×10^{-3}	0.011
	QCD jets J1	0.036	0.043	0.049
	QCD jets J2	0.40	0.41	0.42
	QCD jets J3	0.92	0.92	0.92
L1_TAU20 (seeding tau50_medium)	Minimum Bias	1.8×10^{-4}	1.1×10^{-3}	1.4×10^{-3}
	QCD jets J0	-	1.1×10^{-3}	1.7×10^{-3}
	QCD jets J1	2.6×10^{-3}	3.7×10^{-3}	4.5×10^{-3}
	QCD jets J2	0.12	0.12	0.13
	QCD jets J3	0.72	0.72	0.72

Table 4.5: Monte Carlo estimates of the effect of in-time pileup on background acceptance of different L1 trigger items. The numbers show the fraction of accepted events for a given trigger chain and background type (defined in tab. 4.2). The statistics of the J0 sample was too small for the scenario without pile-up for the two higher thresholds. The statistical uncertainty of all entries varies between 0.02% (TAU6 acceptance for J3 without pile-up) and 19.8% (TAU20 acceptance for J0 for case with 7 vertices).

trigger	sample	1 Vx	4+ Vx	7+ Vx
L2_tau16_loose	Minimum Bias	1.6×10^{-3}	9.1×10^{-3}	0.012
	QCD jets J0	3.6×10^{-3}	0.013	0.018
	QCD jets J1	0.056	0.058	0.061
	QCD jets J2	0.23	0.22	0.21
	QCD jets J3	0.44	0.43	0.43
L2_tau16_medium	Minimum Bias	1.1×10^{-3}	5.8×10^{-3}	7.5×10^{-3}
	QCD jets J0	2.0×10^{-3}	7.5×10^{-3}	0.010
	QCD jets J1	0.041	0.039	0.040
	QCD jets J2	0.18	0.16	0.15
	QCD jets J3	0.38	0.36	0.34
L2_tau29_loose	Minimum Bias	3.2×10^{-4}	2.0×10^{-3}	2.7×10^{-3}
	QCD jets J0	-	2.1×10^{-3}	3.4×10^{-3}
	QCD jets J1	0.011	0.012	0.013
	QCD jets J2	0.13	0.12	0.11
	QCD jets J3	0.36	0.35	0.34
L2_tau50_medium	Minimum Bias	1.8×10^{-5}	7.7×10^{-5}	1.1×10^{-4}
	QCD jets J0	-	1.4×10^{-4}	2.6×10^{-4}
	QCD jets J1	4.8×10^{-5}	1.7×10^{-4}	3.3×10^{-4}
	QCD jets J2	0.010	0.010	0.011
	QCD jets J3	0.15	0.14	0.13

Table 4.6: Monte Carlo estimates of the effect of in-time pileup on the background acceptance of different L2 trigger items. The numbers show the fraction of accepted events for a given trigger chain and background type (defined in tab. 4.2). The statistics of the J0 sample was too small for the scenario without pile-up for the two higher thresholds. The statistical uncertainty of all entries varies between 0.2% (tau16 acceptance for J3 without pile-up) and 58.2% (tau50 acceptance for J0 for case with 7 vertices).

trigger	sample	1 Vx	4+ Vx	7+ Vx
EF_tau16_loose	Minimum Bias	5.1×10^{-4}	2.4×10^{-3}	3.0×10^{-3}
	QCD jets J0	6.6×10^{-4}	2.6×10^{-3}	3.6×10^{-3}
	QCD jets J1	0.020	0.015	0.012
	QCD jets J2	0.12	0.086	0.071
	QCD jets J3	0.31	0.28	0.25
EF_tau16_medium	Minimum Bias	3.0×10^{-4}	1.4×10^{-3}	1.6×10^{-3}
	QCD jets J0	3.6×10^{-4}	1.4×10^{-3}	1.5×10^{-3}
	QCD jets J1	0.012	7.1×10^{-3}	5.5×10^{-3}
	QCD jets J2	0.073	0.047	0.037
	QCD jets J3	0.21	0.17	0.14
EF_tau29_loose	Minimum Bias	7.4×10^{-5}	4.6×10^{-4}	5.4×10^{-4}
	QCD jets J0	-	4.9×10^{-4}	6.2×10^{-4}
	QCD jets J1	1.5×10^{-3}	1.5×10^{-3}	1.5×10^{-3}
	QCD jets J2	0.044	0.030	0.024
	QCD jets J3	0.19	0.15	0.13
EF_tau50_medium	Minimum Bias	4.3×10^{-6}	-	-
	QCD jets J0	-	-	-
	QCD jets J1	-	-	-
	QCD jets J2	2.4×10^{-3}	1.7×10^{-3}	1.7×10^{-3}
	QCD jets J3	0.044	0.031	0.025

Table 4.7: Monte Carlo estimates of the effect of in-time pileup on background acceptance of different EF trigger items. The numbers show the fraction of accepted events for a given trigger chain and background type (defined in tab. 4.2). The statistics of some samples was too small for the scenario without pile-up for the two higher thresholds. The statistical uncertainty of all entries varies between 0.2% (tau16 acceptance for J3 without pile-up) and 15.8% (tau50 acceptance for J2 for case with 7 vertices).

	W$\rightarrow \tau\nu$			A(800)$\rightarrow \tau\tau$		
	1 Vx	4+ Vx	7+ Vx	1 Vx	4+ Vx	7+Vx
L1_TAU6	0.24	0.25	0.25	0.87	0.87	0.88
L1_TAU11	0.14	0.14	0.15	0.86	0.87	0.87
L1_TAU20	0.042	0.043	0.043	0.86	0.86	0.86
L2_tau16_loose	0.19	0.18	0.17	0.84	0.83	0.83
L2_tau16_medium	0.18	0.16	0.14	0.84	0.82	0.82
L2_tau29_loose	0.11	0.10	0.10	0.84	0.82	0.82
L2_tau50_medium	7.4×10^{-3}	7.2×10^{-3}	7.3×10^{-3}	0.81	0.79	0.79
EF_tau16_loose	0.15	0.12	0.11	0.82	0.79	0.79
EF_tau16_medium	0.12	0.089	0.073	0.81	0.78	0.78
EF_tau29_loose	0.046	0.039	0.035	0.80	0.77	0.77
EF_tau50_medium	3.2×10^{-3}	2.7×10^{-3}	2.3×10^{-3}	0.74	0.70	0.69

Table 4.8: Monte Carlo estimates of the effect of in-time pileup on signal acceptance of different trigger chains. The numbers above show the fraction of accepted events for a given trigger chain and signal type (defined in tab. 4.1). The first three rows correspond to L1 seeds of the HLT chains in bottom 8 rows. The statistical uncertainty entries for W$\rightarrow \tau\nu$ with pile-up varies between 0.6% and 14.8%, for W$\rightarrow \tau\nu$ without pile-up it varies between 0.4% and 3.9%. The statistical uncertainty for all A(800)$\rightarrow \tau\tau$ entries is between 0.2% and 0.6%.

	loose			medium		
	1 Vx	4+ Vx	7+ Vx	1 Vx	4+ Vx	7+ Vx
L1_TAU6	0.70	0.73	0.74	0.70	0.73	0.75
L1_TAU11	0.42	0.45	0.50	0.42	0.46	0.51
L1_TAU20	0.13	0.15	0.16	0.13	0.15	0.17
L2_tau16_loose	0.59	0.59	0.57	0.61	0.61	0.60
L2_tau16_medium	0.55	0.53	0.51	0.57	0.56	0.54
L2_tau29_loose	0.35	0.36	0.38	0.36	0.38	0.40
L2_tau50_medium	0.023	0.027	0.031	0.024	0.026	0.032
EF_tau16_loose	0.49	0.46	0.43	0.51	0.49	0.47
EF_tau16_medium	0.41	0.35	0.31	0.44	0.39	0.36
EF_tau29_loose	0.15	0.16	0.15	0.16	0.17	0.17
EF_tau50_medium	0.011	0.011	0.010	0.011	0.012	0.011

Table 4.9: Monte Carlo estimates of the effect of in-time pileup on offline efficiency of different trigger chains. Left part of the table shows efficiency of a given trigger item with respect to reconstructed τ passing loose ID criteria. Right part refers to the medium ID. The τ candidates are from W$\rightarrow \tau\nu$ events. The first three rows correspond to L1 seeds of the HLT chains in bottom 8 rows. The statistical uncertainty entries for loose efficiency varies between 0.3% and 18.8%. For medium efficiency, the statistical uncertainty is 0.3% to 19.9%.

	loose			medium		
	1 Vx	4+ Vx	7+ Vx	1 Vx	4+ Vx	7+ Vx
L1_TAU6	1.0	1.0	1.0	1.0	1.0	1.0
L1_TAU11	0.99	0.99	0.99	0.99	0.99	0.99
L1_TAU20	0.97	0.98	0.98	0.97	0.98	0.98
L2_tau16_loose	0.97	0.97	0.96	0.98	0.97	0.97
L2_tau16_medium	0.97	0.96	0.96	0.97	0.97	0.96
L2_tau29_loose	0.96	0.96	0.95	0.97	0.96	0.96
L2_tau50_medium	0.92	0.91	0.91	0.92	0.92	0.96
EF_tau16_loose	0.94	0.93	0.92	0.95	0.94	0.94
EF_tau16_medium	0.93	0.92	0.91	0.94	0.93	0.92
EF_tau29_loose	0.92	0.90	0.90	0.93	0.92	0.91
EF_tau50_medium	0.83	0.81	0.80	0.85	0.84	0.83

Table 4.10: Monte Carlo estimates of the effect of in-time pileup on offline efficiency of different trigger chains. Left part of the table shows efficiency of a given trigger item with respect to reconstructed τ passing loose ID criteria. Right part refers to the medium ID. The τ candidates are from A(800)$\rightarrow \tau\tau$ events. The first three rows correspond to L1 seeds of the HLT chains in bottom 8 rows. The statistical uncertainty entries for loose and medium efficiency varies between 0.03% and 0.4%.

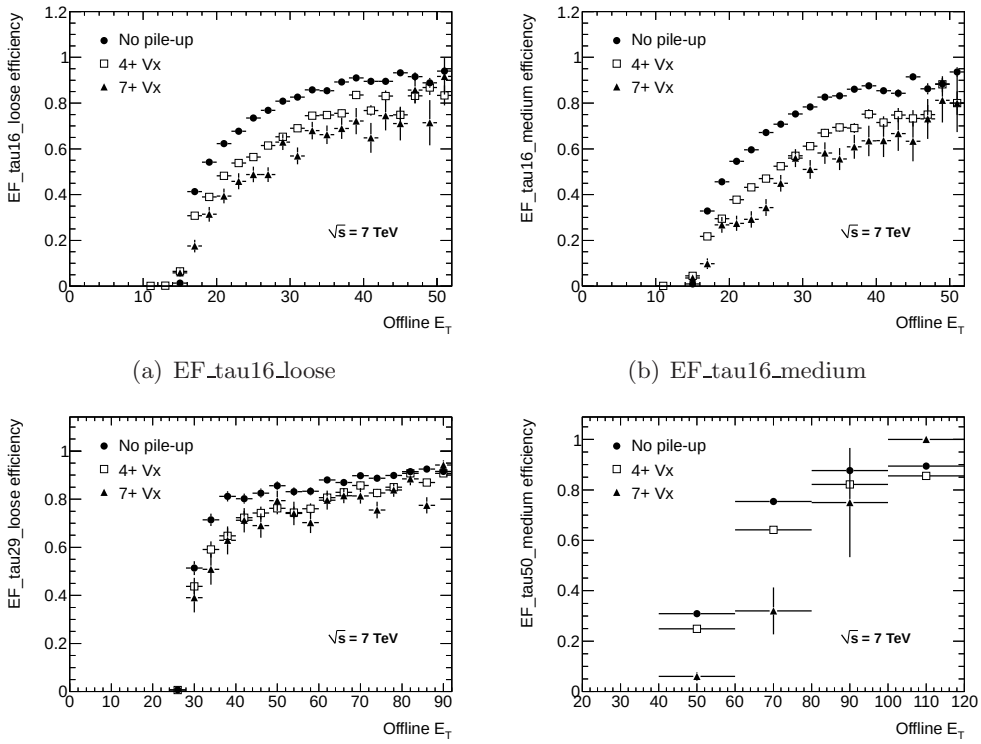

(a) EF_tau16_loose

(b) EF_tau16_medium

(c) EF_tau29_loose

(d) EF_tau50_medium

Figure 4.19: Fraction of offline reconstructed and identified events selected by different trigger chains as a function of the reconstructed E_T. In plots 4.19(a) and 4.19(c) loose offline ID tau identification criteria are used and plots 4.19(b) and 4.19(d) use medium offline ID selection. The τ candidates in plots 4.19(a) and 4.19(b) are from W$\rightarrow \tau\nu$ decays. Fig. 4.19(c) and 4.19(d) from A$\rightarrow \tau\tau$. Note the different E_T scale in fig. 4.19(c) and 4.19(d).

	Rates [Hz]			Signal rate [mHz]		
	1 Vx	4+ Vx	7+ Vx	1Vx	4+ Vx	7+ Vx
μ	1.0	5.6	7.6	1.0	5.6	7.6
inst. lumi. [10^{30}cm^{-2}s^{-1}]	50	280	380	50	280	380
L1_TAU6	14,341	101,176	138,634	108	623	840
L1_TAU11	2,887	19,759	27,462	62	361	504
L2_tau16_loose	4,673	26,705	35,118	86	448	557
L2_tau16_medium	3,177	16,982	21,858	78	393	480
L2_tau29_loose	925	5,923	7,856	49	261	339
EF_tau16_loose	1,490	6,998	8624	66	304	357
EF_tau16_medium	878	3,971	4690	55	224	246
EF_tau29_loose	215	1,341	1,563	21	99	119

Table 4.11: Effect of in-time pileup on the total rates and the rates from signal events for different trigger chains. The rates were estimated using minimum bias Monte Carlo and normalized to the luminosity of roughly 50×10^{30}cm^{-2}s^{-1} for the scenario without pile-up. The increase in the mean number of collisions - μ - brings increase in instantaneous luminosity as well, which is reflected in the top 2 rows to the table. The statistical error on the rates is between 0.3% and 9.2%. The error on signal rates is between 0.4% and 4.5%. In both cases, the statistical error is increasing from left to right and from top to bottom.

4.6 Selection optimization with pile-up

4.6.1 Offline selection optimization

Section 4.5 shows that the presence of additional collisions in an event leads to a clear degradation of the tau trigger performance. One can, however, improve the performance by adapting the selection to the new situation. This is the goal of this section. Obviously, it will be valid for only one particular case of pile-up and the optimization will have to be redone in case the pile-up level changes. The plots presented in 4.5.1 indicate that discrimination between signal and background using different cuts should be possible for pile-up with less than 10 interactions per event with a moderate loss in the trigger efficiency. For the pile-up higher than that, a dedicated simulation and additional study is necessary.

One of the main trigger goals is to maintain high efficiency with respect to offline: there is no use in triggering on events which obtain tau candidates which would be rejected by offline identification algorithms. So it is vital to have some knowledge of offline tau ID with pile-up. Unfortunately, at the time of writing of this note, no offline selection has been optimized for pile-up above the average of 3-4 collisions per event observed in the end 2010 run. Therefore the simple cut-based offline ID has been privately optimized for the purpose of this note for higher level of pile-up in order to provide estimate and benchmark of tau performance in pile-up environment. The trigger optimization would then try to match this optimized offline performance.

The offline optimization was performed using W$\rightarrow \tau\nu$ MC sample[9] with 6 collisions per event (the same as in the previous sections). The aim was to obtain a selection as simple as possible (i.e. with few variables). The tests done with the ROOT Toolkit for Multivariate Analysis (TMVA, [101]) showed that optimal selection is possible with just 2 variables: $\mathcal{R}_{\mathrm{cal}}$ and $\mathcal{R}_{\mathrm{trk}}$. This is presented in fig. 4.20 which show the performance of the variables defined in section 2.3.1. The variable referred to as "Et/Pt$_{\mathrm{lead}}$" in the plots is $1/f_{\mathrm{track}}$.

The procedure for finding the optimal set of variables is the following: At first several variables, which can be used for tau identification, are tested to find an optimal selection using rectangular cuts and also Boosted Decision Trees (BDT) for a comparison (this check should spot possible correlation in the variables which can be missed by cut-based approach). The performance is defined as a rejection for given efficiency and visualized with curves like those in fig. 4.20. This plot shows the backround efficiency (i.e. a probablity that background event is selected) as a function of the signal efficiency. Different curves correspond to different sets of variables used for the selection. The goal is to have backround efficiency as small as possible for a given signal efficiency. Therefore the lower the curve is, the better selection it corresponds.

Next, the variable which is performing worst according to BDT ranking is removed and TMVA is asked to find a new optimal selection. The new performance curve is compared with the old one and if does not change, another variable is removed. The whole process continues until removal of a variables leads to a performance loss. In this case one of the remaining variables is removed and performance is checked again. The process is repeated until removal of any variable leads to a performance loss.

In this way the smallest set of variables with following properties is constructed:

- The combined performance of the variables in the subset is the same or better than the combined performance of all used tau ID variables
- Removal of any variable from the subset leads to a significant performance loss (small drops compatible with statistical fluctuation were not considered)

[9] Because only sample was used, the selection is optimized for an E_T and η spectra typical for τ's from W. For more complex optimization, more samples will be needed.

Afterwards, the cuts are selected in such a way to obtain signal efficiency of 90% ("loose"), 70% ("medium") and 50% ("tight"). Different set of cuts are used for single- and multiprong τ candidates. The cut values and the corresponding efficiencies for τ's from W decays are displayed in tab. 4.12.

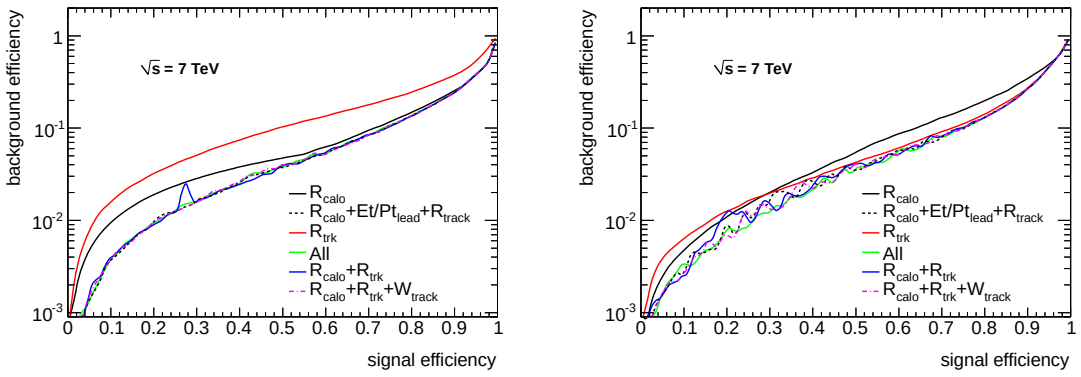

(a) 1-prong (b) multiprong

Figure 4.20: Comparison of the performance of different offline variables and their combinations in pile-up scenario. Left plot shows single prong τ candidates, while the other shows multi prong τ's. Both plot show that a combination of $\mathcal{R}_{\text{cal}}$ and $\mathcal{R}_{\text{trk}}$ is the best one or as-good-as any more complex variable combination.

	Loose		Medium		Tight	
	single prong	multi prong	single prong	multi prong	single prong	multi prong
$\mathcal{R}_{\text{cal}}$	< 0.13	< 0.18	< 0.10	< 0.18	< 0.08	< 0.18
$\mathcal{R}_{\text{trk}}$	< 0.18	< 0.10	< 0.10	< 0.06	< 0.10	< 0.05
efficiency	0.9	0.91	0.68	0.68	0.47	0.55

Table 4.12: Cuts on the offline variables optimized for a pile-up scenario with on average 6 pile-up events for 3 different efficiency requirements. The last row shows the corresponding signal efficiencies.

4.6.2 HLT selection optimization

Having defined the offline reference in the previous section, it is now possible to modify the HLT selection to select efficiently the offline τ candidates while keeping the trigger rates within the allocated bandwidth. Similarly to offline selection optimization, the first step is to find optimal subset of variables on which to cut. It is done exactly in the same way as described in section 4.6.1: start with all relevant variables and remove one by one until the state is reached when another removal would harm the performance. This variable evaluation is done at first separately for L2 and EF variables and afterwards with combined L2 and EF variables to check for possible correlations. The variables used in the optimization study are defined in sections 2.3.1 and 2.3.2.

During this study the performance of different combinations of variables is evaluated. $W \rightarrow \tau\nu$ hadronic decays are used as "signal" and for background the QCD samples J0, J1 and J2 (cf. tab. 4.2) reweighed according to their cross-section are used.

Fig. 4.21 depicts the performance of different combinations of L2 variables and shows that the most performing combination is the one using $\mathcal{R}_{\mathrm{EM}}$, $\mathcal{R}_{\mathrm{trk}}$, $\sum p_T^{(\mathrm{iso})} / \sum p_T^{(\mathrm{core})}$ (referred to as "iso/core" in the plot) and $\mathrm{N}_{\mathrm{trk}}^{(\mathrm{core})}$. $\mathcal{R}_{\mathrm{trk}}$ is defined at L2 in the same way as in EF and its distribution is shown in fig. 4.22. You can see that this variable is more stable against pile-up than its EF counterpart (cf. fig: 4.12). This is caused by higher p_T applied at L2 (1.5 GeV), so one gets less fakes (cf. fig. 4.17). On the other hand, the separation between signal and background is worse because the QCD jets tend to have more very low-p_T tracks then τ jets.

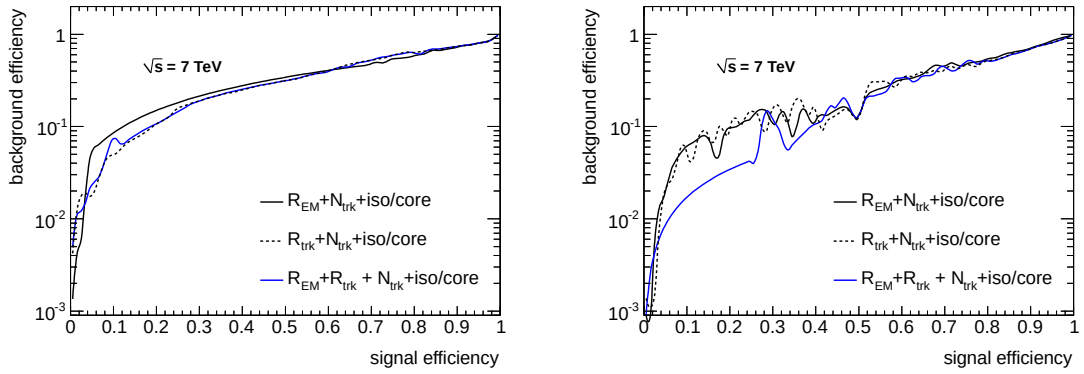

(a) 1-prong (b) multiprong

Figure 4.21: Comparison of the performance of different L2 variables and their combinations in pile-up environment. All L2 τ candidates have been matched to offline reconstructed τ's identified by medium identification criteria (defined in section 4.6.1). The left plot shows L2 τ candidates matched to offline single prong τ candidates, while the other shows the L2 τ's matched to offline multi prong τ's. Both plot show that combination of $\mathcal{R}_{\mathrm{EM}}$, $\mathcal{R}_{\mathrm{trk}}$, $\sum p_T^{(\mathrm{iso})} / \sum p_T^{(\mathrm{core})}$ and $\mathrm{N}_{\mathrm{trk}}^{(\mathrm{core})}$ is the best one for efficiency 0.4-0.6, which is expected at L2.

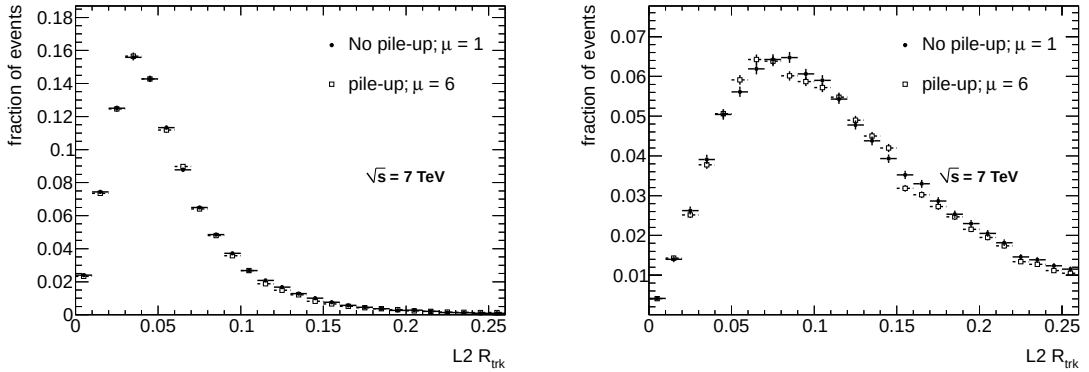

(a) L2 $\mathcal{R}_{\mathrm{trk}}$ of τ candidates from W$\rightarrow \tau\nu$ (b) L2 $\mathcal{R}_{\mathrm{trk}}$ of τ candidates from QCD dijets

Figure 4.22: $\mathcal{R}_{\mathrm{trk}}$ reconstructed at L2 with and without pile-up. Fig. 4.22(a) shows the distribution for signal events, fig. 4.22(b) for background events.

The optimization results for EF are very similar to those from the offline optimization. The performance is dominated by $\mathcal{R}_{\mathrm{trk}}$ and $\mathcal{R}_{\mathrm{EM}}$, but when using more variables it is actually possible to get slightly better rejection while keeping the efficiency. The additional variables are the track spread $\mathcal{W}_{\mathrm{trk}}$ and centrality fraction f_{core}.

Note, however, that the result above is fully valid only if EF would be allowed to make a decision about all events passing L1. However, the EF input is biased by the L2 selection. Therefore fig. 4.24 presents detailed comparison of $\mathcal{R}_{\mathrm{EM}}$ and $\mathcal{R}_{\mathrm{calo}}$ performance as well as comparison of $\mathcal{R}_{\mathrm{trk}}$ and $\mathcal{W}_{\mathrm{trk}}$. It clearly shows that it is more advantageous to cut on $\mathcal{R}_{\mathrm{calo}}$ instead of $\mathcal{R}_{\mathrm{EM}}$ and that there is no need of cutting on both $\mathcal{R}_{\mathrm{trk}}$ and $\mathcal{W}_{\mathrm{trk}}$: using $\mathcal{R}_{\mathrm{trk}}$ gives (almost) full performance and brings EF selection closer to offline which is using it as well.

To sum up, the resulting variables for EF selection are $\mathcal{R}_{\mathrm{trk}}$, $\mathcal{R}_{\mathrm{calo}}$ and f_{core}. Fig. 4.25 shows that those 3 variables indeed have best possible performance which is higher than performance of $\mathcal{R}_{\mathrm{trk}}$ and $\mathcal{R}_{\mathrm{calo}}$ alone.

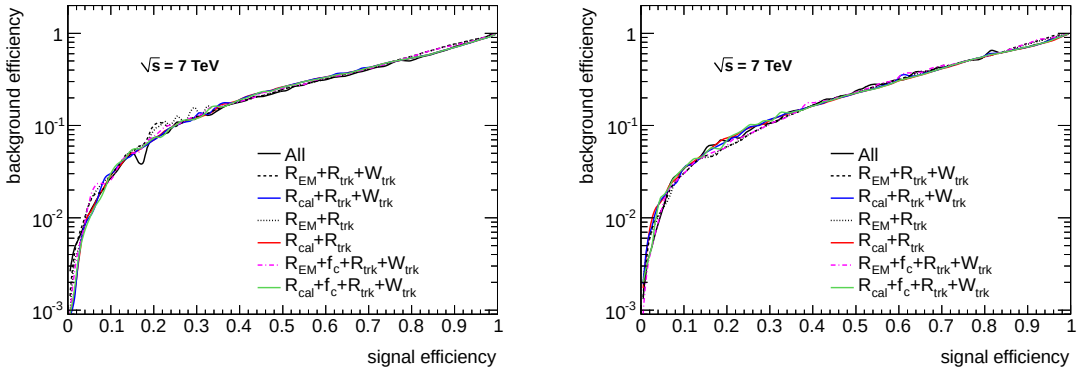

(a) 1-prong (b) multiprong

Figure 4.23: Comparison of the performance of different EF variables and their combinations in the pile-up environment. All EF τ candidates have been matched to offline reconstructed τ's identified by medium identification criteria (defined in section 4.6.1). The left plot shows EF τ candidates matched to offline single prong τ candidates, while the other one shows the EF τ's matched to offline multi prong τ's. Both plot show that combination of $\mathcal{R}_{\mathrm{calo}}$, $\mathcal{R}_{\mathrm{trk}}$, $\mathcal{W}_{\mathrm{trk}}$ and f_{core} (dark green line) is the best one for most of the efficiency range.

Having identified variables which are optimal for HLT selection in this pile-up scenario, it is possible to find a new set of cuts which would partially cure the efficiency losses inflicted by additional interactions in the event. As explained in section 4.5.3, the presence of pile-up decreases the chance that an event with the hadronic τ will be selected by the tau trigger. The efficiency with respect to the offline selection is decreased as well. Therefore two different optimizations were tried: the first one tried to increase the probability that recorded event would contain hadronic τ using tighter selection (and thus higher rejection in order to obtain rates similar to no pile-up case). The other approach tried to restore the offline efficiency close to the values observed without pile-up. Three triggers were optimized: tau12_loose, tau16_loose and tau50_medium. The cut values for both optimizations and all three items are in tab. 4.13. Note that for finding the cut values for the first two trigger items, the W$\rightarrow \tau\nu$ sample was used, while for the optimization of tau50_medium, the signal sample was A(800)$\rightarrow \tau\tau$.

It is noted in the beginning of this chapter that only one signal sample is used for the optimization of each trigger chain (W$\rightarrow \tau\nu$ for tau12 and tau16 and A$\rightarrow \tau\tau$ for tau50). This can bring kinematic bias to the optimized selection. The efficiency of the tau12 after optimizations with respect to the medium offline identification is shown in fig. 4.26. The plots show that no significant bias (besides the one coming from lower E_T cut) is introduced by this selection.

To test these new optimizations, the following test is done. The changes in signal content and in offline efficiency are shown in tab. 4.14. The "optimization 1", designed to restore the

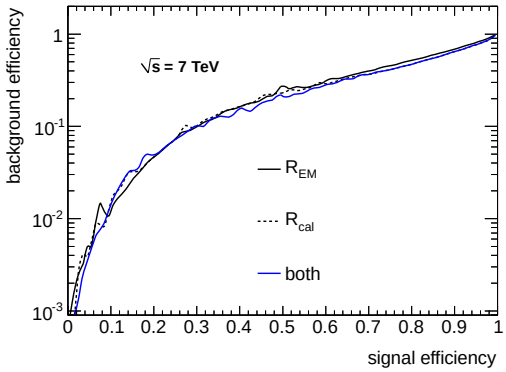

(a) all

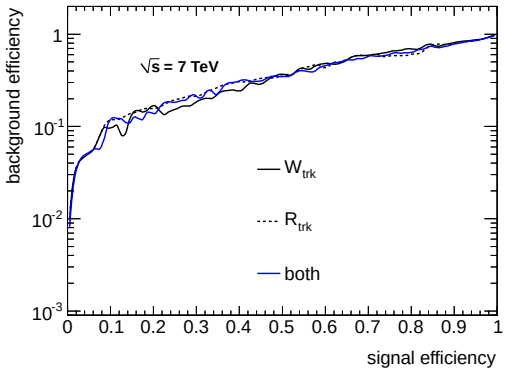

(b) 1-prong

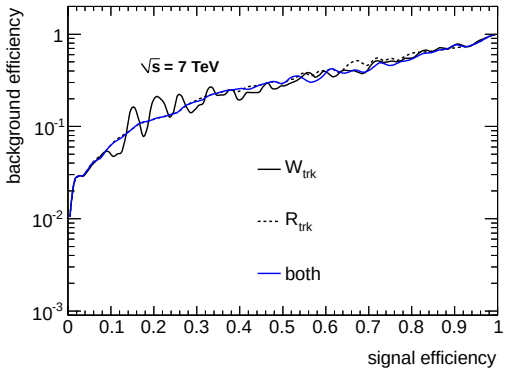

(c) multiprong

Figure 4.24: Detailed performance of the most powerful EF variables after making the L2 selection. Fig. 4.24(a) compares the $\mathcal{R}_{\mathrm{EM}}$ and $\mathcal{R}_{\mathrm{calo}}$ performance and shows that it is better to use $\mathcal{R}_{\mathrm{calo}}$ and that there is no gain in combining those two variables. The bottom two plots compare tracking based variables $\mathcal{R}_{\mathrm{trk}}$ and $\mathcal{W}_{\mathrm{trk}}$ and show that there is very little difference in their performance and no gain from combining the two variables - therefore any of them can be used for efficient selection.

signal content is indeed efficient in restoring the signal-to-background ratio to almost the values expected for events without pile-up. The price paid is quite a loss in offline efficiency due to an increased rejection. On the other hand, the "optimization 2" manages to record almost all events containing a hadronic τ that would be rejected when pile-up is present. Unfortunately, the looser selection also allows a lot of background to pass, thus decreasing signal-to-background ratio even further compared to situation without pile-up. It is clear, that such optimization would lead to increase in rate which is disproportional to the luminosity increase which would cause the trigger item to be prescaled more than originally designed, further decreasing the signal statistical significance.

The best approach would be the merger of the two optimizations. The main trigger with the tight selection and high rejection running without prescale for the recording of the relatively pure signal sample, and a prescaled back-up trigger with the loose selection to have a handle on the background from the data instead of relying on MC.

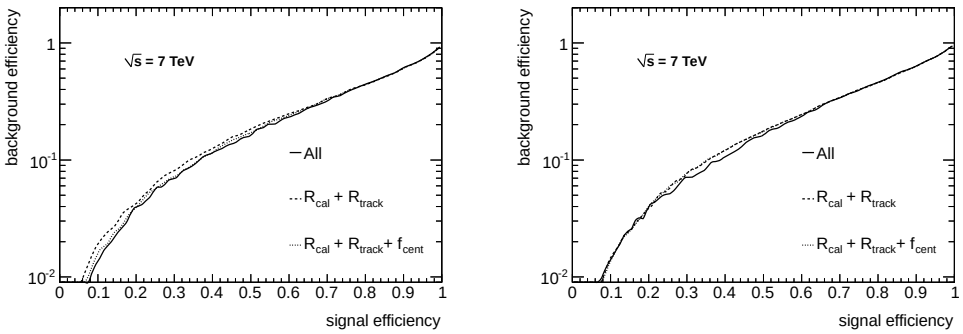

(a) 1-prong (b) multiprong

Figure 4.25: Comparison of the performance of different EF variables and their combinations in pile-up scenario after making the L2 selection. All EF τ candidates have been matched to offline reconstructed τ's identified by medium identification criteria (defined in section 4.6.1). The left plot shows EF τ candidates matched to offline single prong τ candidates, while the other one shows the EF τ's matched to offline multi prong τ's. Both plots show that a combination of $\mathcal{R}_{\rm calo}$, $\mathcal{R}_{\rm trk}$ and $f_{\rm core}$ is performing as well combination of all variables currently defined (little worse for multi prong cases) and it is performing better than simple combination of $\mathcal{R}_{\rm calo}$ and $\mathcal{R}_{\rm trk}$.

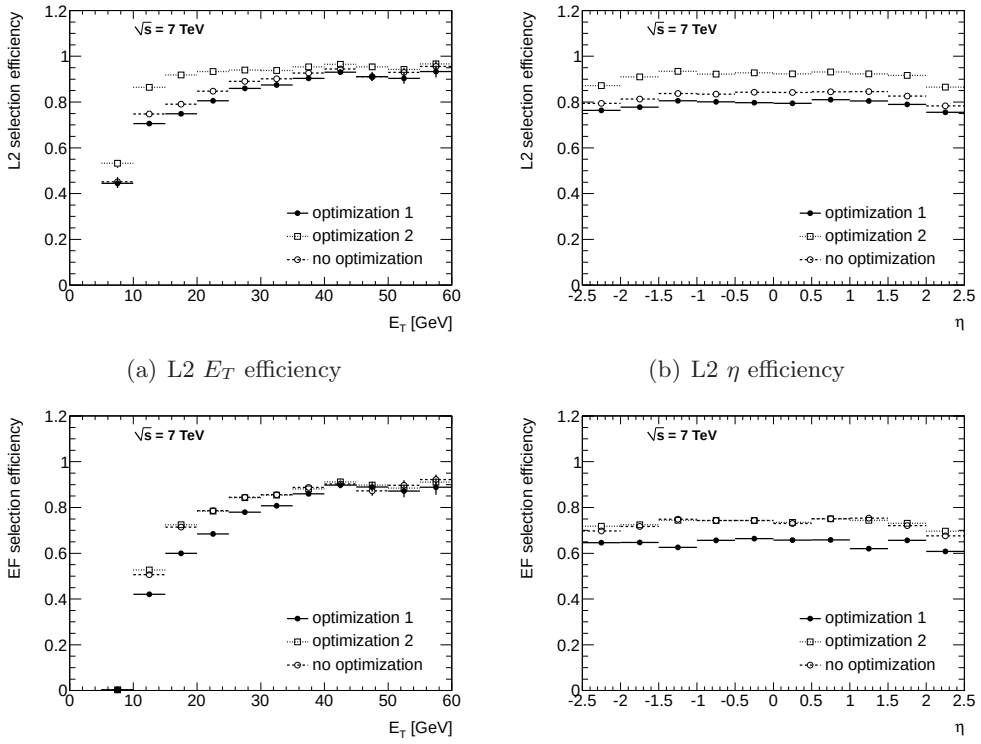

(a) L2 E_T efficiency (b) L2 η efficiency

(c) EF E_T efficiency (d) EF η efficiency

Figure 4.26: Efficiency of tau12 trigger selection with respect to the offline reconstructed τ's identified by medium identification criteria (defined in section 4.6.1). Figs. 4.26(a) and 4.26(c) show the efficiency as a function of the offline E_T, figs. 4.26(b) and 4.26(d) show the efficiency as a function of the pseudorapidity. The L2 (top line) and EF (bottom line) selections are shown. The trigger cuts correspond to "optimization 1" and "optimization 2" of tau12 (cf. tab. 4.13). For comparison, also the performance of the tau12 trigger before optimization is shown. All offline τ candidates have been matched to the true hadronically decaying τ's from W$\rightarrow \tau\nu$ events.

Optimization 1						
	tau12_loose		tau16_loose		tau50_medium	
	1 Trk	>1 Trk	1 Trk	>1 Trk	1 Trk	>1 Trk
EF $\mathcal{R}_{\rm cal}$	<0.09	<0.106	<0.10	<0.12	<0.07	<0.10
EF $\mathcal{R}_{\rm trk}$	<0.15	<0.15	<0.15	<0.15	<0.04	<0.04
EF $f_{\rm core}$	>0.50	>0.30	>0.60	>0.40	>0.75	>0.75
EF E_T [GeV]	>12	>12	>16	>16	>50	>50
L2 $\mathcal{R}_{\rm EM}$	<0.015		<0.06		<0.005	
L2 $\mathcal{R}_{\rm trk}$	<0.12		<0.05		<0.04	
L2 $\sum p_T^{\rm (iso)} / \sum p_T^{\rm (core)}$	<0.12		<0.15		<0.07	
L2 $\mathrm{N}_{\rm trk}^{\rm (core)}$	1-6		1-7		1-7	
L2 $E_T^{\rm (narrow)}$ [GeV]	>7.5		>10.4		>36	
Optimization 2						
	tau12_loose		tau16_loose		tau50_medium	
	1 Trk	>1 Trk	1 Trk	>1 Trk	1 Trk	>1 Trk
EF $\mathcal{R}_{\rm cal}$	<0.12	<0.13	<0.12	<0.14	<0.08	<0.10
EF $\mathcal{R}_{\rm trk}$	<0.16	<0.16	<0.13	<0.14	<0.05	<0.05
EF $f_{\rm core}$	>0.30	>0.35	>0.50	>0.30	>0.70	>0.70
EF E_T [GeV]	>12	>12	>16	>16	>50	>50
L2 $\mathcal{R}_{\rm EM}$	<0.034		<0.10		<0.012	
L2 $\mathcal{R}_{\rm trk}$	<0.17		<0.20		<0.06	
L2 $\sum p_T^{\rm (iso)} / \sum p_T^{\rm (core)}$	<0.50		<0.20		<0.07	
L2 $\mathrm{N}_{\rm trk}^{\rm (core)}$	1-6		1-7		1-7	
L2 $E_T^{\rm (narrow)}$ [GeV]	>7.5		>10.4		>36	

Table 4.13: Cuts on HLT variables with two different optimizations for pile-up scenario (see text) for 3 different trigger items. Note that single prong are all candidates with exactly 1 track at EF, while multiprongs have more tracks.

	tau12				tau16				tau50			
	1 Vx	5 Vx	Opt1	Opt2	1Vx	5 Vx	Opt1	Opt2	1 Vx	2 Vx	Opt1	Opt2
ε	0.62	0.56	0.42	0.64	0.51	0.45	0.29	0.48	0.85	0.81	0.70	0.83
S/B	2.22	2.10	2.22	2.06	4.42	4.35	4.38	4.34	4.90	4.30	12.0	3.90

Table 4.14: Effect of the optimization on the HLT performance with in-time pileup for different trigger chains. The efficiency ε is a fraction of offline reconstructed τ candidates identified by medium identification criteria which pass also the trigger requirements. "Optimization 1" is able to restore signal-to-background ratio almost to the values expected for events without pile-up, while decreasing the offline efficiency. "Optimization 2" is able to restore offline efficiency while being less pure and thus increasing the rate. Note that the signal-to-background ratio in the second row is multiplied by 10^5 for the first 8 columns, and by 10^9 for the final 4 columns. The signal sample used for tau12 and tau16 was W$\rightarrow \tau\nu$, while for tau50 it was A(800)$\rightarrow \tau\tau$. The statistical error on the efficiency is between 0.07 and 1.5 %, the error on the signal-to-background ratio is between 1.1 and 3.5 %.

4.7 Summary

The effect of pile-up on the tau trigger has been studied using 2010 data and Monte Carlo samples. Data collected in 2010 contain both in-time and out-of-time pile-up and show clear shifts in the distributions of the variables used for tau identification in the events with pile-up. It is also shown that there is no significant effect from out-of-time pile-up in 2010 on the tau trigger performance.

Signal Monte Carlo sample of $W \to \tau\nu$ and $A \to \tau\tau$ and a sample of simulated QCD dijets for background with high statistics are overlaid with on average 5 minimum bias collisions, so it corresponds to situation with μ (average number of interactions per event) equal to 6. The bunch spacing in the MC samples is large enough (900 ns) to prevent any interference between different colliding bunches, so no out-of-time pile-up is present in MC. The effect of in-time pile-up on tau trigger is presented in section 4.5.3.

Besides the rate increase the main effect of pile-up is a decrease of the offline efficiency due to pile-up adding tracks and E_T depositions to the τ candidates. For the same reason the signal-to-background ratio is getting worse. It is shown that the rate increases slightly faster than the luminosity at L1, slightly slower than the luminosity at EF and roughly proportional to the luminosity at L2. The efficiency loss for triggers which are efficient for a given τ signal is quite small (10-15 %) for pile-up from up to 7.5 collisions per event on average. However, for triggers which have smaller efficiency, but higher purity, the loss in signal-to-background ratio is up to 25 %. The HLT rejection with respect to L1 is increasing with pile-up (20% - 30% less background events passing for tau16 triggers, and 10% less background passing for the tau29 trigger).

The presence of in-time pile-up decreases the performance of tracking and calorimetry, so the variables constructed from this inputs have shifted and smeared distributions. Nevertheless, the offline reconstruction is more robust than EF and less prone to pile-up effects than the reconstruction at EF. Therefore, the difference between trigger and offline reconstruction quantities increases with the amount of pile-up.

The performance of the trigger can be partially restored by optimizing the selections using the variables which are reasonably stable against pile-up. This is presented in section 4.6.2. It has been shown that by changing the cuts it is possible to restore the signal-to-background ratio or the offline efficiency, but unfortunately not both.

It is shown that the best performance can be reached with just a couple of variables: one to exploit τ containment in the calorimeter (e.g. $\mathcal{R}_{\text{calo}}$) and one using track collimation in the inner detector (e.g. $\mathcal{R}_{\text{track}}$). Those variables should be used at all HLT levels as well as in the offline selection.

Already during 2011 some corrections to tracking (higher rejection of fakes) and the energy reconstruction (subtraction of pile-up deposits) have been implemented in both offline and online software to help prevent performance loss seen in section 4.5.3.

For the even higher pile-up levels expected in 2012 new optimizations are clearly needed, but more importantly, Therefore it is planned to use the results of this study as an example of the hadronic tau selection optimization with pile-up and optimize the trigger selection accordingly to maintain high tau trigger performance also in 2012.

Chapter 5

Thesis summary

5.1 Search for evidence of low mass supersymmetric Higgs Boson

The theoretical motivation for the existence of a pseudoscalar Higgs boson a_1 is presented in section 1.3.3. The previous experiments using indirect production of the a_1 boson in the decay of a heavier particle, have constrained the possible mass to be close to the mass of Υ resonances. Also, the scenarios with $\tan\beta > 30$ have been largely excluded prior to the start of this work [19].

The LHC allows direct production of the low mass a_1 Higgs boson via gluon fusion and a quark loop. The decay $a_1 \to \mu\mu$ has been searched for in 2010 data with no evidence of a_1 in a range 6–9 GeV and 11–12 GeV [77]. The analysis presented in chapter 3 is the first one to directly probe the mass region close to Υ, namely the range 9–10.5 GeV.

The decay $a_1 \to \tau\tau$ is used to bypass the main limitation of the muon channel: small branching fraction and large background from Υ decays. The search in the tau channel presented in this thesis focuses on leptonic τ decay modes where one of the τ leptons decays to electron and the other to muon.

Due to high trigger momentum thresholds, the search for a_1 is limited to the events where a_1 is heavily boosted and its decay products very collimated. This requirement allows to suppress the most of the background events with $\Upsilon \to \tau\tau$ decay. Due to the different production mechanism, it is more likely that a_1 is boosted enough to pass the trigger requirements than it is the case for Υ.

Section 3.7 shows that the main background for the $a_1 \to \tau\tau \to e\mu$ decay is $b\bar{b}$ events where one of the B hadrons decays di-leptonically, thus producing an electron and a muon with opposite sign very close to each other faking the signature of an a_1 decay. However, due to large mass difference between the mass of B hadrons and the (expected) mass of a_1, it is possible to reduce the contributions from this background by limiting the search to a specific region in electron–muon invariant mass: 5.5 GeV$< M_{e\mu} <$11 GeV.

In the selected mass region the background is a mix of remaining single B hadron decays and other processes involving decays of bottom and charm hadrons. The contribution of this mixed background is estimated from data using the "ABCD" method. The number of expected background events and the number of observed events after the analysis of 1.01 fb^{-1} of ATLAS data collected in 2011 is

$$\begin{aligned} N^{\text{obs}} &= 98.0 \pm 2.2 \text{ (sys.)} \\ N^{\text{exp}}_{BG} &= 94.3 \pm 21.9 \text{ (stat.)} \pm 3.4 \text{ (sys.)} \end{aligned}$$

The number of expected signal events, assuming the cross-section of 7 nb is for the masses of 9 GeV, 10 GeV and 10.5 GeV.

$$\begin{aligned} N^{\text{exp}}_{a_1(9000)} &= 21.9 \pm 4.3\ (\text{stat.}) \pm 4.5\ (\text{sys.}) \\ N^{\text{exp}}_{a_1(10000)} &= 51.0 \pm 7.7\ (\text{stat.}) \pm 10.5\ (\text{sys.}) \\ N^{\text{exp}}_{a_1(10500)} &= 63.8 \pm 9.1\ (\text{stat.}) \pm 13.1\ (\text{sys.}) \end{aligned}$$

where numbers in brackets indicate the mass in MeV.

No evidence for new physics is observed and using the method of profile likelihood, the CL_s value is calculated to set the upper limit on $\sigma(gg \to a_1) \times BR(a_1 \to \tau\tau)$. The resulting upper 95% exclusion limits are repeated in tab. 5.1.

mass	observed upper limit	expected upper limit
9 GeV	29 nb	27±15 nb
10 GeV	12 nb	11± 5 nb
10.5 GeV	10 nb	10± 4 nb

Table 5.1: The upper 95% exclusion limits on $\sigma(gg \to a_1) \times BR(a_1 \to \tau\tau)$ as a function of the a_1 mass.

The consequences of these results are discussed in section 3.11. This analysis sets new limits on $\tan\beta$ in type-II 2-Higgs doublet models in a region that was poorly constrained from B-factories and not studied at hadron colliders: $\tan\beta < 2$ for 10 GeV$\leq m_{a_1} \leq$10.5 GeV. The limits below 10 GeV are weaker than results from B-factories due to the limited analysis acceptance for $m_{a_1} < 10$ GeV.

The cross-section limits in tab. 5.1 are used also to constrain the magnitude of the NMSSM mixing angle $|\cos\theta_A|$. For $m_{a_1} \geq 10$ GeV and $\tan\beta \geq 3$ (10), the upper limit on $|\cos\theta_A|$ is 0.65 (0.2). For $m_{a_1} \geq 9$ GeV and $\tan\beta = 10$, the $|\cos\theta_A|$ should be smaller than 0.4.

These new limits put severe constraints on the possible realizations of type-II 2HDM's with low mass a_1 including some NMSSM models. However, the Ideal Higgs Scenario itself is not constrained more compared to previously existing limits in tab. 1.6 because its limitations from LEP searches are already very strong.

The possible ways to improve the results of this analysis are discussed in section 3.12. The main source of uncertainty in the analysis is statistical fluctuation of background estimation and also the uncertainty about the NLO signal production model. Therefore the analysis result can be improved by using the full 2011 dataset. On top of having four times more data that was used in this analysis, the additional 4 fb^{-1} of data have been collected with a dedicated trigger designed to select electrons and muons that are close to each other with a high efficiency.

The uncertainty on NLO production model can be decreased by using additional NLO Monte Carlo generators like Powheg. It is not unreasonable to expect that with those improvements, the uncertainty on expected number of background and signal events can be reduced considerably, resulting in a limit smaller by a factor 3 or more.

With such a result, it will be possible to start excluding Ideal Higgs Scenario for larger values of $\tan\beta$. For example, for $\tan\beta = 10$, the Ideal Higgs Scenario is required to have $|\cos\theta_A| < 0.12$ and the limit for this value of $\tan\beta$ set by this analysis is 0.2. Similarly, for $\tan\beta = 3$, there is less than a factor of 2 difference between the limit set by LEP and the one set by this analysis, so 4 times smaller limit (achievable with the improvements just mentioned) on cross-section can result in a new exclusion.

5.2 Optimization of the tau trigger

The tau trigger is a key element in ATLAS searches for low mass Higgs boson. In the context of the NMSSM Higgs searches, it can be used effectively in the search for the process $h_1 \to a_1 a_1 \to 4\tau$: when high luminosity (like in 2012) demands the transverse momentum threshold of a single lepton trigger to be very high to sustain the output rate, a combined trigger instead can be designed to keep transverse momentum thresholds low, by requesting already online several of the tau lepton decay products to be found in the same event. Additionally, for the very same reason, the tau trigger is an essential component in the search for low mass SM Higgs, and several SUSY Higgs scenarios where branching ratio into tau lepton pairs is dominant.

The LHC is a high intensity hadron collider, meaning that already in the end 2010 more than one interaction was observed in the reconstructed collision events. This phenomenon is called pile-up and it has significant influence on the tau trigger performance. Section 4.5 shows the effect of pile-up on the tau trigger. The study has been conducted in 2010 data and also in Monte Carlo simulation that offered much higher statistics. The presence of additional tracks and calorimeter depositions from pile-up events make hadronic τ decays look more like regular jets and so degrades the trigger discrimination power.

To remedy this effect, several different identification variables are studied. It is shown that identification variables based on tracks are less affected by pile-up and therefore suitable for the trigger selection in the pile-up environment.

In order to get realistic estimate of a possible improvement by smarter trigger selection, the offline selection is optimized for the tau identification in the pile-up environment first and subsequently being used as a reference for the trigger selection efficiency. The optimization procedure is described in section 4.6. It uses cut-based approach to single out the best variables for the tau selection at all levels.

The performance of the tau trigger can be partially restored with optimized selection. The best performance can be reached with just two selection variables: one using the information from inner detector to select tau candidates with highly collimated tracks (e.g. $\mathcal{R}_{\text{track}}$) and one using the calorimeter information (e.g. calorimeter radius $\mathcal{R}_{\text{calo}}$) to select narrow deposits. In the optimal case, the event filter and offline reconstruction should use identical variables for tau identification. The level 2 trigger algorithms are different than those used at event filter, but it is possible to define the identification variables in an analogue way at both HLT levels. If this is done, optimal performance is reached.

The study presented in chapter 4 provides guidelines for preparing the tau trigger selection for 2012 run, where pileup of about 20 collisions per event is expected. Optimizing the selection is crucial in order to maintain high performance and select interesting events for the discovery of the Higgs boson in 2012.

5.3 Conclusion

The ultimate focus of the research work carried out and described in this PhD thesis is to unveil the mechanism behind the origin of mass for the fundamental particles. The theory formulating such mechanism is described, for the SM and for theories beyond the SM. Then the experimental search for signatures validating such theoretical explanation is described, and ideas for improvements in the near future are pointed out, including a better trigger strategy. This line of research provides an important input to the quest for a more definite explanation on the origin and composition of matter.

Bibliography

[1] I. W. Griffiths, *J. J. Thomson – the Centenary of His Discovery of the Electron and of His Invention of Mass Spectrometry*, Rapid Communications in Mass Spectrometry **11** (1997) no. 1, 2–16.

[2] E. Rutherford, *The Scattering of α and β Particles by Matter and the structure of the Atom*, Phil. Mag. **21** (1911) 669–688.

[3] B. M. Peake, *The Discovery of the Electron Proton and Neutron*, J. of Chem. Ed. **66** (1989) no. 9, 738.

[4] N. Bohr, *On the Constitution of Atoms and Molecules, Part I*, Phil. Mag. **26** (1913) 1–24.

[5] J. Chadwick, *Possible Existence of a Neutron*, Nature **129** (1932) 312.

[6] J. Blank, P. Exner, and M. Havlíček, *Hilbert-Space Operators in Quantum Physics*. American Institute of Physics, 1994.

[7] B. R. Martin and G. Shaw, *Particle Physics*. Wiley, 2008.

[8] K. Riesselmann, *Logbook: Neutrino Invention*, Symm. Mag. **4** (2007) no. 2, http://www.symmetrymagazine.org/cms/?pid=1000450.

[9] J. Hořejší, *Fundamentals of electroweak theory*. Karolinum Press, 2002.

[10] M. E. Peskin and D. V. Schroeder, *Introduction to quantum field theory*. Westview Press, 1995.

[11] L. H. Ryder, *Quantum Field Theory*. Cambridge University Press, 1996.

[12] J. Street and E. Stevenson, *New evidence for the existence of a particle of mass intermediate between the proton and electron*, Phys.Rev. **52** (1937) 1003–1004.

[13] C. Lattes, G. Occhialini, and C. Powell, *Observations on the tracks of slow mesons in photographic emulsions. 1*, Nature **160** (1947) 453–456.

[14] G. Rochester and C. Butler, *Evidence for the existence of new unstable elementary particles*, Nature **160** (1947) 855–857.

[15] J. Chýla, *Quarks, partons and Quantum Chromodynamics*, PRA-HEP-04-01 (2004) .

[16] D. Gross and F. Wilczek, *Ultraviolet Behavior of Nonabelian Gauge Theories*, Phys.Rev.Lett. **30** (1973) 1343–1346.

[17] H. Politzer, *Reliable Perturbative Results for Strong Interactions?*, Phys.Rev.Lett. **30** (1973) 1346–1349.

[18] Particle Data Group Collaboration, K. Nakamura et al., *Review of particle physics*, J.Phys.G **G37** (2010) 075021.

[19] R. Dermíšek and J. F. Gunion, *New constraints on a light CP-odd Higgs boson and related NMSSM Ideal Higgs Scenarios*, Phys.Rev. **D81** (2010) 075003, arXiv:1002.1971 [hep-ph].

[20] P. Jež, *The search for NMMSM "Ideal Higgs Scenario" at ATLAS*, ATLAS-COM-PHYS-2011-1084 (2011) .

[21] P. Jež, *Performance and the evolution of the ATLAS tau trigger during 2011 data taking period*, ATLAS-DAQ-PROC-2011-026 (2011) . Proceedings of 13th ICATPP.

[22] P. Jež, *ATLAS High-Level Calorimeter Trigger Algorithms Performance with First LHC pp Collisions*, ATLAS-DAQ-PROC-2010-022 (2010) . Proceedings of PLHC'10.

[23] P. Jež *et al.*, *Optimization of tau trigger selection and pileup effects*, ATLAS-DAQ-INT-2010-008 (2010) .

[24] P. Jež, *Effect of Pile-up on Tau Trigger Performance*, ATLAS-DAQ-INT-2011-002 (2011) .

[25] Y. L. Dokshitzer, V. A. Khoze, A. H. Mueller, and S. Troian, *Basics of perturbative QCD*. Gif-sur-Yvette, France, 1991.

[26] H. Georgi, *Lie algebras in particle physics. From isospin to unified theories*, Front.Phys. **54** (1982) 1–255.

[27] C. Geng and R. Marshak, *Uniqueness of quark and lepton representations in the standard model from the anomalies viewpoint*, Phys.Rev. **D39** (1989) 693.

[28] J. Minahan, P. Ramond, and R. Warner, *A comment on anomaly cancellation in the standard model*, Phys.Rev. **D41** (1990) 715.

[29] F. Wilczek, *Beyond the standard model: An Answer and twenty questions*, arXiv:hep-ph/9802400 [hep-ph].

[30] J. Goldstone, A. Salam, and S. Weinberg, *Broken Symmetries*, Phys.Rev. **127** (1962) 965–970.

[31] D. Rainwater, *Searching for the Higgs boson*, arXiv:hep-ph/0702124 [HEP-PH].

[32] ALEPH Collaboration, DELPHI Collaboration, L3 Collaboration, OPAL Collaboration, LEP Electroweak Working Group Collaboration, J. Alcaraz et al., *A Combination of preliminary electroweak measurements and constraints on the standard model*, arXiv:hep-ex/0612034 [hep-ex].

[33] Super-Kamiokande Collaboration, Y. Fukuda et al., *Evidence for oscillation of atmospheric neutrinos*, Phys.Rev.Lett. **81** (1998) 1562–1567, arXiv:hep-ex/9807003 [hep-ex].

[34] Super-Kamiokande Collaboration, S. Fukuda et al., *Determination of solar neutrino oscillation parameters using 1496 days of Super-Kamiokande I data*, Phys.Lett. **B539** (2002) 179–187, arXiv:hep-ex/0205075 [hep-ex].

[35] M. R. Buckley and H. Murayama, *How can we test seesaw experimentally?*, Phys.Rev.Lett. **97** (2006) 231801, arXiv:hep-ph/0606088 [hep-ph].

[36] OPERA Collaboration, T. Adam et al., *Measurement of the neutrino velocity with the OPERA detector in the CNGS beam*, arXiv:1109.4897 [hep-ex].

[37] F. Zwicky, *On the Masses of Nebulae and of Clusters of Nebulae*, Astrophys. J. **86** (1937) 217.

[38] S. P. Martin, *A Supersymmetry primer*, arXiv:hep-ph/9709356 [hep-ph].

[39] M. Drees, *An Introduction to supersymmetry*, arXiv:hep-ph/9611409 [hep-ph].

[40] M. Drees, R. Godbole, and P. Roy, *Theory and phenomenology of sparticles: An account of four-dimensional N=1 supersymmetry in high energy physics*. World Scientific, 2004.

[41] S. R. Coleman and J. Mandula, *All possible symmetries of the s matrix*, Phys.Rev. **159** (1967) 1251–1256.

[42] R. Haag, J. T. Lopuszanski, and M. Sohnius, *All Possible Generators of Supersymmetries of the s Matrix*, Nucl.Phys. **B88** (1975) 257.

[43] J. Wess and J. Bagger, *Supersymmetry and supergravity*. Princeton Univ. Press, 1992.

[44] ATLAS Collaboration, G. Aad et al., *Search for new phenomena in final states with large jet multiplicities and missing transverse momentum using sqrt(s)=7 TeV pp collisions with the ATLAS detector*, arXiv:1110.2299 [hep-ex].

[45] ATLAS Collaboration, G. Aad et al., *Search for squarks and gluinos using final states with jets and missing transverse momentum with the ATLAS detector in sqrt(s) = 7 TeV proton-proton collisions*, arXiv:1109.6572 [hep-ex].

[46] A. Djouadi, M. Drees, U. Ellwanger, R. Godbole, C. Hugonie, et al., *Benchmark scenarios for the NMSSM*, JHEP **0807** (2008) 002, arXiv:0801.4321 [hep-ph].

[47] S. Weinberg, *A New Light Boson?*, Phys.Rev.Lett. **40** (1978) 223–226.

[48] F. Wilczek, *Problem of Strong p and t Invariance in the Presence of Instantons*, Phys.Rev.Lett. **40** (1978) 279–282.

[49] U. Ellwanger, A. Florent, and D. Zerwas, *Discovering the constrained NMSSM with tau leptons at the LHC*, JHEP **1101** (2011) 103, arXiv:1011.0931 [hep-ph].

[50] R. Dermíšek and J. F. Gunion, *Direct production of a light CP-odd Higgs boson at the Tevatron and LHC*, Phys.Rev. **D81** (2010) 055001, arXiv:0911.2460 [hep-ph].

[51] J. F. Gunion, *A Light CP-odd Higgs boson and the muon anomalous magnetic moment*, JHEP **0908** (2009) 032, arXiv:0808.2509 [hep-ph].

[52] J. R. Ellis, J. Gunion, H. E. Haber, L. Roszkowski, and F. Zwirner, *Higgs Bosons in a Nonminimal Supersymmetric Model*, Phys.Rev. **D39** (1989) 844.

[53] J. F. Gunion, H. E. Haber, G. L. Kane, and S. Dawson, *The Higgs hunter's guide*, Front.Phys. **80** (2000) 1–448.

[54] U. Ellwanger, J. F. Gunion, and C. Hugonie, *NMHDECAY: A Fortran code for the Higgs masses, couplings and decay widths in the NMSSM*, JHEP **0502** (2005) 066, arXiv:hep-ph/0406215 [hep-ph].

[55] R. Dermíšek and J. F. Gunion, *The NMSSM Close to the R-symmetry Limit and Naturalness in h→ aa Decays for m(a) < 2m(b)*, Phys.Rev. **D75** (2007) 075019, arXiv:hep-ph/0611142 [hep-ph].

[56] ALEPH Collaboration, S. Schael et al., *Search for neutral Higgs bosons decaying into four taus at LEP2*, JHEP **1005** (2010) 049, arXiv:1003.0705 [hep-ex].

[57] L. Evans, (ed.) and P. Bryant, (ed.), *LHC Machine*, JINST **3** (2008) S08001.

[58] H. Arpad, *LHC octants*, 2006. http://commons.wikimedia.org/wiki/File:LHC_octants.png. [Online; accessed 29-October-2011].

[59] ALICE Collaboration, K. Aamodt et al., *The ALICE experiment at the CERN LHC*, JINST **3** (2008) S08002.

[60] LHCb Collaboration, A. Alves et al., *The LHCb Detector at the LHC*, JINST **3** (2008) S08005.

[61] CMS Collaboration, R. Adolphi et al., *The CMS experiment at the CERN LHC*, JINST **3** (2008) S08004.

[62] J. Pequenao, *Computer generated image of the whole ATLAS detector*, 2008. http://cdsweb.cern.ch/record/1095924.

[63] ATLAS Collaboration, *ATLAS Experiment at the CERN Large Hadron Collider.*, JINST **3:S08003** (2008) 1–437.

[64] ATLAS Collaboration, *ATLAS public outreach page*, 2008. http://atlas.ch.

[65] J. Pequenao, *Computer generated image of the ATLAS inner detector*, 2008. http://cdsweb.cern.ch/record/1095926.

[66] J. Pequenao, *Computer Generated image of the ATLAS calorimeter*, 2008. http://cdsweb.cern.ch/record/1095927.

[67] J. Pequenao, *Computer generated image of the ATLAS Muons subsystem*, 2008. http://cdsweb.cern.ch/record/1095929.

[68] ATLAS Collaboration, G. Aad et al., *Performance of the ATLAS Trigger System in 2010*, arXiv:1110.1530 [hep-ex].

[69] ATLAS Collaboration, G. Aad et al., *The ATLAS Simulation Infrastructure*, Eur.Phys.J. **C70** (2010) 823–874, arXiv:1005.4568 [physics.ins-det].

[70] ATLAS Collaboration, G. Duckeck, (ed.) et al., *ATLAS computing: Technical design report*, CERN-LHCC-2005-022 (2005) .

[71] ATLAS Collaboration, G. Aad et al., *Expected Performance of the ATLAS Experiment - Detector, Trigger and Physics*, arXiv:0901.0512 [hep-ex].

[72] ATLAS Collaboration, *Reconstruction, Energy Calibration, and Identification of Hadronically Decaying Tau Leptons*, ATLAS-CONF-2011-077 (2011) .

[73] C. Belanger-Champagne *et al.*, *Tau trigger: configuration and performance in release 15 (Fall 2009)*, ATL-DAQ-INT-2010-005 (2010) .

[74] I. Rottlaender, *Development of a benchmark parameter scan for Higgs bosons in the NMSSM model and a study of the sensitivity for $H \to AA \to 4\tau$ in vector boson fusion with the ATLAS detector*. PhD thesis. CERN-THESIS-2008-064.

[75] D0 Collaboration, V. Abazov et al., *Search for NMSSM Higgs bosons in the $h \to aa \to \mu\mu\mu\mu$, $\mu\mu\tau\tau$ channels using $p\bar{p}$ collisions at $\sqrt{s} = 1.96$ TeV*, Phys.Rev.Lett. **103** (2009) 061801, arXiv:0905.3381 [hep-ex].

[76] CDF Collaboration, *Search for NMSSM Higgs in Top Quark Decays*, . http://www-cdf.fnal.gov/physics/new/top/2009/tprop/nMSSMhiggs/.

[77] ATLAS Collaboration, *A Search for a Light CP-Odd Higgs Boson Decayint to $\mu^+\mu^-$ in ATLAS*, ATLAS-CONF-2011-020 (2011) .

[78] P. Nason, G. Ridolfi, O. Schneider, G. Tartarelli, P. Vikas, et al., *Bottom production*, arXiv:hep-ph/0003142 [hep-ph].

[79] S. Drell and T.-M. Yan, *Massive Lepton Pair Production in Hadron-Hadron Collisions at High-Energies*, Phys.Rev.Lett. **25** (1970) 316–320.

[80] S. Frixione and B. R. Webber, *Matching NLO QCD computations and parton shower simulations*, JHEP **06** (2002) 029, arXiv:hep-ph/0204244.

[81] G. Corcella, I. G. Knowles, G. Marchesini, S. Moretti, K. Odagiri, P. Richardson, M. H. Seymour, and B. R. Webber, *HERWIG 6: an event generator for hadron emission reactions with interfering gluons (including supersymmetric processes)*, Journal of High Energy Physics **2001** (2001) no. 01, 010.

[82] S. Jadach, J. H. Khn, and Z. Was, *TAUOLA - a library of Monte Carlo programs to simulate decays of polarized leptons*, Computer Physics Communications **64** (1991) no. 2, 275 – 299.

[83] T. Sjostrand *et al.*, *Pythia 6.4*, JHEP **05** (2006) 026.

[84] M. L. Mangano, F. Piccinini, A. D. Polosa, M. Moretti, and R. Pittau, *ALPGEN, a generator for hard multiparton processes in hadronic collisions*, Journal of High Energy Physics **2003** (2003) no. 07, 001.

[85] ATLAS Collaboration, *Charged particle multiplicities in pp interactions at $\sqrt{s} = 0.9$ and 7 TeV in a diffractive limited phase space measured with the ATLAS detector at the LHC and a new PYTHIA 6 tune*, ATLAS-CONF-2011-031 (2011) .

[86] ATLAS Collaboration, *First tuning of HERWIG/JIMMY to ATLAS data*, ATLAS-PHYS-PUB-2010-014 (2010) .

[87] CLEO Collaboration, D. Payne, *Recent B physics results from CLEO-II*, Nucl.Instrum.Meth. **A351** (1994) 19–30.

[88] ATLAS Collaboration, G. Aad et al., *Measurement of the $W \to \ell\nu$ and $Z/\gamma^* \to \ell\ell$ production cross sections in proton-proton collisions at $\sqrt{s} = 7$ TeV with the ATLAS detector*, JHEP **1012** (2010) 060, arXiv:1010.2130 [hep-ex].

[89] ATLAS Collaboration, G. Aad et al., *Electron performance measurements with the ATLAS detector using the 2010 LHC proton-proton collision data*, arXiv:1110.3174 [hep-ex].

[90] ATLAS Collaboration, *Muon Momentum Resolution in First Pass Reconstruction of pp Collision Data Recorded by ATLAS in 2010*, ATLAS-CONF-2011-046 (2011) .

[91] ATLAS Collaboration, *Muon reconstruction efficiency in reprocessed 2010 LHC proton-proton collision data recorded with the ATLAS detector*, ATLAS-CONF-2011-063 (2011) .

[92] CMS Collaboration, V. Khachatryan et al., *Upsilon production cross section in pp collisions at $\sqrt{s} = 7$ TeV*, Phys.Rev. **D83** (2011) 112004, arXiv:1012.5545 [hep-ex].

[93] ATLAS Collaboration, *Luminosity Determination in pp Collisions at sqrt(s) = 7 TeV using the ATLAS Detector in 2011*, ATLAS-CONF-2011-116 (2011) .

[94] M. Aliev, H. Lacker, U. Langenfeld, S. Moch, P. Uwer, et al., *HATHOR: HAdronic Top and Heavy quarks crOss section calculatoR*, Comput.Phys.Commun. **182** (2011) 1034–1046, arXiv:1007.1327 [hep-ph].

[95] ATLAS Collaboration, G. Aad et al., *Measurement of the inclusive $W^{\pm}$ and Z/γ cross sections in the electron and muon decay channels in pp collisions at $\sqrt{s} = 7$ TeV with the ATLAS detector*, arXiv:1109.5141 [hep-ex].

[96] P. Nason, *A New method for combining NLO QCD with shower Monte Carlo algorithms*, JHEP **0411** (2004) 040, arXiv:hep-ph/0409146 [hep-ph].

[97] ATLAS Collaboration, *Performance of the ATLAS tau trigger in p-p collisions at $\sqrt{s} = 900$ GeV*, ATLAS-CONF-2010-021 (2010) .

[98] ATLAS Collaboration, *ATLAS High Level Calorimeter Trigger Software Performance for First LHC Collision Events*, ATLAS-CONF-2010-030 (2010) .

[99] ATLAS Collaboration, *Reconstruction, Energy Calibration, and Identification of Hadronically Decaying Tau Leptons*, ATLAS-COM-CONF-2011-057 (2011) .

[100] ATLAS Collaboration, G. Aad et al., *Measurement of inclusive jet and dijet cross sections in proton-proton collisions at 7 TeV centre-of-mass energy with the ATLAS detector*, Eur.Phys.J. **C71** (2011) 1512, arXiv:1009.5908 [hep-ex].

[101] A. Hoecker *et al.*, *TMVA4: Toolkit for Multivariate Data Analysis with ROOT*, CERN-OPEN-2007-007 (2007) , arXiv:physics/0703039 [physics].

[102] F. Berezin, *The method of second quantization*, Pure Appl.Phys. **24** (1966) 1–228.

Appendix A

Introduction to SUSY

A.1 SUSY generators

Let's assume, that we have a single SUSY generator ("supercharge") Q and its conjugate $\overline{Q}$. Note that because of fermionic characteristics these operators are 2-component Weyl spinors. Now we can set the anticommutators which define the superalgebra:

$$\{Q_\alpha, Q_\beta\} = \{\overline{Q}_{\dot{\alpha}}, \overline{Q}_{\dot{\beta}}\} = 0 \qquad \{Q_\alpha, \overline{Q}_{\dot{\beta}}\} = 2\sigma^\mu_{\alpha\dot{\beta}} P_\mu$$

Spinor indices are denoted α and β, dotted in the case of spinor conjugate. They can take values 1 or 2. P_μ is the momentum generator, σ^0 is identity matrix and σ^i are Pauli matrices. The commutator $[Q_\alpha, P_\mu]$ is zero, as a result of the Coleman–Mandula theorem.

Now that we have SUSY algebra, we would like to know how does a SUSY transformation look like. It is convenient to introduce new space-time coordinates on which SUSY will act. It will be fermionic Grassmann (anticommuting) variables θ and $\overline{\theta}$. The anticommutativity means this:

$$\{\theta, \theta\} = \{\overline{\theta}, \theta\} = \{\overline{\theta}, \overline{\theta}\} = 0$$

Quantities dependent on these anticommuting coordinates, as well as on the normal space-time coordinates, are called superfields. Note, that because each θ has 2 degrees of freedom, we have effectively doubled the dimensions of space-time.

Then, in accordance with our previous experience with the symmetry generators, we can write a SUSY transformation matrix as

$$S(x, \theta, \overline{\theta}) = \exp[i(\theta Q + \overline{Q\theta} - x_\mu P^\mu)]$$

where x_μ is the classical spacetime 4-vector and θ, $\overline{\theta}$ are coordinates in the Grassmann variables. Obviously, S is an element of a group corresponding to the SUSY algebra. Let's multiply two elements of this group to find the explicit form of SUSY action:

$$S(0, \xi, \overline{\xi}) G(x^\mu, \theta, \overline{\theta}) = G(x^\mu + i\theta\sigma^\mu\overline{\xi} - i\xi\sigma^\mu\overline{\theta}, \theta + \xi, \overline{\theta} + \overline{\xi}) \tag{A.1}$$

Here, we have used Hausdorff's formula $e^A e^B = e^{A+B+\frac{1}{2}[A,B]+\cdots}$ and the fact, that the SUSY algebra can be rewritten in terms of commutators, when we use also Grassmann variables:

$$[\theta Q, \overline{\theta Q}] = 2\theta\sigma^\mu\overline{\theta} P_\mu$$

All other commutators are zero. Notice also, that in this case the Hausdorff's formula is exact, because all terms with product of three and more θ's vanish. The group multiplication (A.1)

induces the following action in the parameter space:

$$g(\xi,\overline{\xi}) : (x^\mu,\theta,\overline{\theta}) \to (x^\mu + i\theta\sigma^\mu\overline{\xi} - i\xi\sigma^\mu\overline{\theta}, \theta+\xi, \overline{\theta}+\overline{\xi})$$

This now allows us to write the infinitesimal SUSY transformation

$$\delta_S(0,\xi,\overline{\xi})\Phi(x^\mu,\theta,\overline{\theta}) = \left[\xi\frac{\partial}{\partial\theta} + \overline{\xi}\frac{\partial}{\partial\overline{\theta}} - i(\xi\sigma_\mu\overline{\theta} - \theta\sigma_\mu\overline{\xi})\frac{\partial}{\partial x_\mu}\right]\Phi(x^\mu,\theta,\overline{\theta})$$

Now we can immediately write the explicit representation of the SUSY operators, which will allow us to find the SUSY invariant action useful in the construction of the SUSY Lagrangian.

$$Q_\alpha = \frac{\partial}{\partial\theta^\alpha} - i\sigma^\mu_{\alpha\dot\beta}\overline{\theta}^{\dot\beta}\partial_\mu\ ; \qquad \overline{Q}_{\dot\alpha} = -\frac{\partial}{\partial\overline{\theta}^{\dot\alpha}} + i\theta^\beta\sigma^\mu_{\beta\dot\alpha}\partial_\mu \tag{A.2}$$

The SUSY operators contain "translation" in SUSY space together with parts coming from the anticommutativity. We also observe, that these operators mix with the ordinary space-time derivatives, so it is convenient to introduce SUSY-covariant derivatives which commute with SUSY transformations and are therefore SUSY invariant:

$$D_\alpha = \frac{\partial}{\partial\theta^\alpha} + i\sigma^\mu_{\alpha\dot\beta}\overline{\theta}^{\dot\beta}\partial_\mu\ ; \qquad \overline{D}_{\dot\alpha} = -\frac{\partial}{\partial\overline{\theta}^{\dot\alpha}} - i\theta^\beta\sigma^\mu_{\beta\dot\alpha}\partial_\mu \tag{A.3}$$

Important corollary of (A.2) and (A.3) is that SUSY trasformation is not invariant under complex conjugation thus it acts differently on the fields and their complex conjugates.

A.2 Representations of the Supersymmetry

A.2.1 Chiral Superfields

The construction of the SM showed us the importance of the appropriate choice of representation. The same is true in this case. For further study of SUSY it is better to use chiral representations which treat Grassmann variables on different footing. We can define L-representation:

$$\delta_S\Phi_L = \left(\xi\frac{\partial}{\partial\theta} + \overline{\xi}\frac{\partial}{\partial\overline{\theta}} + 2i\theta\sigma^\mu\overline{\xi}\partial_\mu\right)\Phi_L\ ; \qquad D_L = \frac{\partial}{\partial\theta} + 2i\sigma^\mu\overline{\theta}\partial_\mu\ ; \qquad \overline{D}_L = -\frac{\partial}{\partial\overline{\theta}}\ , \tag{A.4}$$

and R-representation:

$$\delta_S\Phi_R = \left(\xi\frac{\partial}{\partial\theta} + \overline{\xi}\frac{\partial}{\partial\overline{\theta}} - 2i\xi\sigma^\mu\overline{\theta}\partial_\mu\right)\Phi_R\ ; \qquad \overline{D}_R = -\frac{\partial}{\partial\overline{\theta}} - 2i\theta\sigma^\mu\partial_\mu\ ; \qquad D_R = \frac{\partial}{\partial\theta}\ . \tag{A.5}$$

Finally, we need irreducible representations. The simplest way to achieve this is to demand

$$\overline{D}\Phi_L = 0 \qquad \text{and} \qquad D\Phi_R = 0\ .$$

Comparing with (A.4) and (A.5), we find that in the first case the field is independent of $\overline{\theta}$ while in the second case it is independent of θ. This allows us to write an expansion of the superfields in terms of Grassmann variables:

$$\Phi_L(x,\theta) = \phi(x) + \sqrt{2}\theta^\alpha\psi_\alpha(x) + \theta^\alpha\theta^\beta\varepsilon_{\alpha\beta}F(x)\ . \tag{A.6}$$

This expansion is exact, because any combination of more than 2 θ's is automatically zero since in that case there must be two identical components and $\theta^\alpha\theta^\alpha = \theta^\beta\theta^\beta = 0$ as a simple

consequence of anticommutativity. Fields ϕ and F are scalars, while ψ is spinor. So we can see the first sign of SUSY: bosonic and fermionic fields are combined in one representation. On the other hand we have 4 bosonic (fields ϕ and F) and only 2 fermionic degrees of freedom, but it will be shown that not all of them are physical, so the symmetry between fermions and bosons is exact.

Now it is time to investigate how the field (A.6) transforms under infinitesimal SUSY (A.4):

$$\begin{aligned}\delta_S\Phi_L &= \sqrt{2}\xi^\alpha\psi_\alpha(x) + 2\xi^\alpha\theta^\beta\varepsilon_{\alpha\beta}F(x) \\ &\quad +2i\theta^\alpha\sigma^\mu_{\alpha\dot\beta}\overline{\xi}^{\dot\beta}\partial_\mu\phi(x) + 2\sqrt{2}i\theta^\alpha\sigma^\mu_{\alpha\dot\beta}\overline{\xi}^{\dot\beta}\theta^\beta\partial_\mu\psi_\beta + 2i\theta^\alpha\sigma^\mu_{\alpha\dot\beta}\overline{\xi}^{\dot\beta}\theta^\alpha\theta^\beta\varepsilon_{\alpha\beta}F(x) \\ &\equiv \delta_S\phi + \sqrt{2}\theta\delta_S\psi + \theta\theta\delta_S F\,. \end{aligned} \tag{A.7}$$

The last term on the second line is zero, because of three θ's and on the last line spinor indices were dropped and SUSY "dot product" introduced: $\theta\theta = \varepsilon_{\alpha\beta}\theta^\alpha\theta^\beta$. We can see that the SUSY transformation of L-chiral superfields are again L-chiral superfields.

Finally, let's examine the form of the component fields after the transform:

$$\delta_S\phi = \sqrt{2}\xi\psi \tag{A.8}$$
$$\delta_S\psi = \sqrt{2}\xi F + i\sqrt{2}\sigma^\mu\overline{\xi}\partial_\phi \tag{A.9}$$
$$\delta_S F = -i\sqrt{2}\partial_\mu(\psi\sigma^\mu\overline{\xi}) \tag{A.10}$$

This means that the boson field is transformed to fermion field, the fermion is transformed to a boson and the field F is transformed to a total derivative. Now we have shown that SUSY works in the way we wanted it to. Extremely important is the equation (A.10), because it shows how we should construct the SUSY invariant Lagrangian: the addition of total derivatives does not change the action.

A.2.2 Vector Superfields

So far we have found representations for scalars (spin-0 bosons, e.g. Higgs) and spin-1/2 fermions (e.g. leptons and quarks). However, the SM contains also spin-1 vector bosons: these are all gauge bosons. So that we must find some representation for them.

For that reason we will introduce another irreducible representation of SUSY algebra: Vector superfields. The condition is

$$V(x,\theta,\overline{\theta}) = V^\dagger(x,\theta,\overline{\theta})\,.$$

This means that vector superfields are self-conjugate. The general form of this field is a bit lengthy, but it is instructive to show it.

$$\begin{aligned} V(x,\theta,\overline{\theta}) &= C(x) + i\theta\chi(x) - i\overline{\theta}\overline{\chi}(x) + \frac{i}{2}\theta\theta\left[M(x)+iN(x)\right] - \frac{i}{2}\overline{\theta}\overline{\theta}\left[M(x)-iN(x)\right] \\ &- \theta\sigma^\mu\overline{\theta}A_\mu(x) + i\theta\theta\overline{\theta}\left[\overline{\lambda}(x) - \frac{i}{2}\overline{\sigma}^\mu\partial_\mu\chi(x)\right] - i\overline{\theta}\overline{\theta}\theta\left[\lambda(x) + \frac{i}{2}\sigma^\mu\partial_\mu\overline{\chi}(x)\right] \\ &+ \frac{1}{2}\theta\theta\overline{\theta}\overline{\theta}\left[D(x) + \frac{1}{2}\Box C(x)\right] \end{aligned} \tag{A.11}$$

In this case, the fields C, M, N, and D are real scalars (spin-0 bosons), χ and λ are Weyl spinors (spin-1/2 fermions) and field A^μ is a spin-1 vector field. This is of course not the only possible choice of coefficients in the θ, $\overline{\theta}$ expansion. This one was inspired by the hermitian field which

was constructed from chiral fields (A.6). As the vector superfields contain both θ and $\overline{\theta}$ it is good to write L-chiral field in R-representation and vice versa. For that we can use simple trick allowing transition between representations:

$$\Phi(x_\mu, \theta, \overline{\theta}) = \Phi_L(x_\mu + i\theta\sigma_\mu\overline{\theta}, \theta, \overline{\theta}) = \Phi_R(x_\mu - i\theta\sigma_\mu\overline{\theta}, \theta, \overline{\theta}) \; .$$

So that the L-chiral field (A.6) in R-representation is:

$$\begin{aligned} \Phi &= \phi(x) + i\theta\sigma^\mu\overline{\theta}\partial_\mu\phi(x) + \frac{1}{4}\theta\theta\overline{\theta}\overline{\theta}\Box\phi(x) \\ &+ \sqrt{2}\theta\psi(x) - \frac{i}{\sqrt{2}}\theta\theta\partial_\mu\psi(x)\sigma^\mu\overline{\theta} + \theta\theta F(x) \; . \end{aligned} \tag{A.12}$$

When working out this expression, Taylor expansion in x^μ and also spinor algebra is used (for more details see [43]). Now we can write the hermitian field which can be constructed by adding a chiral field and its conjugate

$$\begin{aligned} \Phi + \Phi^\dagger &= \phi + \phi^* + \sqrt{2}(\theta\psi + \overline{\theta\psi}) + \theta\theta F + \overline{\theta\theta}F^* + i\theta\sigma^\mu\overline{\theta}\partial_\mu(\phi - \phi^*) \\ &+ \frac{i}{\sqrt{2}}\theta\theta\overline{\theta}\sigma^\mu\partial_\mu\psi + \frac{i}{\sqrt{2}}\overline{\theta\theta}\theta\sigma^\mu\partial_\mu\overline{\psi} + \frac{1}{4}\theta\theta\overline{\theta\theta}\Box(\phi + \phi^*) \; . \end{aligned} \tag{A.13}$$

In the case of vector field (A.11) the vector boson field A^μ is the coefficient of $\theta\sigma^\mu\overline{\theta}$. In hermitian field $\Phi + \Phi^\dagger$ the coefficient standing at this combination is $i\partial_\mu(\phi - \phi^*)$, i.e. gradient of a real scalar, something very similar to the gauge transformation in the ordinary $U(1)$ gauge theory. So that let's define SUSY generalization of a gauge transformation:

$$V \to V + \Phi + \Phi^*$$

Under this transformation the bosonic and fermionic fields do

$$\begin{aligned} C &\to C + \phi + \phi^* \\ \chi &\to \chi - i\sqrt{2}\psi \\ M + iN &\to M + iN - 2iF \\ A_\mu &\to A_\mu - i\partial_\mu(\phi - \phi^*) \\ \lambda &\to \lambda \\ D &\to D \end{aligned}$$

We observe, that λ and D are gauge invariant - this will be important in constructing Lagrangian. Next, remembering that a chiral superfield has 4 bosonic and 2 fermionic degrees of freedom, we can choose the gauge (i.e. the transforming chiral superfield) in such a way that C, χ, M and N are identically zero and still has one "ordinary" gauge degree of freedom remaining. This gauge is called Wess-Zumino (WZ) gauge.

Applying WZ gauge greatly simplifies the form of vector superfield, making it easier to calculate infinitesimal SUSY transformation. Nevertheless, the calculation and results are still not particularly enlightening, so I will only quote one important conclusion: as in the case of chiral superfield, the coefficient at $\theta\theta\overline{\theta\theta}$ (i.e. the largest number of θ's) transform itself into total derivative, making itself useful in constructing Lagrangian.

A.3 Constructing SUSY Lagrangian

If we want to turn SUSY into a regular theory, we must construct its Lagrangian. The natural demand is the invariance of the action under all symmetries, including SUSY. The space-time invariance is already solved, so our demand on the Lagrangian is

$$\delta_S \int \mathrm{d}^4 x \mathscr{L}(x) = 0 \,,$$

where δ_S is infinitesimal SUSY transformation. In the previous sections we discovered that this is the property of F-terms in chiral superfields and D-terms in vector superfields. Because they both are the coefficients standing at the highest number of θ's ($\theta\theta$ and $\theta\theta\overline{\theta}\overline{\theta}$, respectively), we can write the action as

$$S = \int \mathrm{d}^4 \left(\int \mathrm{d}^2\theta \mathscr{L}_F + \int \mathrm{d}^2\theta \mathrm{d}^2\overline{\theta} \mathscr{L}_D \right) .$$

The integration over Grassmann variables ensures that only coefficients of $\theta\theta$ and $\theta\theta\overline{\theta}\overline{\theta}$ survive and all other vanish. For details about the integration of Grassmann variables see for example [102] or any other QFT textbook.

Our basic blocks are chiral and vector superfields. What can we construct from them? First notice, that if Φ_1 and Φ_2 are chiral superfields, $\Phi_1\Phi_2$ is also a superfield of the same chirality. So we can construct new terms as a product of chiral superfields. Let's have a look on the F-term of the product of the two superfields (all other terms are skipped, as they will vanish in the integration):

$$\Phi_1\Phi_2 \,|_{\theta\theta} = \phi_1 F_2 + \phi_2 F_1 - \psi_1\psi_2 \,. \tag{A.14}$$

where $|_{\theta\theta}$ denotes the evaluation of only those terms that are proportional to $\theta\theta$. Now we can start to see some physics in SUSY: the last term in previous equation looks like the fermion mass term. We can also make a product of three chiral superfields:

$$\Phi_1\Phi_2\Phi_3 \,|_{\theta\theta} = \phi_1\phi_2 F_3 + \phi_1 F_2 \phi_3 + \phi_1\phi_2 F_3 - \psi_1\phi_2\psi_3 - \phi_1\psi_2\psi_3 - \psi_1\psi_2\phi_3 \,. \tag{A.15}$$

It is easy to see that the last three terms are in fact scalar-fermion-fermion interaction. Now we would like to continue in this fashion, but it would not do any good, because in product of 4 superfields we would get terms with the mass dimension higher than 4 and then the Lagrangian would lose its renormalizability.

Instead, we can construct something else: a product of the chiral superfield and its conjugate. In this case the result would not be chiral but a vector superfield. We need L-chiral field in R-representation (eq. (A.12)). After evaluation of the product of a chiral field with with its conjugate we can easily check, that the D-term is

$$\Phi\Phi^\dagger \,|_{\theta\theta\overline{\theta}\overline{\theta}} = FF^* - \phi\Box\phi^* - i\overline{\psi}\sigma_\mu\partial^\mu\psi \,. \tag{A.16}$$

Here we can clearly identify the kinetic term for both scalar and fermionic component. We can also see, that there is no kinetic term for F, indicating it can be integrated out.

First step in the process of getting rid of F is to define a superpotential f:

$$f(\Phi_i) = \sum_i k_i\Phi_i + \frac{1}{2}\sum_{i,j} m_{ij}\Phi_i\Phi_j + \frac{1}{3}\sum_{i,j,k} g_{i,j,k}\Phi_i\Phi_j\Phi_k \,. \tag{A.17}$$

Superpotential is therefore formal expression of the fact, that the F-term Lagrangian is constructed from product of superfields. Also, we have seen that it contains mass and interaction

terms, so that is where the name "potential" came from. Note that is a function only of the superfields and not of their conjugates. This is the consequence of the requirement of the SUSY invariance.

The superpotential can be used to rewrite SUSY Lagrangian in a compact way:

$$\mathscr{L} = \sum_i (F_i F_i^* + |\partial_\mu \phi_i|^2 - i\overline{\psi_i}\sigma_\mu \partial^\mu \psi_i) + \left[\sum_j \frac{\partial f(\phi_i)}{\partial \phi_j} F_j - \frac{1}{2} \sum_{j,k} \frac{\partial^2 f(\phi_i)}{\partial \phi_j \partial \phi_k} \psi_j \psi_k + h.c. \right] . \quad \text{(A.18)}$$

The first sum is the D-term Lagrangian, where we have done integration per partes. Compare to the eq. (A.16). The second is the F-term in terms of superpotential - it is straightforward to convince oneself that it reproduces the equations (A.14) and (A.15). Now Euler-Lagrange equations of motion for the F_j are

$$F_j = - \left[\frac{f(\phi_i)}{\partial \phi_j} \right]^* .$$

so the Lagrangian is

$$\mathscr{L} = \mathscr{L}_{kin} - \left[\sum_{j,k} \frac{\partial^2 f(\phi_i)}{\partial \phi_j \partial \phi_k} \psi_j \psi_k + h.c. \right] - \sum_j \left| \frac{\partial f(\phi_i)}{\partial \phi_j} \right|^2 . \quad \text{(A.19)}$$

The last missing piece are the gauge interactions and gauge kinetic terms. To find the first, usual way is to do SUSY version of minimal coupling: $\Phi^\dagger \Phi \to \Phi^\dagger e^{2gV} \Phi$. We can now expand the exponential function in powers of θ (again, there are only several first terms) and work out the the multiplication. The term proportional to $\theta\theta\overline{\theta}\overline{\theta}$ is

$$\Phi^\dagger e^{2gV} \Phi \mid_{\theta\theta\overline{\theta}\overline{\theta}} = |D_\mu \phi|^2 - i\overline{\psi}\sigma_\mu D_\mu \psi + g\phi^* D\phi + ig\sqrt{2}(\phi^* \lambda\psi - \overline{\lambda\psi}\phi) + |F|^2 . \quad \text{(A.20)}$$

In this equation the ordinary gauge covariant derivative was introduced: $D_\mu = \partial_\mu + igA_\mu$, so that the first two terms describes normal scalar-gauge boson interaction and fermion-gauge boson interaction. More interesting is the fourth term where we have field λ, i.e. SUSY partner of A_μ called gaugino. This means that this term describes fermion-(Higgs)boson-gaugino (or higgsino-sfermion-gaugino) interaction.

Final step is the construction of the gauge kinetic term. First, we have to find SUSY equivalent of the field strength $F_{\mu\nu}$. Good candidate is the field

$$W_\alpha = -\frac{1}{4} \overline{DD} D_\alpha V .$$

It is easy to show that this superfield is left-chiral, i.e. $\overline{D} W = 0$. This means that the product of these fields is also left-chiral and its $\theta\theta$ component can be used in the Lagrangian:

$$\frac{1}{32g^2} W_\alpha W^\alpha \mid_{\theta\theta} = -\frac{1}{4} F_{\mu\nu} F^{\mu\nu} + \frac{1}{2} DD + (-\frac{i}{2} \lambda \sigma_\mu \partial^\mu \overline{\lambda} + \text{h.c.}) . \quad \text{(A.21)}$$

Apart from expected ordinary gauge kinetic term, we have also obtained kinetic term for gaugino. Note that everything was done for abelian U(1) gauge theory. If we suppose non-abelian gauge group, we would have more indices and lengthier expressions. Most significant difference would be the term with the gauge boson-gaugino interactions.

Last step is to integrate out the unphysical field D. It is done in the same way as in case of F-term - we calculate Euler-Lagrange equations of motion:

$$D = -g \sum_{ij} \phi_i^* \phi_j \ .$$

The total contribution from the third term of eq. (A.20) and second term of eq. (A.21) is

$$-V_D = -\frac{1}{2} \left| \sum_{i,j} g \phi^* \phi_j \right|^2 \ . \tag{A.22}$$

The complete SUSY Lagrangian is now combination of equations (A.19), (A.20), (A.21) and (A.22).

Acknowledgement

This thesis would never come to an existence without the help of many people. I would like to use this opportunity to thank at least some of them.

First, I would like to thank my supervisor Stefania Xella, for providing me an opportunity to obtain my PhD at the Niels Bohr Institute. I am very grateful that she helped me found in the beginning the topics which now form core parts of this thesis. I would like to thank her for the patient and reliable support during all the time of my PhD. I especially appreciate the help and care she provided in the final months of my study without which this thesis will never be finished.

I am also very grateful to Mogens Dam, for all his insightful comments, and always having time for my questions.

The work on the study of the light Higgs boson will not possible without the discussions with and support from the members of HSG4 group in ATLAS. Out of many, I would especially like to thank all group conveners: Markus Schumacher, Junichi Tanaka, Jürgen Kroseberg and Trevor Vickey. They all provided important guidance and comments in a different stages of my analysis.

I would like to thank to the $a_1 \to \mu\mu$ analysis subgroup, namely to Yi Yang, Hal Evans and Chris Potter. Our weekly and bi-weekly meetings provided invaluable feedback to my work.

The study of the performance of the tau trigger will be impossible without the support of the tau trigger group. There, I would like to thank to Olya Igonkina, Mansoora Shamim and Jörg Mechnich for many useful discussions about the tau trigger and their support during my stay at CERN.

When implementing the new electron-muon topological trigger, many people from the trigger group provided useful comments and made sure I prepared a functional algorithm. I would like to thank to Alessandro Tricolli, Tomasz Bold, Brian Petersen, Simon George, Fabrizio Salvatore and David Strom for supporting me during this work.

I am deeply indebted to all members of the ATLAS collaboration for designing and running the detector I used in this thesis, as well as for providing large amount of software and support to help with the analysis.

During my whole PhD study I profited and enjoyed a lot the friendly working environment at the Niels Bohr Institute. I would like to thank group leaders Dines Hansen and Peter Hansen for supporting and funding all my activities. I wish to cordially thank to all my friends and colleagues for the great time I was having in Copenhagen. I would especially like to thank Peter Kadlečík for many interesting discussions and support when needed and to Zofia Czyczula for showing me many interesting places in Copenhagen and Geneva I would never have found on my own and for many other good advices. I am also grateful to Jørgen B. Hansen for the checking of the theory part of this thesis and to Gorm Galster for checking the Danish abstract.

I would also like to express my gratitude towards our computing administrators Björn Nilsson, Petter Urkedal and Frederic Orellana for always providing prompt support and to all our group secretaries Jane Nielsen, Helle Rasmussen and Anette Uhl for solving all my administration problems.

Last, but not the least, I am very grateful to my family and friends for their constant support even when I, for the lack of time, often neglected them in the past years.